Mémoire présenté en vue de l'obtention de l'Habilitation à Diriger des Recherches

Caroline Martel

To cite this version:

Caroline Martel. Mémoire présenté en vue de l'obtention de l'Habilitation à Diriger des Recherches. Géologie appliquée. Université d'Orléans, 2009. tel-00403123

Mémoire présenté en vue de l'obtention de l'Habilitation à Diriger des Recherches

par

Caroline MARTEL

Chargée de Recherche

à l'Institut des Sciences de la Terre d'Orléans (ISTO)

Soutenue le 26 Juin devant le jury composé de

M. Pietro ARMIENTI	**Professeur, Università de Pisa, Italie ……….... Rapporteur**
M. Edouard KAMINSKI	**Professeur, IPG Paris ……………………….... Rapporteur**
M. Didier LAPORTE	**Directeur de Recherche, LMV Clermont Fd .... Rapporteur**
M. Michel PICHAVANT	**Directeur de Recherche, ISTO Orléans …….... Examinateur**
M. Jean-Louis BOURDIER	**Professeur, ISTO Orléans ……………………... Examinateur**

SOMMAIRE

Caroline MARTEL

Née le 5 septembre 1969 à Guérande (Loire-Atlantique)

Nationalité Française
Mariée, 2 enfants

Domicile: 76 Impasse des Chardonnerets
45590 Saint Cyr en Val

POSTE ACTUEL

Chargée de recherche à l'Institut des Sciences de la Terre d'Orléans depuis Avril 2001.

ISTO
1A rue de la Férollerie
45071 Orléans cedex 2 (France)

Téléphone: 33 (0)2 38 25 52 52
Fax: 33 (0)2 38 63 64 88
e-mail: cmartel@cnrs-orleans.fr

ACTIVITE DE RECHERCHE ACTUELLE

- Etude expérimentale des processus syn-éruptifs (dégazage, cristallisation) des volcans d'arc ; Exemple de la Montagne Pelée (Martinique)
- Conditions pré-éruptives des trachytes de la chaîne des Puys
- Rhéologie / perméabilité des magmas bulleux

ACTIVITE DE RECHERCHE POST-DOCTORALE

Décembre 1996 à Mars 2001
Post-doctorat à l'Institut de Géologie de Bayreuth (BGI), Allemagne

- Investigation of the fragmentation process under rapid decompression of silicic bubble- and crystal-bearing melts
- In-situ high-pressure and high-temperature bubble growth in silicic melts
- Decompression experiments as an insight into magma ascent rates.

CURSUS UNIVERSITAIRE

Juin 1996
Doctorat "Matériaux et Minéraux", Université des Sciences d'Orléans (mention: très honorable avec félicitations du Jury)
Intitulé : Conditions pré-éruptives et dégazage des magmas andésitiques de la Montagne Pelée (Martinique, F.W.I.): étude pétrologique et expérimentale
Direction : M. Pichavant, J.-L. Bourdier et H. Traineau

Juillet 1992:
DEA "Processus magmatiques et métamorphiques – Volcanologie ", Université Blaise Pascal de Clermont-Ferrand
Stage de recherche : "Croissance des volcans: effet de la mise en place des systèmes intrusifs"; Direction : J.-F. Lénat et A. Provost

Juin 1991 : Maîtrise de géologie, Université Blaise Pascal de Clermont-Ferrand
Juin 1990 : Licence de géologie fondamentale et appliquée, Université des sciences de Nantes
Juin 1989 : DEUG B Sciences de la Vie et de la Terre, Université des Sciences de Nantes
Juin 1987 : Baccalauréat série D, Lycée Grand Air, La Baule

AVANT-PROPOS

Comme pour beaucoup, les volcans représentent pour moi une fascination d’enfance, les coulées de lave rougeoyante de l’Etna en 1973 y sont forcément pour quelque chose… Les Sciences de la Terre et plus particulièrement la Volcanologie sont alors devenues le fil directeur de mes études, avec la ferme intention, dès le collège, d’étudier le plus loin possible cette matière, au mépris du manque évident de débouchés ! Cet entêtement (pour être au moins sûre de ne rien regretter plus tard) m'a poussé à quitter la faculté des Sciences de Nantes qui enseignait naturellement beaucoup plus de sédimentologie que de magmatisme, pour des régions plus sombres, mais plus volcaniques... A Clermont-Ferrand, la découverte de vrais volcans au cours de stages de terrain (Massif Central, Stromboli, Etna, Piton de la Fournaise) a été un ravissement. Marcher sur les coulées incandescentes de l’Etna en 1992 (pensée pour Guy Camus), s’intoxiquer au soufre du Vulcano, gérer une crise sismique à 4 heures du matin à l’Observatoire du Piton de la Fournaise (merci à Jean-François Lénat) resteront d’intenses et inoubliables souvenirs. L’incertitude en Juillet 1992 sur l’obtention de la bourse de thèse suite à mon stage de DEA sur la modélisation de la croissance du dôme du Piton de la Fournaise par injections de dykes m’a incité à choisir un sujet de magmatologie sur le volcanisme d’arc des Antilles, proposé au CRSCM à Orléans. Il est clair que l'irrésistibilité du sujet ne tenait pas dans sa localisation géographique, ni a priori dans son programme de pétrologie expérimentale… mais plutôt dans la promesse de mission d’échantillonnage sur la Montagne Pelée et sa fameuse éruption du 8 mai 1902.

La région Orléanaise est certes peu volcanique (à tous points de vue), la Montagne Pelée a priori moins flamboyante et télégénique que le Piton de la Fournaise, et la pétrologie expérimentale un domaine obscur de premier abord peu convivial! Mais après le stage d’échantillonnage en Février 1993, ce volcan va révéler toute son attractivité : une grande diversité de styles éruptifs (et un pinceau à la place du traditionnel marteau pour l'échantillonnage), un gros potentiel explosif (source de tant de frénésie scientifique depuis la catastrophe du 8 mai 1902) et un délicieux planteur... Merci beaucoup à Hervé Traineau et Jean-Louis Bourdier pour cette initiation (au terrain, biensûr). Et finalement, la pétrologie expérimentale va devenir une véritable hygiène de vie scientifique, la seule approche en laquelle on croît vraiment. Un grand merci à Michel Pichavant pour m’avoir transmis tant d’enthousiasme face aux tâches ménagères (passer l’aspirateur dans le Gros Bleu…), ainsi qu'à Bruno Scaillet et François Holtz pour les discussions autour du Gros Bleu. Cet encadrement de travail privilégié m'a permis de réaliser la thèse de doctorat dans des conditions particulièrement agréables.

Pendant les cinq ans qui suivent, la Montagne Pelée est mise en stand-by au profit de problématiques dynamiques de décompression et de fragmentation magmatiques réalisées au cours de mon post-doctorat au Bayerisches GeoInstitut (BGI) de Bayreuth en Allemagne. Trois premières années mémorables passées à exploser des échantillons dans une bombe de fragmentation, pour lesquelles I sincerely thank Don Dingwell pour la confiance qu’il m’a accordée et vielen Dank à Oliver Spieler pour sa grande disponibilité et précieuse aide technique. Suit un an pour une initiation au jouet favori d’Hélène Bureau, la cellule à enclume de diamant, afin d’observer le dégazage in-situ des magmas (merci!), puis une dernière année dédiée à la décompression des magmas de Soufrière Hills de Montserrat pour en étudier la cristallisation et le dégazage, pour laquelle je danke sehr Burkhard Schmidt (und für die andere sieben Jahren auch).

Avec mon intégration en 2001 en tant que Chargée de Recherche à l'ISTO sous la direction d'Elisabeth Lallier-Vergès, mes premiers amours reprennent : la Montagne Pelée et son troublant potentiel explosif. Enrichie d'expériences dynamiques de dégazage et de cristallisation par décompression, je tente (encore actuellement) des explications au moyen d'une systématique d'expériences de décompressions. Tout n'est pas encore résolu, et pourtant, la Montagne Pelée est a priori un cas d'école, quand on connaît la complexité de certains autres systèmes volcaniques… Force est d'avouer que des réservoirs magmatiques profonds à la dynamique éruptive, les volcans d'arc renferment un certain nombre de mystères quant à la nature de leurs éruptions futures, dont l'élucidation risque encore de nécessiter quelques années d'étude. C'est pour tenir sur cette longue distance que j'ai besoin du soutien de Rémi, Timothé et Lily…

L'objectif principal de mes travaux a été de rechercher l'origine de la dualité éruption effusive / explosive que l'on observe fréquemment sur les volcans d'arc, et ce mémoire présente une synthèse de mes travaux de recherche de 1993 à 2008, dont la présentation ne suit pas l'ordre chronologique de leur réalisation, mais une logique naturellement volcanique, du réservoir de stockage du magma à l'éruption en surface. Ils sont présentés sous la forme d'articles publiés agrémentés d'une à trois pages de résumé et des projets qui les ont complétés (stages de M1, M2, thèses). Le mémoire se termine par les projets d'étude envisagés pour les prochaines années.

PARTIE I- SYNTHESE DE L'ACTIVITE DE RECHERCHE

I.1- PROBLEMATIQUE SCIENTIFIQUE GENERALE

A la suite de mon DEA concernant les volcans "rouges" à coulées de lave, je me suis intéressée au cours de mon doctorat aux éruptions très explosives et dangereuses des volcans "gris". De facto, de problématiques de surveillance et de prévision des éruptions, je me suis intéressée à des problématiques de compréhension fondamentale des mécanismes éruptifs. Le volcanisme d'arc résulte de la subduction d'une plaque océanique sous une autre plaque océanique (ex : Arc insulaire des Aléoutiennes, du Japon, des Petites Antilles; Figure 1) ou sous une plaque continentale (ex : Arc continental des Andes ou de la Chaîne des Cascades).

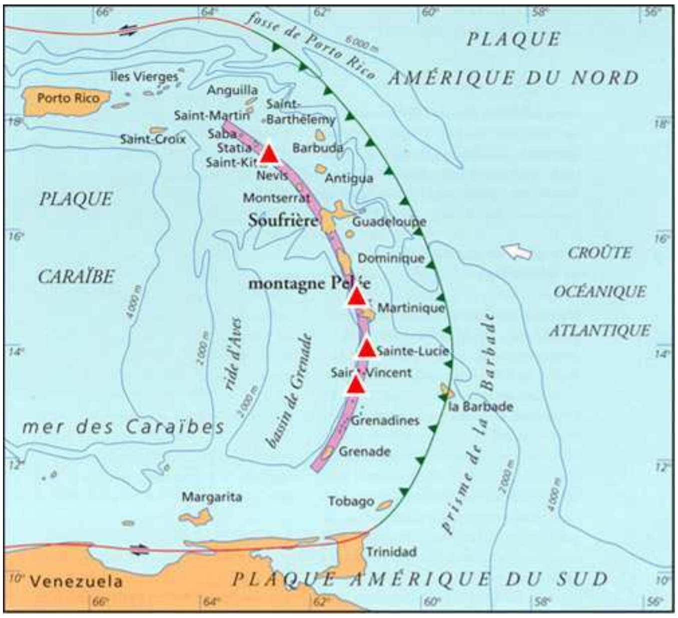

Figure 1. Arc volcanique des Petites Antilles. L'arc résulte de la subduction de la croûte océanique de la Plaque Nord Américaine sous la plaque océanique des Caraïbes, avec une vitesse d'avancement relativement faible, de 2 cm/an en moyenne.

Les volcans d'arc se caractérisent par une grande diversité de styles éruptifs, allant de la croissance effusive de dôme à des éruptions très explosives. Parmi les éruptions magmatiques explosives, on peut citer les évènements associés à la destruction d'un dôme de lave, telles que les nuées ardentes de déstabilisation gravitaire de type Mérapi, les déferlantes ou nuées ardentes dirigées latéralement de type Péléennes et les nuées ardentes verticales de type Vulcaniennes. Le paroxysme de l'explosivité est représenté par les éruptions Pliniennes, caractérisées par l'émission en régime d'une colonne de pyroclastes ponceux. La description de ces éruptions et des produits émis a été extensivement étudiées dans la littérature, parfois sous des appellations différentes. La nomenclature des dynamismes éruptifs et des dépôts que j'utiliserai dans ce mémoire est explicitée dans les publications rassemblées dans le chapitre suivant et est ici rappelée brièvement dans le Tableau 1. Au cours de leur histoire, certains de ces volcans n'ont montré qu'un style éruptif particulier, alors que d'autres alternent des éruptions à dômes et déstabilisations associées avec des éruptions très explosives de type Plinien. Certains volcans alternent même de manière réversible les styles éruptifs au cours de la même séquence éruptive.

Tableau 1. Nomenclature et succincte description des principales éruptions magmatiques et dépôts associés (faciès dominant) du volcanisme d'arc.

Type éruptif	**Degré d'explosivité**	**Dynamique de mise en place**	**Extension des dépôts / Granoclassement**	**Taille / Texture des pyroclastes (faciès dominant)**
Dôme	effusif	Extrusion du magma sous forme d'un dôme	Localisés au dôme	Magma cristallisé et dense; faible porosité (< 30 vol. %)
Nuée ardente de type Mérapi	peu explosif	Ecroulement gravitaire du dôme avec légère auto-explosivité	Canalisés dans les vallées	Blocs millimétriques à métriques / très cristallisés / faiblement vésiculés (< 30 vol. %)
Déferlante ou Nuée ardente de type Peléen	très explosif	Explosion latéralement dirigée à partir d'un dôme sous forme d'écoulement très turbulent	Large débordement des vallées / Peu de granoclassement	Cendres et blocs centimétriques / très cristallisés / faiblement vésiculés (< 30 vol. %)
Nuée de type vulcanienne	moyennent explosif	Explosions verticales courtes et répétées à partir du dôme sous forme d'écoulements turbulents	Faible extension, dépôts canalisés dans les vallées + retombées	Cendres et blocs ponceux centimétriques / cristallisés / vésiculés (~ 30-70 vol. %)/ Bombes en croûtes de pain
Colonne et retombées Pliniennes	très explosif	Colonne verticale en régime très riche en gaz	Très large extension des dépôts; bien calibrés	Ponces cendreuses à centimétriques / très peu cristallisées / très vésiculées (~ 60-80 vol. %)
Coulées ponceuses associées	moyennement explosif	Coulées basales résultant de la décroissance énergétique de la colonne	Canalisées dans les vallées; granoclassement	

Le problème principal posé par le volcanisme d'arc est que l'on ne peut pas prédire le style (ni la date) de la prochaine éruption d'un système volcanique, ce qui engendre un haut degré de complexité quant à l'établissement de cartes de risques pour les populations. Ce n'est généralement pas le cas du volcanisme de point chaud ou de systèmes extensifs (ride océanique ou continentale) pour lesquels les produits sont émis sous forme de coulées ou de fontaines de lave faiblement explosives. Pour ce dernier type de volcans, la problématique volcanique n'est d'ailleurs pas vraiment de savoir sous quelle forme va sortir le magma, mais plutôt de prédire temporellement et géographiquement le point d'émission du magma et la nature et quantité de gaz relâchés. Pour le volcanisme d'arc en revanche, la problématique est bien en amont, au niveau de la compréhension des processus fondamentaux menant à une éruption effusive ou explosive et des causes des transitions souvent observées entre ces deux styles.

En raison de leur rareté et de leur dangerosité, l'observation directe d'éruptions est en général difficile (rappelons nous le couple Kraft tentant d'observer une déferlante de l'Unzen en 1991). En revanche, lorsque cette observation est possible, les avancées dans la compréhension des mécanismes éruptifs et des dépôts associés sont considérables. C'est actuellement le cas de Soufrière Hills à Montserrat, volcan en éruption depuis 1995, qui permet peu à peu de mieux comprendre les mécanismes associés aux éruptions à dôme de type nuées vulcaniennes, de relier les caractéristiques des dépôts au dynamisme éruptif, et de déceler les éventuels prémices des crises éruptives. Cette surveillance active est plutôt rare, et de manière générale pour ces volcans d'arc, les objets dont nous disposons pour étudier les éruptions sont quelques témoignages historiques et les produits éruptifs qui sont alors plus difficilement interprétables en termes de dynamisme éruptif, d'estimation des durées d'éruption, du temps écoulé entre deux évènements, et par conséquent d'échelles de temps de remplissage des réservoirs et d'ascension des magmas.

L’avancement de la recherche dans le domaine de la compréhension du volcanisme d’arc passe avant tout par l'investigation des processus pré- et syn-éruptifs (du réservoir au conduit magmatiques). Ma contribution à cet effort collectif est l'apport d'information par une approche expérimentale, dont la finalité est de déterminer des conditions de stockage et d’ascension des magmas d’arc en termes de pression (profondeur), température, conditions d’oxydoréduction, teneurs en éléments volatils, et des cinétiques des processus de dégazage et de cristallisation. La méthode est empirique, consistant en une adéquation de composition et de texture entre des produits naturels d'éruption et des produits obtenus par des expériences sous des conditions parfaitement contrôlées. L’intérêt apporté par l’expérimentation pour cette problématique est qu’elle permet de replacer de vraies compositions de magma dans des conditions magmatiques réalistes, auxquelles on n'a pas accès naturellement dans le volcan. Elle est en ce sens l’alliée idéale des études fines de terrains qui en constituent le point de départ (par le choix des produits et de la gamme de conditions expérimentales à investiguer) et la finalité (ce sont ces caractéristiques naturelles qu'il faut reproduire expérimentalement) et alimente en retour en base de données et en validation des processus les modélisations numériques des processus éruptifs.

L’idée directrice de mes travaux de recherche a été de vérifier si les raisons menant à des éruptions effusives ou explosives étaient dues à des différences de conditions de stockage du magma, notamment des variabilités en teneurs initiales en gaz dissous, ou si elles résultaient de différentes évolutions des caractéristiques du magma au cours de son ascension dans le conduit volcanique (Figure 2).

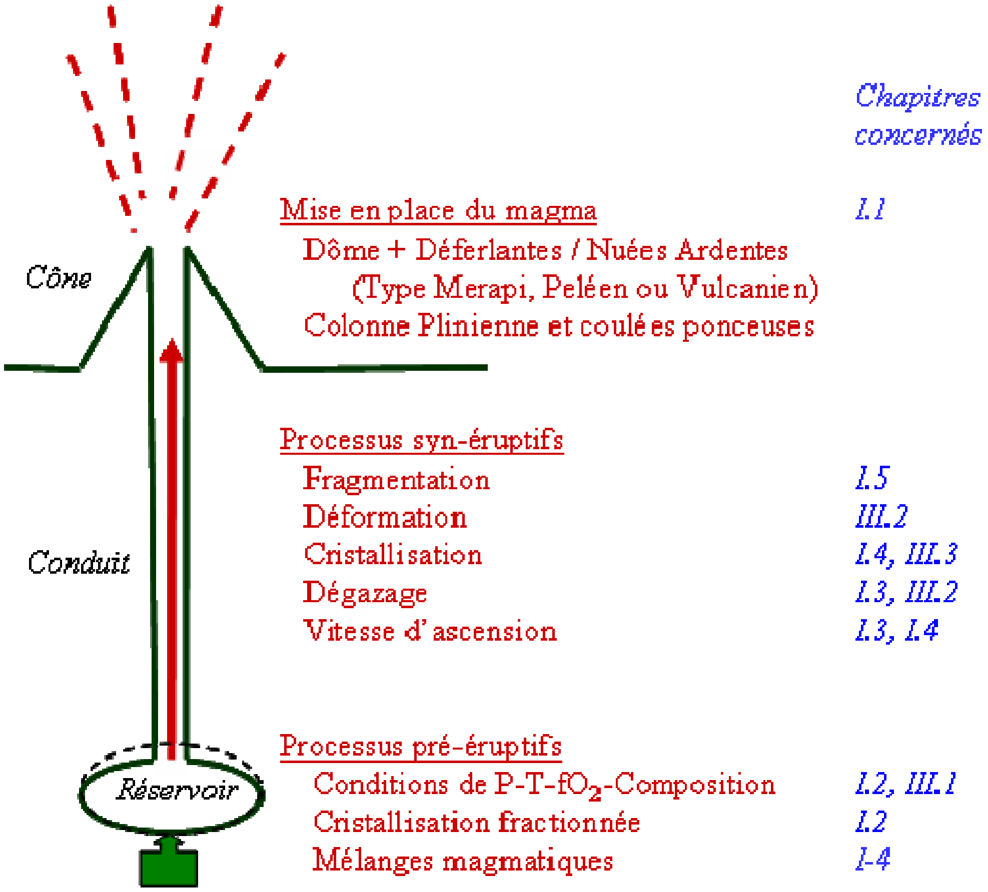

Figure 2. Schéma d’un volcan et processus pré- et syn-éruptifs associés. Les numéros en bleu à droite font références aux numéros des chapitres concernés par les processus indiqués.

Le Tableau 2 présente les différentes questions que j'ai traitées en relation avec la problématique posée précédemment. Le plan du mémoire proposé ci-après pour présenter mes travaux de recherche ne suit pas cette chronologie, mais une démarche d'étude des conditions pré-éruptives puis des conditions d'éruption au travers des processus de dégazage, cristallisation et fragmentation magmatique.

Tableau 2. Récapitulatif chronologique de l'activité de recherche

Année	Fonction	Institut	Titre du projet	Méthodologie		
1992	*DEA*	*LMV, Clermont-F*^{d}	*Croissance du dôme du Piton de la Fournaise (Réunion) par injection de dykes*			***M***
1992 1996	Doctorat	(CRSCM) ISTO, Orléans	Détermination expérimentale des conditions pré-éruptives de la Montagne Pelée (Martinique)	**N**	**E**	
1996 2001	Post-doctorat	BGI, Bayreuth (Allemagne)	Fragmentation des magmas siliceux riches en bulles et cristaux		**E**	
			Etude in-situ du dégazage des magmas		**E**	**M**
			Simulation de l'ascension des magmas par des expériences de décompression		**E**	
2001 actuel	CR	ISTO, Orléans	Cinétiques d'ascension des magmas de la Montagne Pelée	**N**	**E**	
			Conditions pré-éruptives des trachytes de la Chaîne des Puys (Massif Central)	**N**	**E**	
			Rhéologie des magmas bulleux		**E**	
			Modélisation de la croissance des microlites de plagioclase	**N**	**E**	**M**

N = Approche naturaliste; **E** = Pétrologie et Simulation expérimentales; **M** = Modélisation numérique.

I.2- CONDITIONS PRE-ERUPTIVES

L'étude des causes de l'alternance des éruptions à dôme et Pliniennes est tout d'abord recherchée au niveau des conditions de stockage des magmas d'arc, notamment au travers d'éventuelles différences de teneurs en éléments volatils dissous dans le magma du réservoir. Un magma riche en gaz dissous dans la chambre magmatique serait potentiellement plus explosif lors de l'exsolution de ces gaz qu'un magma initialement appauvri en élément volatils. La détermination expérimentale des conditions pré-éruptives des éruptions Pliniennes et à dôme des éruptions récentes de la Montagne Pelée de la Martinique (Arc des Petites Antilles) a constitué l'objet de mon sujet de thèse à Orléans (1992-1996). A l'époque, il n'y avait qu'une publication existante sur la détermination expérimentale des conditions pré-éruptives d'un système volcanique, i.e., Mount St. Helens (Rutherford et al., 1985), dont nous nous sommes inspirés. Notre objectif était de définir un jeu de conditions de pression, température, fugacité d'oxygène et de teneurs en éléments volatils dissous réaliste pour la chambre magmatique de la Montagne Pelée, par reproduction expérimentale des compositions des phases en équilibre dans le réservoir (phénocristaux + liquide silicaté les baignant). Les phénocristaux sont souvent chimiquement zonés, témoignant d'une histoire complexe. Dans le but d'étudier les conditions prévalant juste avant le déclenchement de l'éruption, les compositions de bordure de ces phénocristaux ont été privilégiées, ayant plus de chance d'être en équilibre thermodynamique avec le liquide environnant. Cependant, ce liquide silicaté baignant les phénocristaux dans la chambre magmatique ne se retrouve pas sous sa forme initiale dans les produits émis en surface, en raison du dégazage et de l'éventuelle cristallisation de microlites subis au cours de l'ascension du magma dans le conduit. Les seuls témoins de ce liquide originel sont les inclusions vitreuses piégées dans les phénocristaux lors de leur croissance, à condition qu'elles n'aient pas subi de modifications après leur piégeage (Figure 2).

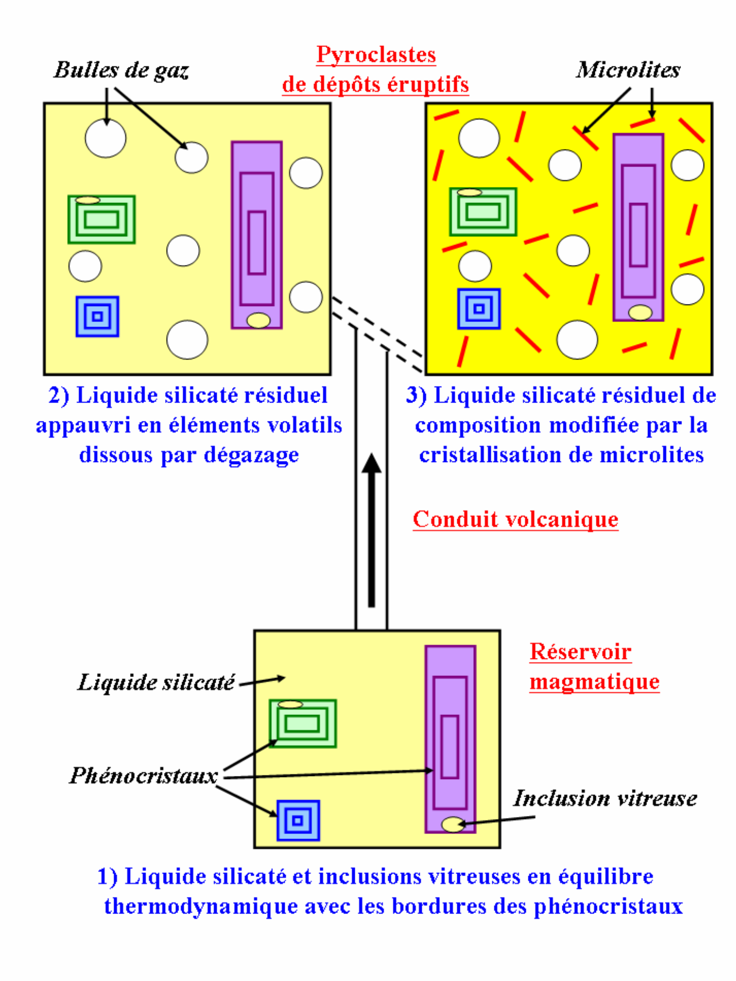

Figure 2. Evolution de la composition du liquide silicaté en équilibre thermodynamique avec les bordures des phénocristaux au cours de l'éruption. Le liquide silicaté résiduel subit des modifications de composition chimique, notamment de sa teneur en volatils dissous et en silice, par dégazage et cristallisation des microlites lors de son ascension dans le conduit volcanique. Sa composition originelle, en équilibre thermodynamique avec les compositions de bordures des phénocristaux, a pu être préservée par les inclusions vitreuses piégées lors de la croissance des phénocristaux dans la chambre magmatique, à condition que ces inclusions vitreuses n'aient pas subi de modifications post-piégeage (fuite d'éléments volatils, cristallisation ou dévitrification).

L'intérêt de connaître la composition originelle du liquide silicaté dans la chambre magmatique réside dans le fait que c'est la phase qui contient les éléments volatils dissous, et que la quantité et la nature de ces volatils a une influence directe sur le processus de dégazage du magma. De plus, l'adéquation des compositions des verres naturels et expérimentaux constitue une ultime validation des conditions pré-éruptives proposées, dans la mesure où un désaccord de proportion ou de composition des cristaux expérimentaux par rapport à l'assemblage naturel est directement enregistré par la composition du verre expérimental (phase résiduelle).

Ce type d'approche a été mis en œuvre afin de déterminer les conditions pré-éruptives de la Montagne Pelée par adéquation des produits naturels et expérimentaux, donnant lieu à plusieurs publications :

- les caractéristiques compositionnelles et texturales des produits naturels (Martel et al., 2000a)
- les conditions pré-éruptives de la Montagne Pelée (Martel et al., 1998 ; présenté ci-après)
- l'effet de l'eau et de la fugacité d'oxygène sur les relations de phases des andésites entre 2 et 4 kbars (Martel et al., 1999).

Article présenté : MARTEL C., PICHAVANT M., BOURDIER J.-L., TRAINEAU H., HOLTZ F. & SCAILLET B. (1998) Pre-eruptive conditions and control of explosive volcanism at Mount Pelée (Martinique, F.W.I.). *Earth Planet. Sci. Lett. 156, 89-99.*

Travaux réalisés dans le cadre de la thèse de doctorat : MARTEL C. (1996) Conditions pré-éruptives et dégazage des magmas andésitiques de la Montagne Pelée (Martinique, F.W.I.): étude pétrologique et expérimentale. *Thèse de l'Université d'Orléans, 250 p.* Direction : M. Pichavant, J.-L. Bourdier et H. Traineau.

Financements : Bourse MRT ; **Moyens** : Programmes Nationaux sur les Risques Naturels (PNRN) de 1994 à 1997.

Au cours des derniers 5 000 ans de sa période récente d'activité, la Montagne Pelée a alterné 6 éruptions pliniennes et 12 éruptions à dôme, principalement des croissances de dômes associées à des nuées ardentes de type Mérapi et des déferlantes de type Peléen. Rappelons ici la tristement célèbre déferlante du 8 Mai 1902 qui entraîna la mort de 30 000 personnes et l'anéantissement de la ville de Saint Pierre. En Février 1993, nous avons échantillonné 3 dépôts pour mener les expériences d'équilibre de phase: le dôme en place de 1929, des blocs lithiques de la déferlante du 8 Mai 1902 et des ponces de la dernière retombée Plinienne (P1, 650 ans BP), texturalement et compositionnellement représentatifs des évènements respectifs, (roche totale andésitique, ~61 pds% SiO_2 ; Norme CIPW pour les 3 échantillons: ~$Qz_{16}Ab_{31}Or_6An_{28}Hy_{15}Di_3Ilm_1$). La porosité totale des échantillons, la proportion modale et la composition des phénocristaux, la composition et la teneur en éléments volatils dissous des verres résiduels et des inclusions vitreuses des phénocristaux, ainsi que les compositions des microlites de ces échantillons ont été analysés (Martel et al., 2000a). Ces échantillons naturels ont été fondus et hydratés en vue des expériences de cristallisation en autoclave à chauffage interne (ISTO, Orléans) sous contrôle des conditions de pression, température, fugacité d'oxygène et teneur en volatils dissous. La comparaison des assemblages et des compositions des phases naturelles et expérimentales a permis de définir un jeu de conditions de stockage du magma andésitique de la Montagne Pelée, identique pour les trois types éruptifs investigués (dôme de 1929, déferlante de 1902, retombée Plinienne de P1), à savoir une pression de 2 ±0.5 kbars, une température de 875-900°C, une fugacité d'oxygène de ΔNNO+ 0.4-0.8 et 5.3-6.3 pds% d'eau dissoute dans le liquide silicaté résiduel de composition rhyolitique (75-77 pds% SiO_2) soit une activité d'eau d'environ 0.9 (faible sous-saturation). Par conséquent, nous avons conclu que la bifurcation entre les éruptions pliniennes et éruptions à dôme de la Montagne Pelée n'était pas à attribuer à différentes conditions de stockage du magma dans le réservoir magmatique, notamment une variabilité de teneur en gaz dissous (comme il peut exister pour des chambres magmatiques de gros volume, tel le Bishop Tuff; Dunbar et Hervig, 1992). De fait, les causes de l'alternance entre les styles éruptifs est ici plutôt à rechercher au niveau de différences des conditions syn-éruptives.

ELSEVIER

Earth and Planetary Science Letters 156 (1998) 89–99

EPSL

Magma storage conditions and control of eruption regime in silicic volcanoes: experimental evidence from Mt. Pelée

C. Martel[a], M. Pichavant[a,*], J.-L. Bourdier[b], H. Traineau[c], F. Holtz[a], B. Scaillet[a]

[a] CRSCM-CNRS, 1A rue de la Férollerie, 45071 Orléans Cedex 2, France
[b] Département des Sciences de la Terre and UMR 6530, Université d'Orléans, BP 6759, 45067 Orléans, France
[c] BRGM, Service Géologique National, BP 6009, 45060 Orléans Cedex 2, France

Received 4 December 1996; revised version received 4 December 1997; accepted 26 December 1997

Abstract

Differences of eruption regimes in silicic volcanoes, e.g. effusive versus explosive, have commonly been ascribed either to stratification of volatiles in the magma storage region or to gas loss through permeable conduit walls. Recent Plinian and Pelean eruptions of silicic andesite magmas from Mt. Pelée (P1: 650 yr B.P., 1902, 1929) show no systematic variations in bulk rock and phenocryst and glass compositions. Rare coexisting Fe–Ti oxide pairs in Pelean products yield T between 840 and 902°C, and ΔNNO between +0.4 and +0.8. Pre-eruptive melt H_2O contents, calculated from plagioclase–melt equilibria, span values from 1.9 to 5.5 wt%. Glass inclusions from the P1 Plinian fallout have H_2O contents between 4.2 and 7.1 wt%. In contrast, the Pelean inclusions have H_2O contents commonly <3 wt%, due to post-entrapment modifications upon eruption. Phase equilibrium studies allow pre-eruptive conditions to be precisely determined and demonstrate that recent eruptions, either Plinian or Pelean, tapped magmas with melt H_2O contents of 5.3–6.3 wt%, stored at 2 ± 0.5 kbar, 875–900°C and ΔNNO = +0.4–0.8. Differences in eruptive style at Mt. Pelée are unrelated to systematic variations in pre-eruptive magmatic H_2O concentrations, but may be caused by contrasting modes of degassing in the conduit. © 1998 Elsevier Science B.V. All rights reserved.

Keywords: eruptions; magmas; experimental studies; Mount Pelée

1. Introduction

Arc volcanoes are capable of various styles of eruptive behaviour and of generating hazards of different types and magnitude. Understanding the factors that control eruptive styles and influence the transition between explosive and effusive eruptions is necessary for hazard assessment. A commonly proposed explanation for a sequence of initial explosive Plinian eruptions followed by effusion of lava domes has been based on the existence of pre-eruptive volatile gradients in the tapped magma body [1,2]. Recently, the volatile stratification model has been challenged and alternative explanations have been developed, assuming magma bodies with uniform volatile distributions. Mechanisms of gas loss through permeable conduit walls have been proposed to control the transition from explosive activity to dome formation [3–5]. The degassing model has received widespread recognition, yet several aspects have been criticized [6] and the model needs to be checked against well-characterized eruptive systems.

---

[*] Corresponding author.

0012-821X/98/$19.00 © 1998 Elsevier Science B.V. All rights reserved.
PII S0012-821X(98)00003-X

One way to distinguish between the volatile stratification and degassing models is to determine the pre-eruptive volatile (H_2O being the most important) content and distribution in magma bodies tapped by eruptions of different styles from a given volcano. Although there have been several determinations of pre-eruptive conditions in silicic magma chambers [7], few studies have attempted to relate in a systematic way the pre-eruptive volatile concentrations with the textural characteristics of eruption products and eruptive style. Differences in pre-eruptive volatile concentrations have been demonstrated between Plinian tephra and ignimbrite from both the Bishop Tuff and the Lower Bandelier Tuff [8–10]. In contrast, other studies [3,11] have shown that domes can be formed from H_2O-rich melt, provided that the eruptive environment allows the magma to degas passively, rather than explosively. The variably explosive deposits from the Taupo eruption were demonstrated to be derived from a magma that was homogeneous with respect to H_2O [12]. A lack of correlation between pre-eruptive H_2O content, determined from melt inclusions in phenocrysts, and explosivity has been demonstrated on two examples of peralkaline rhyolite [13,14].

Mt. Pelée is a key example of an active andesitic volcano. Recent activity includes both Plinian and Pelean (dome-forming) eruptions, providing an excellent opportunity to compare pre-eruptive H_2O contents between these two strongly contrasted eruptive styles. In this paper, compositional data on phenocrysts and glasses are used together with new experimental data to determine the pre-eruptive conditions for both Plinian and dome products. Our new data on Mt. Pelée indicate that differences in eruptive regime are unrelated to systematic variations of H_2O concentrations in the magma storage region, but instead reflect contrasting modes of degassing during ascent.

2. Mt. Pelée: recent activity and description of samples

Mt. Pelée (Martinique, FWI) is one of the active stratovolcanoes of the Lesser Antilles island arc. The 1902 dome-generated pyroclastic flows were among the first to be directly observed and described anywhere [15–17]. Since then, Mt. Pelée has been the type volcano for Pelean eruptions involving lava dome growth and associated nuées ardentes. A key aspect of the recent activity at Mt. Pelée is the duality of eruptive styles. The stratigraphic record for the last 13,500 years reveals alternating phases of Pelean (lava domes, block-and-ash flow and lithic surge deposits) and Plinian eruptions (pumice flow and fallout deposits) [18,19]. 'Reverse' transitions from lava extrusion to a Plinian regime may also occur, as illustrated by the 650 yr B.P. P1 eruption [20]. These two eruptive styles generate various hazards, with, in the case of the Pelean eruptions, the possibility of laterally directed surges [21], as in the May 8, 1902 eruption responsible for the loss of 30,000 lives and the destruction of the town of St. Pierre.

Samples representative of both Plinian (pumices from the Plinian fallout and upper pumice flow of the P1 eruption) and Pelean (lithic clasts from the P1 basal and May 8, 1902 surges, and samples from the 1929 lava dome and block-and-ash flows) eruptive styles were collected for detailed studies [22]. Products of the recent eruptions from Mt. Pelée are uniformly silicic andesites, except for the presence of mafic enclaves [17,23]. New analyses confirm the older data and demonstrate no significant change in whole-rock major element chemistry with eruptive style. The rocks are crystal-rich pyroxene andesites [17,23], with phenocryst modal proportions ranging from $\approx$35 to 55 vol%, in agreement with older modal data [17]. The phenocryst and microphenocryst assemblage is plagioclase (29–44 vol%), orthopyroxene (4–9%), magnetite (1–2%), clinopyroxene (<1%), amphibole (<1%) and ilmenite (trace). Olivine is found only in mafic enclaves [17,23]. Amphibole shows systematic resorption to orthopyroxene–plagioclase–magnetite assemblages, a textural feature noted in previous studies [17].

Compositions of phenocrysts were determined in both Plinian and Pelean products. Plagioclase phenocrysts are typically zoned [17,23]. Rim compositions (assumed to be in equilibrium with a melt having the composition of the matrix glass) range from An_{50-55} for the 1929 dome and block-and-ash flows, to An_{55-60} for the P1 samples, from either the Plinian fallout or basal surge; the compositions for the May 8, 1902 surge are intermediate (Table 1).

Table 1

Compositions of glasses and coexisting mineral phases in recent Plinian and Pelean eruptions of Mt. Pelée and in selected experiments

	Glasses											Phenocrysts		
	Type	SiO_2 (wt%)	TiO_2 (wt%)	Al_2O_3 (wt%)	FeO_t (wt%)	MgO (wt%)	MnO (wt%)	CaO (wt%)	Na_2O (wt%)	K_2O (wt%)	H_2O (wt%)	An (mol%)	En (mol%)	Mt (mol%)
Eruption products														
Pl fallout	I	75.5	0.2	13.0	2.7	0.4	0.1	2.2	3.8	2.1	5.2	58	53	69 (0)
	M	76.7 (2)	0.2 (0)	12.6 (1)	2.2 (2)	0.3 (0)	0.0 (0)	2.2 (1)	3.8 (1)	1.9 (1)	nd			
Pl surge	I	76.1	0.3	11.7	3.2	0.6	0.1	1.6	4.1	2.2	2.9	56	55	70 (0)
	M	75.4 (4)	0.3 (0)	13.0 (1)	2.5 (3)	0.4 (0)	0.1 (1)	2.3 (1)	3.9 (2)	2.0 (1)	nd			
May 8, 1902 surge	I	78.0	0.4	9.5	3.3	0.5	0.2	1.1	3.1	4.1	1.0	55	52	69
1929 block-and-ash flows	I	75.8	0.3	12.1	2.2	0.4	0.1	1.7	4.4	3.2	<0.1	51	54	70 (2)
	M	76.3	0.3	12.7	1.6	0.3	0.1	1.9	4.5	2.4	nd			
Experiments														
(*P*/°C/ΔNNO)														
2.0/850/+2.5		78.1 (3)	0.3 (1)	12.2 (1)	1.4 (2)	0.4 (0)	0.1 (1)	2.1 (1)	2.9 (1)	2.5 (2)	6.1 (4)	61	68 (0)	89
2.1/900/0		74.9	0.3	13.3	2.7	0.3	0.2	2.5	3.4	2.4	5.5	54	45	nd
2.2/900/+0.4		73.6 (5)	0.5 (0)	13.6 (1)	3.2 (3)	0.4 (1)	0.1 (1)	2.6 (1)	3.5 (0)	2.5 (1)	5.5 (11)	56	51 (1)	57 (3)
2.0/900/+0.7		71.6 (4)	0.4 (0)	14.5 (3)	3.5 (2)	0.8 (0)	0.1 (1)	3.5 (2)	3.8 (1)	1.8 (0)	6.1 (2)	60	59 (1)	76 (2)
2.2/900/+0.8		73.1 (2)	0.4 (0)	14.2 (1)	3.3 (3)	0.6 (1)	0.1 (1)	3.0 (1)	3.3 (1)	2.1 (1)	5.8 (9)	57 (1)	57 (1)	71 (1)
2.1/875/+0.8		74.4	0.4	13.3	2.6	0.3	0.1	2.4	4.1	2.4	6.2	56 (1)	54 (1)	68
3.11/925/+0.7		69.9 (3)	0.6 (0)	14.7 (1)	4.7 (2)	0.8 (1)	0.1 (1)	3.9 (1)	3.6 (0)	1.7 (1)	5.8 (4)	58	48 (1)	56

Natural glasses and phenocrysts analyzed in the same thin section except the 1929 samples. When multiple analyses are available, the average values are given together with the standard deviation (number in brackets) in terms of the least unit cited. Magnetite compositions for the May 8, 1902 surge from [23]. Except for H_2O, all analyses are electron microprobe data obtained using well-established techniques including corrections for Na and K migration [24]. Oxide concentrations except H_2O are normalized to 100% anhydrous. H_2O contents of glasses were determined mainly by the by-difference method for inclusions <20 μm in size, microlite-bearing samples and experimental charges with high crystal fractions, and by FTIR. Both methods were based on the use of three rhyolitic glasses, experimentally synthesized from the Mt. Pelée matrix glasses, and containing 1.99, 4.59 and 6.33 wt% H_2O, as determined by Karl–Fischer titration [25] (analytical error, ±0.2 wt%). The by-difference method [26] was improved by analyzing in each electron microprobe session the three rhyolitic standard glasses (analytical error, ±0.5 wt%). The FTIR measurements were performed on a Nicolet 710 instrument equipped with a Nicplan microscope [25]. $\Delta NNO = \log f_{O_2} - \log f_{O_2}$ of the NNO buffer calculated at the pressure of interest FeO_t = total Fe as FeO. I = glass inclusion; M = matrix glass; An = $CaAl_2Si_2O_8$ in plagioclase (rim composition); En = $MgSiO_3$ in orthopyroxene; Mt = Fe_3O_4 in magnetite; nd = not determined.

Orthopyroxene phenocryst compositions range between En_{52} and En_{58} irrespective of textural type (Table 1), except in the 1929 dome where compositions up to En_{65} are found. These magnesian compositions are interpreted to reflect re-equilibration of orthopyroxenes under near-surface oxidizing conditions. Orthopyroxenes are either homogeneous or weakly zoned, with core-to-rim variations <6% En. Magnetites are generally homogenous, except in the 1929 dome samples, where they contain exsolved ilmenite lamellae. The compositions of unexsolved magnetites range between Mt_{66} to Mt_{70} (Table 1) in all eruption products analyzed.

Glass inclusions are abundant in plagioclase, but can also be found in orthopyroxene phenocrysts. They have average sizes of ≈20 μm, rarely exceeding 50 μm. Inclusions in phenocrysts from the Plinian products are generally light brown in colour and they often contain a bubble. In contrast, most of the inclusions from the Pelean products are either partially or totally crystallized. Matrix glasses in Pelean products contain microlites in varying proportions. In the May 8, 1902 surge and 1929 dome, the matrix glasses are almost completely crystallized. In contrast, microlites in matrix glasses from the Plinian products are either absent or present in small proportions (<10% vol). Both matrix glasses and glass inclusions have rhyolitic composition (Table 1). Inclusion and matrix glasses from the P1 eruption have nearly identical major element compositions (Table 1). In contrast, most glasses from the 1902 and 1929 Pelean products have higher SiO_2 and K_2O, and lower Al_2O_3 and CaO, than the P1 glasses (Table 1), the difference being attributed to post-entrapment modifications and crystallization of microlites in the Pelean products. The representative glass analyses shown in Table 1 are for: (1) glass inclusions with no visible signs of crystallization and leakage; and (2) matrix glasses either microlite-free (P1 fallout and surge) or the least modified by the crystallization of microlites (1929 block-and-ash flows). The lack of large variations in bulk rock and phenocryst and glass compositions constitutes a first indication of near-identical magma chemistries and pre-eruptive conditions, irrespective of eruptive style.

3. Using eruption products to constrain magma storage conditions: results and limitations

Various methods may be employed to constrain pre-eruptive magma storage conditions in intermediate to silicic systems [7]. Mineral–mineral equilibria yield precise results for parameters such as T and f_{O_2}, but melt H_2O contents obtained by using either dehydration equilibria or mineral–melt (such as plagioclase–melt) equilibria are generally much less precise, given the uncertainties in experimental calibrations and solution models for solid and melt phases. These latter calculations also require values for pressure and temperature (and sometimes f_{O_2}).

At Mt. Pelée, the presence of ilmenite microphenocrysts is exceptional and this limits the use of coexisting Fe–Ti oxides to calculate pre-eruptive temperatures and f_{O_2}. The available Fe–Ti oxide data for recent eruptions are compiled in Table 2. For internal consistency, all T–$\log f_{O_2}$ data are recalculated using the same formulations of the oxide geothermobarometer [27,28]. The two formulations used yield ΔNNO values ($\Delta NNO = \log f_{O_2} - log f_{O_2}$ of the NNO buffer, calculated at a reference pressure of 2 kbar) in good agreement, but temperatures differ from each other by at least 40°C (Table 2). Here, calculations after [27] are preferred because, when applied to experimentally crystallized Mt–Ilm pairs, T–$\log f_{O_2}$ values in close agreement with experimental conditions are obtained (Table 2). Temperatures for the 4 natural Fe–Ti oxide pairs available are between 840 and 902°C, the two new pairs from 1929 block-and-ash flows lying in the middle of the range (865 and 880°C, Table 2). Redox conditions are moderately oxidizing, slightly above the NNO buffer ($\Delta NNO = +0.4$–0.8). For comparison, one Fe–Ti oxide pair from an andesite sample of the historical eruptions of Mt. Pelée [17] yields a temperature of 969°C and a $\log f_{O_2}$ of -10.2 ($\Delta NNO = +0.4$). It is stressed that the $T - \log f_{O_2}$ data for recent eruptions (Table 2) pertain to Pelean products only.

With temperatures estimated from Fe–Ti oxides, melt H_2O contents can be determined from plagioclase–melt equilibria. Housh and Luhr [29] studied the distribution of albite and anorthite components between plagioclase and melt as a function of the H_2O content of the melt between 1 and 4

Table 2
Fe–Ti oxide compositions in recent andesites from Mt. Pelée

Eruption:	1902		1929		1929		1929		Experiment	
Style:	Pelean		Pelean		Pelean		Pelean		P/°C/ΔNNO	
Sample:	6		12		MT35Z		MT35Z		2.1/900/0	
Phase:	Mt	Ilm	Mt	Ilm	Mt	Ilm	Mt	Ilm	Mt	Ilm
SiO_2	0.05	0.00	0.02	0.02	0.11	0.34	0.10	0.08	0.68	0.20
TiO_2	10.67	46.54	10.61	44.24	10.51	45.44	10.34	46.11	13.79	46.64
Al_2O_3	2.33	0.00	2.33	0.00	2.12	0.21	2.46	0.23	3.29	0.15
FeO_t	80.52	48.70	81.63	51.86	79.74	50.88	80.64	50.72	70.15	46.02
MnO	0.57	0.78	0.63	0.82	0.40	0.73	0.53	1.06	0.64	0.79
MgO	1.40	2.32	1.11	1.62	0.84	1.86	0.86	1.70	1.31	2.29
Cr_2O_3	0.08	0.07	0.00	0.00	–	–	–	–	–	–
Total	95.62	98.34	96.33	98.56	93.72	99.46	94.93	99.90	89.86	96.09
Mt (mol%)	71	–	71	–	69	–	70	–	56	–
Hem (mol%)	–	14	–	18	–	16	–	15	–	12
Calculations after [28]										
T (°C)	800		841		832		821		816	
$\log f_{O_2}$ (bar)	–13.3		–12.1		–12.5		–12.7		–13.6	
ΔNNO	+0.6		+0.9		+0.7		+0.7		–0.1	
Calculations after [27]										
T (°C)	840		902		880		865		899	
$\log f_{O_2}$ (tear)	–12.7		–11.1		–11.7		–12.0		–12.2	
ΔNNO	+0.4		+0.8		+0.5		+0.5		–0.3	

Compositional data for samples 6 and 12 taken from [23]. Duration of the experiment: 327 h. ΔNNO calculated at 2 kbar.

kbar. Here, both the albite–melt and anorthite–melt formulations [29] are applied to calculate the H_2O content of the melt, for temperatures of 850 and 900°C, and assuming a pressure of 2 kbar. For the P1 eruption, plagioclase rim and matrix glass compositions from either the fallout or surge are used (Table 1). The albite–melt expression [29] yields melt H_2O contents of 5.5–5.0 and 4.1–3.8 wt% (depending on the plagioclase rim composition used) for 850 and 900°C, respectively. Melt H_2O contents obtained from the anorthite–melt expression [29] are lower by 1–2% in comparison with the albite–melt expression (3.0–2.8 and 2.1–1.9 wt% for 850 and 900°C, respectively). Thus, calculated pre-eruptive melt H_2O contents span values from 1.9 to 5.5 wt% in the temperature range considered. However, although plagioclase–melt equilibria [29] fail to provide precise estimates of melt H_2O contents, it is interesting to compare the relative differences between eruptions. For the 1929 Pelean products, (plagioclase rim and matrix glass compositions from Table 1), melt H_2O contents calculated for the same P–T conditions as above are lower by 0.5 wt% than for P1. Overall, the plagioclase–melt equilibrium modelling supports a maximum difference in pre-eruptive melt H_2O contents of 0.5 wt% between recent eruptions, either Plinian or Pelean.

Use of hornblende dehydration equilibria to calculate f_{H_2O} has not been attempted, in part because of the uncertainties inherent in such calculations [30], but also because amphibole is not considered to be a stable phase under pre-eruptive conditions. Amphibole shows resorption textures in both Plinian and Pelean products, suggesting that it became unstable in the magma chamber and not during ascent from the chamber to the surface. Amphibole compositions in recent Mt. Pelée andesites are, for the very large majority, close to the pargasite end-member ($Al^{IV} = 1.5$–1.8, cations in A site = 0.6–0.8 pfu) (see also [17,23]). Edenitic amphiboles richer in Si and poorer in Al are also found at Mt. Pelée, in rare felsic rocks such as dacites and dioritic cumulates [17,23]. In experiments performed on Mt. Pelée andesite and basaltic andesite bulk compositions [31], crystallization of pargasitic hornblende takes place only for relatively high pressures (4 kbar) and temperatures (≥925°C). In contrast, amphiboles crystallizing at lower pressures and temperatures (2 kbar, ≤875°C) are edenitic [31]. Thus, the available textural, compositional and experimental evidence suggests that amphiboles in the Mt. Pelée andesites are mostly relics from a higher pressure, higher temperature crystallization stage of magmas parental to the erupted andesites [31,32]. During ascent of these magmas towards the upper parts of the magma storage region, depressurization and volatile loss resulted in the progressive resorption of amphibole.

Glass inclusions trapped in phenocrysts can be used to obtain directly the concentration of H_2O (and of other volatiles) in the melt prior to eruption [7]. This approach requires glass inclusions unmodified during magma ascent and eruption and, for this reason, is most useful for rapidly cooled Plinian products. Another potential problem with glass inclusions is that they may be trapped at various levels in the magma storage region, thus reflecting a range of pre-eruptive conditions and not necessarily those prevailing in the part of the chamber tapped by the eruptions. Water (H_2O) contents were measured in glass inclusions from both Plinian and Pelean products (Fig. 1; Table 1). Almost all the data were obtained using an improved version of the by-difference method [26], owing to the small size of the glass inclusions. Only one glass inclusion could be measured by FTIR (Fig. 1). Both methods were based on three rhyolitic glasses, experimentally synthesized from the Mt. Pelée matrix glasses, and containing 1.99, 4.59 and 6.33 wt% H_2O, as determined by Karl-Fischer titration [25]. These glasses served to standardize the FTIR measurements [25]. They were also used to calibrate the by-difference method and to correct the electron microprobe analyses of glasses for alkali migration [24]. Most inclusions analyzed come from plagioclase, and only a few from orthopyroxene. However, no systematic difference in H_2O concentration with type of host mineral was found. Glass inclusions from the P1 Plinian fallout have H_2O contents ranging between 4.2 and 7.1 wt% (Fig. 1), 5.8 ± 0.7 wt% on average ($n = 14$). The inclusion analyzed by FTIR has a water concentration of 6.7 wt% and lies close to the maximum of the range (Fig. 1). Dissolved CO_2 was below detection in the inclusion. In contrast, glass inclusions from the Pelean products have H_2O contents lower on average than in the Plinian pumices, especially the samples from the 1902 and 1929 eruptions (Fig. 1; Table 1). The P1 surge is characterized by a large dispersion of water concentrations (Fig. 1). Although inclusions with water concentrations < 3 wt% are common, other inclusions reach concentrations as high as in the Plinian pumices (Fig. 1). The low water concentrations, the dispersion of the data and the fact that concentrations as high as in the Plinian pumices can be found consistently suggest that the Pelean inclusions suffered post-entrapment modifications and leakage to various extents upon ascent and eruption [33]. Therefore, H_2O concentrations in glass inclusions from the Pelean eruptions are probably not representative of pre-eruptive melt H_2O concentrations.

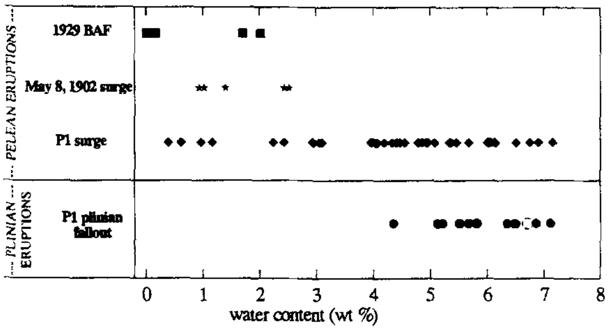

Fig. 1. Water contents in glass inclusions from recent Pelean and Plinian eruptions of Mt. Pelée. Filled symbols: determination by the by-difference method. Open symbol: determination by FTIR. See Table 1 for analytical procedures. *BAF* = block-and-ash flows.

4. Experimental constraints

Fe–Ti oxide compositions, plagioclase–melt equilibria and H_2O contents of glass inclusions have furnished constraints on pre-eruptive magma storage conditions at Mt. Pelée. However, systematic T–$\log f_{O_2}$ data are lacking, especially for the Plinian eruptions. Glass inclusions show a large spectrum of H_2O concentrations, in part due to post-entrapment modifications. Therefore, the pre-eruptive conditions need to be confirmed from another approach. Experimental phase equilibria [34–36] were studied for three silicic andesite samples from the different eruptive styles (P1 fallout and surge, 1929 dome). Their whole-rock compositions (60.75–61.11 SiO_2, 0.43–0.48 TiO_2, 17.47–17.74 Al_2O_3, 5.94–6.05 FeO_t, 2.17–2.29 MgO, 0.17–0.18 MnO, 6.15–6.24 CaO, 3.45–3.53 Na_2O, 0.97–1.05 K_2O, 0.37–1.68 H_2O, in wt%) are sufficiently similar to make the experimental results independent of the starting sample. The experiments were performed at ≈2 (2.0–2.3), 3.1 and 4.2 (±0.02) kbar, between 850 and 1040 (±5)°C, in an internally heated pressure vessel fitted with a modified semi-permeable H_2 membrane [37], allowing redox conditions to be precisely controlled and monitored from $\Delta NNO = 0$ to $+2.5$ (±0.2). A rapid-quench device [38] was used in some runs. Most runs lasted for 8–14 days, depending on temperature. Starting materials (mostly glasses, but some crushed rock powders) were contained in Au capsules. From electron microprobe analyses of capsules and mass-balance calculations, Fe-loss was found to be negligible. Melt H_2O contents were varied using H_2O–CO_2 fluid mixtures (generated from doubly distilled demineralized H_2O and $Ag_2C_2O_4$) and H_2O contents of quenched glasses were analysed using the same techniques as for the natural glasses (see above and Table 1).

Values of P–T–f_{O_2}–melt H_2O content in the magma storage region are bounded by using charges with experimental phase assemblages inconsistent with the phenocryst assemblage. Charges at 4.2 kbar are characterized by the presence of amphibole [31], which occurs as a near-liquidus phase at 925°C, $\Delta NNO = +0.6$ and for water-saturated conditions (melt H_2O content = 10.8 wt%). Experiments performed under strongly oxidizing conditions ($\Delta NNO = +2$) at 2.3 kbar, 930°C and for a melt H_2O content of 6.9 wt% yield a phase assemblage lacking orthopyroxene, but with both amphibole and clinopyroxene. By contrast, the phenocryst assemblage is adequately reproduced in experiments performed under moderately oxidizing conditions ($\Delta NNO = 0$ to $+1$) at ≈2 kbar. Under these P–f_{O_2} conditions, plagioclase, orthopyroxene and magnetite coexist at equilibrium with melt for a substantial range of T–melt H_2O contents. Clinopyroxene is found sporadically in the experimental charges and ilmenite only in the most reduced runs ($\Delta NNO = 0$, Table 2), closely reproducing the mineralogical features of the andesites. The T–melt H_2O content domain where plagioclase, orthopyroxene, magnetite and melt coexist is bounded towards the high temperatures by the disappearance of orthopyroxene ($T \geq$ 960–940°C for melt H_2O = 5–7 wt%) and towards the low temperatures by the crystallization of amphibole ($T \leq$ 830–875°C for melt H_2O = 6–7 wt%), since amphibole is not considered to be stable under the pre-eruptive conditions.

Comparison of compositions of natural glasses and phenocrysts with experimental compositions allows the pre-eruptive conditions to be precisely determined [34–36]. Here, the compositions of the four main phases (plagioclase, orthopyroxene, magnetite, glass) are used together for the determination of the pre-eruptive conditions. Taking $P \approx 2$ kbar, ΔNNO = +0.4–0.8 and T between 875 and 950°C as initial conditions, plagioclases and orthopyroxenes provide consistent values of melt H_2O contents of 4.5–6.5 and 4.8–6.3 wt%, respectively (Fig. 2a,b; Table 1). For H_2O contents in the 4.5–6.5 wt% range, oxide–melt H_2O plots (see Fig. 2c for SiO_2 and also Table 1) consistently show that only glasses from the 875 and 900°C isotherms can coincide with matrix glass compositions. Taking the intersection of the plagioclase, orthopyroxene and glass data as the melt H_2O content (5.3–5.5 wt% at 900°C, 5.7–6.3 wt% at 875°C, Fig. 2), experimental magnetites match the natural compositions for log f_{O_2} values of ≈NNO +0.6–0.8 at 900°C (Fig. 2d; Table 1), and ≈NNO +0.4–0.8 at 875°C (Fig. 2d, note that magnetite compositions are almost independent of T for fixed f_{O_2} and melt H_2O). Plots such as Fig. 2d, but for orthopyroxene lead to the same f_{O_2} range (ΔNNO = +0.4–0.8) for 875–900°C and melt H_2O contents as above, thus confirming the range of f_{O_2} initially chosen. A pre-eruptive temperature of 850°C is unlikely since it would require melt H_2O contents ≥6.5 wt% (Fig. 2c), thus leading to experimental magnetites and orthopyroxenes higher, respectively, in Mt and En than the natural phases (Fig. 2b,d). It is concluded that experimental conditions between T = 875–900°C, ΔNNO = +0.4–0.8, melt H_2O = 5.3–6.3 wt% bracket the pre-eruptive magma storage conditions. Plagioclases, orthopyroxenes, magnetites and glasses obtained under these experimental conditions (Table 1) enclose compositions of matrix glasses and coexisting phenocrysts. Although exper-

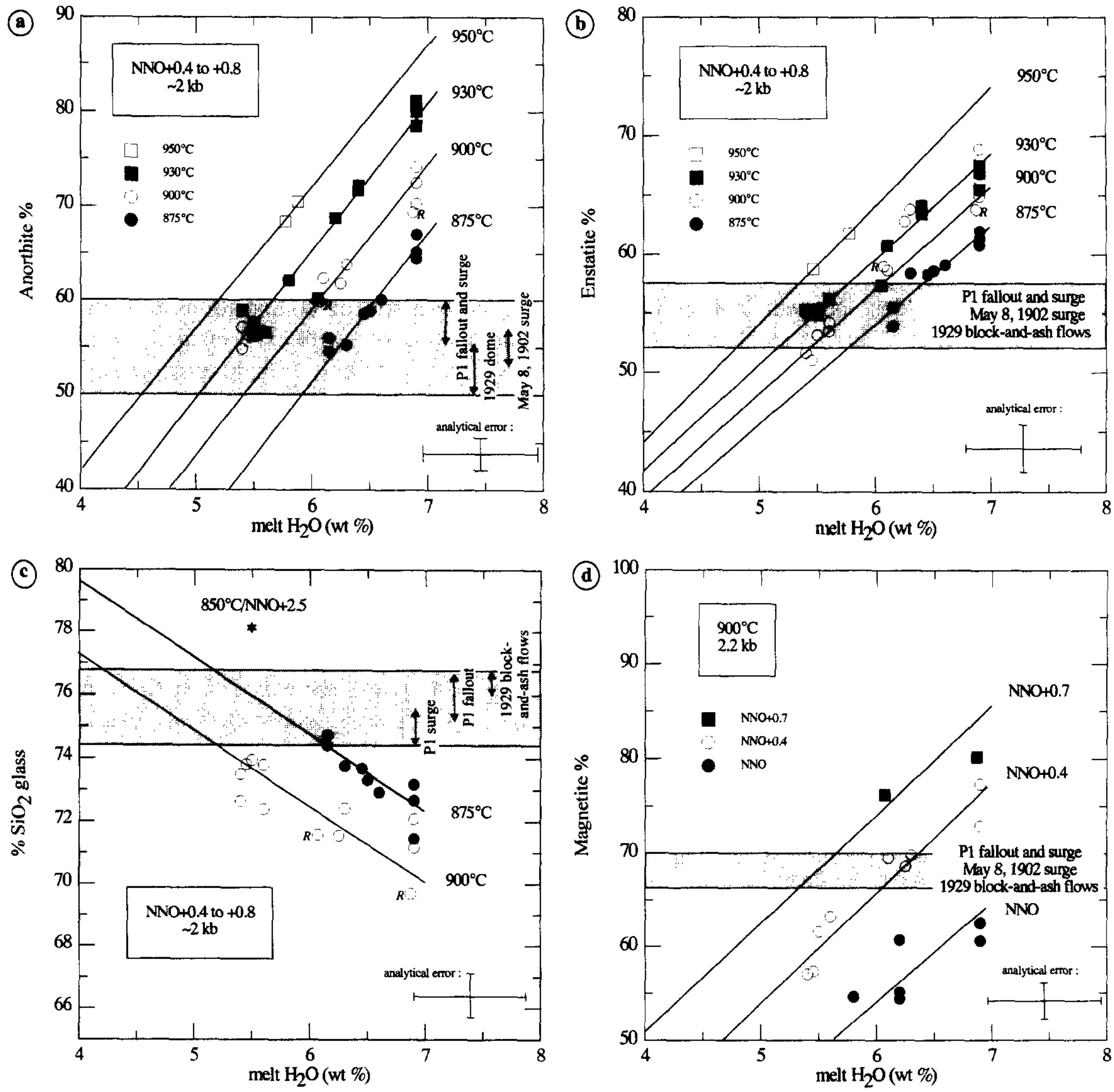

Fig. 2. Compositions of experimental plagioclase (a), orthopyroxene (b), glass (c) and magnetite (d) as a function of the H_2O content of the glass, and comparison with natural compositions from recent eruptions. Each point represents either one analysis or the average of multiple analyses for a given phase in a given charge, with standard deviations (1σ) equal or lower than analytical error. The data points are labelled as a function of experimental conditions, charges from different starting samples being represented under the same symbol. *R* denotes data from rapid-quench experiments. For plagioclase, only rim compositions are compared and, for glasses, only matrix glasses are used in the comparison (see text).

iments below 2 kbar are lacking, the lower bound of melt H_2O determined above (5.3 wt%) requires a lithostatic pressure of ca. 1.6 kbar [39] minimum for the magma storage region. In the following, a conservative value of 1.5 kbar will be adopted. Pressures substantially above 2 kbar can be ruled out since compositions from experiments at pressures above 2–2.3 kbar (either 3.1 or 4.2 kbar) fail to define consistent melt H_2O contents. This is because, upon increasing pressure above 2 kbar, progressively *higher* melt H_2O contents are required for plagioclase and orthopyroxene compositions to match the natural compositions, while progressively *lower* melt H_2O contents are needed for experimental and natural glass compositions to overlap. Therefore, the depth of the andesitic magma reservoir can be estimated at ca. 7–12 km (2 ± 0.5 kbar), taking a density of 2.2 g/cm^3 for upper crustal volcanic rocks.

5. Discussion and implications for control of eruption regime

The recent Plinian and Pelean eruptions of Mt. Pelée (650 yr B.P., 1902, 1929) have been used to test between the existing models for the transition between explosive and effusive eruptions in silicic volcanoes. To do so, the pre-eruptive H_2O concentrations and storage conditions for eruptions of different styles have been precisely determined, from experiments performed on the natural andesite samples. The experimental T–f_{O_2} data (875–900°C, $\Delta NNO = +0.4$–0.8) are in agreement with Fe–Ti oxide data, especially the two new pairs (865–880°C, $\Delta NNO = +0.5$, Table 2). The range of pre-eruptive melt H_2O contents inferred from the experiments (5.3–6.3 wt%) encloses the average H_2O concentrations of glass inclusions from the Plinian fallout (5.8 wt%, Fig. 1). It markedly differs from the average values found in the inclusions from Pelean products (Fig. 1), thus confirming a posteriori that the majority of these inclusions were modified during ascent and eruption. Most inclusions in block-and-ash flows and surge deposits from Mt. Pelée do not reflect pre-eruptive H_2O concentrations. The depth of the andesitic magma body tapped by the recent eruptions has been estimated at ca. 7–12 km. Therefore, the experimental results provide precise data on the conditions of storage of andesitic magmas at Mt. Pelée, prior to their ascent and eruption.

Although the experiments define a narrow range of pre-eruptive conditions, the data do not totally rule out the possibility of small fluctuations in magma storage conditions from one eruption to the other. However, these fluctuations have to be of small amplitude (i.e., ±10–15°C, ±0.5 kbar, ±0.5 wt% H_2O and ±0.2 log f_{O_2} units). It follows that the recent eruptions tapped magma bodies having either identical H_2O concentrations or H_2O concentrations differing only by small amounts (0.1% range). For the Pelean and Plinian phases of the P1 eruption, the pre-eruptive H_2O concentrations must have been identical, since no differences in bulk composition, glass and phenocryst compositions can be detected. This conclusion is in contrast with previous models which have proposed that the eruptive behaviour of Mt. Pelée is controlled by gas content [17]. It is worth stressing that the absence of significant volatile stratification, as demonstrated here, concerns only that zone of the magma storage region tapped by the recent eruptions. However, glass inclusions with H_2O concentrations higher ($\approx$7 wt%, Fig. 1) than the inferred pre-eruptive H_2O values have been found. In the same way, there are indications of more mafic magma (basaltic andesite) being stored at $P \geq 4$ kbar [40]. Therefore, the existence of in-depth compositional variations (or heterogeneities) beneath Mt. Pelée is beyond doubt. However, there is no evidence that such variations in either volatile concentration or magma composition are significant in the storage zone of silicic andesite magmas tapped by the recent eruptions. On the contrary, the data presented here stress the chemical homogeneity of the tapped magma bodies. This is consistent with the small volumes (0.1–0.5 km^3) of eruptions in recent times and, in fact, supports the two-stage geometry for the magma storage region that has been proposed independently [17,40]. Eruption of small volumes of physically and chemically homogeneous magmas, such as at Mt. Pelée, contrasts with large silicic systems, where zonation in volatiles, major and trace elements, temperature and phenocrysts content has been documented [9,10,41].

Results from this paper essentially rule out the volatile stratification model for explaining the transition between recent explosive and effusive eruptions at Mt. Pelée. Therefore, the transition between Plinian and Pelean eruptive styles is unrelated to systematic variations of H_2O concentrations in the magma storage region beneath Mt. Pelée. This implies that the distinction between Plinian and Pelean eruptive regimes is acquired during magma ascent from the storage zone to the surface, thus confirming one important aspect of the degassing model [3–5].

6. Conclusions

(1) The recent activity of Mt. Pelée is characterized by strongly contrasted eruptive styles, with

eruption of either Plinian or Pelean andesitic products of identical bulk rock and phenocryst and glass compositions, thus providing a unique opportunity to test between existing models of eruption regime.

(2) Fe–Ti oxide compositions, plagioclase–melt equilibria and H_2O contents of glass inclusions furnish constraints on pre-eruptive magma storage conditions. However, systematic T–log f_{O_2} data are lacking, especially for the Plinian eruptions. Glass inclusions show a large spectrum of H_2O concentrations, in part due to post-entrapment modifications.

(3) Pre-eruptive H_2O concentrations and storage conditions for eruptions of different styles have been precisely determined from experiments performed on three natural andesite samples. $T-f_{O_2}$ data (875–900°C, ΔNNO = +0.4–0.8) are in agreement with the two new Fe–Ti oxide pairs analyzed (865–880°C, ΔNNO = +0.5). Melt H_2O contents determined from the experiments (5.3–6.3 wt%) encloses the average H_2O concentrations of glass inclusions from the Plinian fallout (5.8 wt%, Fig. 1). In contrast, most inclusions in block-and-ash flows and surge deposits do not reflect pre-eruptive H_2O concentrations.

(4) Mt. Pelée provides one example where the transition between Plinian and Pelean eruptive styles is unrelated to systematic variations of H_2O concentrations in the magma storage region, but is acquired during magma ascent from the storage zone to the surface.

Acknowledgements

This paper benefitted from informal reviews by B. Evans and R. Macdonald. We thank M. Carroll and an anonymous referee for their reviews and F. Albarède for editorial handling. This study was supported by PNRN. *[FA]*

References

[1] J.C. Eichelberger, H.R. Westrich, Magmatic volatiles in explosive rhyolitic eruptions, Geophys. Res. Lett. 8 (1981) 757–760.

[2] J.H. Fink, Structure and emplacement of a rhyolitic obsidian flow: Little Glass Mountain, Medicine Lake Highland, northern California, Geol. Soc. Am. Bull. 94 (1983) 362–380.

[3] J.C. Eichelberger, C.R. Carrigan, H.R. Westrich, R.H. Price, Non-explosive silicic volcanism, Nature 323 (1986) 598–602.

[4] C. Jaupart, C.J. Allègre, Gas content, eruption rate and instabilities of eruption regime in silicic volcanoes, Earth Planet. Sci. Lett. 102 (1991) 413–429.

[5] A.W. Woods, T. Koyaguchi, Transitions between explosive and effusive eruptions of silicic magmas, Nature 370 (1994) 641–644.

[6] J.H. Fink, S.W. Anderson, C.R. Manley, Textural constraints on effusive silicic volcanism: beyond the permeable foam model, J. Geophys. Res. 97 (1992) 9073–9083.

[7] M.C. Johnson, A.T. Anderson, M.J. Rutherford, Pre-eruptive volatile content of magmas, in: Carroll, M.R., Holloway, J.R. (Eds.), Volatiles in Magmas, M.S.A. Rev. Mineral. 30 (1994) 281–330.

[8] A.T. Anderson Jr., S. Newman, S.N. Williams, T.H. Druitt, C. Skirius, E. Stolper, H_2O, CO_2, Cl and gas in Plinian and ash-flow Bishop rhyolite, Geology 17 (1989) 221–225.

[9] N.W. Dunbar, R.L. Hervig, Petrogenesis and volatile stratigraphy of the Bishop Tuff: evidence from melt inclusion analysis, J. Geophys. Res. 97 (1992) 15129–15150.

[10] N.W. Dunbar, R.L. Hervig, Volatile and trace element composition of melt inclusions from the Lower Bandelier Tuff: implications for magma chamber processes and eruptive style, J. Geophys. Res. 97 (1992) 15151–15170.

[11] S. Newman, S. Epstein, E. Stolper, Water, carbon dioxide, and hydrogen isotopes in glasses from the ca. 1340 A.D. eruption of the Mono craters, California: constraints on degassing phenomena and initial volatile content, J. Volcanol. Geotherm. Res. 35 (1988) 75–96.

[12] N.W. Dunbar, P.R. Kyle, Lack of volatile gradient in the Taupo plinian–ignimbrite transition: evidence from melt inclusion analysis, Am. Mineral. 78 (1993) 612–618.

[13] J. Barclay, M.R. Carroll, B.F. Houghton, C.J.N. Wilson, Pre-eruptive volatile content and degassing history of an evolving peralkaline volcano, J. Volcanol. Geotherm. Res. 74 (1996) 75–87.

[14] J.B. Lowenstern, G. Mahood, New data on magmatic H_2O contents of pantellerites, with implications for petrogenesis and eruptive dynamics at Pantelleria, Bull. Volcanol. 54 (1991) 78–83.

[15] A. Lacroix, La Montagne Pelée et ses Eruptions, Masson, Paris, 1904, 662 pp.

[16] G. Boudon, A. Gourgaud (Eds.), Mt. Pelée, J. Volcanol. Geotherm. Res. (Special Issue) 38 (1989) 1–213.

[17] A.L. Smith, M.J. Roobol, Mt. Pelée, Martinique, A Study of an Active Island-Arc Volcano, Mem. Geol. Soc. Am. 175, 105 pp.

[18] M.J. Roobol, A.L. Smith, Mt. Pelée, Martinique, a pattern of alternating eruptive style, Geology 4 (1976) 521–524.

[19] D. Westercamp, H. Traineau, The past 5,000 years of volcanic activity at Mt. Pelée Martinique (FWI): implications for assessment of volcanic hazards, J. Volcanol. Geotherm. Res. 17 (1983) 159–185.

[20] B. Villemant, G. Boudon, J.-C. Komorowski, U-series dis-

equilibrium in arc magmas induced by water–magma interaction, Earth Planet. Sci. Lett. 140 (1996) 259–267.

[21] J.-L. Bourdier, G. Boudon, A. Gourgaud, Stratigraphy of the 1902 and 1929 nuée-ardente deposits Mt. Pelée, Martinique, J. Volcanol. Geotherm. Res. 38 (1989) 77–96.

[22] C. Martel, Conditions pré-éruptives et dégazage des magmas andésitiques de la Montagne Pelée (Martinique): étude pétrologique et expérimentale, Thesis, University of Orléans, Orléans, 1996, 247 pp.

[23] A. Gourgaud, M. Fichaut, J.-L. Joron, Magmatology of Mt. Pelée (Martinique, FWI). I. Magma mixing and triggering of the 1902 and 1929 Pelean nuées ardentes, J. Volcanol. Geotherm. Res. 38 (1989) 143–169.

[24] M. Pichavant, Effects of B and H_2O on liquidus phase relations in the haplogranite system, Am. Mineral. 72 (1987) 1056–1070.

[25] H. Behrens, C. Romano, M. Nowak, F. Holtz, D.B. Dingwell, Near-infrared spectroscopic determination of water species in glasses of the system $MAlSi_3O_8$ (M = Li Na, K): an interlaboratory study, Chem. Geol. 128 (1996) 41–63.

[26] J.D. Devine, J.E. Gardner, H.P. Brack, G.D. Layne, M.J. Rutherford, Comparison of microanalytical methods for estimating H_2O contents of silicic volcanic glasses, Am. Mineral. 80 (1995) 319–328.

[27] M.S. Ghiorso, R.O. Sack, Fe–Ti oxide geothermometry: thermodynamic formulation and estimation of intensive variables in silicic magmas, Contrib. Mineral. Petrol. 108 (1991) 485–510.

[28] D.J. Andersen, D.H. Lindsley, P.M. Davidson, QUILF: a PASCAL program to assess equilibria among Fe–Mg–Ti oxides, pyroxenes, olivine and quartz, Comput. Geosci. 19 (1993) 1333–1350.

[29] T.B. Housh, J.F. Luhr, Plagioclase–melt equilibria in hydrous systems, Am. Mineral. 76 (1991) 477–492.

[30] R.J. Arculus, K.J.A. Wills, The petrology of plutonic blocks from the Lesser Antilles island arc, J. Petrol. 21 (1980) 743–799.

[31] M. Pichavant, C. Martel, J.-L. Bourdier, Significance of amphibole in the recent andesites of Mt. Pelée. EOS 77 (1996) F800.

[32] J.S. Beard, A. Borgia, Temporal variation of mineralogy and petrology in cognate gabbroic enclaves at Arenal volcano, Costa Rica, Contrib. Mineral. Petrol. 103 (1989) 110–122.

[33] S. Tait, Selective preservation of melt inclusions in igneous phenocrysts, Am. Mineral. 77 (1992) 146–155.

[34] M.J. Rutherford, H. Sigurdsson, S. Carey, A.J. Davis, The May 18, 1980 eruption of Mt. St. Helens 1. Melt composition and experimental phase equilibria, J. Geophys. Res. 90 (1985) 2929–2947.

[35] M.J. Rutherford, J.D. Devine, The May 18, 1980 eruption of Mt. St. Helens 3. Stability and chemistry of amphibole in the magma chamber, J. Geophys. Res. 93 (1988) 11949–11959.

[36] J.E. Gardner, M.J. Rutherford, S. Carey, H. Sigurdsson, Experimental constraints on pre-eruptive water contents and changing magma storage prior to explosive eruptions of Mt. St. Helens volcano, Bull. Volcanol. 57 (1995) 1–17.

[37] B. Scaillet, M. Pichavant, J. Roux, Experimental crystallization of leucogranitic magmas, J. Petrol. 36 (1995) 663–705.

[38] J. Roux, A. Lefèvre, A fast quench device for IHPV, Eur. J. Mineral. 4 (1992) 279–281.

[39] C.W. Burnham, The importance of volatile constituents, in: H.S. Yoder Jr. (Ed.), The Evolution of Igneous Rocks: Fiftieth Anniversary Perspective, Princeton University Press, Princeton, NJ, 1979, pp. 439–482.

[40] M. Fichaut, R.C. Maury, H. Traineau, D. Westercamp, J.-L. Joron, A. Gourgaud, C. Coulon, Magmatology of Mt. Pelée (Martinique, FWI). III. Fractional crystallization versus magma mixing, J. Volcanol. Geotherm. Res. 38 (1989) 189–213.

[41] W. Hildreth, Gradients in silicic magma chambers, implications for lithospheric magmatism, J. Geophys. Res. 86 (1981) 10153–10192.

Etude complémentaire

Stage de recherche M1 : Elisabeth TRY (2008, Orléans) *Etude pétrographique et minéralogique de quelques éruptions pliniennes de la période récente de la Montagne Pelée.*

Direction : M. Pichavant et C. Martel.

Les conditions de stockage du magma andésitique au cours des éruptions historiques de la Montagne Pelée semblent donc être relativement stables, mais qu'en est-il des éruptions plus anciennes ? Ce sujet de stage de recherche de M1 visait à estimer d'éventuelles variations des conditions de stockage des magmas pliniens au travers une analyse des proportions modales des phénocristaux et des compositions des bordures des phénocristaux et des verres interstitiels des ponces d'éruptions Pliniennes plus anciennes que P1 (650 ans BP), telles que P2 (1140 ans BP), P3 (2010 ans BP) et P4 (2440 ans BP). Les résultats acquis lors de ce stage montrent que les ponces de P4 sont chimiquement plus évoluées (roche totale dacitique, verre résiduel à 79 pds % de SiO_2) que les autres Pliniennes étudiées (roche totale andésitique, verres résiduels ~75 pds % de SiO_2). Cependant, les proportions modales et les compositions de bordures des phénocristaux de P4 semblent comparables à celles des éruptions historiques. En revanche, les profils de bordures de phénocristaux de l'éruption P3 se distinguent par un enrichissement en composant anorthitique du plagioclase.

Il existe des différences compositionnelles réelles entre les ponces des éruptions Pliniennes de la période récente d'activité. Ces caractéristiques nécessitent à présent une étude plus approfondie afin de pouvoir interpréter ces différences en termes de variabilité des conditions des réservoirs magmatiques au cours du temps, par exemple grâce à des analyses des inclusions vitreuses, des éléments mineurs et traces dans les cristaux, et des expériences d'équilibre de phase.

I.3- DEGAZAGE

Les conditions de stockage des magmas des futures éruptions explosives et effusives de la Montagne Pelée (et potentiellement de volcans dont la chambre magmatique est de petite taille, i.e., < 1 km^3) étant comparables, nous avons recherché l'origine des différents styles éruptifs au niveau des processus intervenant lors de l'ascension du magma dans le conduit volcanique. Il a été proposé par Jaupart et Allègre (1991) que l'éruption était déclenchée par une surpression du réservoir magmatique de l'ordre de la dizaine de bars au minimum, et que différentes magnitudes de ces surpressions pouvaient être à l'origine de différentes vitesses d'ascension initiale du magma dans le conduit volcanique, impliquant alors différentes modalités de dégazage. Par dégazage au sens large, je considère 1) un processus de vésiculation de bulles, par lequel le gaz dissous dans le liquide silicaté s'exsolve, nucléant des bulles qui croissent et éventuellement coalescent et 2) le caractère fermé ou ouvert du système, c'est-à-dire le fait que le gaz reste dans le magma sous forme de bulles ou est échangé avec l'extérieur. Il est à noter que contrairement aux magmas mafiques, la forte viscosité des magmas riches en silice ne permet pas sur le temps de l'éruption, de ségrégation significative des bulles de gaz par flottabilité (également vérifié par l'observation in-situ), i.e., il n'y a pas de vitesses relatives entre les bulles et le liquide silicaté. La relation entre le dégazage et le caractère explosif d'une éruption découle en partie des modalités de vésiculation des bulles (pression de nucléation, densité numérique, taille, et importance de la coalescence) et du caractère ouvert ou fermé du dégazage. En effet, lors de l'ascension du magma dans le conduit, le volume des gaz augmente considérablement, car leur solubilité et leur densité diminuent de manière non-linéaire avec la baisse de pression. Dans le cas d'un dégazage en système fermé, la faible extensibilité du conduit volcanique en réponse à cette forte augmentation de volume crée de fortes surpressions gazeuses dans les bulles et la diminution de la densité globale du magma peut provoquer une forte accélération menant à une éruption explosive de type Plinien (Sparks 1978; Wilson et al., 1980). En revanche, un magma dégazant en système ouvert perd dans une certaine mesure son potentiel explosif par fuite des gaz sous pression dans l'encaissant ou au travers de la colonne magmatique devenue perméable (Eichelberger et al., 1986). Il y a dans ce cas compétition entre la vitesse d’ascension du magma et le temps nécessaire au développement de la perméabilité magmatique, c'est-à-dire à l'instauration de chenaux d’échappement des gaz par coalescence des bulles.

Le dégazage magmatique est par conséquent un processus dynamique, dont les caractéristiques évoluent constamment en cours d’ascension, et dont la limite entre système fermé et ouvert peut être franchie à plusieurs reprises. Cependant, un produit émis ne nous révèle que l'état final du dégazage, au moment de sa trempe. L’interprétation de cette porosité en termes de vitesse d’ascension, de développement de perméabilité et de potentiel explosif nécessite en amont des études détaillées des conditions de vésiculation des bulles et de pertes en gaz. La section I.3a ci-dessous traite du processus de vésiculation des bulles au travers d’une étude in-situ de la croissance de bulles d’eau dans un magma riche en silice (Martel et Bureau, 2001) et de nouvelles données apportées sur la nucléation et la coalescence des bulles par les travaux de thèse de C. Gondé (2008). La section I.3b traite du caractère ouvert ou fermé du système de dégazage par une étude des produits naturels de la Montagne Pelée (Martel et al., 2000a).

I.3a. Etude in-situ du processus de vésiculation (nucléation, croissance et coalescence de bulles)

La nucléation et la croissance de bulles dans les magmas ont été extensivement étudiées par des approches expérimentales ou numériques. Les simulations numériques sont notamment de plus en plus réalistes, passant d’un modèle de croissance de bulle unique dans un magma infini à des réseaux de bulles juxtaposées interagissant, et passant d’une croissance à pression constante à des croissances en décompression continue. Ces modèles théoriques sont basés sur la résolution des équations de diffusion des gaz dissous dans les liquides, de conservation de masse des volatils à l’interface gaz/liquide et de déformation visqueuse du liquide silicaté. Leur validité est apportée par des expériences de vésiculation de bulles en conditions magmatiques réalistes. Cependant, la plupart des produits expérimentaux sont analysés post-mortem (après expérience), ce qui représente potentiellement une source de perte d’information, notamment en ce qui concerne les processus aux cinétiques rapides, tels qu’un évènement de nucléation. D'autre part, l'étude de l'évolution de la vésiculation au cours de la décompression requiert des expériences sériées en temps dont la mise en œuvre est très consommatrice en temps. L'outil haute pression et haute température idéal pour l'expérimentaliste serait transparent, de manière à suivre en une seule expérience les différentes étapes de la vésiculation. En faisant la connaissance d'Hélène Bureau en post-doctorat au BGI en Allemagne, nous avons eu l’idée d’utiliser sa cellule à enclumes de diamants (CED) pour une étude in-situ inédite du dégazage d’un magma sous pression. En effet, la CED est un outil haute pression et haute température permettant d'une part les décompressions et d'autre part une observation in-situ de haute résolution.

Article présenté : MARTEL C. & BUREAU H. (2001) In-situ high-pressure and high-temperature bubble growth in silicic melts. *Earth Planet. Sci. Lett. 191, 115-127.*

Financements : Programme "Visiting Scientists" du Bayerisches GeoInstitut, Bayreuth, Allemagne et du Programme Européen "IHP-Access to Research Infrastructures" (D.C. Rubie).

L'article présenté traite de l'observation in-situ de la nucléation et de la croissance de bulles dans un liquide haplogranitique saturé en eau (79 pds% SiO_2 ; Norme CIPW : $Qz_{36}Ab_{38}Or_{25}$; composition analogue simplifiée d'un liquide rhyolitique naturel), par décompression dans une cellule hydrothermale à enclumes de diamant (CED) de type Bassett. Cette CED hydrothermale impose que la décompression soit pilotée par la baisse de la température du four (c'est le refroidissement de l'eau dans un volume contraint qui génère la décompression du système). Le processus de vésiculation a été filmé et les images ont été traitées pour déterminer les pressions de nucléation, le nombre d'évènements de nucléation, les lois de croissance des bulles et les températures de transition vitreuse de l'haplogranite.

La plupart des résultats obtenus ne sont pas directement comparables aux résultats des expériences et des modèles théoriques isothermes de la littérature, en raison de la forte baisse de température (200 à 300°C) accompagnant la décompression. Nos bulles montrent des croissances logarithmiques (proche d'une loi en racine cubique), alors que les croissances isothermes de la littérature suivent des lois en racine carrée, contrôlées par la diffusion de l'eau dans le liquide silicaté. De plus, la gamme de pression d'utilisation de la CED est de 3-22 kbars environ, alors que les pressions requises pour la simulation de l'ascension d'un liquide rhyolitique dans un conduit volcanique seraient plutôt < 2 kbars. Nos résultats montrent que le processus de nucléation des bulles peut être influencé par la taille des globules de liquide silicaté (essentiellement des plus petits d'entre eux), par le comportement du globule vis-à-vis des faces des diamants (nucléation hétérogène versus homogène) et peut-être aussi par la petite taille de la chambre à échantillon (< 500 µm de long pour une épaisseur entre les deux diamants de 250 µm, bien que nous n'ayons pas d'arguments pour le prouver). Néanmoins, cette première étude in-situ du dégazage d'un magma par décompression a montré que les CED sont des outils potentiellement puissants pour ce genre d'étude, permettant l'observation directe du processus de nucléation, de croissance, et de coalescence des bulles en fonction de la pression et du temps, avec une excellente résolution optique. Le dispositif nécessite à présent d'être techniquement modifié afin de pouvoir obtenir des conditions de dégazage réalistes pour les magmas (notamment de faibles pressions finales et un découplage pression / température).

ELSEVIER

Earth and Planetary Science Letters 191 (2001) 115–127

EPSL

www.elsevier.com/locate/epsl

In situ high-pressure and high-temperature bubble growth in silicic melts

Caroline Martel [a,*], Hélène Bureau [a,b]

[a] *Bayerisches Geoinstitut, Universität Bayreuth, D-95440 Bayreuth, Germany*
[b] *LPS-CEA/CNRS-CE Saclay, F-91191 Gif-sur-Yvette, France*

Received 15 March 2001; accepted 14 June 2001

Abstract

We present the first investigation of in situ high-pressure and high-temperature bubble growth in silicic melts. In a hydrothermal diamond-anvil cell, a haplogranite melt (79 wt% SiO_2) is hydrated then subjected to cooling and decompression. With decreasing pressure, water exsolves from the melt and bubbles grow. The whole experiment is observed through an optical microscope and video-recorded, so that bubble nucleation, bubble growth, and the glass transition are directly monitored. Bubbles nucleate and expand in melt globules having radii from 15 to 70 μm. Bubbles reached 3.6–9.1 μm in radius within 6.1–11.7 s (until the glass transition is attained) while temperature decreases from 709–879°C to 482–524°C, corresponding to decompressions from 7.0–21.9 to 3.4–15.2 kbar. Bubbles nucleated either in a single event occurring within the first second or in successive pulses over a period of up to 7 s when the melt globules are in contact with a diamond culet of the cell. In these experiments, bubble growth can be fitted to the cube root or a logarithm of time, mainly ascribable to the combination of large water oversaturations due to rapid cooling and decompression. At pressures of 3.4–15.2 kbar, we measure glass transition temperatures that are 20–80°C higher than those calculated at atmospheric pressure.

Keywords: bubbles; high pressure; high temperature; growth rates; silicate melts

---

1. Introduction

Magma degassing occurs during volcanic eruptions due to the exsolution of the volatiles dissolved in the melt at depth. This results from the decrease of the volatile solubility in melts with decreasing pressure [1]. Bubbles grow by diffusion of the volatiles dissolved in the melt through the melt–vapor interface and by gas expansion as pressure decreases. These processes drastically change the physical and chemical properties of the magmas, the flow properties within the conduit, and therefore the ascent rates that finally control the eruption regime. Therefore, much effort has been devoted to understand the dynamics of bubble growth in magmas in order to model volcanic eruptions.

Bubble growth models have evolved from the consideration of a single bubble expanding in a superheated infinite one-phase system [2] to many

---

* Corresponding author. Present address: ISTO-CNRS, 1A rue de la Férollerie, F-45071 Orléans cedex 2, France. Tel.: +33-2-3825-5252; Fax: +33-2-3863-6488.

E-mail address: cmartel@cnrs-orleans.fr (C. Martel).

PII: S0012-821X(01)00407-1

identical cells of one bubble surrounded by melt, in which the bubble grows from a volatile-oversaturated melt at constant pressure and temperature [3–5] or under decompression [3,5–7]. Theoretical results are obtained by solving equations of volatile diffusion in the melt, viscous deformation of the melt, and mass balance of volatiles at the bubble interface. At constant pressure and temperature and for relatively long durations, models predict that bubble growth is proportional to a square root of time mainly controlled by the volatile diffusivity in the melt.

Theoretical models have been experimentally tested at atmospheric pressure under increasing temperature using heating stage devices [8–10]. These in situ methods allow the direct observation of the process of bubble growth and enable the precise observation of the timescale of vesiculation. However, these experiments better simulate bubble growth in domes (under cooling at constant pressure) than during magma ascent in the conduit (under decompression at nearly constant temperature). To better simulate bubble growth in ascending magmas, experiments have been performed in rapid-quench autoclaves, in which bubbles nucleate at constant pressure and temperature from an oversaturated rhyolitic melt [11,12] or under controlled decompression [13]. After quench, bubble sizes and number density are measured. Although the procedure better compares with natural process, it is not an in situ observation and does not allow the monitoring of the entire vesiculation process.

Here, we present the first in situ high-pressure and high-temperature study of bubble growth in silicic melts using a hydrothermal externally heated diamond-anvil cell. The procedure allows us to observe and measure the timescales of bubble nucleation, bubble growth, and the glass transition that can be compared to theoretical and analytical models.

2. Materials and methods

2.1. Starting materials

The starting material is a synthetic bubble-free haplogranite glass (HPG8, SiO_2: 78.6, Al_2O_3: 12.5, Na_2O: 4.6, K_2O: 4.2 wt%, microprobe analyses). This glass was synthesized by fusing a mixture of dry powders of Si and Al oxides with Na and K carbonates at 1400–1675°C and 1 atm. The fused batches were loaded into a box furnace and stirred until it becomes homogeneous and devoid of bubbles. In order to enhance the further hydration in the diamond-anvil cell, we started with pre-hydrated glasses. This pre-hydration was performed by sealing the required amount of HPG8 glass powder and distilled water into Pt capsules and annealing it for 6 days at 1000°C and 3 kbar (Institut für Mineralogie, Hannover, Germany). The water content of the hydrated glass was measured by Fourier transform infrared spectroscopy at 2.4 wt%. Thin fragments of glass were crushed to the size corresponding to the sample chamber (<100 μm thick, ~ 300 μm Ø).

2.2. Experiments

Bubble nucleation and growth are observed in situ at high pressures and high temperatures in a modified Bassett-type hydrothermal diamond-anvil cell [14,15]. In this cell, the sample is contained in a hole bored in the center of a rhenium gasket, compressed by two type-I diamonds of 0.21 carat with 1 mm flats. Heating is achieved by passing a high electrical current through molybdenum wires around tungsten carbide seats holding the diamonds. During the entire experiment, an Ar–H_2 gas mixture (2 vol% H_2) is introduced into the cell to prevent oxidation of the diamonds and the molybdenum heater. The temperature is measured by two thin wire K-type thermocouples attached to the diamonds. The temperature in the sample chamber is calibrated against these thermocouples by measuring the melting points of $NaNO_3$, CsCl, NaCl, sulfur, and ice in the cell at room pressure. The calibration curve has a standard error of ± 2°C. Temperatures may be measured every 0.1 s.

Pressures at any given temperature may be computed from the equation of state of water [16,17] and the knowledge of its density at a known temperature. The pressure estimation during the experiments is based on the fact that the sample cavity is filled with water and remains of constant volume on cooling [14,15]. In order to stabilize the volume of the sample chamber during cooling, the hole of the gasket was first filled with water and an air bubble to give the desired bulk density and cycled through the relevant temperature range several times, until the homogenization temperature of the fluid becomes virtually constant. The initial sample chamber diameter is 500 μm. During gasket stabilization this diameter is reduced to about 400 μm, and then diminishes progressively during the successive experiments until the available volume becomes too small for good observation. This is due to the fact that during heating, the metal gasket softens and yields under the force applied to the diamonds. Variations in the volume of the sample cavity modify the density of the fluid (which becomes higher for each heating–cooling cycle), so that pressure increases with successive experiments.

For an experiment, the cell is loaded with the sample (pieces of glass), water and an air bubble and heated to the desired temperature. The water density prevailing during the experiment is calculated [18] by measuring the homogenization temperature of the air bubble after cooling (100–200°C). At these low temperatures, we assume that the fluid has properties similar to pure water, based on the low solubility of silicate glasses in water at these conditions [19]. This density is used for pressure calculation at the run conditions [16,17]. The error on the calculated pressure is estimated to be maximum ± 2 kbar.

3. Results

3.1. Progress of the experiment

The whole experiment can be described in the following steps. The first step is the melting of the glass fragments and their hydration at a given temperature, which defines the pressure and therefore the melt water content (both calculated at the conclusion of the experiment). Once globules of silicate melts have equilibrated with the aqueous phase at the chosen maximum temperature, we switch off the power of the heater (corresponding to time = 0 s), causing a non-linear cooling rate of 2–8°C/s during the first second to ~32°C/s after 2 s. This cooling induces decompression rates of 300–600 bar/s. For one experiment (#8), cooling was manually controlled (without switching off the furnace) at a rate of 2°C/s, giving a decompression rate of 24 bar/s (Fig. 1). Because water solubility decreases with decreasing pressure and temperature [1] in this second step, water exsolves from the melt. Water exsolution is physically observed by bubble nucleation in the melt globules. As temperature and pressure both decrease, these bubbles grow until the glass transition temperature is reached (except for experiment #8) marking the end of the experiment. As the experiments are video-recorded, together with temperature and time, the processes and the timescales of bubble nucleation, bubble growth, and glass transition are precisely observed and the bubble sizes may be measured on frame-captured images every 0.2 s using an image analysis software. Very few bubbles (zero to five, usually only one) can be satisfactorily measured per experiment due to the lim-

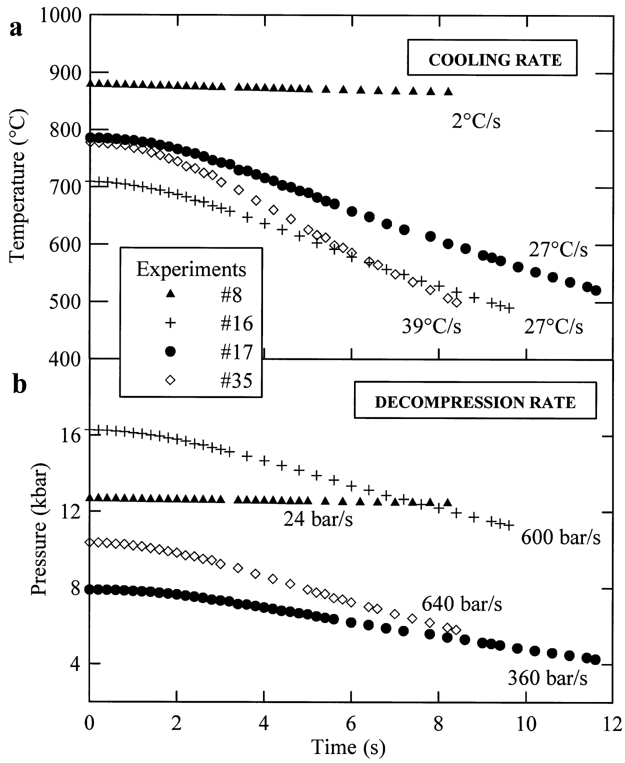

Fig. 1. Cooling rates (a) and corresponding decompression rates (b) of four selected experiments.

Table 1
Experimental and analytical conditions

Exp #	Initial conditions ($t = 0$ s) and first nucleation event			Last nucleation event		Final conditions at the glass transition (except for #8)							ΔT	ΔP	ΔC_w
	T_i (°C)	P_i^a (kbar)	C_{wi}^b (wt%)	T (°C)	t (s)	T_f^c (°C)	P_f^a (kbar)	C_{wf}^b (wt%)	t (s)	q^d (°C/s)	R_m^e (μm)	R^e (μm)	(°C)	(kbar)	(wt%)
31[f]	784	7.0	12.4	597	5.4	493	3.4	6.6	8.1	37	67	~8	291	3.6	5.8
24[f]	808	7.0	12.7	650	5.1	520	3.4	6.9	9.1	36	40	9.1	288	3.6	5.8
30A[f]	712	7.8	12.3	580	4.4	520	5.0	7.6	6.1	35	~40	7.6	192	2.8	4.7
17[f]	785	7.9	13.6	783	0.8	524	4.4	7.3	11.7	27	29	3.6	261	3.5	6.3
32A[f]	794	8.1	14.0	600	6.6	498	4.6	7.2	9.5	36	31	7.6	296	3.5	6.8
26[f]	791	8.9	15.0	661	4.6	503	4.6	7.2	9.5	34	46	8.4	288	4.3	7.8
32B[f]	793	8.9	15.0	608	6.4	482	4.3	6.8	10.1	34	~60	~8	311	4.6	8.2
30B[f]	734	9.2	14.3	582	5.4	502	5.5	7.5	7.7	36	40	7.6	232	3.7	6.8
27	743	9.6	14.9	737	0.6	505	5.8	7.7	7.7	33	39	7.8	238	3.8	7.2
35	778	10.4	16.8	570	6.2	503	5.9	7.7	8.3	39	28	7.6	275	4.5	9.1
29	728	10.5	15.5	726	0.4	522	6.9	8.2	7.3	34	29	6.5	206	3.6	7.3
10_1	775	12.3	19.4	767	1.6	504	7.4	8.1	10.7	31	20	5.1	271	4.9	11.3
10_2	775	12.3	19.4	767	1.6	504	7.4	8.1	10.7	31	22	4.5	271	4.9	11.3
4	821	13.0	22.3	820	0.4	508	7.4	8.1	11.7	33	22	6.5	313	5.6	14.2
15_1	750	15.5	22.5	748	0.6	502	10.2	8.3	11.3	27	22	6.5	248	5.3	14.2
15_2	750	15.5	22.5	748	0.6	502	10.2	8.3	11.3	27	26	6.0	248	5.3	14.2
16	709	16.3	20.7	708	0.4	492	11.4	8.0	9.5	27	31	6.2	217	4.9	12.7
5	743	21.9	30.4	663	4.8	493	15.2	7.8	11.5	27	28	6.5	250	6.7	22.6
8	879	12.6	23.9	–	–	867	12.4	23.0	8.2	2	70	7.0	12	0.2	0.9

[a] Pressure calculated after [16] (±1 kbar for pressures <15 kbar to ±2 kbar for pressures >15 kbar).

[b] Water content calculated after [20] (±1.5 wt% at pressures <15 kbar to ±3 wt% at pressures >15 kbar).

[c] Final temperatures assumed to be the glass transition temperatures (except for #8; maximum ±20°C, see text).

[d] Cooling rate after 2 s.

[e] R_m is the radius of the melt globule that contains the water bubble of final radii R (±0.3 μm).

[f] Experiments where the melt globules are in contact with the lower-diamond culet.

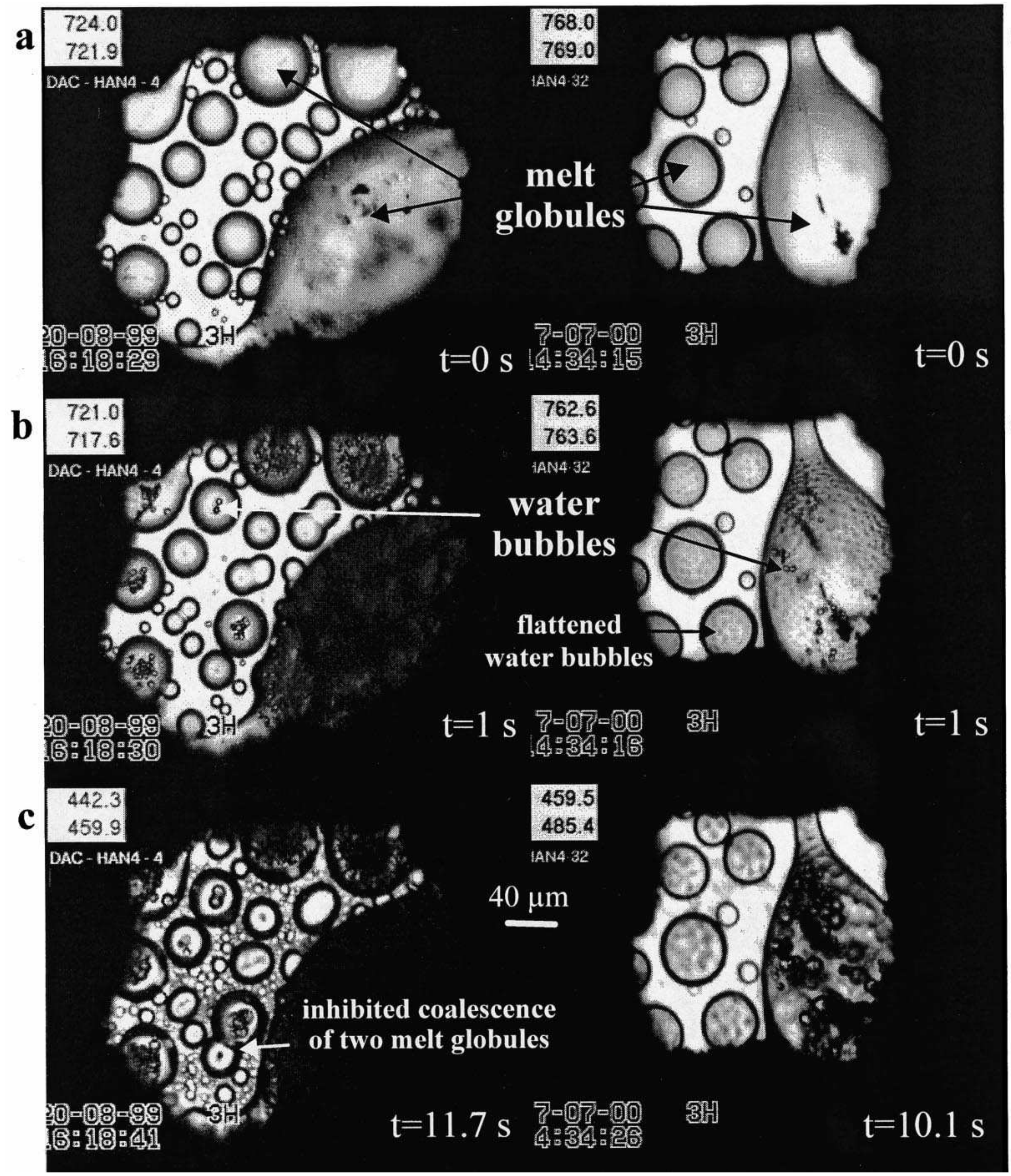

Fig. 2. Frame-captured images of experiments #4 (a–c) and #32B (d–f). Top pictures are taken at 0 s time, when the power of the heater was switched off. Melt globules are devoid of crystals and bubbles. The middle pictures are at $t = 1$ s, showing that water exsolved and bubbles grew in the melt globules. The bottom pictures are at the glass transition, after 11.7 and 10.1 s for experiments #4 and #32B, respectively. Temperatures (not corrected) given by the two thermocouples and time appear on each picture on the upper and bottom left corners, respectively. Note that pictures e and f of #32B show flattened water bubbles resulting from the contact between the melt globules and the lower-diamond culet.

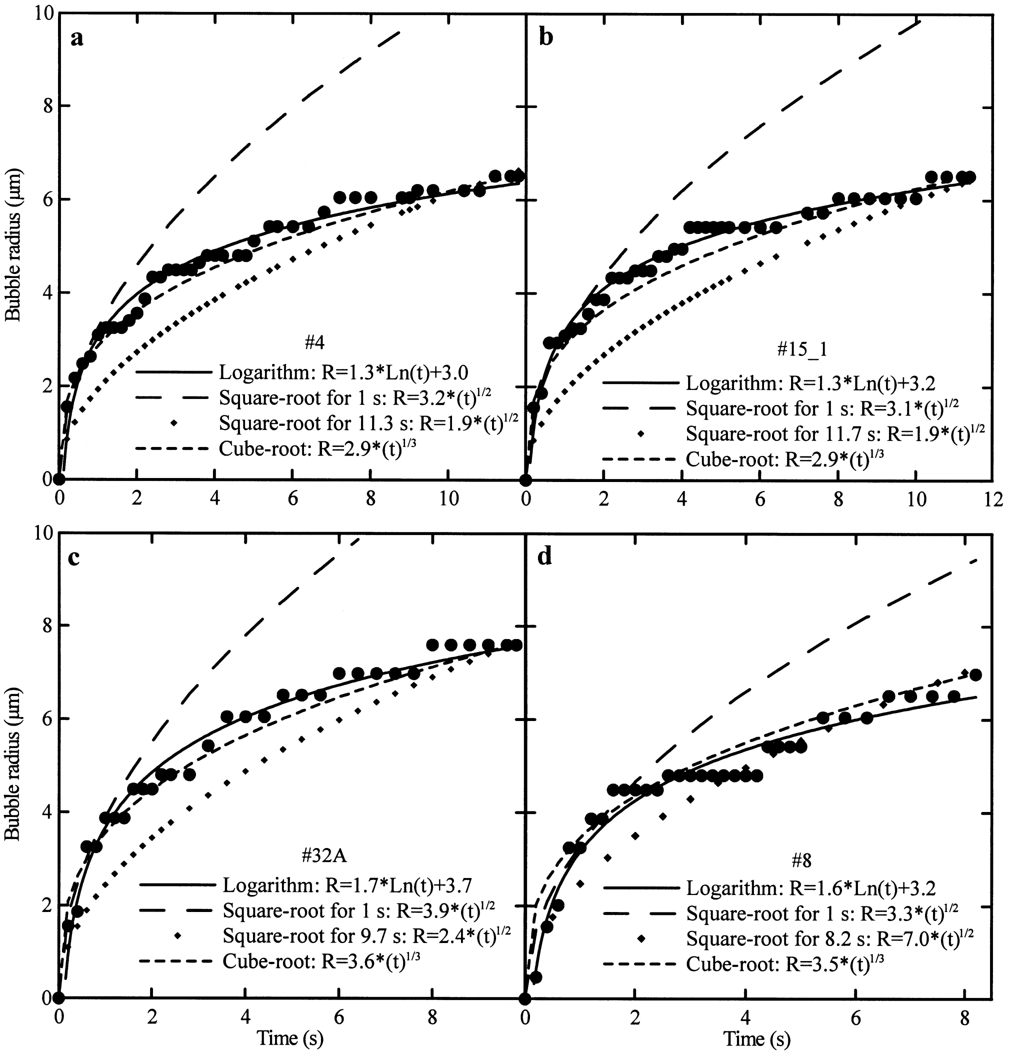

Fig. 3. Bubble growth. a: Experiment #4; b: experiment #15; c: experiment #32A; d: experiment #8. The plain circles represent the measured bubble radius (±0.3 µm) as a function of time. The logarithm law (plain line) is a fit of these experimental data. The coefficients of the square-root laws are calculated for the bubble radius at 1 s (long-dashed line) and final time (diamonds). The coefficient of the time cube-root law is defined for the bubble radius at the final time (short-dashed line).

itation of the focus of the microscope. Indeed, the focus (fixed during the decompression) gives us a thin layer through the whole volume of the sample chamber, and therefore a small number of bubbles. Among these potentially measurable bubbles, we have to rule out the coalescing bubbles and the moving bubbles that go out of focus. The experimental conditions are reported in Table 1.

Initial temperatures range from 709 to 879°C and corresponding water pressures are between 7.0 and 21.9 kbar [16]. We calculated the water contents in the melt after the model of [20], which is valid for haplogranite compositions at temperatures of 500–1350°C and pressures up to 8 kbar. This model requires water fugacities that we calculated after [21]. We extrapolated the calculation of [20] for pressures higher than 8 kbar (up to 22 kbar). This may be justified as we compute an initial water content of 22 ± 3 wt% for experiment #15 (750°C, 15.5 kbar) which is in good agreement with the 26 ± 8 wt% determined in situ by infrared spectroscopy measurements using the same diamond-anvil cell, for a haplogranite

Table 2
Bubble growth laws

Exp #	Logarithm		Square-root law			Cube-root law	
			$t < 1$ s		whole t range	$t > 1$ s	whole t range
	$R = A \times \ln(t) + B$		$R = C1 \times (t)^{1/2}$		$R = C2 \times (t)^{1/2}$	$R = C3 \times (t)^{1/3}$	
	A	B	$C1$	$\log(t)/\log(R)$	$C2$	$\log(t)/\log(R)$	$C3$
31[a]	1.6	4.1	4.5	1.6	2.8	3.2	4.0
24[a]	–	–	(2.9)	(2.3)	(3.0)	(1.8)	(4.4)
30A[a]	–	–	4.5	–	3.1	4.0	4.2
17[a]	(0.8)	(1.6)	(1.6)	(1.3)	(1.0)	(3.1)	(1.6)
32A[a]	1.7	3.7	3.9	1.7	2.4	2.9	3.7
26[a]	1.9	4.1	4.0	1.1	2.7	3.9	4.0
32B[a]	2.0	4.0	3.9	1.8	2.5	4.2	3.7
30B[a]	1.8	3.7	3.9	1.1	2.7	3.4	3.9
27	1.7	4.0	3.9	1.9	2.8	3.2	3.9
35	1.7	3.9	4.5	0.7	2.6	3.4	3.8
29	1.4	3.7	3.4	2.1	2.4	3.2	3.4
10	1.1	2.7	2.9	1.2	1.6	4.3	2.3
4	1.3	3.0	3.2	2.4	1.9	3.1	2.9
15	1.3	3.2	3.1	2.1	1.9	3.4	2.9
16	–	–	(1.7)	(1.2)	2.0	–	2.9
5	1.5	2.7	2.5	2.1	1.9	2.9	2.9
8	1.6	3.2	3.6	0.8	(7.0)	3.6	3.5
Average[b]	1.6 ± 0.2	3.4 ± 0.5	3.7 ± 0.6	1.6 ± 0.5	2.4 ± 0.4	3.5 ± 0.4	3.5 ± 0.5

[a] Experiments with extrinsic nucleation mode.

[b] Statistics calculated without the values in parentheses, for which we suspect abnormal bubble growth.

composition, at pressure and temperature conditions similar to our experiment #15 [22].

3.2. Bubble nucleation

Bubbles nucleated in crystal-free melt globules of radius sizes from ~20 to 70 μm (Fig. 2). No nucleation occurred in melt globules below 15 μm in radius and within the outer rim of ~10–22 μm of larger globules. We observe two different types of bubble nucleation, an intrinsic mode where bubbles nucleate at random within the melt globules and an extrinsic mode where bubbles nucleate at diamond–melt interfaces when globules touch the culets. Intrinsic nucleation prevails for initial pressures > 9.5 kbar (Table 1) and can be delayed up to 1 s, depending on the size of the melt globule. For instance in experiment #27, at $t = 0.2$ s, the first bubbles occur in the two globules with radii > 50 μm, followed by nucleation in the 39 μm radius globule at 0.6 s, the last bubbles occurring in the 34 μm globule at 1.0 s. We emphasize here that only one nucleation event occurs per melt globule, leading to round bubbles. The extrinsic nucleation mode is restricted to initial pressures < 9.5 kbar and leads to many flattened (non-measurable) bubbles that are actually hemispheres wetted on the lower-diamond culet. This main nucleation event is followed by further intrinsic nucleations (giving measurable round bubbles) within the same melt globule occurring over periods up to 7 s (Fig. 2e,f; Table 1). This type of nucleation is particularly well illustrated in experiment #31 (the lowest initial pressure), in which a late nucleation event occurred at $t = 5.4$ s in a 67 μm radius melt globule, strongly obscuring the observation of the previous bubbles.

3.3. Bubble growth

Bubbles expanded during 6.1–11.7 s, reaching radii between 3.6 and 9.1 μm for temperature differences of 192–313°C, corresponding to decompressions of 2.9–6.6 kbar and water losses of 4.7–

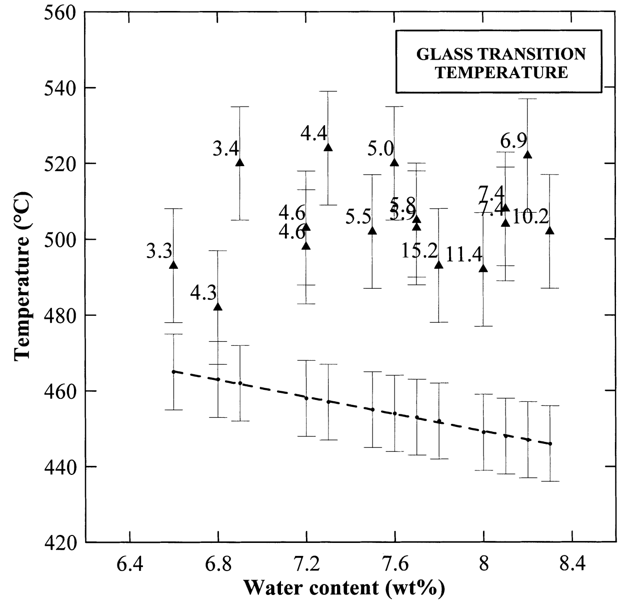

Fig. 4. Glass transition temperatures (T_g) as a function of the final water content. The plain triangles are the observed T_g (±15°C) labelled with the final pressures in kbar. The dots are the T_g (±10°C) calculated after [33] at atmospheric pressure for a cooling rate of 32°C/s. The dashed line is the best linear fit of the calculated T_g.

22.6 wt% (Table 1). The bubble measured in experiment #8 reached 7 μm in radius for a temperature decrease of 12°C, corresponding to a decompression of 0.2 kbar. Comparing bubble sizes in experiments #26 and #32B performed at similar pressure and temperature show that the radius of the melt globule in which the bubble expanded (46 and ~60 μm, respectively) has no significant influence on the final bubble radius (8.4 and ~8 μm, respectively). At pressures below 10 kbar, bubbles have an average radius of 7.5 ± 1.5 μm, compared to 6.1 ± 0.8 μm above 10 kbar (Table 1). Fig. 3 displays the measured bubble radius versus time of four selected experiments. Bubble radii seem to expand in steps which length increases with time. Unfortunately, the measurement errors (precision is not better than ±0.3 μm) do not enable us to discern between a step by step and a continuous growth with time. The final radii of the melt globules grew at most 0.5 μm relative to their initial radius (before bubble nucleation).

We observed little bubble coalescence, mainly occurring at the very first stage of the bubble growth. Little coalescence results from both little bubble movement within the melt and a drastic increase of melt viscosity as temperature drops [23]. Coalesced bubbles were not considered in the measurements.

3.4. Bubble quench – glass transition

Bubbles cease expansion when the melt viscosity reaches a high threshold value at temperatures close to the glass transition temperature (T_g). Visible evidence for achieving high melt viscosities is the inhibition of the coalescence process between melt globules as illustrated in Fig. 2c. We determined T_g when all bubbles cease growth and movement within the melt globules, corresponding to temperatures between 482 and 524°C over a water content range of 6.6–8.3 wt% at pressures between 3.4 and 15.2 kbar (Table 1). For a given pressure, T_g can vary up to 40°C (e.g. at 4.3–4.4 kbar), ascribable to the fact that the glass transition is actually a progressive process occurring over a range of several tens of degrees [24].

4. Discussion

4.1. Bubble nucleation

The lack of bubble nucleation both in melt globules below 15 μm in radius and within an outer rim of 10–22 μm in larger melt globules probably reflects diffusive water escape from the melt into the surrounding water medium. Any further consideration first requires the determination of the initial water diffusivities in the melt. Zhang and Behrens [25] have recently proposed a calculation of the water diffusivity in rhyolitic melts at temperatures between 400 and 1200°C, pressures up to 8.1 kbar and for water contents < 8 wt%. Although the initial water contents in our experiments are > 12 wt%, we calculated the initial water diffusivity for the five first experiments in Table 1 (for which initial pressures are ≤ 8.1 kbar) and found values between 8×10^{-9} and 4×10^{-8} m^2/s (#31 and #32A, respectively). These values do not fall in the common range of water diffusivities in rhyolitic melts ($\sim 10^{-11}$–

10^{-12} m^2/s, [26–28]), but are more comparable to those in basaltic melts [26,29]. The similarity with water diffusion in basalts also translates to comparable viscosities (initial viscosities $< 10^4$ Pa s [30], extrapolated for water contents > 8 wt%). The combined increase of water content (> 8 wt%) and pressure (> 8.1 kbar) would lead to faster diffusivities [25]. We use the simple diffusion equation $x^2 \sim D_w \times t$ (where x is the distance in m, here the globule radius, D_w the diffusivity in m^2/s and t the time in s) to determine how fast water can diffuse from the melt globules to the surrounding water medium. Water diffusivities of the order of 10^{-9} m^2/s would lead to water depletion in a 15 μm radius melt globule within 0.2 s. This depletion is fast enough to explain the absence of bubble nucleation in globules < 15 μm in radius and within the outer 10–20 μm rims of larger globules.

In globules > 40 μm in radius, the delay to bubble nucleation is always < 0.4 s, which corresponds to decompressions < 30 bars. This agrees with the low supersaturation pressures required to initiate heterogeneous nucleation as reported by [12].

The extrinsic nucleation prevailing at pressures < 9.5 kbar implies that the melt globules sank down on the diamond. The calculated density contrast between the hydrated melt globules and the water is lower at low than high pressures (melt density [31]−water density [16] = 1805 and 2637 kg/m^3 at 7.0 and 21.9 kbar for experiments #31 and #5, respectively). This would favor the flotation of the melt globules at low pressures, in contrast to the observation. We propose that the flotation of the melt globules at high pressures is due to the narrowing of the immiscibility gap between water and melt at the approach of the supercritical conditions that results in a density increase of the fluid by silica enrichment while a density decrease of the melt by water addition. At pressures < 9.5 kbar, the melt globules tend to sink (as predicted by the density contrast) and the contact between the diamond and the melt provides a preferential site for bubble nucleation by substantially reducing the theoretical supersaturation pressure. We propose that this localized (extrinsic) nucleation creates gradients in the melt water content, i.e. water enrichment towards the far-field melt relative to the melt at the diamond boundary, so that further successive intrinsic nucleations can take place in the far-field melt as decompression goes on.

4.2. Bubble growth law

While most of the published theory and analytical solutions on bubble growth assume constant temperature and pressure, the processes in our experiments are rather complex, especially because they involve the simultaneous variation of many time-dependent parameters, such as temperature, pressure, and water content (thus, viscosity, density, and diffusivity). Therefore, development of analytical solutions of our bubble growth during cooling-induced decompressions is kept for future purposes. In this section, we compare our experimental bubble sizes with published growth models. Because our experimental conditions are quite remote from near-equilibrium bubble growth we expect that their sizes should remain smaller than equilibrium values. Close to equilibrium, Navon and Lyakhovsky [32] have shown that bubble radii (R_{eq}) may be expressed by:

$$R_{eq}^3 = S_0^3(C_{wi} - C_w)(\rho_m/\rho_w)$$

where $S_0^3 = 3/(4\pi N_d)$, in which N_d is the bubble number density (in m^{-3}) per melt globule; C_{wi} is the initial water content of the melt (Table 1); C_w the melt water content [20]; ρ_m and ρ_w the density of the hydrated melt [31] and the water in the bubble [16], respectively (the four last parameters being calculated at a given time). The bubbles in experiment #8, for which the decompression rate is only 24 bar/s, presumably grow the closest to equilibrium: at $t = 5.8$ s and $t = 8.2$ s, the calculated R_{eq} (counting ~40 bubbles in the 70 μm in radius melt globule) is 5.5 and 6.3 μm in comparison to 4.8 and 7.0 ± 0.3 μm, respectively. However, in the experiments where we could determine N_d (with an intrinsic nucleation), measured bubbles are always smaller than equilibrium sizes. For instance, in experiment #35 (four bubbles in the melt globule of 28 μm in radius), the calculated equilibrium radius at $t = 3.8$ s and $t = 6.4$ s equals

9.0 and 10.7 μm instead of measured radius of 6.0 and 7.0 ± 0.3 μm, respectively (the final equilibrium radius would be 11.3 μm, but the bubble was quenched with 7.6 μm in radius). In experiment #4 (two bubbles in the melt globule of 22 μm in radius), the calculated equilibrium radius at $t = 3.8$ s and $t = 6.4$ s equals 8.9 and 13.2 μm instead of measured radius of 4.8 and 5.4 ± 0.3 μm, respectively. This non-equilibrium degassing is ascribable to both the rapid decompression (299–583 bar/s) and the viscous quench that occurs approaching the glass transition.

Having verified that bubble growth is slower than quasi-equilibrium models, we may compare our experimental data with literature models for bubble growth.

4.2.1. Growth proportional to the square root of time

Bubble growth approaching equilibrium for constant pressure, temperature, viscosity and diffusivity has been found to be proportional to a square root of time. Although all these parameters are drastically varying during our experiments, we tested that law because it is the one used in the literature. The law is given by $R = C2 \times (t)^{1/2}$, where R is the bubble radius in μm, t the time in s, and $C2$ a constant that we calculated for the final bubble radius (Table 2). As expected, this law significantly misfits the experimental bubble growth (Fig. 3). In addition, restricting the growth to the first second, during which the cooling rate is very low, the inverse of the slopes in the log(R) versus log(t) coordinates gives 1.6 ± 0.5 instead of 2.0 for a true square-root law (Table 2).

We applied the analytical solution of [11] for isothermal and isobaric diffusivity-controlled bubble growth in rhyolites, based on the numerical model of [4] and defined by:

$$R^2 = [2 \times D_\mathrm{w} \times \rho_\mathrm{m} \times (C_\mathrm{wi} - C_\mathrm{wf}) / \rho_\mathrm{w} \times t] - [2 \times D_\mathrm{w} \times \eta \times \rho_\mathrm{m} \times (2 \times C_\mathrm{wi} + C_\mathrm{wf}) \times \log(\Delta P / \eta \times t) / 3 \times P_\mathrm{f} \times \rho_\mathrm{w})]$$

where ρ_m is the density of the hydrated melt [31], ρ_w the water density in the bubble [16], C_wi and C_wf the initial and final water contents of the melt, respectively [20], ΔP the decompression, η the melt viscosity [30] and D_w the water diffusivity [25], the two last parameters being extrapolated to water contents > 8 wt%. This analytical solution is poorly sensitive to melt viscosity, but strongly relies on water diffusivity. We calculated final radii of 181 and 445 μm instead of ∼8 and 7.6 μm measured in experiments #31 and #32A, respectively. Therefore, a growth proportional to a square root of time largely overestimates the size of bubbles expanding during a cooling-induced decompression. Integrating the cooling effect on water diffusivity, melt viscosity, melt and gas densities in the analytical solution of [11] does not reconcile the experimental and analytical data.

4.2.2. Growth proportional to the cube root of time

Although it has never been used to describe bubble growth, we investigated the law following the cube root of time, given by $R = C3 \times (t)^{1/3}$, where $C3$ is a constant determined for the final radius (Table 2). We found that bubble growth nearly follows the cube root of time, although such a law often slightly overestimates the bubble size during the first seconds and systematically underestimates it after ∼2 s. This size underestimation is also suggested by the 3.5 ± 0.4 value given by the inverse of the slopes in the log(R) versus log(t) coordinates, instead of 3.0 for a perfect cube-root law (Table 2). However, Fig. 3 shows that the deviation between the experimental and calculated data, although systematic, is still included within the analytical error on the radius measurements. Approximate fit to a cube root of time means that there is a linear relationship between bubble volume and time, which may be explained if growth is dominated by decompressive expansion of the bubbles.

4.2.3. Growth proportional to the logarithm of time

The experimental data are most closely fit to a logarithmic curve ($R = A \times \ln(t) + B$; Fig. 3 with parameters A and B given in Table 2). Although each set of conditions of pressure and temperature gives unique values for A and B, these parameters vary little over the set of experiments (1.6 ± 0.2

and 3.4 ± 0.5, respectively). This is in keeping with the small variability of the final bubble radii (7.5 ± 1.5 μm below 10 kbar, 6.1 ± 0.8 μm above 10 kbar) that may be explained by the strong non-linearity of the water density with pressure, resulting in little volume changes of the bubbles at high pressures compared to low pressures for a given temperature. The bubble growth in experiment #8 with controlled decompression is also satisfactorily fitted by the logarithmic law, suggesting that even bubbles growing nearer to equilibrium can follow this law. In the literature, the only reference to a logarithmic law is that ensuing from the numerical model of [26], after the authors incorporated parametric interactions between closely spaced bubbles resulting from small cooling ($\Delta T < 100°C$). These authors found that the logarithmic growth particularly applies to low pressures (< 0.1 kbar) or high water oversaturation. Although our experiments cannot be compared to their simulation, we, like them, ascribe the strong deviation from a square root of time to the combined effects of cooling (12°C in experiment #8 or between 192 and 313°C for the other experiments), high water oversaturation in the melt and concurrent decompression.

4.3. Glass transition

The experiments we performed allow us to provide data on glass transition temperatures (T_g) at high pressures (3.4–15.2 kbar) that can be compared with the current models valid for atmospheric pressures. Dingwell [33] combined T_g measurements from the literature to propose a T_g calculation for haplogranite composition as a function of water content (≤8.1 wt%) at atmospheric pressure (exception of data acquired at 2.5 kbar) and for a cooling rate of 0.1°C/s. We first have to modify this calculation for the cooling rates prevailing in our experiments. The isokom of $\log(\eta) = 12.4$ Pa s given by [33] gives a shift factor $k = 11.4$, that can be used to calculate the isokom for $q = 32°C/s$, following $\log(\eta) = k - \log(q) = 9.9$ Pa s. A melt viscosity decrease of 2.5 log units at 500°C corresponds to a temperature increase of 110°C [30], so that we can calculate T_g (± 10°C) for a cooling rate of 32°C/s after [33] following: T_g (K) = $(786-83.47 \times \ln(C_w))+110$. The calculated T_g values are 20–80°C lower than the measured T_g (Fig. 4). Therefore, the effect of pressures of 3.3–15.2 kbar on the T_g determination is an increase of several tens of degrees. The slight decrease of the calculated T_g ($\sim 15°C$) with water contents increasing from 6.6 to 8.3 wt% does not appear in the measured T_g, probably due to the large errors in the T_g determinations.

4.4. Applications to natural volcanic systems

Although the experiments are not directly applicable to magma ascent in volcanic systems, this study provides a major step in the understanding of bubble growth process that is necessary for further investigations of magma rheology and eruption mechanisms. During experiments, both temperatures and pressures decrease at a fast rate unlike their variations during magma ascent. However, degassing and crystallization of the ascending magma cause temperature fluctuations that have significant impacts on the bubble growth dynamics [26]. We emphasize here that the effects of cooling and rapid decompression cause growth to strongly deviate from the square root of time that applies during isothermal degassing. Second, our diamond-anvil cell operates at pressures between 5 and 25 kbar, which is probably not relevant to the degassing of rhyolites in a volcanic conduit. A more relevant study would imply either lower pressures (< 2 kbar, therefore water contents < 6 wt%) for a rhyolite composition, or basalt compositions with a CO_2 fluid phase at the present pressure range. However, we present a new technique providing in situ data that were never collected before. Technical and strategic changes of the present device to make it relevant to volcanic systems are quite straightforward.

If the results are not quantitatively applicable to natural volcanic systems, they are probably of qualitative relevance: (1) single versus several nucleation events that lead to characteristic bubble size distributions in natural erupted products is a hotly debated task. Our results suggest that during magma ascent, an early bubble nucleation on preferential sites (i.e. crystals) would result in gradients in the gas dissolved in the melt and subsequent generations of degassing events; (2) bubble growth during cooling is probably relevant to what happens in volcanic domes; (3) the glass transition is a major process that drastically changes the physical properties of melts so that its precise determination (especially under pressure) is crucial, and (4) this experimental study provides a novel data base and growth laws that can be used for further developments of analytical solutions of bubble growth.

Acknowledgements

This project was funded by the 'Visiting Scientists' Program' and the EU 'IHP-Access to research Infrastructures' program (Contract No. HPRI-1999-CT00004 to D.C. Rubie) of the Bayerisches Geoinstitut. We would like to thank M. Wilke for the hydration experiment of the starting material, K. Klasinski for technical assistance on the diamond-anvil cell, H. Keppler, S. Mackwell, C. Mourtada-Bonnefoi for helpful discussions, B.C. Schmidt and M.P. Semet for improving the manuscript, O. Navon and J. Gardner for constructive reviews.***[AC]***

References

[1] F. Holtz, H. Behrens, D.B. Dingwell, W. Johannes, H_2O solubility in haplogranitic melts: compositional, pressure, and temperature dependence, Am. Mineral. 80 (1995) 94–108.

[2] L.E. Scriven, On the dynamics of phase growth, Chem. Eng. Sci. 10 (1959) 1–10.

[3] A. Toramaru, Numerical study of nucleation and growth of bubbles in viscous magmas, J. Geophys. Res. 100 (1995) 1913–1931.

[4] A.A. Proussevitch, D.L. Sahagian, A.T. Anderson, Dynamics of diffusive bubble growth in magmas: isothermal case, J. Geophys. Res. 98 (1993) 22283–22307.

[5] J. Barclay, D.S. Riley, R.S.J. Sparks, Analytical models for bubble growth during decompression of high viscosity magmas, Bull. Volcanol. 57 (1995) 422–431.

[6] Y. Bottinga, M. Javoy, MORB degassing: bubble growth and ascent, Chem. Geol. 81 (1990) 255–270.

[7] A.A. Proussevitch, D.L. Sahagian, Dynamics of coupled diffusive and compressive bubble growth in magmatic systems, J. Geophys. Res. 101 (1996) 17447–17455.

[8] O. Navon, A. Chekhmir, V. Lyakhovsky, Bubble growth in highly viscous melts: theory, experiments, and autoexplosivity of dome lavas, Earth Planet. Sci. Lett. 160 (1998) 763–776.

[9] N.S. Bagdassarov, D.B. Dingwell, M.C. Wilding, Rhyolite magma degassing: an experimental study of melt vesiculation, Bull. Volcanol. 57 (1996) 587–601.

[10] Y. Liu, Y. Zhang, Bubble growth in rhyolitic melt, Earth Planet. Sci. Lett. 181 (2000) 251–264.

[11] V. Lyakhovsky, S. Hurwitz, O. Navon, Bubble growth in rhyolitic melts: experimental and numerical investigation, Bull. Volcanol. 58 (1996) 19–32.

[12] S. Hurwitz, O. Navon, Bubble nucleation in rhyolitic melts: experiments at high pressure, temperature, and water content, Earth Planet. Sci. Lett. 122 (1994) 267–280.

[13] J.E. Gardner, M. Hilton, M.R. Carroll, Experimental constraints on degassing of magma: isothermal bubble growth during continuous decompression from high pressure, Earth Planet. Sci. Lett. 168 (1999) 201–218.

[14] A.H. Shen, W.A. Bassett, I.M. Chou, Hydrothermal studies in a diamond anvil cell: pressure determination using the equation of state of H_2O, in: Y. Syono, M.H. Manghnani (Eds.), High Pressure Research: Applications to Earth and Planetary Sciences, Geophysical Monograph 67 of the American Geophysical Union, Washington, DC, 1992, pp. 61–68.

[15] W.A. Bassett, A.H. Shen, M. Bucnum, A new diamond anvil cell for hydrothermal studies to 2.5 GPa and from 190 to 1200°C, Rev. Sci. Instrum. 64 (1993) 2340–2345.

[16] A. Saul, W. Wagner, A fundamental equation for water covering the range from the melting line to 1273 K at pressures up to 25 000 MPa, J. Phys. Chem. 18 (1989) 1537–1565.

[17] W. Wagner, A. Saul, A. Prub, International equations for the pressure along the melting and along the sublimation curve of ordinary water substance, J. Phys. Chem. Ref. Data 23 (1993) 515–527.

[18] L. Haar, J.S. Gallagher, G.S. Kell, NBS/NRC Steam Tables. Thermodynamic and Transport Properties and Computer Programs for Vapor and Liquid States of Water in SI Units, McGraw Hill, New York, 1984.

[19] A. Paul, Chemistry of Glasses, 2nd edn., Chapman and Hall, 1990, 367 pp.

[20] Y. Zhang, H_2O in rhyolitic glasses and melts: measurement, speciation, solubility, and diffusion, Rev. Geophys. 37 (1999) 493–516.

[21] K.-D. Grevel, D. Chatterjee, A modified Redlich-Kwong equation of state for H_2–H_2O fluid mixtures at high pressures and at temperatures above 400°C, Eur. J. Mineral. 4 (1992) 1303–1310.

[22] H. Bureau, H. Keppler, Complete miscibility between silicate melts and hydrous fluids in the upper mantle: experimental evidence and geochemical implications, Earth Planet. Sci. Lett. 165 (1999) 187–196.

[23] R.A. Herd, H. Pinkerton, Bubble coalescence in basaltic

lava: its impact on the evolution of bubble populations, J. Volcanol. Geotherm. Res. 75 (1997) 137–157.

[24] D.B. Dingwell, The brittle–ductile transition in high-level granitic magmas: material constraints, J. Petrol. 38 (1997) 1635–1644.

[25] Y. Zhang, H. Behrens, H_2O diffusion in rhyolitic melts and glasses, Chem. Geol. 169 (2000) 243–262.

[26] A.A. Proussevitch, D.L. Sahagian, Dynamics and energetics of bubble growth in magmas: Analytical formulation and numerical modelling, J. Geophys. Res. 103 (1998) 18223–18251.

[27] Y. Zhang, E.M. Stolper, G.J. Wasserburg, Diffusion of water in rhyolitic glasses, Geochim. Cosmochim. Acta 55 (1991) 441–456.

[28] M. Nowak, H. Behrens, An experimental investigation on diffusion of water in haplogranitic melts, Contrib. Mineral. Petrol. 126 (1997) 365–376.

[29] Y. Zhang, E.M. Stolper, Water diffusion in a basaltic melt, Nature 351 (1991) 1393–1404.

[30] K.U. Hess, D.B. Dingwell, Viscosities of hydrous leucogranitic melts: non-arrhenian model, Am. Mineral. 81 (1996) 1297–1300.

[31] R.L. Lange, I.S.E. Carmichael, Thermodynamic properties of silicate liquids with emphasis on density, thermal expansion and compressibility, in: J. Nicholls, K.J. Russel (Eds.), Modern Methods of Igneous Petrology: Understanding Magmatic Processes, Reviews in Mineralogy 24, Mineral. Soc. Am., 1990, pp. 25–64.

[32] O. Navon, V. Lyakhovsky, Vesiculation processes in silicic magmas, in: J.S. Gilbert, R.S.J. Sparks (Eds.), The Physics of Explosive Volcanic Eruptions, Geol. Soc. London Special Publications 145, 1998, pp. 27–50.

[33] D.B. Dingwell, The glass transition in hydrous granitic melts, Phys. Earth Planet. Int. 3409 (1998) 1–8.

Etude complémentaire

Thèse : Charlotte GONDE (2008, Orléans) *Etude expérimentale in-situ du dégazage d'un magma rhyolitique.*
Direction M. Pichavant ; **Encadrement** H. Bureau (LPS Saclay / IMPMC) et C. Martel (50 %).
Financements : Bourse CEA. **Moyens** : ANR CATT "Explosivité des dômes de lave, approche analytique, expérimentale et numérique; Application aux volcans antillais" (EXPLANT), 01/2006-06/2009 (C. Martel).

De retour en France en tant que Chargées de Recherche, encouragées mais non pleinement satisfaites par ces premiers résultats d'étude in-situ du dégazage dans les cellules à enclumes de diamant (CED), Hélène Bureau et moi avons décidé d'élaborer un sujet de thèse portant sur l'étude in-situ du dégazage dans des conditions magmatiques réalistes, notamment par la remise en route d'un "vieil" autoclave à chauffage interne et à fenêtres transparentes (ACIT) ayant été utilisé pour la dernière fois à la fin des années 1980 au Laboratoire Pierre Süe de Saclay. Ce projet constituait un défi technologique ambitieux, l'autoclave nécessitant d'importantes modifications et une remise en état, dans un laboratoire dont l'activité principale n'est pas l'expérimentation. Nous avons pensé qu'il serait alors plus sage d'assurer des résultats par une série d'expériences de décompression en CED afin d'étudier le processus de coalescence auquel nous avions prêté peu d'attention précédemment, et qui est pourtant à la base du développement des perméabilités magmatiques. Effectivement, la mise en route de l'ACIT et les améliorations apportées au CED ont été une bataille technologique pendant 3 ans, mais les deux outils haute pression-haute température à fenêtres transparentes ont fonctionné et ont été validés par l'observation du dégazage d'un magma. Les principaux résultats obtenus sont présentés ci-dessous.

L'ACIT peut atteindre 3 kbars et 1000°C et est muni de fenêtres de saphir transparentes permettant l'observation de l'échantillon (Laboratoire Pierre Süe, CEA Saclay). Une chambre à échantillon et un système optique d'observation ont été spécialement conçus pour optimiser les expériences. Les nouvelles caractéristiques techniques de cet outil ont fait l'objet d'une publication (Gondé et al., 2006). La composition du magma choisi pour les expériences de décompression est un verre haplogranitique de la composition précédemment utilisée par Martel et Bureau (2001) (79 pds% SiO_2 ; Norme CIPW : $Qz_{36}Ab_{38}Or_{25}$; cylindre de 1 kg préparé par SCHOTT AG, Allemagne), dans lequel sont forés des cylindres de 4 mm de diamètre et 2-3 cm de long que l'on hydrate à 6-7 pds% dans des autoclaves à chauffage interne (ISTO Orléans). Une rondelle d'épaisseur 60 à 1000 µm de cet échantillon hydraté est ensuite manuellement décomprimée dans l'ACIT à partir de 3 kbars, 700-1000°C, à des vitesses de décompression variables. Malgré les efforts de mise à niveau technique, la résolution des films des expériences de décompression s'est avérée très moyenne, en raison d'une distance de travail trop grande entre l'échantillon et la caméra, ce qui n'a pas permis d'observer la croissance ou la coalescence des bulles. Seul l'évènement de nucléation est observable et les échantillons ont été récupérés après expérience pour une analyse des bulles et des teneurs en eau finales. De surcroît, en l'absence de capsule hermétique autour de l'échantillon (qui ne permettrait pas l'observation), l'eau initialement dissoute dans l'échantillon a partiellement ou totalement (en fonction de l'épaisseur de la rondelle d'échantillon) diffusé dans le milieu de pression (argon) de l'autoclave dès le franchissement de la transition vitreuse. Ceci a donc nécessité une estimation du gradient de perte en eau avant toute interprétation plus avancée du processus de vésiculation. En parallèle, les films des expériences de Martel et Bureau (2001) et une nouvelle série d'expérience in-situ en CED ont été utilisés pour une étude détaillée de la nucléation des bulles au travers de déterminations de la densité numérique de bulles, et de la coalescence des bulles. Des techniques de pointe telle que l'implantation des diamants en bore (H. Bureau, IMPMC Paris, en collaboration avec M. Burchard, Bochum, Allemagne) ont également été utilisées afin de déterminer précisément la température et la pression au sein de la chambre à échantillon des CED.

L'application volcanologique des résultats obtenus dans ces deux outils « transparents », la CED et l'ACIT, est une étude de la dépendance de la pression de nucléation et de la densité numérique de bulles à divers paramètres tels que la teneur en eau initiale, la température ou le taux de décompression. Ces résultats ont été comparés aux expériences de la littérature et aux caractéristiques des ponces naturelles (Figure 3), permettant ainsi de valider ces outils pour une étude in-situ du dégazage, et sont en cours de publication (Gondé et al., pour Am. Mineral.). Cette étude a permis de définir un certain nombre de problèmes inhérents à l'observation in-situ du dégazage par décompression et de proposer des améliorations techniques des outils pour les résoudre. L'observation in-situ apportant une crédibilité directe aux processus et permettant un gain de temps considérable en s'affranchissant d'expériences sériées en temps en autoclave "classique", je pense qu'il n'est pas exclu que certaines des solutions envisagées soient testées dans un avenir proche.

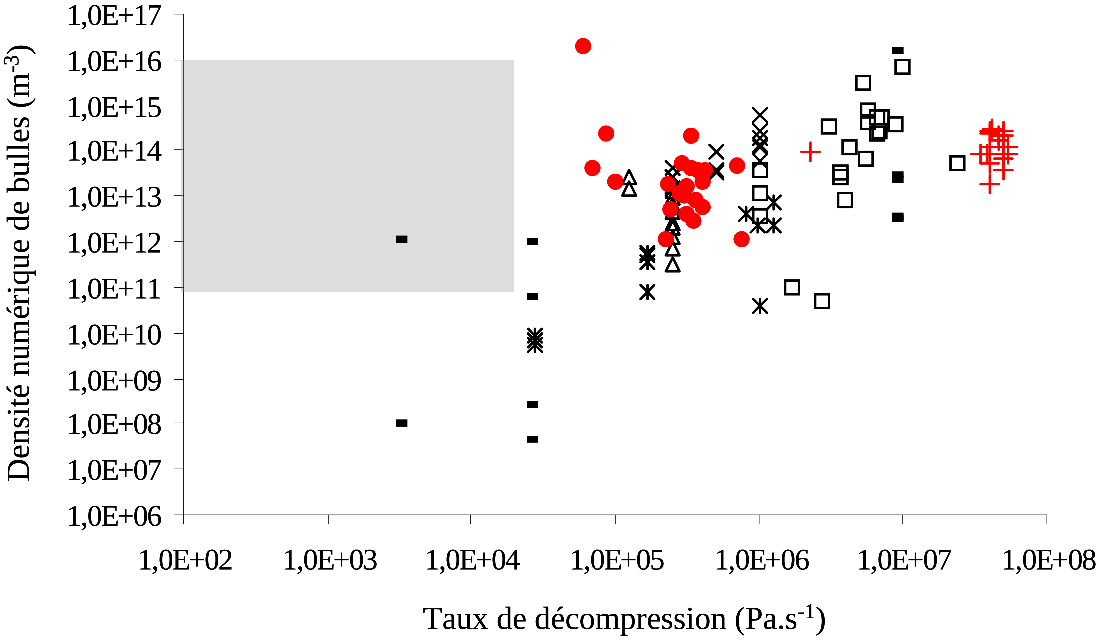

Figure 3. Densité numérique de bulles en fonction du taux de décompression (thèse C. Gondé, 2008). Symboles rouges: expériences in-situ (ronds pleins: en autoclave à chauffage interne; croix: en cellule à enclumes de diamant); Symboles noirs: données de la littérature réalisées en autoclave "classique" pour des compositions rhyolitiques (Gardner et al., 1999, 2000; Mangan et Sisson 2000; Mourtada-Bonnefoi et Laporte, 2002, 2004); Carré gris: champ des ponces naturelles.

I.3b. Dégazage en système ouvert versus fermé

Article: MARTEL C., BOURDIER J.-L., PICHAVANT M. & TRAINEAU H. (2000) Textures, water content and degassing conditions of silicic andesites from recent plinian and dome-forming eruptions at Mt Pelée, Martinique. *J. Volcanol. Geotherm. Res. 96, 191-206.*

Travaux réalisés dans le cadre de la thèse de doctorat : MARTEL C. (1996) Conditions pré-éruptives et dégazage des magmas andésitiques de la Montagne Pelée (Martinique, F.W.I.): étude pétrologique et expérimentale. *Thèse de l'Université d'Orléans, 250 p.* Direction : M. Pichavant, J.-L. Bourdier et H. Traineau.

Financements : Bourse MRT ; **Moyens** : Programme National sur les Risques Naturels (PNRN) de 1994 à 1997.

Le processus de vésiculation des bulles (nucléation, croissance et coalescence) est contrôlé par la composition du magma, sa teneur en volatils, la température, la pression et la vitesse d'ascension. Ces paramètres vont en particulier définir la densité numérique de bulles nucléées et leur taille au cours de la croissance, qui conditionnent à leur tour en partie le développement de la coalescence des bulles. Rappelons qu'en raison de la forte viscosité du magma, il n'y a pas de vitesse relative entre les bulles de gaz et le magma sur la durée de l'éruption et que par conséquent le processus de coalescence des bulles est le résultat de la rencontre de deux bulles (dont les centres sont statiques) par croissances respectives. Un magma atteignant ainsi une forte perméabilité peut alors dégazer en système ouvert, puis s'effondrer sous l'effet de la perte des gaz, résultant un un produit peu poreux. L'objectif de l'article présenté était de rechercher dans les produits naturels de la Montagne Pelée des témoins de dégazage en système ouvert ou fermé pour différents types éruptifs, à savoir les dômes, les nuées ardentes de type Mérapi (BAF : Block-and-Ash Flow), les déferlantes (HPVF : High Velocity Pyroclastic Flow), les retombées Pliniennes et les coulées ponceuses. L'étude a porté principalement sur la détermination des porosités totales par mesures de densité des pyroclastes, des microtextures des matrices (proportions relatives de microlites, verre, et pores ; présence de silice précipitée), des compositions chimiques des verres (résiduels et inclusions vitreuses) et des microlites, et des teneurs en eau des verres par spectroscopie infrarouge et déficience à 100 pds% de l'analyse par microsonde électronique calibrée par des verres standards.

La quantité de gaz exsolvé au cours de l'ascension du magma peut être estimée par la différence entre la teneur pré-éruptive en volatils dissous et celle du verre résiduel trempé après dégazage. Les inclusions vitreuses des phénocristaux, à condition de ne pas avoir subi de modification après piégeage, représentent en effet des témoins des compositions et teneurs en volatils du liquide magmatique pré-éruptif, avant dégazage et cristallisation éventuelle de microlites. Nous montrons que l'étanchéité de ces inclusions vitreuses est liée à la lithologie des échantillons : les inclusions des produits lithiques (denses et microlitisés) ont fui par de multiples fractures du cristal hôte, alors que celles des ponces semblent avoir conservé leur étanchéité en raison probablement d'une trempe plus rapide. Les inclusions des ponces du dépôt plinien de P1 (650 ans B.P.) ont une teneur en eau (seul volatil présent) de 5.8 ±0.7 pds%, en accord avec les déterminations expérimentales (5.3-6.3 pds%). Les verres résiduels de ces ponces ne contiennent plus que 1.8 ±0.3 pds% d'eau. La différence de teneur en eau entre les inclusions vitreuses et les verres résiduels a été traduite en fraction gazeuse calculée à l'équilibre à partir des lois de solubilité de l'eau et des densités respectives de l'eau et du liquide silicaté en température et pression (Jaupart et Tait, 1990). Dans le cas d'un dégazage en système fermé, cette fraction gazeuse calculée et la porosité totale mesurée devrait être comparable, ce qui s'est avéré valide pour les ponces Pliniennes. En revanche, pour les produits des éruptions à dôme, la fraction gazeuse calculée est bien inférieure à la porosité mesurée, traduisant un système ouvert, le magma perdant ses gaz à la faveur du développement d’une forte perméabilité.

Etude complémentaire

Stage de recherche M2 : Alain MOUSSADJI (2006, Orléans) *Dégazage expérimental d'un magma rhyolitique: caractère ouvert versus fermé.*
Direction : C. Martel et A. Burgisser.

L’étude précédente n’apporte qu’une estimation qualitative du caractère ouvert ou fermé du dégazage, et les produits naturels ont perdu la trace de l'histoire du développement de la perméabilité. Des études expérimentales ont été dédiées à l’étude du processus de coalescence et des seuils de perméabilité associés, notamment par des expériences de décompression sériées simulant un dégazage en système fermé (échantillon contenu dans une capsule en or hermétique ; Burgisser et Gardner, 2005 ; Radadi Ali, sujet M2 2005). L’idée du projet proposé ici était d’améliorer la stratégie expérimentale en autoclave en perçant la capsule contenant l’échantillon hydraté, afin qu’une partie des gaz exsolvés puisse s’échapper pendant la décompression, simulant ainsi un dégazage ouvert. Les produits obtenus à partir des verres rhyolitiques ont des textures très hétérogènes, avec des porosités proches de celles attendues à l’équilibre loin des trous percés, des porosités décroissantes à l’approche des trous et de manière générale, une auréole déshydratée et dense (sans bulles) tout autour de l’échantillon (épaisseur dépendante du taux de décompression). La coalescence des bulles a parfois mené à la formation de chenaux de bulles, mais aucun échantillon ne s’est manifestement effondré sous l’effet de la perte de ses gaz.

Les raisons de cette complexité texturale mériterait d’être approfondie, afin de définir quantitativement les conditions d’atteinte de la perméabilité magmatique, en fonction notamment du taux de décompression. Ceci requiert en particulier d’une part, des expériences proprement menées afin que la densité numérique de bulles nucléées soit contrôlée et reproductible et d’autre part, une méthode pour définir précisément en trois dimensions le réseau poreux et le seuil de connexion des bulles (ex., un microtomographe).

I.4- CRISTALLISATION DE MICROLITES

En raison de la diminution de la teneur en volatils dissous du liquide silicaté avec la décompression, des microlites peuvent cristalliser au cours de l'ascension du magma dans le conduit volcanique et /ou de sa mise en place sous forme d'un dôme. Dans le cas des magmas différenciés en contexte d'arc, ces microlites, arbitrairement définis comme < 50 µm de long, sont principalement des plagioclases cristallisant à partir d'un liquide rhyolitique.

Par rapport à la problématique générale de compréhension des mécanismes éruptifs des éruptions explosives versus effusives, l'étude des microlites peut apporter des informations à deux niveaux; premièrement sur l'effet de la nucléation et de la croissance de microlites sur le développement du potentiel explosif du magma; secondement, sur la détermination des vitesses d’ascension. En effet, tant que les processus syn-éruptifs tels que le dégazage et la cristallisation de microlites n'ont pas atteint leur équilibre thermodynamique, leur cinétique peuvent être utilisées pour déterminer des vitesses d'ascension (des taux de décompression). Ainsi, les processus de nucléation et de croissance des bulles de gaz aux cinétiques rapides peuvent apporter des informations sur des vitesses d'ascension rapides, telles que celles des magmas Pliniens, i.e. de l'ordre du m/s. En revanche, les cinétiques de cristallisation dans les liquides rhyolitiques sont plus lentes que celles de vésiculation des bulles, en raison des diffusivités plus lentes des éléments constituant les microlites (Si, Al, Ca, etc…) que celles des espèces volatiles (hydrogène). Ainsi, l'étude des cinétiques de cristallisation pourrait apporter des informations sur les vitesses de remontée des magmas des éruptions à dôme et nuées ardentes proches du mm ou cm/s.

La première section de cette partie fait référence aux textures, morphologies et compositions des microlites naturels afin de définir des caractéristiques propres aux différents styles éruptifs. La seconde section traite des expériences de décompression mises en œuvre pour reproduire les caractéristiques de ces microlites, afin de remonter à des estimations de vitesses d'ascension des magmas.

I.4a- Microlites naturels

Les produits naturels des éruptions récentes de la Montagne Pelée ont été étudiés avec l'espoir de pouvoir classifier les différents styles éruptifs au travers des caractéristiques de composition et de morphologie de leurs microlites. Une telle classification signifierait tout d'abord qu'il existe bien des caractéristiques propres aux différents types éruptifs traduisant de réelles différences de conditions d'éruption (rappelons qu'il n'y a pas de différences de conditions pré-éruptives, i.e., similarité de l'assemblage minéralogique, des proportions modales, et des compositions des phénocristaux entre les produits Pliniens et péléens ; Martel et al., 1998), et que par conséquent, on peut envisager un programme d'expériences de décompression visant à reproduire ces différentes catégories de microlites pour en déduire les conditions de cristallisation. L'étude des microlites a fait l'objet de deux publications complémentaires (Martel et al., 2006 ; Martel et Poussineau, 2007).

Pour ces deux articles, les microlites et les verres résiduels des produits récents de la Montagne Pelée ont été analysés dans des blocs lithiques des éruptions à dômes de 1929, 1902, et P1 (650 ans B.P.) et sur des ponces Pliniennes de P1, P2 (1670 ans B.P.), P3 (2010 ans B.P.) et P4 (2440 ans B.P.). Les analyses en éléments majeurs ont révélé une très large gamme de composition des microlites de plagioclase (phase principale à plus de 90 vol%) : de 35 à 90 mol% d'anorthite (An_{35-90}) pour les produits d'éruptions à dôme et An_{55-90} pour ceux des éruptions Pliniennes. Grâce à des expériences d'équilibre de phase, deux types de microlites ont pu être déterminées (Martel et al., 2006): les microlites aux compositions < An_{55}, qui ont cristallisé au cours de l'ascension dans le conduit volcanique à partir d'un liquide de composition rhyolitique et les microlites aux compositions > An_{80}, qui ont cristallisé à partir d'un liquide mafique du réservoir profond (~1040°C, 4 kbars ; Pichavant et al., 2002) au cours de son injection dans le réservoir andésitique superficiel plus froid (875°C, ~2 kbars ; Martel et al., 1998). Les deux catégories justifient la dénomination de microlites, parce que ce sont des cristaux qui ont poussé rapidement et en fort déséquilibre thermodynamique, les premiers dans le conduit volcanique par décompression et les seconds dans le réservoir par refroidissement brutal du liquide mafique au contact du magma andésitique plus froid. Les microlites hérités du liquide mafique sont présents dans tous les dépôts, mais sont les uniques représentants de la plupart des ponces Pliniennes. La présence de ces microlites hérités a une importance à plusieurs niveaux : a) dans les ponces Pliniennes, ils peuvent constituer la seule trace d’un mélange magmatique pré-éruptif à l'échelle microlitique, en l’absence d’enclaves mafiques, de ”sieve” textures ou de zonages inverses des phénocristaux témoignant de l'effet de réchauffement par un magma mafique (Tsuchiyama, 1985 ; Browne et al., 2006) ; b) lors du choix du produit de départ pour des expériences d’équilibre de phase, la composition de la matrice naturelle (verre interstitiel + microlites du conduit + microlites du réservoirs) n’est dans ce cas pas représentative de la composition du liquide originellement à l’équilibre thermodynamique avec les phénocristaux de la chambre (comme l’explique Pichavant et al. (2007) au travers de la notion de "magma réactif"); c) ces microlites hérités doivent être écartés d’une étude visant à définir les caractéristiques des microlites ayant cristallisés par décompression dans le conduit volcanique.

Article présenté: MARTEL C. & POUSSINEAU S. (2007) Diversity of eruptive styles inferred from the microlites of Mt Pelée andesite (Martinique, Lesser Antilles). *J. Volcanol. Geotherm. Res. 166, 233-254.*

Financements : ACI "Risques Naturels" 2003-2005 (T. Druitt) et ANR CATT "EXPLANT" 01/2006-06/2009 (C. Martel).

L’étude texturale et morphologique des microlites de plagioclase de composition <An_{55}, supposés avoir cristallisé par décompression dans le conduit, représente l’objet principal de la publication présentée ici. La caractérisation morphologique des microlites consiste en une représentation parallélépipédique 3D, convertie de l’analyse 2D d’après le modèle de Morgan et Jerram (2006) et d’une spécification de l’habitus (tabulaire, squelettique ou dendritique). Cette étude a permis de délimiter des champs dans un espace proportion volumique en fonction de la densité numérique et de la morphologie, distincts pour les microlites des pyroclastes des différents dépôts. Ainsi, les produits de dômes et de coulées pyroclastiques de type Merapi sont caractérisés par de faibles densités numériques et de fortes proportions volumiques de larges microlites tabulaires à squelettiques, typiques d’un régime de cristallisation dominé par la croissance. Les rares ponces Pliniennes contenant des microlites de décompression sont caractérisées par de fortes densités numériques et de faibles proportions volumiques de petits microlites aciculaires et dendritiques, assimilées à un régime de cristallisation dominé par la nucléation. Les produits de déferlantes type Péléennes sont intermédiaires, caractérisés par de fortes densités numériques et fortes proportions volumiques de petits microlites squelettiques. Les teneurs en eau analysées (sonde ionique et microsonde électronique) dans les verres interstitiels permettent d’estimer une pression de trempe magmatique à partir des lois de solubilité de l’eau. Ainsi, le dégazage des produits lithiques de 1929 et 1902 a été trempé en deçà de 150 bars, 50 bars en moyenne, alors que les ponces pliniennes auraient pu être trempées aux alentours de 300-600 bars.

Des scénarios d’ascension des magmas pour les différents styles éruptifs observés sur la période d’activité récente de la Montagne Pelée sont proposés. Une meilleure approximation devrait cependant être apportée par les expériences de décompression contrôlée ci-après.

Available online at www.sciencedirect.com
ScienceDirect

Journal of Volcanology and Geothermal Research 166 (2007) 233 – 254

Journal of volcanology and geothermal research

www.elsevier.com/locate/jvolgeores

Diversity of eruptive styles inferred from the microlites of Mt Pelée andesite (Martinique, Lesser Antilles)

Caroline Martel [*], Stéphane Poussineau

Institut des Sciences de la Terre d'Orléans (ISTO), Orléans, France

Received 24 January 2007; accepted 5 August 2007
Available online 15 August 2007

Abstract

We have studied the compositional and textural characteristics of plagioclase microlites from several dome-forming eruptions (dome, block-and-ash flows, and surges) and plinian fallouts of the recent period of activity of Mt. Pelée in order to infer magma ascent dynamics. Dome-forming and plinian samples display a wide range of plagioclase microlite compositions, from An_{35} to An_{90} and An_{55} to An_{90}, respectively. Microlites with compositions $> An_{50-60}$ crystallized from a mafic melt that intruded the andesitic reservoir in proportion of ∼ 10 vol.%. During magma ascent in the conduit, the fraction, number density, and morphology of the decompression-induced microlites (compositions $< An_{50-60}$) suggest that the plinian magmas experienced a nucleation-dominated crystallization regime with high undercooling. In contrast magmas from domes and block-and-ash flows were dominated by a growth regime with low undercooling, and the surges were influenced by both regimes. According to these crystallization regimes and new experimental data on H_2O content of the matrix glasses, we propose magma relative ascent rates and fragmentation pressures for the different eruptive styles observed at Mt. Pelée that may explain why surges are explosive events and why they may or may not be followed by a plinian event.

Keywords: microlites; H_2O content; dome-forming eruptions; Plinian

1. Introduction

Many island-arc volcanic eruptions are characterized by dome-forming events that may produce pyroclastic flows and violent surges. The devastating 1902 May 8th surge at Mt. Pelée (Martinique) reminds us of the potentially high explosivity arising from growing domes. Dome-forming events may be directly followed or preceded by an explosive plinian event, but the transition between both eruptive styles still remains unpredictable and poorly understood. Because these eruptive regimes generate very different hazards, there is a crucial need to understand the factors responsible for either type of eruption, if we are to progress in the effort of evaluating hazards and forecasting island-arc silicic eruptions.

This complex eruptive behavior has been ascribed to different magma ascent rates within the volcanic conduit (Jaupart and Allègre, 1991; Woods and Koyaguchi, 1994) rather than pre-eruptive differences in volatile contents in the magma reservoir (Barclay et al., 1996; Martel et al., 1998). Low magma ascent rates permit bubble connectivity in the vesiculating magma and facilitate permeability developments with the surrounding rocks (Klug and Cashman, 1996; Burgisser and Gardner, 2005). This leads to a non-explosive open-system degassing process, such

---

[*] Corresponding author.
E-mail address: cmartel@cnrs-orleans.fr (C. Martel).

0377-0273/$ - see front matter © 2007 Elsevier B.V. All rights reserved.
doi:10.1016/j.jvolgeores.2007.08.003

as dome growth (Eichelberger et al., 1986). Conversely, high magma ascent rates prevent gas loss, leading to gas overpressure and a subsequent explosive closed-system degassing process, such as plinian events (Villemant et al., 1996; Sparks, 1997; Villemant and Boudon, 1998). However, the ascent conditions that may lead to either explosive or effusive eruptions are not determined.

Upon ascent, gas exsolution from the melt induces an increase of the liquidus temperature of the silicate melt that may result in crystallization. The explosivity associated with high-velocity surges has been ascribed to large gas overpressures generated in highly viscous magmas at shallow depths in response to an extensive degassing-induced crystallization of microlites (Sparks, 1997). Therefore, preserved textures of microlites and degassing in the groundmass may provide valuable information on the magma decompression path and ascent rate, i.e. bubble and microlite sizes and number densities determined by nucleation and growth rates. Several studies have been devoted to the degassing-induced microlite crystallization in domes and block-and-ash flow deposits (Cashman, 1992; Cashman and Mangan, 1994; Nakada et al., 1995; Nakada and Motomura, 1999; Hammer et al., 1999, 2000), but none exists on the microlite characteristics of explosive events (surges and plinian fallouts) or on the comparison between effusive and explosive eruptive styles. Recently, experimental studies have focused on the determination of magma ascent rates through timed decompressed experiments (Geschwind and Rutherford, 1995; Blundy and Cashman, 2001; Hammer and Rutherford, 2002; Martel and Schmidt, 2003; Couch et al., 2003a,b; Larsen, 2005), for which a prerequisite is a good knowledge of the natural products, the experimental charges should be compared with.

The specificity of each volcano in terms of eruptive behaviour, magma composition, and thermodynamic conditions makes necessary to investigate at first individual volcanic systems. We focus here on the recent eruptions of Mt. Pelée (Martinique, Lesser Antilles) for the following reasons: a) Mt. Pelée displays a large variety of eruptive styles from effusive to explosive events, b) the emplacement dynamics of the pyroclastic flows and surges have been carefully described (Lacroix, 1904; Perret, 1935), c) the deposit sequences are characterized in details (Traineau et al., 1989a; Bardintzeff et al., 1989; Bourdier et al., 1989; Charland and Lajoie, 1989; Boudon and Lajoie, 1989; Lajoie et al., 1989; Smith and Roobol, 1990), and d) recent studies provide storage conditions for the andesitic and mafic magma reservoirs (Fichaut et al., 1989; Martel et al., 1998; Pichavant et al., 2002) which constitute important statements for further investigation of the syn-eruptive thermodynamic conditions. In order to understand the eruption style variations observed at Mt. Pelée, we provide here a detailed study of the textural and compositional characteristics of the microlites and interstitial glasses for various eruptive events encompassing domes, pyroclastic flows, surges, and plinian fallouts that may contribute to the understanding of magma dynamics in island arc volcanism context.

2. Volcanological and petrological background

2.1. Eruptive sequences

The volcanic activity of Mt. Pelée is conveniently divided into three periods (Westercamp and Traineau, 1983). During the first stage (> 40 000 yr B.P.), an ancestral volcano formed of similar size and summit position to the present day (paleo-Pelée after Vincent et al., 1989). The second period (from 40 000 to 19 500 yr B.P.), also called the Saint Vincent stage, was dominated by pyroclastic ash-and-scoria flows of basaltic andesite composition (Vincent et al., 1989). During the third stage or recent period (from 13 500 yr B.P. to present), the activity ranged between plinian and dome-forming eruptions of an andesitic magma. Dome-forming eruptions comprise phases of relatively quiescent lava-dome extrusions with associated destabilizations into more or less violent pyroclastic flows. Plinian eruptions are explosive events characterized by sustained columns of several kilometers high that may collapse into basal surges. In the well-documented 5000 yr B.P., the remains deposits of 6 plinian and 12 dome-forming eruptions have been identified (Westercamp and Traineau, 1983; Smith and Roobol, 1990).

The dome-forming eruptions of 1929–32 are the most recent volcanic activity of Mt. Pelée. These eruptions were witnessed and well documented by Perret (1935). The activity consisted of dome extrusion pulses of a relatively degassed andesite in the summit crater coupled with destabilizations into block-and-ash flows channelled in the Rivière Blanche valley (nuées ardentes of Merapi-type) leading to thick deposits (several meters high) of ash and blocks up to metric size (Bourdier et al., 1989). The activity ended with a more quiescent growth of lava spines and domes. The dome-forming eruptions of 1902, first reported by Lacroix (1904) thirty years before, similarly started with pulses of growing domes, the destabilizations of which produced the high-energy and high-velocity unchanneled surges from 1902 May 8th to August 30th (nuées ardentes of pelean-type). The deposits are up to 20 cm in thickness and characterized by ashes and dense to moderately vesiculated grey lithics up to 1–2 cm in diameter (Bourdier et al., 1989; Boudon et al., 1994). These surge events were followed by block-and-ask flows channeled in the Rivière Blanche valley from October 1902 to November 1903.

The P1 eruption in the stratigraphy nomenclature of Westercamp and Traineau (1983) is the last recorded plinian event (dated to 650±20 yr B.P.), preceded by the P2 (1670±40 yr B.P.), P3 (2010±140 yr B.P.), and P4 (2440±70 yr B.P.) plinian events. These deposits suggest a widespread pumice fallout event (~ 0.1 km^3 dense rock equivalent) followed by thick valley-filled pumice flows (Traineau et al., 1989a). The plinian products dominantly consist of juvenile white ashes and pumices with minor fractions of grey dense lithics and oxidized xenoliths. Based on a higher pumice percentage in the P3 fallout and more xenolithics in the pumice flow deposit, P3 appears to be of a slightly higher intensity than the P1 or P2 events (Bardintzeff et al., 1989). The P1, P3, and P4 pumice fall deposits overlay a thin (up to 20 cm) fine-grained deposit of grey ashes and dense lithics. The absence of erosional surface between the ash-and-lithics and the pumice deposits suggests a time interval less than few days. As these lithic deposits have very similar features with the 1902 May 8th deposit (granulometry and geographical extension), they were interpreted as comparable eruptive events (Boudon et al., 1994). Therefore, as Lacroix (1904) reported that the 1902 May 8th surge was initiated from a sub-surface level (the magma was seen at the surface the preceding days), the P1, P3, and P4 surges are likely to have been initiated at very shallow levels. The P1, P3, and P4 eruptions offer the rare opportunity to study the transition between the dome-forming (surge) and plinian eruptive style.

2.2. Magma compositions and pre-eruption conditions

The recent activity of Mt. Pelée tapped a homogeneous andesitic magma ($58 < SiO_2 < 65$ wt.%, 62 wt.% in average). The andesite is composed of 35 to 58 vol.% of phenocrysts (47 vol.% in average), encompassing 29–49 vol.% plagioclase, 4–9 vol. % orthopyroxene, 1–2 vol.% magnetite, minor (< 1 vol.%) clinopyroxene, ilmenite and apatite, destabilized amphibole and olivine (both with reacted zones of plagioclase+orthopyroxene+magnetite) (Gourgaud et al., 1989; Martel et al., 1998). These phenocrysts are embedded in a rhyolitic matrix glass (74–77 wt.% SiO_2; Martel et al., 2000). The lack of variations in the physical and chemical conditions of magma storage preceding the recent eruptions stresses the bulk chemical homogeneity of the tapped andesitic magma body. The pre-eruptive storage conditions proposed for the andesitic part (62 wt.% SiO_2) of the magma reservoir are 875–900 °C, 200±50 MPa, an oxygen fugacity between NNO + 0.4 and + 0.8 and melt H_2O contents of 5.3–6.3 wt.% (Martel et al., 1998). Yet, there is evidence for magma mixing in the 1902–1929 products recorded as mafic enclaves (51–59 wt.% SiO_2) and few banded rocks (Fichaut et al., 1989; Gourgaud et al., 1989). Additionally, both plinian and dome-forming products contain a minor proportion of inherited phenocrysts, which originally grew from more mafic melt compositions (Gourgaud et al., 1989; Pichavant et al., 2002). Despite the lack of eruptions of mafic lavas in the recent period of activity (except as enclaves), we need to consider a broader context of a chemically-zoned magma chamber in the recent eruptive history, including a mafic reservoir (53 wt.% SiO_2) at 950–1050 °C, 400 MPa, oxygen fugacity between NNO and NNO + 4 and a melt H_2O contents around 6–8 wt.% (Pichavant et al., 2002). Therefore, it is extremely likely that both fractional crystallization and magma mixing are important in the petrogenesis of Mt. Pelée, but the respective role and proportion of these two processes remain undefined.

The products considered for our study are andesitic in bulk-rock composition with a rhyolitic matrix glass and come from various deposits that show unambiguous mechanisms of emplacement. These are dense lithics from the 1929 and 1902 domes, dense and vesiculated lithics from the 1929 block-and-ash flows (BAFs), the 1902 May 8th, 1902 August 30th, and P1 surges, and pumices from the P1, P2, P3, and P4 plinian fallouts (Table 1).

3. Methods

3.1. Textural analyses

The samples chosen for the groundmass textural analyses (Table 1) belong to a much larger sampling of Mt. Pelée recent eruptions that was available for this study. For each eruptive sequence, we chose samples with representative microlite features (according to scanning electron microscopy (SEM) observations) and densities (according to the frequency histograms of the clast density/vesicularity in Martel et al., 2000). Thus, the surge samples of the 1902 May 8th were taken in the given mean porosity range, i.e., 31±6 vol.%. The P1 surge displays a bimodal clast density distribution, so that we chose one sample in the mean mode (~ 30 vol. %) and a second in the low density part of the histogram. Both samples of the P1 plinian pumice are close to the mean porosity, but one is representative of the general pumice features, i.e., microlite-poor, whereas the second

Table 1
Selected samples

Eruption unit	Eruption type	Lithology	Sample number
1929–32	Dome	Lithics	MT34P [a, b]
	Pelean BAFs	Lithics	MT37N1 [c,a], MT37N58[a], MT37N16 [d], MT37N17[d], MT37N6[d]
1902–04	Dome	Lithics	MT34M[a]
1902, May 8th	Pelean surge	Lithics	MT37B19[c,a], MT37B56[c,a], MT37B51[c,a], MT37B82[d], MT37B6[d], MT37B55[d]
1902, Aug 30th	Pelean surge	Lithics	MT36V15[a,b], MT36V50[d], MT36V66[d], MT36V52[d]
P1 (650 yr BP)	Plinian fallout	Pumice	MT25E1[c,a], MT33C[a]
	Pelean surge	Lithics	MT36P6[c,a], MT36P7[c,a]
P2 (1670 yr BP)	Plinian fallout	Pumice	MT37F[c,a]
P3 (2010 yr BP)	Plinian fallout	Pumice	MT35G1[c,a]
P4 (2440 yr BP)	Plinian fallout	Pumice	MT32W[c,a]

[a] Microlite fraction, size, and shape analyses.
[b] Porosity measurements determined by image analysis.
[c] Microlite compositional analyses.
[d] H_2O content determined by ion probe.

one represents rare microlite-rich pumices. The 1929 BAFs display the widest range of textural groundmasses (porosity from 5 to 65 vol.% and microlite-free to highly crystallized groundmasses; Martel et al., 2000). We chose samples with different porosity fractions and microlite contents representative of most of the observed samples. Such histograms are not available for the 1902 August 30th surge deposit and for the P2, P3, and P4 fallout deposits, but the chosen samples seem to be representative of the observed main characteristics.

Thin sections of the natural products were imaged by SEM, using a JEOL JSM-6400 (Polytech, Orléans). The crystal morphologies (symmetry axes and areas), areal fraction (Φ), and number density (N_A) were determined by image analysis (Scion Image and SPO software; Launeau and Robin, 1996; Launeau and Cruden, 1998). We corrected stereologically the two-dimensional (2D) parameters (major and minor axis) to provide true three-dimensional (3D) crystal habits using the spreadsheet program of Morgan and Jerram (2006). The database used in this program compares the sample's 2D measurements of minor-axis to major-axis ratios for non-foliated samples with standard 2D curves obtained from crystals of 703 different habits (ranging from 1:1:1–1:1:10–1:10:10 Short:Intermediate:Long axis). The output gives the five best-match standard curves and corresponding crystal habits based on a least-squares fit between sample and database. The authors suggest a minimum of ~ 200 crystal sections to robustly determine crystal habits if crystals are acicular in shape. The reliability of the shape is quoted as R^2, the fractional measure of the variation in the sample explained by the best-fit shape of the database (R^2 values over 0.8 denote a good statistical fit, although care has to be taken when dealing with sample sets that involve less than about 200 crystal sections). Five of the eleven performed stereological conversions deal with less than 200 objects, with 3 of them having R^2 values between 0.6 and 0.7. However, natural populations tend to display broader distributions than the idealised shapes of the database, mainly because they often exhibit non-unique shapes (Morgan and Jerram, 2006).

3.2. Microlite and glass compositions

Microlites and glasses were analysed using a Cameca SX 50 electron microprobe (BRGM-ISTO, Orléans) with a 6-nA beam current, a 15-kV accelerating voltage, 10-s counting time on peak, a focused beam for the crystals, focused and defocused beams of ~ 6 μm in diameter for the glasses. The analytical errors on the oxide analyses are 1% relative for SiO_2 and Al_2O_3, 2% for CaO, 3% for FeO, MgO, and TiO_2, and 5% for MnO, Na_2O and K_2O. Following the procedure of Pichavant (1987), alkali migration in glasses was corrected using hydrated rhyolitic glasses as standards with known alkali contents (determined by wet chemistry at the CRPG Nancy, France). Because the smallest population of the natural plagioclase microlites was below the effective beam size (~ 2 μm) of the electron microprobe, their chemical compositions had to be recalculated from analyses of plagioclase–glass mixtures. This assumes a known glass composition, analyzed with the same conditions as the crystals (focused beam, no correction for alkali loss, and no recalculation to 100 wt.%). However, when the total of the oxide analysis of the mixture was close to 100 wt.% (suggesting a dehydrated glass), the recalculation was performed with the glass recalculated to 100 wt.%. The recalculation procedure consisted of incrementally subtracting glass to the mixed composition until the resulting plagioclase composition (structural formula calculated on 8 oxygens) fulfilled the following conditions: total cations between 4.95 and 5.03, alkalis (Na + K + Ca) between 0.95 and 1.03, cations in the tetrahedral site (Si + Al) between 3.95 and 4.00, and an iron content (counted as FeO) below 1 wt.%. This recalculation sometimes provided slightly negative values (up to − 0.10 wt.%) for K_2O, MgO, and TiO_2.

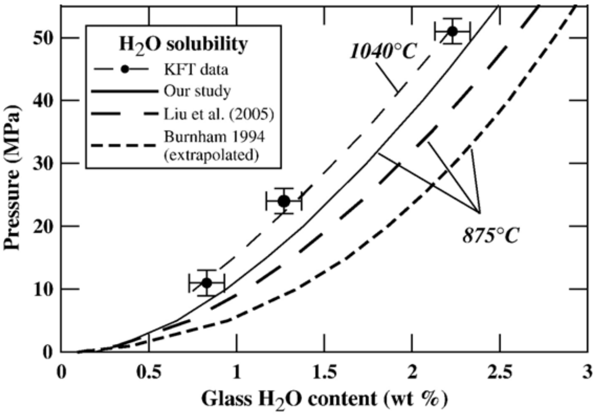

Fig. 1. H_2O solubilities obtained at $P \leq 55$ MPa starting from the rhyolitic crystal-free interstitial glass of P1 fallout pumices. The dots are the average of three Karl Fischer titration (KFT) measurements obtained on our glasses hydrated at 1040 °C. The fit of these data is the deduced solubility law at 1040 °C. The solid line represents our solubility law empirically corrected at 875 °C using the model of Newman and Lowenstern (2002) (see equation in text). Comparison is presented with the H_2O solubility model of Burnham (1994) extrapolated at pressures < 50 MPa and Liu et al. (2005) given with relative uncertainties of 15%.

3.3. Glass H_2O contents

The H_2O concentrations of natural glasses were determined by ion probe (Cameca IMS 3f, CRPG Nancy, France) following the procedure describe in Deloule et al. (1995). This analytical technique requires standard glasses with compositions close to the samples and known H_2O contents. Our hydrated standard glasses have the composition of the microlite-free interstitial glass of P1 fallout pumices (dry composition in wt.%: 76.33 SiO_2, 0.29 TiO_2, 13.33 Al_2O_3, 2.24 FeO, 0.45 MgO, 2.93 Na_2O, 2.43 CaO, 1.89 K_2O). The H_2O contents of the standards were determined by Karl–Fischer Titration (Mettler Toledo DL37) and Fourier Transform Infrared spectroscopy. The glasses from the P2 plinian fallout were determined by the "by-difference" method using the electron microprobe, and calibrated for the glass H_2O-dependence of the alkali loss (Devine et al., 1995).

In order to estimate the quenching/fragmentation pressures of our natural glasses using their H_2O contents, we needed H_2O solubility laws. Several reasons led us to get our own H_2O solubility data: 1) H_2O solubility models depend on glass composition (i.e., the alkali content; Burnham, 1979); 2) small uncertainties in the determination of the glass H_2O contents lead to large variations in the saturation pressures at low pressures; 3) Data on H_2O solubility are sporadic and scattered at pressures ≤ 50 MPa (Liu et al., 2005, and references herein). Therefore, we performed H_2O solubility experiments at pressures ≤ 50 MPa starting with the interstitial glass composition of Mt. Pelée (same as the ion probe standards below). Bubble-free glass pieces (~ 100 mg) were sealed into Au capsules with excess deionized H_2O (~ 10 wt.%) and loaded in an internally-heated pressure vessel (Basset Type, Ar pressure medium, Mo wires, isobaric quench) at 1040 °C and 51, 24 and 11 MPa for 170 h. Glass H_2O contents were determined by Karl Fischer Titration: 2.23 (0.01), 1.13 (0.00), 0.98 (0.04) wt.% at 51, 24, and 11 MPa, respectively (average of three analyses with statistical error in bracket). The H_2O solubility ($C_{H2O(P,T)}$) for our Mt. Pelée glass compositions at T (°C; empirically corrected using the model of Newman and Lowenstern, 2002) and P (MPa; ≤ 55 MPa) can be expressed as following:

$$C_{H2O(P,T)} = \sqrt[1.6216]{\frac{P}{15.36}} + [2.79 \cdot 10^{-3} \times P + 8.66 \cdot 10^{-4} \times (1040 - T)]$$

The uncertainty is 10% for C_{H2O} and ± 2 MPa for P corresponding to the manometer resolution at low pressures. At 50 MPa and 875 °C, Fig. 1 shows that the model of Burnham (1994) overestimates H_2O solubility by 0.5 wt.%. However, this model is extrapolated for pressures < 50 MPa. The model of Liu et al. (2005) combines compiled experimental data from the literature with new experimental data at low pressures (0.1–25 MPa). Our data are slightly lower than those of Liu et al. (2005): a difference of 0.2 wt.% at 50 MPa and 0.1 wt.% at 10 MPa and 875 °C. Although, these solubility laws are close to the uncertainty of 15 and 10% given by Liu et al. (2005) and us, respectively, we will further use our solubility law for consistency with our natural products (comparable composition and analytical procedure).

4. Results

The microlite paragenesis of the rhyolitic groundmass of Mt. Pelée andesite consists of plagioclase (> 95 vol.%), orthopyroxene (< 5 vol.%), Fe–Ti oxides (< 1 vol.%), and rare clinopyroxenes, as illustrated in Fig. 2. In this study, we will only consider plagioclase microlites, the other phases being not representative enough. We defined microlites on size and habit criteria. To a first approximation, we chose to consider a broad range of microlite sizes, with areas up to 3000 μm^2 and long axes up to 100 μm, as arbitrarily defined by Murphy et al. (2000). However, the morphological study concerns the microlite fraction with length below

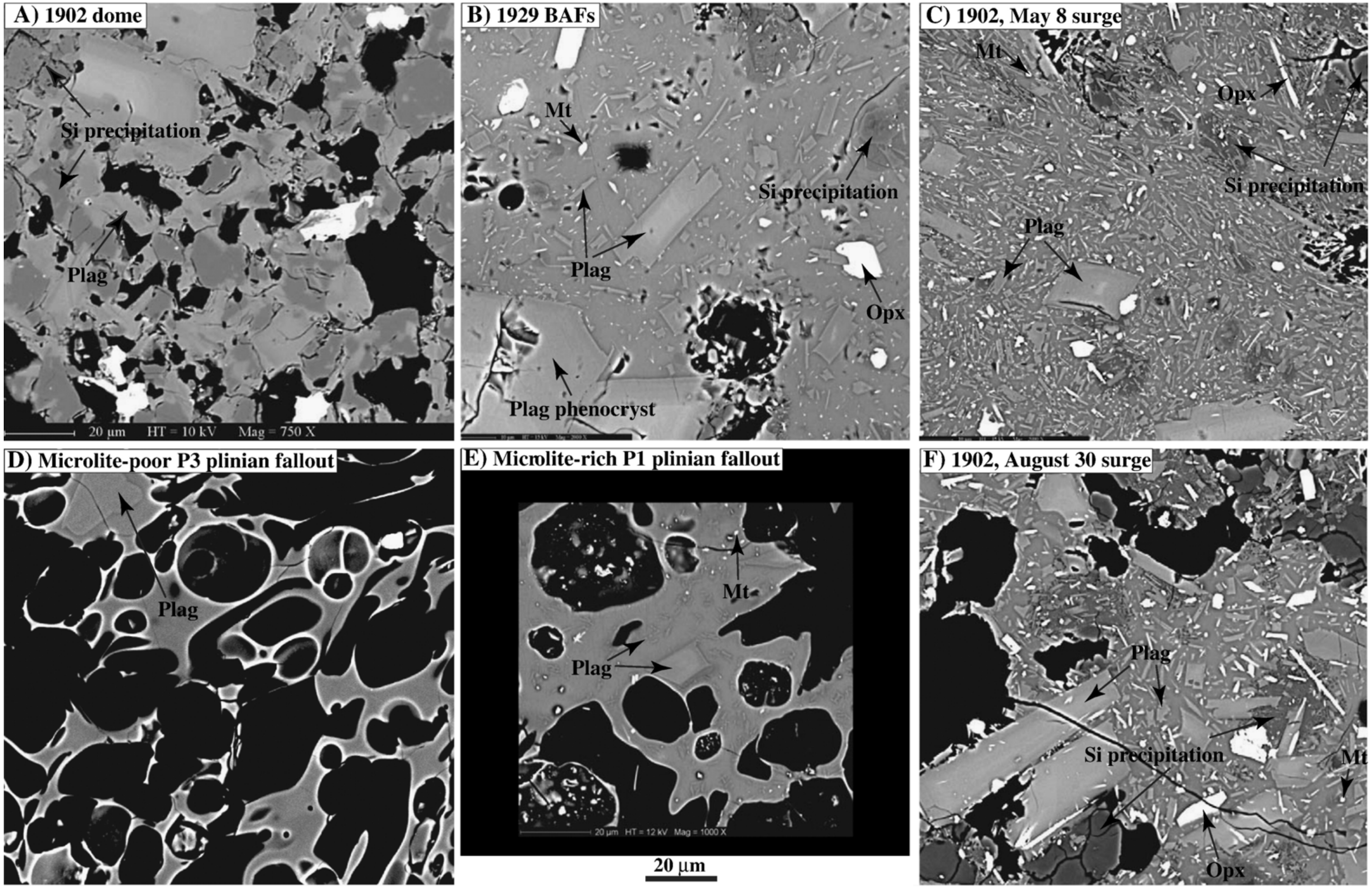

Fig. 2. SEM images showing the microlite textural characteristics in recent eruptive products of Mt. Pelée. A) MT34M, B) MT37N1, C) MT37B23, D) MT35G1, E) MT25E1, and F) MT36V15 (see Table 1). Scale bar of 20 µm for all images.

Table 2
Compositions and sizes of the plagioclase microlites

Eruption	Sample	No.	Size (μm^2)	Composition [a]									
				f	SiO_2	FeO	Na_2O	K_2O	Al_2O_3	MgO	CaO	Total	An
1929 BAFs	MT37N1	Q69	Glass	1.00	78.95	1.79	2.44	3.02	9.63	0.07	0.74	96.90	–
		Q72	30	0.25	60.32	0.47	7.26	0.18	23.88	0.01	7.53	99.57	36.06
		Q74	4	0.43	61.40	0.22	7.36	0.10	22.53	− 0.05	7.62	99.08	36.19
		Q77	8	0.06	60.92	0.62	6.66	0.37	23.45	–	7.82	99.91	38.50
		Q78	10	0.56	60.49	0.58	7.15	0.02	23.65	0.19	7.08	99.32	35.32
		Q79	6	0.17	57.92	0.63	6.60	0.03	24.42	0.03	8.52	98.23	41.56
		Q70	Glass	1.00	78.07	1.42	2.68	2.76	10.91	0.10	1.12	97.43	–
		Q75	4	0.35	61.07	0.31	6.99	− 0.08	24.09	0.06	7.77	100.19	38.05
1902 May 8th surge	MT37B19	Q112	Glass	1.00	79.94	1.75	1.67	3.12	10.06	0.09	0.62	97.68	–
		Q84	6	0.15	58.32	0.68	6.05	0.17	25.29	0.01	9.69	100.18	46.50
		Q85	5	0.36	60.12	0.70	6.29	− 0.03	24.39	0.05	9.16	100.68	44.59
		Q91	15	0.08	57.97	0.43	5.72	0.16	25.78	0.04	10.60	100.76	50.14
		Q92	2	0.35	61.73	0.39	7.09	0.01	22.71	− 0.05	7.89	99.76	38.06
		Q94	4	0.25	60.07	0.34	6.67	0.06	24.25	− 0.03	8.78	100.02	41.97
		Q104	5	0.20	58.94	0.63	6.25	0.08	24.78	0.03	9.61	100.37	45.73
		Q107	6	0.17	57.13	0.54	5.79	0.12	25.96	0.06	10.36	100.06	49.38
		Q110	4	0.24	59.00	0.39	6.16	0.12	25.33	0.05	9.83	101.02	46.54
		Q113	3	0.36	61.52	0.69	6.50	0.12	24.34	− 0.02	8.82	101.93	42.56
		Q114	4	0.31	60.36	0.73	6.40	–	24.35	0.01	9.15	101.05	44.13
	MT37B56	Q132	Glass	1.00	79.52	1.88	2.13	2.61	10.03	0.07	0.90	97.61	–
		Q149	10	0.26	59.46	0.82	6.60	0.98	25.11	0.05	7.79	100.85	37.27
		Q153	8	0.30	60.41	0.70	6.45	1.38	23.51	0.04	7.76	100.34	36.82
		Q155	5	0.18	59.45	0.54	6.08	0.94	24.33	− 0.02	8.59	99.89	41.47
		Q156	5	0.31	60.79	0.75	6.16	1.72	23.31	0.04	7.71	100.46	36.88
		Q157	16	0.18	57.68	0.75	5.76	0.58	25.72	0.03	9.86	100.46	47.01
		Q164	8	0.17	60.61	0.89	6.48	1.11	23.21	0.03	7.72	100.10	37.17
	MT37B51	Q115	9	0.10	54.94	0.32	4.86	0.12	27.97	0.07	11.85	100.16	57.00
		Q116	6	0.36	59.53	0.36	6.40	0.25	24.22	–	8.82	99.50	42.61
		Q117	9	0.32	58.59	0.61	6.07	0.49	24.24	0.03	8.96	99.03	43.65
		Q123	15	0.19	58.89	0.47	5.97	0.33	25.17	0.05	9.90	100.86	46.93
		Q124	10	0.06	57.15	0.87	5.23	0.14	26.28	–	10.78	100.51	52.81
		Q126	8	0.23	58.53	0.61	6.22	0.26	25.37	–	9.30	100.23	44.57
		Q127	12	0.26	59.30	0.64	6.54	0.14	24.53	0.10	8.57	99.73	41.66
		Q128	7	0.32	59.16	0.48	6.25	0.21	24.76	0.07	9.34	100.21	44.69
		Q134	4	0.18	59.30	0.50	6.30	0.15	25.37	− 0.02	9.62	101.29	45.38
		Q135	8	0.25	60.98	0.59	6.77	0.14	24.67	0.04	9.10	102.34	42.29
		Q136	9	0.23	59.89	0.42	6.21	0.34	23.96	0.04	9.33	100.17	44.49
		Q138	10	0.21	58.82	0.34	6.01	0.32	25.03	0.03	9.70	100.28	46.29
		Q139	6	0.19	58.35	0.31	6.23	0.10	25.16	0.02	9.54	99.79	45.57
		Q140	3	0.27	59.22	0.29	5.89	0.28	25.25	−0.03	10.23	101.16	48.20
		Q141	12	0.20	57.24	0.71	5.76	0.16	25.31	0.14	9.98	99.31	48.46
		Q143	12	0.21	60.26	0.60	6.32	0.10	25.62	0.01	10.05	102.90	46.51
P1 fallout	MT25E1	T3	Glass	1.00	75.42	2.73	1.48	2.07	12.93	0.33	2.06	97.26	–
		T9	40	0.14	58.90	0.40	6.75	–	25.21	0.03	8.50	99.87	41.03
P1 surge	MT36P7	Q4	9	0.00	54.51	0.59	3.93	0.26	27.82	–	12.79	100.05	63.27
		Q14	22	0.00	52.29	0.30	3.97	0.14	28.89	0.04	13.75	99.48	65.18
		Q15	10	0.00	57.84	0.68	5.53	0.28	25.79	–	10.48	100.71	50.31
		Q11	Glass	1.00	75.57	2.61	2.29	1.97	11.26	0.28	2.16	96.59	–
		Q3	3	0.61	59.47	0.59	6.88	0.14	25.34	0.22	8.50	101.16	40.25
		Q5	8	0.07	56.66	0.68	5.40	0.13	26.97	–	10.92	100.77	52.38
		Q30	Glass	1.00	77.57	2.34	1.76	2.23	10.81	0.18	1.95	97.22	–
		Q17	12	0.15	53.92	0.31	4.69	0.15	25.62	0.04	11.20	96.01	56.38
		Q18	4	0.14	57.45	0.63	5.17	0.01	26.01	0.05	10.65	100.04	53.20
		Q19	9	0.29	57.74	0.57	5.70	0.11	25.66	− 0.07	10.25	100.04	49.53
		Q20	10	0.42	57.22	0.64	5.97	0.19	24.01	− 0.10	9.08	97.18	45.15
		Q21	18	0.34	56.33	0.98	6.18	0.27	25.33	0.17	9.12	98.44	44.22

(continued on next page)

Table 2 (*continued*)

Eruption	Sample	No.	Size (μm^2)	Composition[a]									
				f	SiO_2	FeO	Na_2O	K_2O	Al_2O_3	MgO	CaO	Total	An
		T43	1200	0.00	50.79	0.38	3.33	0.06	31.28	0.02	14.79	100.71	70.80
		T44	3000	0.00	46.09	0.60	1.33	0.06	34.00	0.07	18.35	100.51	88.15
		T45	1200	0.00	46.62	0.63	1.78	0.05	33.96	0.09	17.82	100.99	84.48
		T47	1000	0.00	51.73	0.66	3.76	0.06	30.36	0.08	14.25	101.10	67.47
	MT36P6	Q37	Glass	1.00	79.07	2.28	2.03	2.33	10.32	0.21	1.35	97.97	–
		Q34	13	0.07	55.99	0.46	5.23	0.07	27.23	−0.02	11.18	100.11	53.94
		Q40	9	0.14	58.31	0.36	5.68	0.31	25.27	0.05	10.05	100.02	48.56
		Q41	6	0.34	59.58	0.44	6.12	0.24	25.12	–	9.56	100.96	45.70
		Q42	4	0.38	59.05	0.72	6.34	0.12	24.67	−0.10	9.33	100.23	44.54
		Q43	12	0.17	58.96	0.64	5.97	0.17	24.96	−0.04	9.93	100.61	47.43
		Q46	6	0.36	60.77	0.18	6.65	0.29	24.80	−0.10	8.98	101.56	42.04
		Q57	Glass	1.00	77.16	1.85	2.47	2.07	11.96	0.08	2.07	98.15	–
		Q47	15	0.24	55.63	0.71	5.27	0.16	26.80	−0.02	10.80	99.39	52.61
		Q48	6	0.33	56.42	0.37	5.10	0.09	29.96	0.01	11.72	103.69	55.66
		Q51	10	0.23	57.52	0.49	5.88	0.14	25.82	−0.02	9.84	99.74	47.66
		Q55	5	0.42	58.57	0.54	5.99	0.04	25.95	0.05	10.18	101.26	48.32
		Q58	12	0.06	56.38	0.40	4.96	0.30	26.51	–	11.24	99.85	54.63
		T33	1250	0.00	46.40	0.47	1.19	0.05	34.15	–	18.35	100.61	89.23
		T34	2400	0.00	51.31	0.61	3.58	0.05	30.86	0.08	14.48	101.04	68.90
		T35	600	0.00	49.86	0.56	2.92	0.08	31.22	0.11	15.01	99.87	73.58
		T36	3000	0.00	52.36	0.45	3.94	0.06	30.06	0.02	13.17	100.07	64.67
		T37	1500	0.00	49.68	0.53	2.68	–	32.89	0.06	15.56	101.40	76.25
		T38	1500	0.00	50.50	0.78	3.01	0.04	31.53	0.08	14.90	100.84	73.05
		T39	2000	0.00	53.13	0.62	4.26	0.09	29.63	0.06	13.10	100.91	62.62
		T40	600	0.00	53.42	0.46	4.57	0.09	28.81	0.02	12.21	99.75	59.31
		T41	1500	0.00	51.85	0.71	3.96	–	29.66	0.06	13.62	99.88	65.55
		T42	1800	0.00	45.53	0.61	1.29	0.04	34.37	–	18.31	100.15	88.49
P4 fallout	MT32W	T54c	500	0.00	47.92	0.51	2.02	–	32.66	0.01	16.04	99.24	81.46
		T55r	500	0.00	54.68	0.36	4.67	0.16	28.24	–	11.90	100.02	57.92
		T57	2000	0.00	54.28	0.47	4.71	0.13	29.09	0.02	11.82	100.52	57.66
		T60	1500	0.00	52.57	0.38	4.12	0.11	30.04	0.06	12.86	100.22	62.86
		T61	1600	0.00	55.07	0.31	4.81	0.12	28.53	–	11.32	100.37	56.14
		T63	Glass	1.00	74.39	1.63	2.36	1.74	12.42	0.22	2.40	95.43	–
		T50	60	0.11	58.27	0.39	6.02	0.01	26.67	0.01	9.68	101.14	47.02
		T51	75	0.07	58.33	0.34	6.21	0.14	26.16	–	9.18	100.40	44.60
		T52	25	0.47	57.51	0.29	6.76	0.21	24.68	0.07	7.80	97.49	38.46

[a] Chemical composition in wt.% (MnO and $TiO_2 < 0.2$ wt.%; see text for the recalculation procedure); An for anorthite content in mol.%; All Fe as FeO; *f* for the calculated mixing fraction between the glass (composition referred as "Glass") and the following plagioclases.

20 μm, small and large microlites having different genetic origins, as explained later in the discussion. Some of the plagioclases with apparent sizes in the range defined above were clearly pieces of broken crystals, as they were not crystal faceted or displayed abruptly interrupted chemical zonings. Broken crystals appear in nearly all eruptive deposits (particularly in P2 fallout), and were not included in our study.

4.1. Microlite compositions

The dataset of 296 analyses of plagioclase microlites from various eruptive sequences of Mt. Pelée given in Martel et al. (2006) is supplemented here by 92 new analyses mainly concerning the smallest population size (1–5 μm), for which a procedure of composition recalculation was necessary (Table 2).

The plagioclase microlite compositions for the recent eruptions of Mt. Pelée are displayed along the ordinate axis of Fig. 3. The compositional range actually varies from a thin section to another within a particular eruptive sequence. These heterogeneities are not attributed to variations in the sample groundmass porosity (calculated by image analyses or from density measurements in Martel et al., 2000) and seem to reflect true compositional variations within a particular eruptive deposit. Plagioclase microlites in samples from dome-forming eruptions (domes, BAFs, and surges from the 1929,

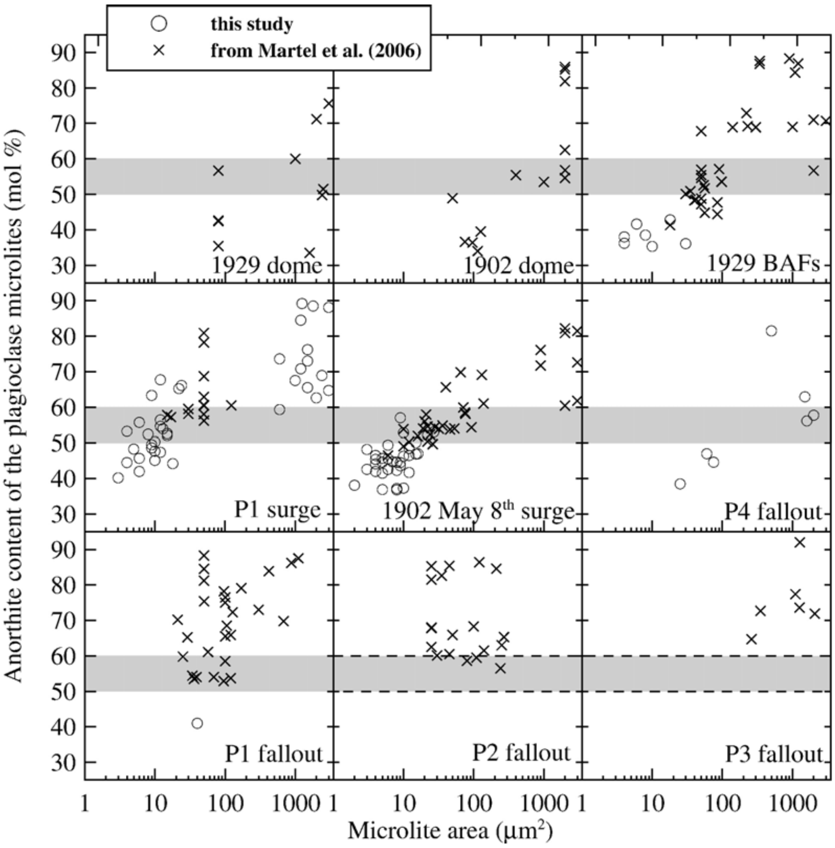

Fig. 3. Composition-size relation of the plagioclase microlites for different eruptive style deposits at Mt. Pelée. Chemically zoned microlites have been plotted with their core composition. The grey areas represent the An_{50-60} rim composition of the plagioclase phenocrysts (Martel et al., 1998), yet not statistically validated for the P2 and P3 eruptions (2 to 5 analyses of each deposit suggest similar or slightly more mafic (An_{55-65}?) phenocryst rims).

1902, and P1 events) and microlite-rich pumices from the P1 and P4 plinian events show the largest compositional range from An_{30-40} to An_{80-90}. In contrast, microlite-poor (< 1 vol.%) pumices from the P1, P2, and P3 plinian events lack small plagioclases (1–5 μm) and plagioclase less calcic than the phenocryst rims, i.e. < An_{50-60} (with one exception in P1). The largest plagioclase microlites (> 20 μm in length) often show visible zonings, the analytical profiles of which reveal a calcic-rich core (An_{80-90}) surrounded by a sodic rim (< An_{60}; Fig. 4). In the 10–20 μm microlite size range, plagioclase cores only reach An_{65-70} (Fig. 4C–D). Below 10 μm in length, most of the microlites lack visible chemical zonings, generally with compositions below the phenocryst rims (Fig. 5A–B), although some plinian pumices display small (5–10 μm) highly-calcic microlites (Fig. 5C).

4.2. Areal fraction Φ, number density N_A, and size of the plagioclase microlites

The plagioclase-microlite Φ and N_A, both recalculated on a phenocryst-and bubble-free basis, and the corresponding mean size S_n (= $(\Phi/N_A)^{0.5}$) are reported in Table 3. In dome products, Φ and N_A are difficult to determine, first because the microlite outlines are barely distinguishable from the surrounding matrix (Fig. 2A), and second because of the precipitation of abundant amorphous silica. In fact, the 1929 BAFs and the 1902 surge deposits show two main textures of silica precipitations that we attribute to different mechanisms. The first texture is pervasive silica throughout the glass (Fig. 2B; middle of Fig. 2F) that we attribute to precipitations from the melt once SiO_2 saturation is reached upon decompression and/or cooling (to quartz-feldspar cotectic; Blundy and Cashman, 2001). This hypothesis is mainly supported by phase equilibria experiments performed starting with a rhyolite melt at high temperatures (800–850 °C) and low pressures (< 125 MPa), in which a pervasive silica phase precipitates without any contribution of external fluid percolation (Martel and Schmidt, 2003; Martel et al., 2006). The second texture is described as spots of cracked silica located along the pores or with a recognizable pore shape (upper right and lower left corners of Fig. 2F) that could result from silica

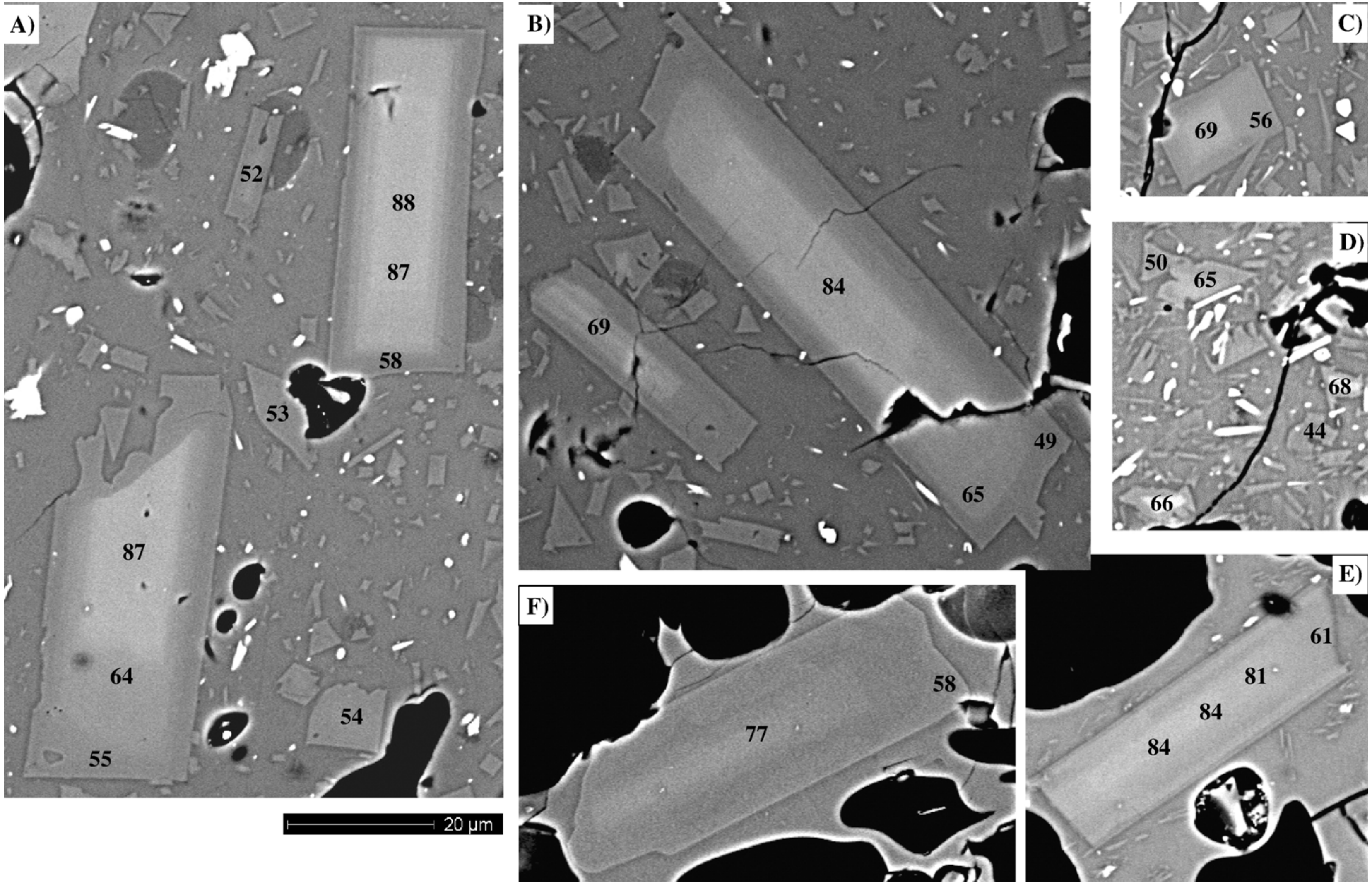

Fig. 4. SEM images of chemically-zoned plagioclase microlites. A–B) 1929 BAFs (MT37N1); C) 1902, May 8th surge (MT37B51); D) P1 surge (MT36P7); E) P1 plinian fallout (MT25E1); F) P3 plinian fallout (MT35G1). Scale bar of 20 μm for all images. Numbers are the analyzed anorthite molar content of the plagioclase (Martel et al., 2006).

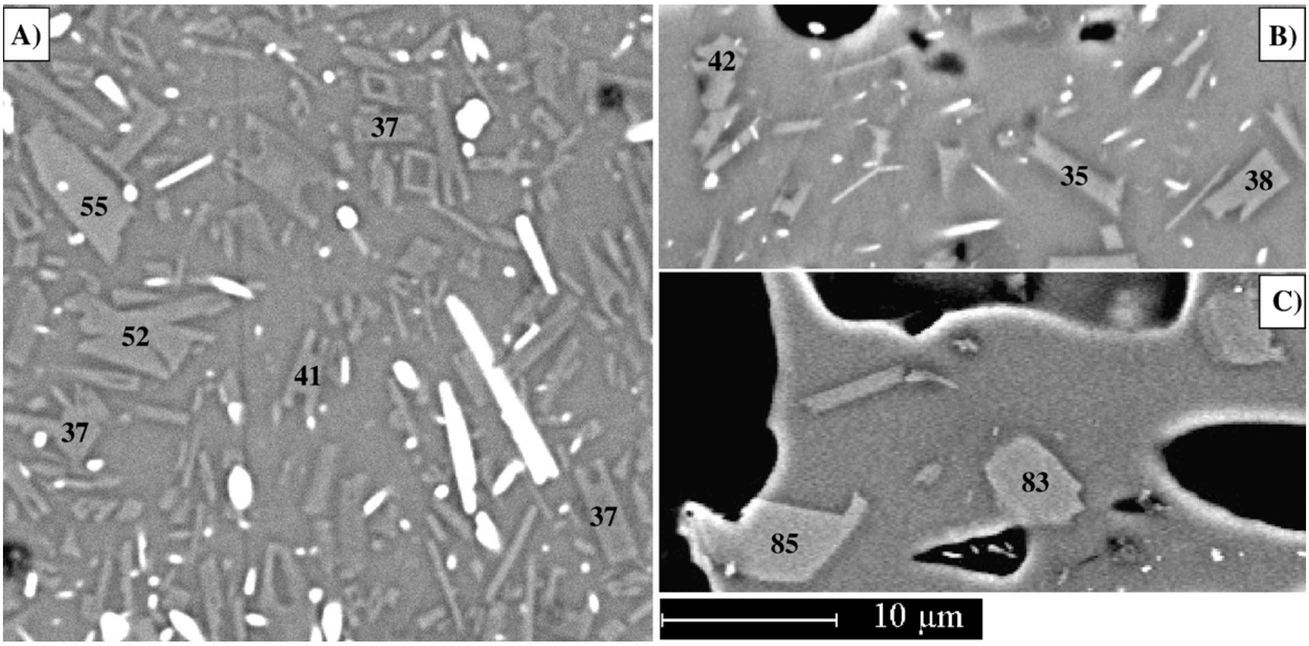

Fig. 5. SEM images of chemically-unzoned plagioclase microlites. A) 1902, May 8th surge (MT37B56); B) 1929 BAFs (MT37N1); and C) P2 fallout (MT37F). Numbers are the analyzed anorthite molar content of the plagioclase.

deposition during fluid percolation in the pore network. In this latter case, the estimation of Φ and N_A (recalculated on a pore-free basis) should not take into account the silica volume that represents material addition. In contrast, silica precipitations from the melt may represent a real volume of this melt and thus may be counted as groundmass. In the dome samples, there are large areas of cracked silica that may be ascribed to deposition from fluid percolation. However, the origin of the silica that resembles the pervasive type is difficult to attribute, because they largely touch pores (Fig. 2A). Moreover, a significant contribution of fluid percolation would not be surprising, given that the domes of Mt. Pelée are intensively percolated by hot fluids (Traineau et al., 1989b). Therefore, for the domes, we recalculated both Φ and N_A for the supposed cases of silica-bearing and silica-free matrix glass, suspecting the true value is in between these two extreme cases.

Table 3 and Fig. 6 show that the 1902 and 1929 dome samples display Φ between 0.30 and 0.60, depending on the origin of the silica phase. The 1902, August 30th and May 8th surges that preceded the 1902 dome have Φ comparable to the lower value of the 1902 dome (recalculated on a silica precipitation-free basis), i.e., between 0.22–0.32. However, if fluid percolation is the dominant process for the silica phase deposition, then the 1902 surge groundmasses are half crystallized compared to the dome. The 1929 BAFs samples have rather small Φ, up to 0.15. The P1 surge samples have comparable Φ (0.22–0.28) to the 1902 surges. The common pumices from the plinian events are microlite-poor, with $\Phi \leq 0.03$ (e.g., P1, P2, P3). However, some of the pumices of these plinian events contain more microlites, with Φ up to 0.15 (e.g., P1, P4), referred here as to microlite-rich plinian pumices. Microlite N_A spans nearly 2.5 orders of magnitude. The domes and the 1929 BAFs have comparable N_A, around 15–40 and $6–27 \times 10^3$ mm^{-2}, respectively. This compares to the $0–10 \times 10^3$ mm^{-2} N_A analyzed in the BAFs deposits of the 1989–1990 dome-collapse eruptions of the Redoubt volcano, Alaska (Wolf and Eichelberger, 1997). In contrast, the 1902 and P1 surges have N_A ten times higher than in the dome and BAFs products, i.e., 117–201 and $141–245 \times 10^3$ mm^{-2}, respectively. The microlite-poor plinian pumices have N_A below 5×10^3 mm^{-2}, whereas the microlite-rich pumices have N_A around $28–176 \times 10^3$ mm^{-2}.

The measured areas of the plagioclase microlites are presented in Table 2 and shown along the abscissa axis of Fig. 3. It appears that microlites with compositions below $\mathrm{An}_{50–60}$ have restricted areas < 200 μm^2, whereas anorthite-richer crystals span the whole range between 10 to 3000 μm^2. Microlite sizes may also be assessed through the mean sizes $S_n = (\Phi/N_A)^{0.5}$ (Table 3 and Fig. 6). The microlites from the domes have large S_n of ~ 4.5 μm. The 1929 BAFs have lower S_n, around 2.4–2.9 μm. The surge samples (1902 and P1) have comparable S_n, from 1.0 to 1.6 μm. The high variability of the N_A in the plinian pumices, while relatively low Φ, results in a large range of S_n, from 0.9 to 5.5 μm.

Table 3
Fractions and textural characteristics of the plagioclase microlites

Deposit	Sample	Porosity fraction	n [a]	2-Dimensions [b]				3-Dimensions [c]		
				Φ	$N_A \times 10^3$ (mm^{-2})	S_n (μm)	Shape	S:I:L axis	R^2	Shape
1929 dome	MT34P	0.15	~ 100	0.30–0.60 [d]	15–40[d]	4.5–3.9[d]	T	n.d.	n.d.	n.d.
1929 BAF	MT37N1	0.44	105	0.15	22	2.6	T+S	1.0:1.5:2.2	0.73	acicular
			83	0.12	14	2.9	T+S			
			2	*0.07*	*< 1*		*T+S*	*n.d.*	*n.d.*	*n.d.*
	MT37N89	0.35	*7*	*0.10*	*< 1*		*T*	*n.d.*	*n.d.*	*n.d.*
	MT37N58	0.15	64	0.15	27	2.4	S+T	1.0:1.5:1.8	0.59	rectangular prism
	MT36A	n.d.	31	0.06	6	3.2	S+T	n.d.	n.d.	n.d.
1902 dome	MT34M	0.15	~ 100	0.30–0.60[d]	15–40[d]	4.5–3.9[d]	T	n.d.	n.d.	n.d.
1902, Aug 30th surge	MT36V15	0.31	110	0.31	125	1.6	S+T	1.0:1.6:8.0	0.67	acicular
			10	*0.18*	*< 1*		*T*	*n.d.*	*n.d.*	*n.d.*
	MT36V4	0.32	*25*	*0.21*	*< 1*	n.d.	*T*	*n.d.*	*n.d.*	*n.d.*
1902, May 8th surge	MT37B56	0.26	237	0.24	135	1.3	S	1.0:2.7:8.0	0.72	acicular
			295	0.22	127	1.3	S			
	MT37B51	0.39	281	0.25	128	1.4	S	1.0:1.5:10.0	0.75	acicular
			443	0.32	117	1.6	S			
			279	0.29	128	1.5	S			
	MT37B19	0.37	338	0.24	180	1.2	S	1.0:1.5:10.0	0.81	acicular
			255	0.26	167	1.2	S			
			374	0.24	189	1.2	S			
	MT37B23	0.35	100	0.29	201	1.2	S	n.d.	n.d.	n.d.
			8	*0.05*	*< 1*		*T*	*n.d.*	*n.d.*	*n.d.*
P1 surge	MT36P6	0.29	443	0.27	141	1.4	S+D	1.0:1.5:10.0	0.73	acicular
			466	0.27	169	1.4	S+D			
			424	0.28	153	1.3	S+D			
	MT36P7	0.68	319	0.25	245	1.0	S+D	1.0:2.1:6.0	0.71	acicular
			221	0.22	181	1.1	S+D			
P1 fallout	MT25E1	0.57	32	0.11	137	0.9	D	1.0:3.0:7.0	0.85	rectangular prism
			74	0.14	176	0.9	D			
			54	0.11	40	1.7	D			
			69	0.09	57	1.3	D			
			76	0.09	64	1.2	D			
	MT33C	0.61	*4*	*0.01*	*< 1*	*3.2*	*T*	*n.d.*	*n.d.*	*n.d.*
			2	*0.01*	*< 1*	*3.2*	*T*	*n.d.*	*n.d.*	*n.d.*
P2 fallout	MT37F	0.72	*7*	*0.03*	*1*	*5.5*	*T*	*n.d.*	*n.d.*	*n.d.*
			36	*0.03*	*4*	*2.7*	*T*	*1.0:2.5:4.0*	*0.64*	*rectangular prism*
P3 fallout	MT35G1	0.66	*1*	*0.01*	*< 1*	*3.2*	*T*	*n.d.*	*n.d.*	*n.d.*
P4 fallout	MT32W	0.79	44	0.07	28	1.6	S	1.0:6.0:10.0	0.73	rectangular prism

n.d. = not determined. Values in italic refer to the basalt-inherited microlites, whereas the other are decompression-induced microlites (see Discussion).

[a] Number of analyzed microlites.

[b] Φ = area fraction; N_A = number density; S_n = mean size, equals to $10^3 \times (\Phi/N_A)^{0.5}$; T for tabular, S for skeletal, and D for dendritic.

[c] 3-D recalculation after Morgan and Jerram (2006). S:I:L for Short, Intermediate, and Long axis, respectively; R^2: fractional measure of the variation.

[d] The first value is calculated on a groundmass including the silica phase; the second value is for a silica-free groundmass melt (see text for explanation).

4.3. Shape of the plagioclase microlites

The crystal morphologies are linked to the temperature or the pressure (H_2O content) difference between the equilibrium phase liquidus and the effective nucleation and growth (Lofgren, 1974). Therefore, observations of the microlite shapes may provide information on their crystallization conditions. Fig. 7 shows the three main morphologies observed in the recent products of Mt. Pelée, i.e., tabular, skeletal, and dendritic. The tabular morphology (Fig. 7A), with rectangular to needle-like shapes depending on the

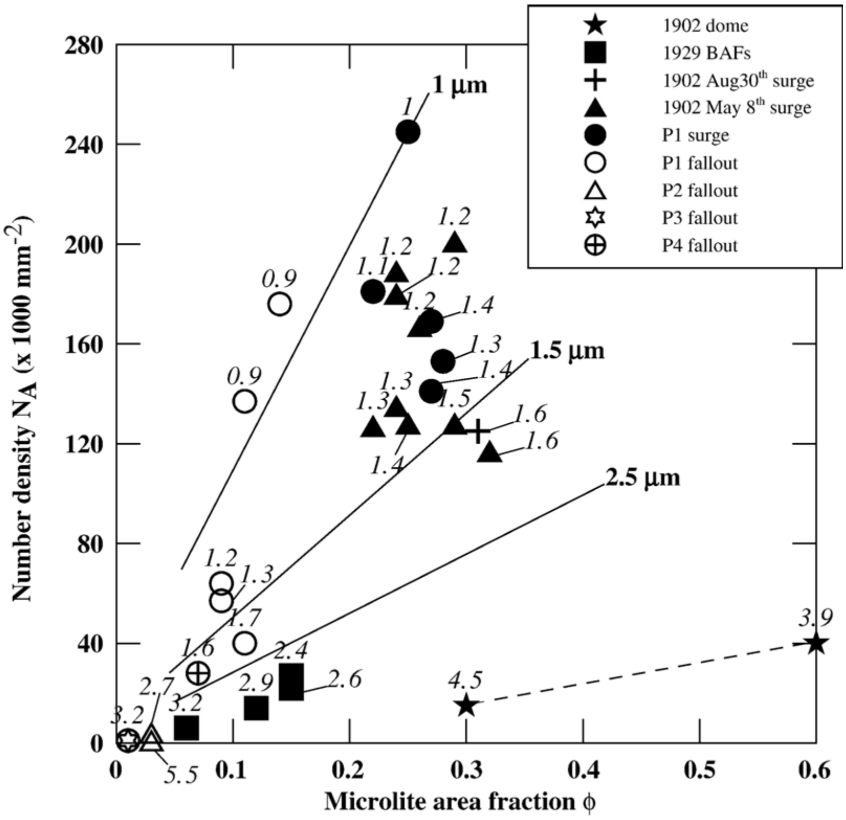

Fig. 6. Decompression-induced microlite Φ versus N_A for different samples from recent eruptions of Mt. Pelée. The lines give the microlite mean size in µm (S_n; Table 3). For samples of a given eruptive event, a vertical trend suggests a nucleation-dominated crystallization regime, and a horizontal trend suggests a growth-dominated crystallization regime (Hammer et al., 1999). The dashed line between the dome samples brackets Φ, depending on whether the microlites are recalculated using the residual glass or the residual glass + silica precipitation (see text).

planar crystal section, is essentially observed in the 1902 and 1929 domes and more rarely in the 1929 BAFs samples (Fig. 2A–B). Most of the 1929 BAFs, the 1902 and P1 surge samples have skeletal morphologies, including hopper and hourglass shapes, depending on the observed cross section (Faure et al., 2003; Fig. 2C, 5A). Few microlites in the surge samples and many of the microlite-rich plinian pumices show dendritic morphologies, including swallowtail overgrowths on a hopper crystal and rod morphologies (Fig. 2E). The large microlites of the microlite-poor plinian pumices are tabular in shape, sometimes slightly rounded (Figs. 2D, 4F). In the 1929 BAFs and surge samples of 1902 and P1, the large zoned microlites are either purely tabular or tabular with skeletal overgrowths (Fig. 4A–B). In the microlite-rich pumices, these large microlites are mainly tabular with small dendritic overgrowths (Figs. 2E, 4E).

For a given sample, the microlite 2D aspect ratios analyzed in different images were gathered to be converted into 3D habits following the method of Morgan and Jerram (2006) (Table 3). Selected frequency histograms are shown in Fig. 8. The dome products, in which the proper outlines of the microlites could not be defined, and the microlite-poor pumices, for which the microlite number was not enough, were not considered. The results for the porous (porosity fraction of 0.44) 1929 BAFs suggest acicular 1.0:1.5:2.2 microlites (Fig. 8A), corroborated by the dense (porosity fraction of 0.15) sample (rectangular prisms of 1.0:1.5:1.8,), although the 64 studied sections that lead to a low R^2 value (0.59) are not enough to confirm the result. The 1902 August 30th, May 8th (Fig. 8B), and the P1 surge (Fig. 8D) samples display remarkable similar acicular microlite habit of 1.0:1.5–2.7:6.0–10.0, with reasonably confident estimations according to natural samples (R^2 values between 0.67–0.81). The microlites in the P1 fallout pumices show rectangular-prism crystal habit of 1.0:3.0:7.0, with a good R^2 value of 0.85 (Fig. 8C). In the P2 and P4 pumices, microlites are also rectangular prisms, but with different dimensions, i.e., 1.0:2.5:4.0 and 1.0:6.0:10.0, respectively. Despite the acceptable R^2 values of 0.64 and 0.73 for P2 and P4 pumices, respectively, the very low number

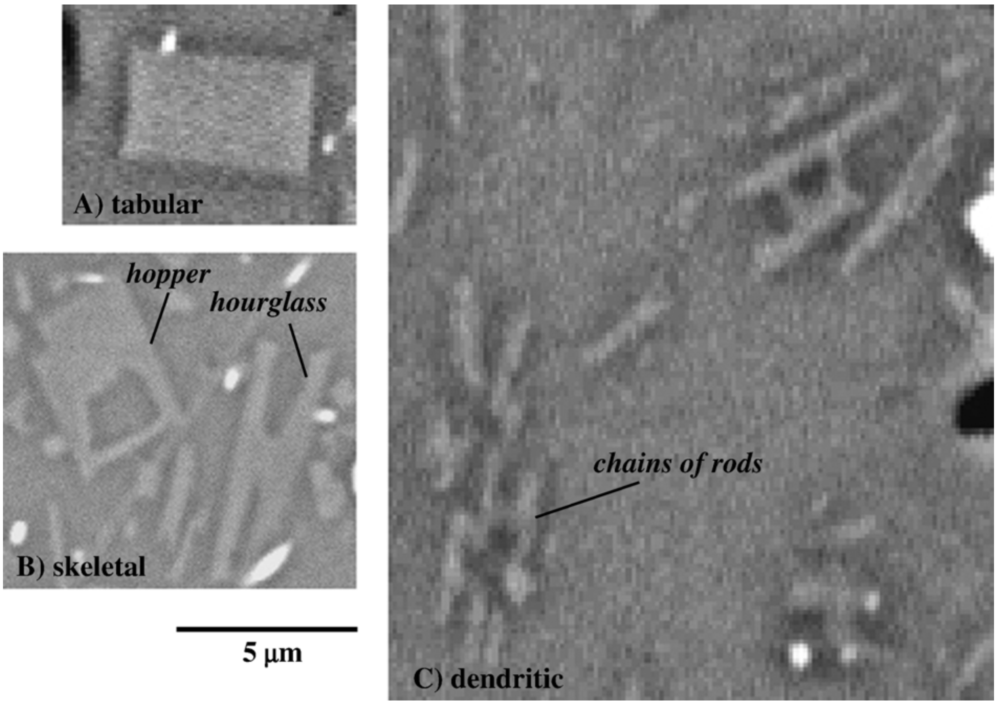

Fig. 7. SEM images of the plagioclase microlites morphologies. A) Tabular habit in a 1929 BAFs sample. The rectangular shape is observed in the [010] crystal orientation. For sections normal to [010], the crystal has an acicular or needle-like shape; B) Skeletal morphology in a 1902, May 8th surge sample, including hopper and hourglass shapes, depending on the axes along which the crystal is observed; C) Dendritic morphology characterized by chains of rods and swallowtails in a microlite-rich P1 plinian pumice.

of analyzed sections (< 50) compels caution when considering these results.

4.4. Composition, H_2O content, and porosity of the groundmasses

The glass compositions and their quartz-feldspar normative compositions are given in Table 4. In contrast to the glass data in Martel et al. (2000) that show an overall compositional range for a given eruptive deposit, the glasses have been analyzed here as close as possible to the microlites in order to trace the melt evolution with microlite crystallization. The matrix glasses are all rhyolitic, with SiO_2 contents ranging between 76 and 80 wt.%, and are around 73 wt.% for the P2 and P3 fallout eruptions.

The BAFs and surge samples show low mean H_2O contents, from 0.17 to 0.84 wt.%, with maximum values of 1.31 wt.% (Table 5). The P1 and P2 plinian fallout deposits are H_2O-rich, with 1.8 ± 0.3 and 2.5 ± 0.3 wt.%, respectively. The H_2O data show a significant variability among several samples from a given eruptive unit, which seems to reflect true heterogeneities in the glass H_2O contents.

The matrix porosities determined either by density measurements or by image analysis are shown in Table 3 and 5.

5. Discussion

5.1. Origin of the microlites and magma mixing process

Martel et al. (2006) identified two different origins for the plagioclase microlites in the recent eruptive products of Mt. Pelée, depending on their anorthite content. The plagioclase microlites with anorthite contents lower than the phenocryst rims (i.e., An_{50-60}) were considered to have crystallized from a water-saturated rhyolitic melt below 200 MPa during ascent towards the surface. This population is best represented in the dome-forming products (domes, BAFs, and surges) from the 1902 and 1929 eruptions, but almost lacks in the plinian eruptive products. The population with high anorthite contents ($< An_{80}$) is ubiquitous in the recent deposits of Mt. Pelée. These crystals must have grown from andesitic to basaltic melts with water contents as high as 6–8 wt.%. Those melts most probably represent injections into the andesite body during episodes of recharge and mixing of the magma reservoir. The liquidus temperature of the basaltic andesite melt is 1050 °C at 400 MPa (Pichavant et al., 2002), so that the pressure and temperature contrast at the contact with the andesite ($T = 875–900$ °C, 200 MPa; Martel et al., 1998) would generate up to 150 °C undercooling, appropriate for microlite crystallization.

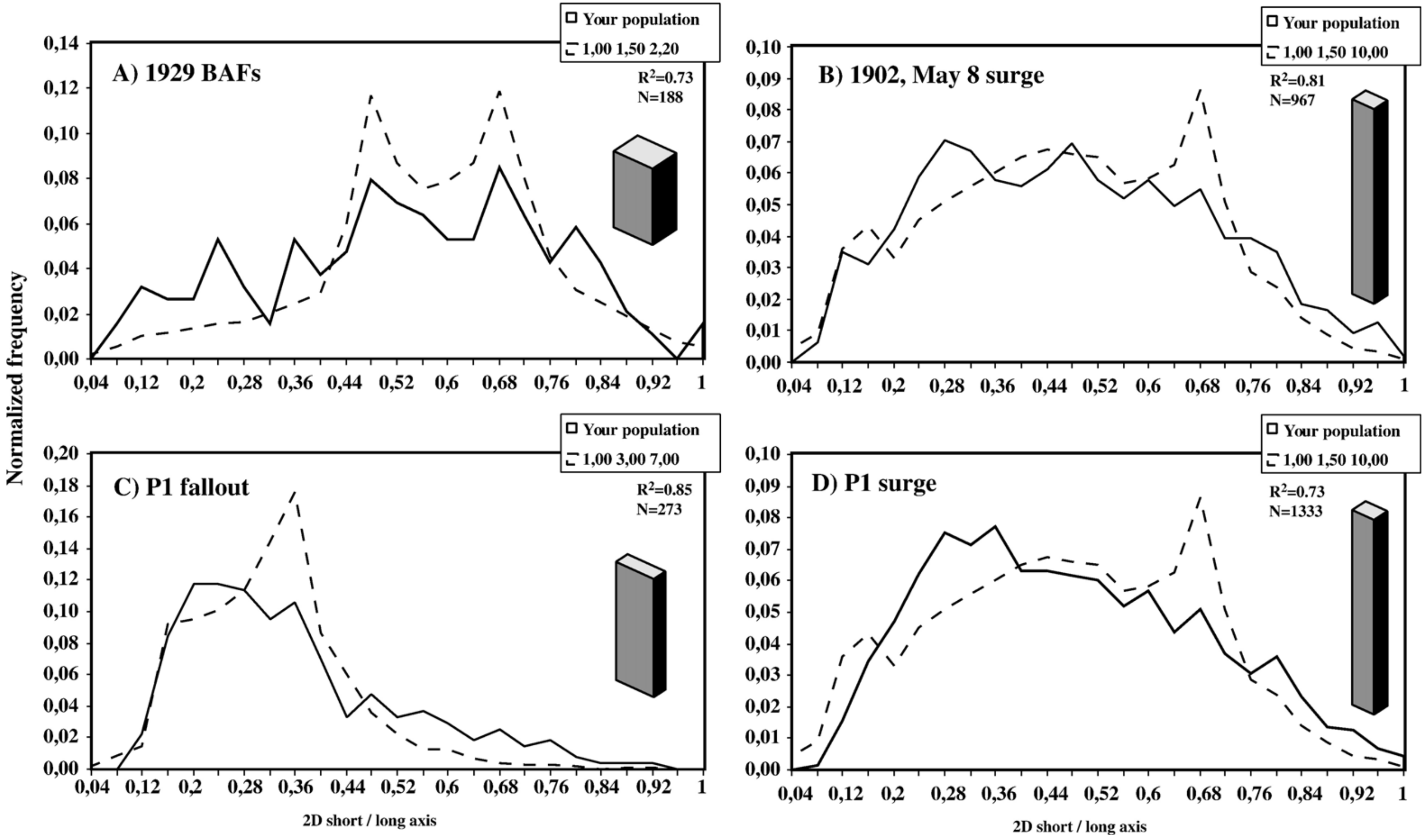

Fig. 8. Three-Dimensional habits of plagioclase microlites calculated after Morgan and Jerram (2006); A) 1929 BAFs (MT37N1); B) 1902, May 8th surge (MT37B19); C) P1 fallout (MT25E1); and D) P1 surge (MT36P6). The plain curves are the frequency histograms of the short to the long axis ratios measured in 2D for our data and the dashed lines represent the best-fit shape curve given for a 3D crystal habit (Long–Intermediate–Short axis). R^2 gives the shape reliability and N is the number of counted microlites.

Table 4
Glass compositions of Mt. Pelée

Eruption	Sample	*n*	SiO_2	FeO	Na_2O	K_2O	Al_2O_3	MgO	CaO	Qz′,Ab′,Or′
1929 BAFs	MT37N1	6	79.44(58)	1.54(32)	4.40(18)	2.92(11)	10.31(41)	0.05(04)	0.88(18)	43,39,18
	MT36A	10	76.92(80)	2.02(26)	4.43(21)	2.31(10)	12.03(40)	0.25(05)	1.65(18)	34,55,11
1902 May 8th surge	MT37B56	10	77.79(67)	2.04(41)	3.79(51)	3.96(23)	10.80(32)	0.07(04)	1.03(21)	39,37,24
	MT37B51	10	80.06(77)	1.74(20)	3.76(31)	2.62(11)	10.26(54)	0.08(04)	1.07(28)	42,44,14
	MT37B19	6	79.56(75)	1.91(10)	3.60(40)	3.03(15)	10.50(21)	0.05(03)	0.89(21)	41,44,15
	MT37B23	2	78.19(73)	1.79(04)	3.08(22)	3.69(02)	11.42(53)	0.16(03)	1.27(03)	38,43,19
P1 surge	MT36P7	7	77.93(79)	2.55(16)	3.19(43)	2.24(15)	11.50(43)	0.18(05)	1.97(28)	35,54,11
	MT36P6	4	79.80(12)	2.19(32)	3.45(28)	2.44(07)	10.34(29)	0.15(12)	1.18(19)	41,46,13
P1 fallout	MT25E1	3	76.37(15)	2.59(09)	3.34(14)	2.10(02)	12.59(06)	0.41(05)	2.23(10)	31,60,9
	MT33C	5	76.72(17)	2.20(10)	3.62(15)	1.93(04)	12.60(13)	0.32(04)	2.21(01)	30,62,8
P2 fallout	MT37F	10	73.36(68)	2.94(14)	4.27(24)	1.80(12)	14.02(20)	0.54(05)	2.83(14)	22,73,5
P3 fallout	MT35G1	5	72.94(22)	2.92(23)	4.27(24)	1.70(08)	14.15(21)	0.59(03)	3.08(09)	22,73,5

Compositions recalculated to 100 wt.%; *n* is the number of analyzes; numbers in brackets are the statistical errors on the two last digits; Qz′,Ab′,Or′ is the normative quartz (Qz′), albite (Ab′), and orthose (Or’) composition obtained from the CIPW norms of the glasses and corrected to account for the displacement of the quartz–feldspar cotectic in presence of normative anorthite (< 20 wt.%; corindon < 1 wt.%), as explained in Blundy and Cashman (2001).

The chemical zonings observed in some of these high-Ca microlites (Fig. 4) suggests the possibility of either multi-stage growth or partial re-equilibration between early-formed crystals and the (rhyolitic) melt of the andesite at pre-eruptive conditions. If an eruption follows the mafic intrusion, further crystallization may occur in the conduit, giving rise to the population of microlite with compositions < An$_{50-60}$ that may form either new crystals and/or rim the high-Ca microlites. This dual model of microlite genesis, i.e., basalt-inherited versus decompression-induced microlites, thus accounts for the whole compositional range of plagioclase microlites observed at Mt. Pelée.

The best way to distinguish between both microlite populations is certainly chemical composition (Martel et al., 2006). Yet, because analyzing each microlite from a particular section is a time-consuming task (specifically when crystals are below the spatial resolution of the electron microprobe beam), morphological information aiming at recognizing basalt-inherited from decompression-induced microlites may be helpful. The original shapes and sizes of the high-Ca basalt-inherited plagioclase microlites depend on their nucleation and growth conditions and on the time spent between the mafic magma intrusion and the reservoir exit. These original morphologies are potentially

Table 5
H_2O contents of the interstitial glasses

Eruption	Sample	Porosity fraction	*n*	H_2O content (wt.%)[a]			Pressure[b] (MPa)	Depth[c] (m)
				Mean (±σ)	Max	Min		
1929 BAFs	MT37N16	0.12	2	0.17 (0.01)	0.17	0.16	0.1	4
	MT37N17	0.30	2	0.67 (0.32)	1.12	0.22	5.1 (3.9–5.8)	231
	MT37N6	0.40	2	0.93 (0.05)	1.03	0.84	9.7 (8.7–10.7)	434
1902 May 8th surge	MT37B82	0.17	7	0.36 (0.05)	0.50	0.21	1.2 (0.9–1.7)	58
	MT37B6	0.30	2	0.40 (0.06)	0.48	0.32	1.6 (1.1–2.2)	71
	MT37B55	0.44	5	0.68 (0.05)	0.81	0.59	5.3 (4.5–6.1)	240
1902 Aug 30th surge	MT36V50	0.13	3	0.41 (0.05)	0.50	0.30	1.7 (1.2–2.2)	80
	MT36V66	0.35	5	0.61 (0.23)	1.14	0.13	4.2 (1.4–8.0)	191
	MT36V52	0.51	2	0.84 (0.33)	1.31	0.38	8.0 (2.8–14.8)	359
P1 fallout[d]	MT33C	0.61	4	1.8 (0.3)	2.3	1.6	31.7 (23.1–41.1)	1414
P2 fallout	MT37F	0.72	10	2.47 (0.33)	3.14	1.34	53.9 (42.4–66.3)	2390

n is the number of analyzed glasses.

[a] Determined by ion probe (see text for analytical procedure), except for the P1 and P2 fallout samples, for which glass H_2O were determined by the “by–difference” method using the electron microprobe.

[b] H_2O saturation pressures deduced from the empirical equation of H_2O solubility at 875 °C (see text) for the mean H_2O content (± σ).

[c] Calculated from saturation pressures with an average rock density of 2.3 g/cm^3.

[d] Data from Martel et al. (2000).

preserved in the plinian samples that lack further crystallization upon ascent to the surface. In these pumices, the highly-calcic plagioclase microlites have mean lengths varying from relatively small (< 10 μm in the P2 pumices) to > 20 μm, with tabular or slightly rounded shapes (Figs. 2D and 5C). If there was time for crystallization or re-equilibration during magma ascent, the original basalt-inherited microlites may be rimmed by low-Ca decompression-induced plagioclase, such as in the microlite-rich pumices or in dome-forming products (domes, BAFs and surges). In this case, microlites are characterized by oscillatory zonings that can be identified by backscattered electron microscopy, they are relatively large (> 20 μm in length) and have tabular shapes (Fig. 4). In contrast, decompression-induced microlites lack visible chemical zonings, are small (< 10 μm in length), and change shape from tabular to skeletal or dendritic with decreasing size. Some small zoned crystals (10–20 μm in length) present in the surge deposits (Fig. 4C–D) are difficult to classify into either basalt-inherited or decompression-induced microlites, because their cores have compositions of An_{65-70}, i.e., higher than the phenocryst rims, but not necessary requiring crystallization from a mafic melt (Martel et al., 2006).

Magma mixing is a well–identified process in the recent period of Mt. Pelée activity, notably through enclaves and banded rocks essentially in the early products of the 1902 (May 8th and 20th) and 1929 eruptions (Gourgaud et al., 1989). These textural features characterize volumetrically small mafic intrusions in comparison with the volume of the host silicic magma and a mechanical mixing process in which chemical equilibration is limited. When the proportion of involved mafic magma is small, the equilibration temperature is not much above the initial temperature of the host (Eichelberger et al., 2000). This may explain the absence of chemical and textural destabilizations of the phenocryst rims (such as reverse zonings and sieve-textures in plagioclases; Gourgaud et al., 1989; Pichavant et al., 2002) that are typical indicators of vigorous magma mixing processes (Tsuchiyama, 1985; Browne et al., 2006). In the products that lack textural traces of magma mingling events, such as the plinian fallouts, evidences of mixing are only provided by the basalt-inherited microlites.

Based on both natural and experimental data, Mt. Pelée magma storage region is viewed as a dynamic zoned reservoir, with a mafic magma intruding an andesitic upper reservoir (Fichaut et al., 1989; Pichavant et al., 2002). When the hot mafic magma (basaltic andesite, ~ 1050 °C, 6–8 wt.% H_2O) intrudes the upper colder andesite (~ 200 MPa, 875 °C, 6±0.5 wt.%; Martel et al., 1998), it cools and crystallizes plagioclase microlites with compositions from An_{81-88} to ~ An_{60}, driving the residual melt from basaltic andesite to rhyodacitic compositions (Martel et al., 2006).

An attempt to better constrain the proportion of the mafic magma involved in the mixing process has been realized through determinations of the number density (N_A) and area fraction (Φ, recalculated on a phenocryst- and bubble-free basis) of the basalt-inherited plagioclase microlites. These data are best estimated in the microlite-poor pumices in which no further decompression-induced crystallization occurred. The P1 and P3 plinian deposits have Φ below 0.01 and N_A of maximum 10^3 mm^{-2}. The P2 plinian pumice has Φ up to 0.04, with N_A of 4×10^3 mm^{-2} (Table 3). In dome-forming products, the proportion of basalt-inherited microlites is much more difficult to assess, notably because of the late crystallizations around the original cores potentially causing re-equilibrations with time. Approximate measurements of Ca-rich cored microlites in the 1929 BAFs, 1902 May 8th and August 30th surges suggest Φ and N_A below 0.21 and 10^3 mm^{-2}, respectively (Table 3). Although slightly underestimated, as a part of the crystallization took place around the pre-existing highly-calcic phenocrysts, this calculation suggests low proportions of magma mixing in Mt. Pelée reservoir during its recent period of activity, i.e., a mafic magma fraction of 0.01–0.10, maybe 0.20 for the 1902 August 30th surge. This is confirmed by the < 0.05 magma fraction estimated using the bulk composition data of the intruding magma (HAB in Pichavant et al., 2002), the pre-eruptive magma represented by the microlite-free P1 fallout (Martel et al., 1999) and the erupted products of the 1902 May 8th and August 30th surges and the 1929 BAFs (Gourgaud et al., 1989).

5.2. Ascent dynamics inferred from the decompression-induced microlites

5.2.1. Crystallization regime

During decompression, H_2O exsolution from the melt raises the liquidus temperature of a water-rich magma. Thus, magma that was above or at the liquidus at high pressures becomes significantly undercooled during decompression, causing extensive groundmass crystallization. Microlite crystallization may be dominated by nucleation of new crystals or by growth around existing sites. Experimental studies have revealed that the nucleation-dominated crystallization regime prevails at low pressures or for high decompression rates because of high undercoolings (supersaturations). In contrast, the growth-dominated crystallization regime is predominant at high pressures or for low decompression rates, for which undercooling is small (Lofgren, 1980; Kirkpatrick, 1981; Hammer and Rutherford, 2002; Couch et al., 2003a; Martel and Schmidt, 2003). At extremely high undercoolings, the large driving force for crystallization is countered by limiting rates of diffusion and the melt may not crystallize.

In a diagram representing the microlite number density (N_A) versus area fraction (Φ), samples for which the crystallization regime is nucleation-dominated over time would be characterized by a large N_A range with comparable Φ, whereas a growth-dominated crystallization regime would show a large range of Φ with comparable N_A (Hammer et al., 1999). In Fig. 6, the P1 fallout samples show similar Φ (around 0.10) for N_A of nearly 2 orders of magnitude, leading to small mean sizes (S_n) of ~ 1 µm. This suggests that the microlite crystallization regime in the plinian pumices is dominated by nucleation. In contrast, the 1929 BAFs samples show a horizontal trend with S_n values around 2.4–3.2 µm, which suggests a crystallization regime dominated by growth on existing sites. The P1 and 1902 May 8th surge samples are overlapping, with S_n varying from 1 to 1.5 µm. The crystallization in these latter samples is probably dominated by a combination between both regimes, as the data trend is rather vertical, but departs horizontally to higher Φ (0.20–0.30) in comparison to the plinian trend. Based on time data for the different surge events at Mt. Pinatubo, the crystal size distribution (CSD) data of Hammer et al. (1999) indicate that supersaturation decreases with time, so that the style of crystallization switches from a nucleation-to a growth-dominated regime. Although we could not deduce any nucleation and growth rates from Mt. Pelée CSDs due to unknown crystallization durations, the comparison of the plots of the 1902 May 8th and succeeding August 30th in Fig. 6 and the presence of some tabular-shaped microlites in the August 30th deposit are consistent with a slight switch to a growth-dominated crystallization regime with time. We can note here that the sample porosity that results from gas loss and bubble collapse processes is not related to Φ and N_A, as the two P1 surge samples with 0.29 and 0.68 pore fraction have comparable Φ and N_A (Table 3). In other words, two samples from a given eruptive event may have crystallized under similar conditions resulting in similar microlite Φ and N_A, while further experiencing different pore interconnectivity and permeability that finally lead to different sample porosities.

Experimental studies suggest a crystal shape evolution from tabular to skeletal and dendritic with the undercooling increase as the final pressure decreases (Geschwind and Rutherford, 1995; Blundy and Cashman, 2001; Hammer and Rutherford, 2002; Couch et al., 2003a; Martel and Schmidt, 2003). This would agree with the variation in microlite morphology we found in Mt. Pelée samples: tabular morphologies are seen where N_A are small, i.e. for growth-dominated crystallization regime under small undercoolings, whereas dendritic shapes appear where N_A are high, in nucleation regimes under high undercoolings (Table 3).

5.2.2. Crystallization depth

The projection of the natural glasses into the synthetic system Qz–Ab–Or–H_2O makes it possible to relate the evolution of the glass chemistry to decompression in sub-volcanic systems (Blundy and Cashman, 2001). The last glass composition may provide a means to infer the pressure (depth) of the last crystallization event at the time of magma quenching (fragmentation or cooling). The compositions of Mt. Pelée interstitial glasses have been reported in Fig. 9. The glass compositions of the P1, 1902, and 1929 events follow a decompression-induced crystallization path, in which the plagioclase microlite fraction increases as the glass composition moves away from the albite component, up to the 50 MPa cotectic. An exception is the 0.13-Φ sample from the 1929 BAFs that comes from an eruption for which magma mixing has been identified to take place up to surface emplacement (Gourgaud et al., 1989), thus causing strong chemical disequilibria. Along the 50 MPa cotectic, the quartz saturation is reached and increasingly potassic feldspar crystallizes. On this projection, the most crystallized samples would suggest a quench level around 50 MPa. The P2 and P3 plinian pumices would suggest a quench event at H_2O saturation pressure around 1000 MPa, which is not realistic. Several explanations can be proposed for these too high pressures. Firstly, we cannot assure P2 and P3 magmas have the same bulk-rock compositions and pre-eruptive conditions as the more recent eruptions. Secondly, the projection was originally designed for a $Qz_{16}Ab_{75}Or_9$ composition (Blundy and Cashman, 2001), whereas our glasses are Qz_{22-43} and contain several other minor normative components (< 6 wt.%; diopside, hypersthene, ilmenite). This may potentially result in a significant shift of the cotectics. Thirdly, crystallization is a rather slow process, especially at low pressures for which kinetics are slow and may result in strong disequilibrium of the glass composition with pressure (experimentally observed at low pressures; Martel and Schmidt, 2003). In conclusion, fragmentation or quenching pressures deduced

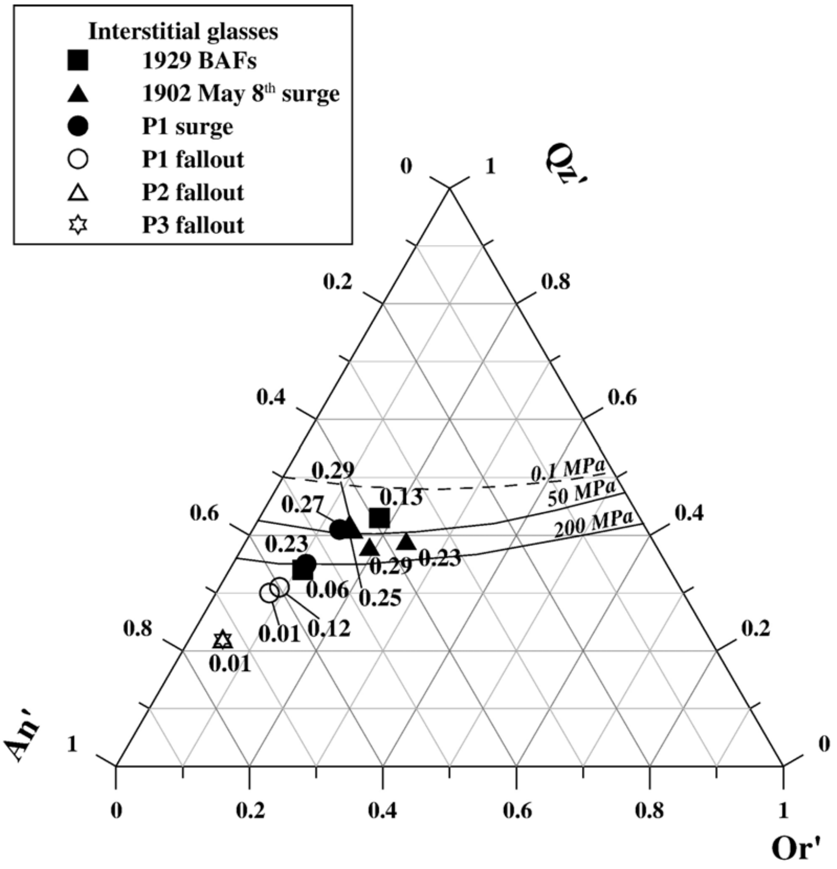

Fig. 9. Matrix glass compositions projected onto a Qz′–Ab′–Or′ ternary, corrected for the presence of normative anorthite (< 15 wt.%); uncertainties up to 2 wt.%; after Blundy and Cashman (2001); The cotectic lines are drawn for a haplogranite melt Qz$_{16}$Ab$_{75}$Or$_9$ at 0.1 MPa (extrapolated), 50, and 200 MPa (Blundy and Cashman, 2001). Point labels give the area fraction of the decompression-induced plagioclase microlites.

from major element melt compositions using the diagram of Blundy and Cashman (2001) do not provide precise enough information.

At low pressures, H_2O contents of the interstitial glasses are better information to estimate fragmentation or quenching pressures than the glass composition data, because degassing and specifically H_2O exsolution from melt is a fast process (Martel and Schmidt, 2003) that can rapidly reach equilibrium with decompression. The H_2O content data suggest that the P1 fallout could have fragmented at 20–40 MPa and the P2 fallout at 40–70 MPa, considering a fragmentation temperature of 875 °C (pre-eruptive temperature; Table 5). This corresponds to fragmentation depths of around 1.5 and 2.5 km for P1 and P2, respectively. However, although degassing is a fast process, there is still the possibility that the extremely fast ascent of plinian magmas prevents degassing completion, resulting in an overestimation of the quenching depth. For dome-forming eruptions during which magma ascents are relatively slow, the H_2O contents of the 1929 BAFs glasses suggest fragmentation or quenching pressures of 0–10 MPa, that is at depth below 450 m. The 1902 surges could have fragmented at pressure of 1–6 and 1–8 MPa for the May 8th and August 30th, respectively, that is between 50 and 400 m depth (Table 5). The heterogeneities in the H_2O contents of different samples from a given eruption may either represent variability in quenching depths or local degassing disequilibrium.

5.2.3. Ascent rates

Following the conclusions of Geschwind and Rutherford (1995) and Wolf and Eichelberger (1997), we think that the observed differences in the groundmass characteristics may be caused by differing rates of magma ascent and crystallization dynamics. The absence of decompression-induced microlites in most of the plinian pumices (Fig. 3) suggests an ascent rate that is too fast for magma crystallization. The delay for plagioclase nucleation has been experimentally determined between 1 and 5 h (Couch et al., 2003a; Larsen, 2005) suggesting that ascent of the plinian magma from the reservoir must have been completed within 5 h. This is in agreement with the P1 eruption duration of 1–3 h proposed by

Bardintzeff et al. (1989) based on grain-size and tephra volume considerations. The presence of a silica phase may also provide information on magma residence time and depth. The 1902 and 1929 eruptions, i.e. domes, BAFs and surges, contain a silica phase that was analyzed as cristobalite by Raman spectroscopy (Martel et al., 2000). A silica phase is also present in the phase equilibrium experiments starting with the rhyolite melt at 850 °C and pressures < 75 MPa (Martel et al., 2006). These experiment durations of 1 week suggest that the domes, 1929 BAFs, and 1902 surges spent at least few days at pressures below 75 MPa. In contrast, the P1 surge samples do not contain any precipitated silica, which would either suggest a fragmentation pressure above 75 MPa or an insufficient residence time at pressure < 75 MPa for silica to precipitate. The former hypothesis can be ruled out by the data published in Martel et al. (2000) that suggest 1.8 wt.% maximum H_2O in the glasses from P1 surge samples, corresponding to a maximum saturation pressure of 32 MPa. It is more likely that the residence time of P1 magma at low pressures was too short for silica precipitation.

5.2.4. Eruption schemes

There could be a link between the small and constant volume proportions of mafic magma intrusions (< 10 vol.%) deduced from the basalt-inherited microlite fractions and the small and constant volumes of the recent emitted products at Mt. Pelée (~0.1 km^3, dense-rock equivalent). If we assume the mafic intrusions triggered the eruptions, the groundmass modifications produced by the mafic magma mingling provide information on ascent dynamics.

In a general manner, the plinian magmas ascend within 1–5 h, which prevents any microlite crystallization before fragmentation at ~ 30–50 MPa. However, some parts of these plinian magmas, maybe along conduit borders, must have slowed down, permitting groundmass crystallization under a nucleated-dominated regime resulting in very small (S_n < 1 μm) dendritic microlites. One of these microlites (An_{41}, Fig. 3) corresponds to the equilibrium composition at 50 MPa or less (875 °C; Martel et al., 2006), in agreement with the fragmentation pressure inferred from glass H_2O contents. The magmas from the domes and the BAFs ascend more slowly than the plinian magmas, as revealed by the characteristics of their decompression-induced microlites, i.e., large, mostly tabular or skeletal in shape, with continuum compositions from An_{50} to An_{35}, and a growth-dominated crystallization regime under small undercoolings (slow decompression rates and crystallization at shallow depth). This agrees with the conclusion of Nakada and Motomura (1999) that lower groundmass cristallinity correlates to higher effusion rates, which may be explained by the sluggish crystallization kinetics at low pressures. The An_{35} microlites correspond to an equilibrium crystallization pressure of 10 MPa at 875 °C (Martel et al., 2006), which compares well with the pressures of 0–10 MPa deduced from the glass H_2O contents (Table 5). The 1929 and 1902 BAFs were followed by dome growths, in which the magma continues to crystallize and silica precipitates from the melt and/or precipitates from fluid percolations. The surface level of crystallization and degassing and the absence of volume constraints (conduit walls) and lithostatic pressure reduce the possibility of dome explosions. The surge magmas must have spent more time at shallow depth than the BAFs, because they crystallized acicular microlites in a nucleation-dominantly crystallization regime (although contribution of a growth regime), that is, at higher pressures or with slower decompression rates than in the BAFs case. This massive groundmass crystallization at shallow level drastically increases the magma viscosity that contributes to generate excess pressures following the self-sealing plug model (Sparks, 1997). The sudden release of this pressure must lead to a violent explosion, as for the surges in 1902 and supposedly P1, P3, and P4. However, the P1 surge samples contain anorthite-rich microlites ($An_{80–90}$) and no silica precipitations. This could suggest a faster ascent rate of the magma before fragmentation than for the 1902 surges, because there was no time for the small basalt-inherited microlites to re-equilibrate at more albitic compositions and for the silica to precipitate at low pressures. It is interesting to note that the P1 surge was followed by a plinian fallout, in contrast to the 1902 surges. A possible hypothesis for the occurrence of the plinian event is that in comparison to the 1902 surges, the proposed higher ascent rate of the P1 magma prior to the surge event possibly prevented significant volatile loss in the surrounding rocks. A further rapid decompression of these trapped volatiles could be particularly violent and capable of triggering a sustained plinian event. In contrast, it is possible that in 1902, the magma ascended more slowly, maybe also closer to the surface, so that the magma column following the surge events had time to degas and finally extruded as a dome.

The next step of the study would concern the precise determination of the ascent rates for the plinian and dome-forming magmas through timed decompression experiments aiming at reproducing the degassing and crystallization processes upon ascent (microlite morphologies and compositions, final porosities and H_2O contents), with the objective of better understand and predict the eruptive style of island-arc volcanism.

Acknowledgments

We greatly thank A. Genty for the scanning electron microscope images, O. Rouer for help with the electron microprobe, E. Deloule and M. Champenois for the ion probe analyzes, and R. Champallier for help with the experimental device. We also thank F. Costa and M. J. Rutherford for constructive reviews of the manuscript. The study was funded by two French national research programs on the Antilles volcanism: ACI Antilles (T. Druitt) and ANR EXPLANT (C. Martel).

References

Barclay, J., Carroll, M.R., Houghton, B.F., Wilson, C.J.N., 1996. Pre-eruptive volatile content and degassing history of an evolving peralkaline volcano. Journal of Volcanology and Geothermal Research 74, 75–87.

Bardintzeff, J.M., Miskovsky, J.C., Traineau, H., Westercamp, D., 1989. The recent pumice eruptions of Mt. Pelée volcano, Martinique. Part II: grain-size studies and modelling of the last plinian phase P1. Journal of Volcanology and Geothermal Research 38, 35–48 Mount Pelée Special Issue.

Blundy, J., Cashman, K.V., 2001. Ascent-driven crystallisation of dacite magmas at Mount St. Helens, 1980–1986. Contributions to Mineralogy and Petrology 140, 631–650.

Boudon, G., Lajoie, J., 1989. The 1902 pelean deposits in the Fort Cemetery of St. Pierre, Martinique: a mode for the accumulation of turbulent nuées ardentes. Journal of Volcanology and Geothermal Research 38, 113–130 Mount Pelée Special Issue.

Boudon, G., Bourdier, J.-L., Traineau, H., 1994. High-energy pyroclastic flows in the recent activity of Mt. Pelée, Martinique. IAVCEI Abstracts, International Volcanological Congress, Ankara, Turkey.

Bourdier, J.-L., Boudon, G., Gourgaud, A., 1989. Stratigraphy of the 1902 and 1929 nuée-ardente deposits, Mt. Pelée, Martinique. Journal of Volcanology and Geothermal Research 38, 77–96 Mount Pelée Special Issue.

Browne, B.L., Eichelberger, J.C., Patino, L.C., Vogel, T.A., Uto, K., Hoshizumi, H., 2006. Magma mingling as indicated by texture and Sr/Ba ratios of plagioclase phenocrysts from Unzen volcano, SW Japan. Journal of Volcanology and Geothermal Research 154, 103–116.

Burgisser, A., Gardner, J.E., 2005. Experimental constraints on degassing and permeability in volcanic conduit flow. Bulletin of Volcanology 67, 42–56.

Burnham, C.W., 1979. The importance of volatiles constituents. In: Yoder, H.S. (Ed.), The Evolution of Igneous Rocks. Princeton University press, Princeton, N.J, pp. 439–482.

Burnham, C.W., 1994. Development of the Burnham model for prediction of H_2O solubility in magmas. In: Carroll, M.R., Holloway, J.R. (Eds.), Volatiles in Magmas. Reviews in Mineralogical Society, American Mineralogy, vol. 30, pp. 123–129.

Cashman, K.V., 1992. Groundmass crystallization of Mount St. Helens dacite 1980–1986: a tool for interpreting shallow magmatic processes. Contributions to Mineralogy and Petrology 109, 431–449.

Cashman, K.V., Mangan, M.T., 1994. Physical aspects of magmatic degassing II. Constraints on vesiculation processes from textural studies of eruptive products. In: Carroll, M.R., Holloway, J.R. (Eds.), Volatiles in Magmas. Reviews in Mineralogical Society, American Mineralogy, vol. 30, pp. 446–478.

Charland, A., Lajoie, J., 1989. Characteristics of pyroclastic deposits at the margin of Fond Canonville, Martinique, and implications for the transport of the nuées ardentes of Mt. Pelée. Journal of Volcanology and Geothermal Research 38, 97–112 Mount Pelée Special Issue.

Couch, S., Sparks, R.S.J., Carroll, M.R., 2003a. The kinetics of degassing-induced crystallization at Soufrière Hills volcano, Montserrat. Journal of Petrology 44, 1477–1502.

Couch, S., Harford, C.L., Sparks, R.S.J., Carroll, M.R., 2003b. Experimental constraints on the conditions of formation of highly calcic plagioclase microlites at Soufrière Hills volcano, Montserrat. Journal of Petrology 44, 1455–1475.

Deloule, E., Paillat, O., Pichavant, M., Scaillet, B., 1995. Ion microprobe determination of water in silicate glasses: methods and applications. Chemical Geology 125, 19–28.

Devine, J.D., Gardner, J.E., Brack, H.P., Layne, G.D., Rutherford, M.J., 1995. Comparison of microanalytical methods for estimating H_2O contents of silicic volcanic glasses. American Mineralogist 80, 319–328.

Eichelberger, J.C., Carrigan, C.R., Westrich, H.R., Price, R.H., 1986. Non-explosive silicic volcanism. Nature 323, 598–602.

Eichelberger, J.C., Chertkoff, D.G., Dreher, S.T., Nye, C.J., 2000. Magmas in collision: rethinking chemical zonation in silicic magmas. Geology 28, 603–606.

Faure, F., Trolliard, G., Nicollet, C., Montel, J.-M., 2003. A developmental model of olivine morphology as a function of the cooling rate and the degree of undercooling. Contributions to Mineralogy and Petrology 145, 251–263.

Fichaut, M., Maury, R.C., Traineau, H., Westercamp, D., Joron, J.-L., Gourgaud, A., Coulon, C., 1989. Magmatology of Mt. Pelée (Martinique, F.W.I). III: Fractionnal crystallisation versus magma mixing. Journal of Volcanology and Geothermal Research 38, 189–213 Mount Pelée Special Issue.

Geschwind, C.H., Rutherford, M.J., 1995. Crystallization of microlites during magma ascent: the fluid mechanics of 1980–1986 eruptions of Mt. St. Helens. Bulletin of Volcanology 57, 356–370.

Gourgaud, A., Fichaut, M., Joron, J.-L., 1989. Magmatology of Mt. Pelée (Martinique, F.W.I.). I: Magma mixing and triggering of the 1902 and 1929 Pelean nuées ardentes. Journal of Volcanology and Geothermal Research 38, 143–169 Mount Pelée Special Issue.

Hammer, J.E., Rutherford, M.J., 2002. An exprimental study of the kinetics of decompression-induced crystallization in silicic melts. Journal of Geophysical Research 107, 1–23 ECV8.

Hammer, J.E., Cashman, K.V., Hoblitt, R.P., Newman, S., 1999. Degassing and microlite crystallization during pre-climactic events of the 1991 eruption of Mt Pinatubo, Philippines. Bulletin of Volcanology 60, 355–380.

Hammer, J.E., Cashman, K.V., Voight, B., 2000. Magmatic processes revealed by textural and compositional trends in Merapi dome lavas. Journal of Volcanology and Geothermal Research 100, 165–192.

Jaupart, C., Allègre, C.J., 1991. Gas content, eruption rate and instabilities of eruption regime in silicic volcanoes. Earth and Planetary Science Letters 102, 413–429.

Kirkpatrick, R.J., 1981. Kinetics of crystallization of igneous rocks. In: Lasaga, A., Kirkpatrick, R.J. (Eds.), Kinetics of geochemical processes. Mineralogical Society of America, Washington DC, pp. 321–397.

Klug, C., Cashman, K.V., 1996. Permeability development in vesiculating magmas: implications for fragmentation. Bulletin of Volcanology 58, 87–100.

Lacroix, A., 1904. La Montagne Pelée et ses éruptions. Masson Paris. 662 p.

Lajoie, J., Boudon, G., Bourdier, J.-L., 1989. Depositional mechanics of the 1902 pyroclastic nuée-ardente deposits of Mt. Pelée, Martinique. Journal of Volcanology and Geothermal Research 38, 131–142 Mount Pelée Special Issue.

Larsen, J.F., 2005. Experimental study of plagioclase rim growth around anorthite seed crystals in rhyodacitic melt. American Mineralogist 90, 417–427.

Launeau, P., Cruden, A.R., 1998. Magmatic fabric acquisition mechanisms in a syenite: results of a combined anisotropy of magnetic susceptibility and image analysis study. Journal of Geophysical Research 103, 5067–5089.

Launeau, P., Robin, P.Y., 1996. Fabric analysis using the intercept method. Tectonophysics 267, 91–119.

Liu, Y., Zhang, Y., Behrens, H., 2005. Solubility of H_2O in rhyolitic melts at low pressures and a new empirical model for mixed H_2O–CO_2 solubility in rhyolitic melts. Journal of Volcanology and Geothermal Research 143, 219–235.

Lofgren, G., 1974. An experimental study of plagioclase crystal morphology: isothermal crystallization. American Journal of Science 274, 243–273.

Lofgren, G., 1980. Experimental studies on the dynamic crystallization of silicate melts. In: Hargraves, R.B. (Ed.), Physics of magmatic processes. Princeton University Press, New York, pp. 487–565.

Martel, C., Schmidt, B.C., 2003. Decompression experiments as an insight into ascent rates of silicic magmas. Contributions to Mineralogy and Petrology 144, 397–415.

Martel, C., Pichavant, M., Bourdier, J.-L., Traineau, H., Holtz, F., Scaillet, B., 1998. Magma storage conditions and control of eruption regime in silicic volcanoes: experimental evidence from Mt. Pelée. Earth and Planetary Science Letters 156, 89–99.

Martel, C., Pichavant, M., Holtz, F., Scaillet, B., Bourdier, J.-L., Traineau, H., 1999. Effect of fO_2 and H_2O on andesite phase relations between 2 and 4 kbars. Journal of Geophysical Research 104, 29453–29470.

Martel, C., Bourdier, J.-L., Pichavant, M., Traineau, H., 2000. Textures, water content and degassing of silicic andesites from recent plinian and dome-forming eruptions at Mount Pelee volcano (Martinique, Lesser Antilles arc). Journal of Volcanology and Geothermal Research 96, 191–206.

Martel, C., Radadi Ali, A., Poussineau, S., Gourgaud, A., Pichavant, M., 2006. Basalt-inherited microlites in silicic magmas: evidence from Mt. Pelée (Martinique, F.W.I.). Geology 34, 905–908.

Morgan, D.J., Jerram, D.A., 2006. On estimating crystal shape for crystal size distribution analysis. Journal of Volcanology and Geothermal Research 154, 1–7.

Murphy, M.D., Sparks, R.S.J., Barclay, J., Carroll, M.R., Brewer, T.S., 2000. Remobilization of andesite magma by intrusion of mafic magma at Soufrière Hills volcano, Montserrat, West Indies. Journal of Petrology 41, 21–42.

Nakada, S., Motomura, Y., 1999. Petrology of the 1990–1995 eruption at Unzen: effusion pulsation and groundmass crystallization. Journal of Volcanology and Geothermal Research 89, 173–196 Unzen volcano Special issue.

Nakada, S., Motomura, Y., Shimizu, H., 1995. Manner of magma ascent at Unzen Volcano (Japan). Geophysical Research Letters 22 (5), 567–570.

Newman, S., Lowenstern, J.B., 2002. VOLATILECALC: a silicate melt-H_2O–CO_2 solution model written in Visual Basic for excel. Computers & Geosciences 28, 597–604.

Perret, F.A., 1935. The eruptions of Mt. Pelée 1929–1932, vol. 458. Carnegie Institute Publications, Washington. 126 p.

Pichavant, M., 1987. The effects of boron and water on liquidus phase relations in the haplogranite at 1 kbar. American Mineralogist 72, 1056–1070.

Pichavant, M., Martel, C., Bourdier, J.-L., Scaillet, B., 2002. Physical conditions, structure, and dynamics of a zoned magma chamber: Mount Pelée (Martinique, Lesser Antilles Arc). Journal of Geophysical Research 107 10.1029.

Smith, A.L., Roobol, M.J., 1990. Mount Pelée, Martinique, A study of an active island-arc volcano. Memoir - Geological Society of America 175. 105 p.

Sparks, R.S.J., 1997. Causes and consequences of pressurisation in lava dome eruptions. Earth and Planetary Science Letters 150, 177–189.

Traineau, H., Westercamp, D., Bardintzeff, J.M., Mikovsky, J.C., 1989a. The recent pumice eruptions of Mt. Pelée volcano, Martinique. Part I: Depositional sequences, description of pumiceous deposits. Journal of Volcanology and Geothermal Research 38, 17–33 Mount Pelée Special Issue.

Traineau, H., Westercamp, D., Benderitter, Y., 1989b. Case study of a volcanic geothermal system, Mount Pelée, Martinique. Journal of Volcanology and Geothermal Research 38, 17–33 Mount Pelée Special Issue.

Tsuchiyama, A., 1985. Dissolution kinetics of plagioclase in the melt of the system diopside–albite–anorthite, and the origin of dusty plagioclase in andesites. Contributions to Mineralogy and Petrology 89, 1–16.

Villemant, B., Boudon, G., 1998. Transition from dome-forming to plinian eruptive styles controlled by H_2O and Cl degassing. Nature 392, 65–69.

Villemant, B., Boudon, G., Komorowski, J.-C., 1996. U-series disequilibrium in arc magmas induced by water–magma interaction. Earth and Planetary Science Letters 140, 259–267.

Vincent, P.M., Bourdier, J.-L., Boudon, G., 1989. The primitive volcano of Mount Pelée: its construction and partial destruction by flank collapse. Journal of Volcanology and Geothermal Research 38, 1–16 Mount Pelée Special Issue.

Westercamp, D., Traineau, H., 1983. The past 5000 years of volcanic activity at Mt. Pelée, Martinique (F.W.I.): Implications for assessement of volcanic hazards. Journal of Volcanology and Geothermal Research 17, 159–185.

Wolf, K.J., Eichelberger, J.C., 1997. Syn-eruptive mixing, degassing, and crystallization at Redoubt Volcano, eruption of December, 1989 to May 1990. Journal of Volcanology and Geothermal Research 75, 19–37.

Woods, A.W., Koyaguchi, T., 1994. Transitions between explosive and effusive eruptions of silicic magmas. Nature 370, 641–644.

I.4b- Expériences de cristallisation par décompression

Article présenté: MARTEL C. & SCHMIDT B.C. (2003) Decompression experiments as an insight into ascent rates of silicic magmas. *Contrib. Mineral. Petrol. 144, 397-415.*

Financements : Programme "Visiting Scientists" du BGI, Bayreuth, Allemagne et du Programme Européen "IHP-Access to research Infrastructures" (D.C. Rubie).

L'analyse des microlites naturels permet de reconstituer des scénarios de remontée des magmas, avec des vitesses relatives entre les éruptions Pliniennes et à dôme, mais ne permet pas de déterminer quantitativement des vitesses d'ascension. L'objectif du projet présenté par l'article ci-dessous était d'obtenir expérimentalement des cinétiques de dégazage et de cristallisation pour les compositions rhyolitiques des verres interstitiels des magmas d'arc.

Les expériences ont été menées dans des autoclaves à chauffage externe et trempe rapide (BGI, Bayreuth) à partir du liquide interstitiel rhyolitique (75 pds SiO_2 ; Norme CIPW : $Qz_{36}Ab_{36}Or_{10}An_{13}Hy_4Ilm_1$) de l'andésite de Soufrière Hills, Montserrat (Arc des Petites Antilles, au Nord de la Guadeloupe). Une série d'expérience d'équilibre de phase (isobares) a été menées à la saturation en eau à 860°C pour des pressions de 1700 à 150 bars. Deux séries d'expériences de décompression à 860°C ont été réalisées avec des taux variant de 0.01 à 9600 bar/min : de 1500 à 500 bars et de 500 à 150 bars.

Les résultats suggèrent que le processus d'exsolution de l'eau n'a pas été achevé pour des vitesses de décompression > 1000 bar/min (ordre de quelques secondes), la teneur en eau dissoute dans le liquide étant supérieure à la solubilité de l'eau attendue à la pression finale. La croissance des bulles n'atteint pas l'équilibre lors de vitesse de décompressions > 1 bar/min (décompressions > 1 minute), la porosité mesurée étant inférieure à celle attendue à l'équilibre d'après Jaupart et Allègre (1991). Pour des taux de décompressions plus lents, la vésiculation (nucléation et croissance) des bulles est en processus qui a atteint son équilibre. Ces résultats expérimentaux peuvent être interprétés en termes de dynamique éruptive. Une explosivité du magma générée par l'exsolution massive des gaz dissous est peu probable, car le processus est très rapidement à l'équilibre, alors qu'une croissance rapide des bulles de gaz après un retard à la croissance généré par des vitesses de décompression > 1 bar/min peut se discuter en termes de source potentielle d'explosivité (voir § 1.5 Fragmentation magmatique).

La cristallisation de plagioclase (et orthopyroxène) est dominée par la nucléation (fortes densités numériques, petites tailles de cristaux) dans les séries décomprimées de 500 à 150 bars, en accord avec le taux maximum de nucléation du plagioclase < 250 bars suggéré par les expériences de Hammer et Rutherford (2002). Au contraire, la cristallisation est dominée par la croissance autour des cristaux existants dans les séries décomprimées de 1500 à 500 bars, en accord avec le taux maximum de croissance du plagioclase vers 1000 bars suggéré par Hammer et Rutherford (2002). Pour la série décomprimée de 500 à 150 bars, la croissance du plagioclase est probablement rendue difficile par la forte viscosité du liquide et la conséquente lente diffusion des éléments, conduisant à des proportions volumiques de plagioclase inférieures à celle attendue à l'équilibre. Cette étude montre également des retards à la nucléation de quelques heures pour l'orthopyroxène et des durées de ré-équilibration chimique de quelques jours pour les oxydes ferro-titanés à 500 bars, en accord avec les observations de Venezky et Rutherford (1999).

Cette étude a apporté un certain nombre d'information sur les processus de cristallisation (délai de nucléation, densité de nucléation, taille des cristaux, rééquilibration chimique) et demande à présent à être valorisée par une étude de cas, pour lequel des séries d'expériences choisies seraient directement comparées aux caractéristiques naturelles des microlites du système volcanique étudié, comme proposé dans les études suivantes sur la Montagne Pelée.

Contrib Mineral Petrol (2003) 144: 397–415
DOI 10.1007/s00410-002-0404-3

Caroline Martel · Burkhard C. Schmidt

Decompression experiments as an insight into ascent rates of silicic magmas

Received: 8 January 2002 / Accepted: 29 July 2002 / Published online: 14 September 2002

Abstract An experimental study of H_2O exsolution, bubble growth and microlite crystallisation during ascent (decompression) of silicic magmas in the volcanic conduit is presented. Isobaric and decompression experiments were performed on a rhyolitic melt at 860 °C, NNO + 1, H_2O saturation, and pressures between 15 and 170 MPa. Two sets of decompression experiments were performed, with decompression rates varying between 0.001 and 960 MPa/min: (1) from 150 to 50 MPa (high-pressure decompression), and (2) from 50 to 15 MPa (low-pressure decompression). The experiments highlight incomplete H_2O exsolution for decompression rates >100 MPa/min, incomplete bubble growth for decompression rates >0.1 MPa/min, crystal nucleation time lags, and incomplete chemical re-equilibration to final pressures. The observed crystallisation process, i.e. growth versus nucleation, depends on the decompression range. Indeed, decompression-induced crystallisation during high-pressure decompressions is dominated by growth of existing crystals, whereas during low-pressure decompressions crystal nucleation is the dominating process. This study provides a means to infer magma ascent rates in eruptions of silicic magmas through a combined petrologic and experimental approach.

Introduction

Most island arc volcanoes are characterised by an alternation of Plinian and dome-forming eruptions (Roobol and Smith 1976; Mullineaux and Crandell 1981; Newhall et al. 1996; Wolf and Eichelberger 1997; Young et al. 1998). In the case of a large-volume magma chamber, a Plinian event followed by dome growth may be explained by the volatile stratification of the magma chamber. In this case, the volatile-enriched magma layers at the top of the reservoir erupt as a Plinian column, and the underlying volatile-depleted magmas lead to dome growth. However, there is some evidence that Plinian events followed by dome-forming eruptions (and vice versa) can be produced from magmas with a similar pre-eruptive volatile content (Westrich et al 1988; Barclay et al. 1996; Martel et al. 1998). The causes for either eruption style are therefore acquired during magma ascent, and result from a competition between the eruption rate and the degassing process in the conduit system (Jaupart and Allègre 1991; Woods and Koyaguchi 1994). Indeed, Plinian magmas ascend rapidly, in the order of m/s (Pallister et al. 1992) up to possible supersonic speeds at the fragmentation depth (Wilson et al. 1980), whereas Plinian magmas ascend at rates below cm/s (Rutherford and Hill 1993; Siswowidjoyo et al. 1995; Nakada and Motomura 1995; Devine et al. 1998a). These contrasting magma ascent rates, in combination with the degree of permeability of both the magma and the surrounding rocks (Klug and Cashman 1996; Jaupart 1998), generate different degassing processes, i.e. close versus open degassing (Eichelberger et al. 1986; Stasiuk et al. 1996; Villemant and Boudon 1998, 1999).

Ascent rate is thus a crucial parameter which influences eruptive scenarios, and requires thorough investigation. Most of the proposed ascent rates are deduced from seismic data which, in the case of explosive eruptions, are sometimes difficult to acquire and to interpret. Magma ascent rates may also be determined by comparison of the petrology between natural and laboratory products obtained from decompression experiments (Rutherford and Hill 1993; Hammer and Rutherford 2002). Experiments may highlight disequilibrium mechanisms, such as time delays in bubble or crystal nucle-

C. Martel (✉) · B.C. Schmidt
Bayerisches Geoinstitut, 95440 Bayreuth, Germany
E-mail: cmartel@cnrs-orleans.fr
Tel.: +33-238-255252
Fax: +33-238-636488

Present address: C. Martel
ISTO-CNRS, 45071 Orléans, France

Editorial responsibility: J. Hoefs

ation or growth, which are key processes in the understanding of the eruptive styles. Real-time decompression experiments at conditions relevant to volcanic conduits aiming at reproducing the natural products constitute a powerful tool to study the syneruptive processes.

In order to study bubble growth processes and to determine the degree of volatile supersaturation in ascending magmas, theoretical studies (Proussevitch and Sahagian 1996, 1998) and dynamic simulations on analogue materials (Phillips et al. 1995; Hammer et al. 1998) or natural magmas (Gardner et al. 1999; Simakin et al. 1999, 2000; Mangan and Sisson 2000) have been conducted. Gardner et al. (1999) concluded that H_2O exsolves efficiently from silicic melts for decompression rates of ≤ 1.5 MPa/min. For faster decompression rates (up to 60 MPa/min), volatile exsolution is delayed and finally attains equilibrium when reaching low pressures (~80 MPa) due to the increasing porosity and bubble size.

As a response to decompression-driven H_2O exsolution, melts crystallise, providing there is sufficient time to overcome crystal nucleation time lags (Metrich and Rutherford 1998), which modifies the magma rheology and therefore may influence the eruption regime (e.g. Klug and Cashman 1994; Nakada and Motomura 1995; Hammer et al. 1999). For instance, Geschwind and Rutherford (1995) studied crystallisation through isothermal decompression experiments to investigate the growth of microlites and the changes in glass chemistry during magma ascent. They concluded ascent duration of 4–8 days for the post-18 May 1980 dacite of Mount St. Helens, USA. Cashman and Blundy (2000) and Blundy and Cashman (2001) have compiled the result of recent petrologic and experimental studies to illustrate the use of both glass chemistry and crystal textures to study ascent-driven and cooling-driven crystallisation, and have reinterpreted magma decompression histories (e.g. Mount St. Helens). Hammer and Rutherford (2002) have performed decompression-induced crystallisation experiments at low pressures to reproduce the natural microlite textures and to infer the crystallisation processes during the emplacement of the dacitic dome of Mount Pinatubo, Philippines. These authors conducted a set of single-step decompression runs (decompression duration < 4 min) and some multistep decompression runs at a constant average decompression rate of 0.02 MPa/min. Both sets were followed by equilibration duration periods ranging from 20 min to ~931 h at final pressure (5–220 MPa).

The present study is an experimental investigation of the kinetics of H_2O exsolution, bubble growth, and crystallisation in a rhyolitic melt, as a function of the decompression rate. The scope of this study is not to reproduce a given natural composition, but rather to provide a general understanding of the characteristics, chronology and kinetics of the decompression-induced degassing and crystallisation processes. This differs from the previous experimental works in the following respects: (1) we study the processes occurring during decompression, so that no equilibration period at constant pressure is observed after the decompression, (2) we simulate magma ascent through a large range of decompression rates (0.001 to 960 MPa/min), and (3) we investigate the relationship between H_2O exsolution plus bubble growth and crystallisation.

Experimental and analytical methods

Starting material

The starting material has a composition close to the most evolved melt inclusion found in the plagioclase phenocrysts of Soufriere Hills, Montserrat, andesite (sample MONT153 in Devine et al. 1998b). This rhyolitic composition may represent the interstitial melt in equilibrium with the phenocryst assemblage in the reservoir, prior to the input of the mafic magma in January 1996. The glass was prepared by mixing appropriate amounts of dry powders of Si, Al, Fe, Mg, Mn, and Ti oxides and Ca, Na, and K carbonates. This mixture was heated in a Pt crucible at 1 atm to 1,100 °C for 30 min to decompose the carbonates and was then melted at 1,600 °C. After 1 h, the crucible was removed from the furnace and put into water in order to quench the melt to a glass. For further homogenisation the glass was finely ground in an automatic agate mortar for 1 h. The melting and grinding procedure was then repeated twice to obtain a homogeneous starting glass powder. Microprobe analyses of this glass (called SHILL2) gave the following H_2O-free composition in wt%: SiO_2: 75.0, Al_2O_3: 13.6, Na_2O: 4.3, CaO: 2.5, FeO: 2.0, K_2O: 1.7, MgO: 0.4, TiO_2: 0.3, MnO: 0.2. Amounts of 20–50 mg glass powder and amounts of distilled H_2O sufficient to saturate the melt (Burnham 1994) were sealed into Au capsules (inner diameter 2.5 or 3 mm, 0.2-mm wall thickness) by arc welding. The sealed capsules were kept for at least 12 h at 150 °C in a drying oven to achieve a homogenous H_2O distribution prior to the experiments.

Experimental apparatus and strategy

Experimental apparatus

All experiments were performed in vertically operating, rapid-quench cold-seal pressure vessels which were inserted from the bottom into tube furnaces. The sample capsules were located in the hot, top part of the vessels, and they were kept in position by a filler rod which was held by an external magnet. The vessels were made of Nimonic 105 Ni–Cr superalloy and were pressurised with water. Temperatures were measured with NiCr–Ni thermocouples located in an external borehole of the autoclave. The sample temperatures were determined previously by calibration of the temperature difference between external (borehole) and internal (vessel) at pressure. The maximum error on temperature is ±10 °C. Pressures were measured using a pressure transducer calibrated against a Heise gauge and are accurate to ±3 MPa. The intrinsic redox conditions of the vessels were determined using Ni–Pd oxygen sensors (Taylor et al. 1992; Pownceby and O'Neill 1994) to be log $fO_2 = NNO + 0.7$ to $+1.3$. The difference in the redox conditions may be attributed to the different ages of the vessels. Quenching was close to isobaric and occurred within 1 to 2 s by dropping the sample capsule from the hot top of the vessel into the water-cooled part of the pressure seal by removing the magnet which held the filler rod and the sample capsule.

Experimental strategy

Two types of experiments were performed: isobaric runs to determine the phase relations at equilibrium at a given pressure, and decompression experiments to simulate magma ascent. The experimental conditions were chosen to reproduce the storage and ascent conditions of the rhyolitic interstitial melt of Soufriere Hills andesite. In 1996, the Soufriere Hills magma chamber was at 820–840 °C, rising to ~880 °C prior to the eruption due to the injection of a mafic magma (Devine et al. 1998b). The hydrostatic pressure was ~130 MPa, and the oxygen fugacity was ~NNO + 1 (Barclay et al. 1998). All experiments were performed at 860 °C (intermediate temperature), NNO + 1 (± 0.3), and H_2O saturation (except for three runs with H_2O activities (a_{H2O}) between 0.9 and 1).

The pressure conditions of the isobaric experiments range from 170 to 15 MPa, which cover depths from the reservoir to the dome. Experimental duration was usually 7 days but a few additional experiments were performed with various other duration periods. For the decompression experiments, initial and final pressures, and decompression rates were chosen to simulate magma ascent from the reservoir depth to the subsurface level at various ascent rates. We performed a first set of experiments consisting of decompressions from 150 to 50 MPa lasting between 15 days and 6 s, hereafter referred as to high-pressure (HP) decompressions. The second set of experiments was decompressed from 50 to 15 MPa in 30 days to 15 s, and is referred hereafter as to low-pressure (LP) decompressions. Both sets of decompression experiments consisted of two stages: an isobaric stage for 7 days at initial pressure to hydrate the melt and equilibrate the crystals (reproducing the isobaric runs), followed by a pressure release to final pressure which was obtained by manually bleeding off the pressure medium (H_2O) from the vessel. Experiments with decompression periods longer than 1 min were decompressed in steps of 5 MPa. Both isobaric and decompression runs were terminated by a rapid quench of less than 2 s. Due to rapid-quench failure, two experiments were isobarically quenched by removing the vessel from the furnace and cooling it with compressed air, while keeping the internal pressure constant. Only capsules whose weights were similar before and after the experiments (cf. no leaks occurred) were considered. The experimental conditions of the isobaric and decompression experiments are reported in Table 1.

Analytical methods

Half a capsule cut lengthways or pieces of the experimental product were embedded into epoxy resin and polished for analyses. The products were first observed by scanning electron microscopy (SEM, LEO Gemini 1530). Image analyses were performed on one to five SEM images per charge (areas of 0.01 to 0.34 mm^2) to determine the melt porosity, the morphology and size distribution of the bubbles, and the texture, volume proportion, size distribution, and number density of the crystals. The volume proportion of plagioclase was not precisely determined at pressures < 50 MPa due to the poor contrast on SEM images between dendritic plagioclases, glass and cristobalite exsolutions. Number densities were sometimes undeterminable for (1) orthopyroxene and Fe-Ti oxide because these crystals become indiscernible on SEM images when small, and (2) for the plagioclase with dendritic morphologies which prevent any demarcation of single crystals.

The crystals and glasses were analysed by electron microprobe (Cameca SX50) under conditions of 15-kV voltage, 6-nA

Table 1 Experimental conditions of the isobaric and decompression experiments (860 °C, NNO + 1)

Run No.	P_{ini} (MPa)	Duration at P_{ini} (day)	P_{fin} (MPa)	Undercooling[a] (°C)	ΔP duration	ΔP step	ΔP rate (MPa/min)
Isobaric runs							
170	170	7	170	–5	None	None	None
150	150	7	150	5	None	None	None
130	130	7	130	10	None	None	None
100	100	7	100	15	None	None	None
75	75	7	75	25	None	None	None
50	50	7	50	> 40	None	None	None
50C	50	7	50	> 40	None	None	None
25	25	7	25	> 100	None	None	None
15A	15	7	15	> 150	None	None	None
Isobaric test runs							
150A[b]	150	12	150	5	None	None	None
100A	100	7	100	15	None	None	None
100B	100	7	100	15	None	None	None
50A	50	7	50	> 40	None	None	None
50B	50	7	50	> 40	None	None	None
HP decompressions							
D5	150	7	50	5 to > 40	15 days	7 MPa/day	0.001
D3	150	7	50	5 to > 40	5 days	5 MPa/4 h	0.014
D4	150	7	50	5 to > 40	10 h	5 MPa/30 min	0.167
D1	150	7	50	5 to > 40	12 min	100 MPa/12 min	8.3
D11	150	7	50	5 to > 40	1 min	100 MPa/1 min	102
D12	150	7	52	5 to > 40	13 s	98 MPa/13 s	450
D18[b]	150	7	51	5 to > 40	13 s	99 MPa/13 s	456
D16[b]	150	7	54	5 to > 40	6 s	96 MPa/6 s	960
LP decompressions							
D15[c]	50	7	15	> 40 to > 150	30 days	5 MPa/4 days	0.001
D6	50	7	15	> 40 to > 150	15 days	5 MPa/2 days	0.002
D7[c]	50	7	15	> 40 to > 150	2 days	5 MPa/4 h	0.012
D8	50	7	15	> 40 to > 150	5 h	5 MPa/30 min	0.117
D10	50	7	15	> 40 to > 150	4 min	35 MPa/4 min	8.8
D9	50	7	15	> 40 to > 150	42 s	35 MPa/42 s	48
D14	50	7	18	> 40 to > 150	15 s	32 MPa/15 s	120
Decompression test runs							
T1	150	7	50	5 to > 40	10 h	7 days at P_{fin}	
T2	50	7	150	> 40 to > 150	10 h	7 days at P_{fin}	

[a] Estimations of the temperature difference between the plagioclase liquidus (see text) and the experiment (860 °C) for the given pressure (extrapolated for pressures ≤ 50 MPa)

[b] For H_2O-undersaturated runs at initial pressure: $0.9 < a_{H_2O} < 1$

[c] For experiments terminated by a slow, isobaric quench

current, 10-s counting time, a focused beam for crystals, and a defocused beam of ~5 μm diameter for the glasses. The compositions of the phases from the low-pressure products were sometimes impossible to obtain because the crystals were too small or hollow.

The H_2O content of the interstitial glasses was measured by infrared (IR) spectroscopy (Bruker IFS 120HR). Measurements were performed on doubly polished glass plates of 60–65 μm thickness, and the H_2O contents were calculated using the extinction coefficients of Zhang et al. (1997). IR spectroscopy could not be used for the products of the isobaric experiments performed at pressure $\leq$ 50 MPa due to their high crystallinity (glass areas $<$ 40 μm). We routinely measured H_2O contents by the "by-difference method" using the electron microprobe (Devine et al. 1995). This method is valid only when carefully calibrated with glass standards with chemical compositions and H_2O contents close to those of the analysed samples. In each microprobe session, we analysed hydrated rhyolitic standards whose H_2O contents were determined by Karl-Fischer titration (2.0, 4.6, and 6.3 ± 0.2 wt% H_2O; Martel et al. 2000) and the dry starting composition (SHILL2).

Results

Phase equilibrium

Isobaric experiments were performed at 860 °C, NNO + 1 ($\pm$0.3), H_2O saturation, and at pressures between 15 and 170 MPa in order to determine the phase assemblage and compositions (Table 2), proportions and number densities (Table 3) at equilibrium. Under these conditions, the phase assemblage of the SHILL2 composition is melt + Fe-Ti oxide ± plagioclase ± orthopyroxene (Fig. 1). The evolution of their chemistry with pressure is shown in Fig. 2.

Interstitial melts have SiO_2 contents ranging from 74.9 wt% at 170 MPa to 80.2 wt% at 50 MPa. At 50 MPa and below, the glass locally contains small cracks which demarcate exsolutions of cristobalite (determined by Raman spectroscopy), which consequently stabilises the melt SiO_2 content to 78–80 wt% down to 15 MPa (Fig. 2). The melt H_2O contents determined by both infrared spectroscopy (absorption coefficients of Zhang et al. 1997) and the "by-difference method" using the electron microprobe agree within an error of $\pm$0.4 wt% with H_2O solubilities calculated after Burnham (1994) for the composition of the interstitial melt of each charge (Fig. 3). This calculation gives H_2O solubilities decreasing from 5.0 wt% at 170 MPa to 1.7 wt% at 15 MPa (Table 2).

The liquidus phase at 170 MPa is a Fe-Ti oxide with a chemical composition in magnetite mol% (Mt) decreasing from Mt_{83} at 130 MPa to Mt_{59} at 25 MPa. For the products obtained at pressures above 130 MPa and below 25 MPa, the Fe-Ti oxide crystals were too small to be analysed by electron microprobe. Extrapolation of the compositions to 150 and 15 MPa would be Mt_{88} and Mt_{51} respectively (Fig. 2). Number density increases with decreasing pressure, from ~500/mm^2 at 150 MPa to ~7,000/mm^2 at 50 MPa (Table 3). Regardless of pressure, this oxide is characterised by diameters of 1–3 μm and proportions below 1 vol%.

Plagioclase appears at ~150 MPa. Its growth and crystal morphology characteristics depend on the degree of effective undercooling, i.e. the difference between the plagioclase liquidus temperature and the run temperature at a given pressure. With decreasing H_2O pressure, the plagioclase liquidus temperature increases (Tuttle and Bowen 1958; Westrich et al. 1988). To infer the plagioclase liquidus temperatures of our starting composition with decreasing pressure, we first assume that the plagioclase and melt liquidi are superimposed (Tuttle and Bowen 1958). The composition recalculated into a CIPW norm contains 11 mol% anorthite (An; Table 2), for which we know the plagioclase liquidus temperatures at 100 MPa (~870 °C, extrapolated, James and Hamilton 1969) and at ~160 MPa (860 °C, from our isobaric experiments). Data at lower pressures are missing from the literature. Therefore, we extrapolated the liquidus temperature at 50 MPa by using the results on the An-free haplogranite system at 100 MPa (770 °C, James and Hamilton 1969), 50 MPa (800 °C, Tuttle and Bowen 1958), and 0.1 MPa (~1,000 °C, Schairer and Bowen 1935). This would lead to a rough liquidus temperature of ~900 °C at 50 MPa, increasing strongly with decreasing pressure. The undercooling estimations are reported in Table 1.

The anorthite component (An, in mol%) of the plagioclases decreases linearly from An_{51} at 150 MPa to An_{36} at 50 MPa. A linear extrapolation to lower pressures would suggest an ~An_{31} plagioclase at 15 MPa. The volume proportions linearly increase from 1 vol% at 150 MPa to 20 vol% at 50 MPa. The expected proportions at 15 MPa (assuming a linear trend) would be ~37 vol% (Fig. 2). The morphology of the plagioclases gradually changes from 150 to 15 MPa. At 150 MPa, plagioclases display euhedral, tabular habits (Fig. 1a), a few being slightly hollow. At 100 and 75 MPa, plagioclases turn hollow and are elongated. At 50 MPa, they have skeletal elongated morphologies, so that it becomes difficult to define individual crystals (Fig. 1b). At 25 MPa, plagioclases have dendritic shapes (Fig. 1c). At 15 MPa, plagioclases form elongated clusters of parallel crystals, with outlines which are barely discernible from the melt + cristobalite matrix (Fig. 1d). Such crystal morphologies have been interpreted as depending on the degree of undercooling which modifies the diffusion rates of the melt components (Lofgren 1974; Fenn 1977; Muncill and Lasaga 1987, 1988). Increasing undercooling from $<$ 100 °C (pressures of 150 to 75 MPa) to 150–200 °C (pressures $\leq$ 50 MPa; Table 1) results in the change from tabular to dendrite morphologies (Lofgren 1974). The crystal sizes could only be determined in the charges from 150 to 50 MPa (Fig. 4), and we emphasise here that the results have to be taken more as indicative than absolute values, due to the small number of analyses permitted by the restricted size of the experimental charges. At 150 MPa, the crystal size is restricted to 10–40 μm in length. Assuming that plagioclases nucleated at the beginning of the experiment, were fully equilibrated at the quench time (after 7 days),

Table 2 Phase assemblages and compositions of the run products (860 °C, NNO + 1). Compositions in italics are linear extrapolations (see Fig. 2); *n.d.* not determined

Run No.	ΔP duration	Matrix								Plagioclase		Orthopyroxene		Fe-Ti oxide	
		Melt H_2O[a]			Porosity[b]	SiO_2[c]		CIPW norm							
		(wt%)			(vol%)	(wt%)				(An mol%)		(En mol%)		(Mt mol%)	
		Probe	IR	B94		X ± σ (*n*)	Range	Qz/Ab/Or/An	Qz′/Ab′/Or′[e]	X ± σ (*n*)	Range	X ± σ (*n*)	Range	X ± σ (*n*)	Range
Isobaric runs															
Shill2	None	0.4 ± 0.8(23)	n.d.	0.1	0	74.6 ± 0.3(23)	74.0–75.3	36/40/13/11	28/63/9	Absent	Absent	Absent	Absent	Absent	Absent
170	None	4.9 ± 0.4(7)	4.9 ± 0.6(6)	5.0	1 ± 1	74.9 ± 0.2(7)	74.6–75.1	42/44/14/14	28/64/8	Absent	Absent	Absent	Absent	*94*	n.d.
150	None	4.7 ± 0.4(5)	4.7 ± 0.2(5)	4.7	4 ± 1	75.1 ± 0.2(5)	75.0–75.4	45/42/13/9	35/55/10	51 ± 1(31)	49–53	Absent	Absent	*88*	n.d.
130	None	4.4 ± 0.7(8)	4.5 ± 0.5(4)	4.4	8 ± 1	76.5 ± 0.2(8)	76.2–76.8	47/41/12/10	35/56/9	48 ± 1(9)	46–50	Absent	Absent	83 ± 1(3)	83–84
100	None	3.6 ± 0.5(6)	4.0 ± 0.4(3)	3.9	13 ± 3	77.4 ± 0.3(6)	76.8–77.7	48/40/12/8	39/51/10	45 ± 1(6)	43–47	54 ± 1(8)	52–55	75	n.d.
75	None	3.1 ± 0.3(6)	3.8 ± 0.2(3)	3.4	13 ± 3	79.1 ± 0.2(6)	78.7–79.3	49/38/13/6	42/47/11	39 ± 1(7)	38–41	50 ± 1(2)	50–50	61 ± 2(2)	60–63
50	None	3.2 ± 0.5(9)	n.d.	2.9	35 ± 3	80.2 ± 0.2(9)[d]	79.9–80.6	50/35/15/4	45/41/14	36 ± 1(5)	34–37	*47*	n.d.	n.d.	n.d.
50C	None	2.4 ± 0.4(6)	n.d.	2.9	n.d.	79.9 ± 0.6(6)[d]	79.0–80.8	n.d.	n.d.	37 ± 1(4)	36–37	*47*	n.d.	64(1)	64
25	None	2.3 ± 0.5(5)	n.d.	2.1	41 ± 3	79.3 ± 0.2(6)[d]	79.2–79.8	44/32/24/2	42/35/23	32	n.d.	*44*	n.d.	59 ± 1(3)	57–60
15	None	1.8 ± 0.7(2)	n.d.	1.7	71 ± 3	78.7 ± 0.5(2)[d]	78.3–79.2	39/33/28/1	38/35/27	31	n.d.	*42*	n.d.	52	n.d.
Isobaric test runs															
150A[f]	12 days	4.6 + 0.3(6)	n.d.	4.7	3 ± 1	76.6 ± 0.3(6)	76.2–77.1	n.d.	n.d.	43 ± 1(3)	42–44	Absent	Absent	80(1)	80
100A	14 days	3.6 ± 0.4(7)	n.d.	3.9	n.d.	77.4 ± 0.2(7)	77.1–77.7	n.d.	n.d.	45 ± 1(7)	43–46	51 ± 1(8)	50–52	n.d.	n.d.
100B	3 days	3.5 ± 0.2(8)	n.d.	3.9	7 ± 1	77.3 ± 0.6(8)	76.9–78.8	n.d.	n.d.	44 ± 2(6)	42–48	51 ± 1(5)	50–53	65 ± 2(3)	63–68
50A	1 day	2.8 ± 0.3(6)	n.d.	2.9	29 ± 3	79.7 ± 0.6(6)	78.6–80.4	n.d.	n.d.	38 ± 1(2)	36–39	n.d.	n.d.	n.d.	n.d.
50B	2 days	2.1 ± 0.2(6)	n.d.	2.9	28 ± 3	78.9 ± 0.7(6)	78.3–80.0	n.d.	n.d.	37(1)	37	n.d.	n.d.	n.d.	n.d.
HP decompressions															
D5	15 days	2.6 ± 0.4(6)	n.d.	2.9	42 ± 3	79.1 ± 0.3(6)	78.5–79.3	48/37/14/5	42/46/12	45 ± 3(15)	40–49	47 ± 1(10)	45–50	64 ± 1(5)	62–66
D3	5 days	2.6 ± 0.4(8)	n.d.	2.9	n.d.	78.2 ± 0.6(8)	77.5–79.5	48/38/14/7	40/48/12	43 ± 3(24)	37–49	51 ± 2(14)	49–53	63 ± 1(3)	62–64
D4	10 h	2.3 ± 0.3(6)	n.d.	2.9	39 ± 3	76.2 ± 0.3(6)	75.8–76.6	45/42/13/11	33/58/9	47 ± 2(21)	44–51	Absent	Absent	85 ± 1(5)	84–86
D1	12 min	2.5 ± 0.3(8)	n.d.	2.9	29 ± 3	76.1 ± 0.2(8)	75.8–76.4	46/42/12/11	34/57/9	46 ± 2(12)	44–49	Absent	Absent	n.d.	n.d.
D11	1 min	2.5 ± 0.3(6)	n.d.	2.9	28 ± 3	76.4 ± 0.2(6)	76.2–76.8	46/40/14/11	34/56/10	47 ± 3(9)	44–51	Absent	Absent	82 ± 1(3)	82–83
D12	13 s	3.5 ± 0.6(11)	n.d.	2.9	30 ± 3	75.4 ± 0.2(11)	75.0–75.6	43/44/13/12	31/60/9	51 ± 1(5)	50–52	Absent	Absent	n.d.	n.d.
D18[f]	13 s	3.3 ± 0.8(7)	n.d.	2.9	25 ± 3	76.1 ± 0.3(7)	75.5–76.5	n.d.	n.d.	45 ± 1(4)	44–45	50 ± 1(5)	49–51	n.d.	n.d.
D16[f]	6 s	4.6 ± 0.7(6)	n.d.	2.9	21 ± 3	76.8 ± 0.3(6)	76.5–77.4	n.d.	n.d.	44 ± 2(7)	42–47	n.d.	n.d.	n.d.	n.d.
LP decompressions															
D15	30 days	1.6(1)	n.d.	1.7	n.d.	79.2(1)[d]	79.2	42/31/27/1	41/33/26	30(1)	30	44(1)	44	58 ± 3(5)	53–63
D6	15 days	1.2 ± 0.3(6)	n.d.	1.7	58 ± 3	80.3 ± 0.6(6)[d]	79.5–80.9	44/33/23/1	43/35/22	32 ± 2(19)	29–35	46 ± 1(2)	45–46	59 ± 2(4)	57–61
D7	2 days	1.3 ± 0.5(7)	n.d.	1.7	59 ± 3	80.3 ± 0.3(7)[d]	79.7–80.5	48/33/19/2	46/36/18	33 ± 2(4)	32–36	n.d.	n.d.	61 ± 3(3)	58–63
D8	5 h	1.2 ± 0.2(6)	n.d.	1.7	51 ± 3	80.0 ± 0.2(6)[d]	79.5–80.2	49/34/17/4	46/38/16	34 ± 1(5)	33–34	48(1)	48	71 ± 1(2)	70–72
D10	4 min	1.0 ± 0.2(5)	n.d.	1.7	51 ± 3	80.0 ± 0.3(5)[d]	79.5–80.3	51/33/16/4	46/39/15	36 ± 1(2)	35–36	n.d.	n.d.	n.d.	n.d.
D9	42 s	1.3 ± 0.2(6)	n.d.	1.7	47 ± 3	79.8 ± 0.3(6)[d]	79.5–80.3	48/35/16/4	44/41/15	36 ± 1(1)	36	n.d.	n.d.	n.d.	n.d.
D14	15 s	2.0 ± 0.1(6)	n.d.	1.7	49 ± 3	80.0 ± 0.2(6)[d]	79.8–80.2	48/35/16/4	43/42/15	35 ± 1(7)	35–38	n.d.	n.d.	n.d.	n.d.
Decompression test runs															
T1	10 h	2.4 ± 0.2(6)	n.d.	2.9	n.d.	79.6 ± 0.4(6)	79.0–80.1	n.d.	n.d.	45 ± 5(40)	34–51	47 ± 1(16)	46–51	64 ± 2(4)	62–67
T2	10 h	4.5 ± 0.6(6)	n.d.	4.7	n.d.	75.8 ± 0.2(5)	75.6–76.0	n.d.	n.d.	44 ± 5(6)	38–51	Absent	Absent	n.d.	n.d.

[a] H_2O content measured by the electron microprobe (probe; analytical error of ± 0.4 wt%), by infrared spectroscopy (IR; analytical error of ± 0.2 wt%) using the absorption coefficients of Zhang et al. (1997), and calculated after the model of Burnham (1994) for H_2O saturation (B94; estimated error of ± 0.2 wt%)

[b] Melt porosity (recalculated on a crystal-free basis). Errors of ± 3 and ± 8 vol% for the HP- and LP-decompression runs respectively

[c] Anhydrous SiO_2 content of the melt, X ± σ (*n*) for mean ± standard deviation (number of analyses)

[d] Presence of cristobalite

[e] CIPW norm recalculated after Blundy and Cashman (2001) for An-bearing compositions

[f] For H_2O-undersaturated runs at initial pressure $(0.9 < a_{H_2O} < 1)$

Table 3 Phase proportion and number density of the run products (860 °C, NNO + 1); *n.d.* Not determined

Run#	ΔP duration	Melt^a	Plagioclase^{a,b}		Orthopyroxene^b	Fe-Ti oxide^b
		(vol%)	(vol%)	(number/mm^2)	(number/mm^2)	(number/mm^2)
Isobaric runs						
170	None	100	Absent	Absent	Absent	467(1)
150	None	99	1	103 ± 28(4)	Absent	559 ± 16(3)
130	None	94	6	377 ± 20(3)	Absent	2,226 ± 390(4)
100	None	89	11	739 ± 102(2)	68 ± 23(2)	2,506 ± 470(2)
75	None	84	16	893 ± 499(5)	259 ± 127(4)	2,036(1)
50	None	80	20	1,248 ± 183(4)	724 ± 211(4)	6,571(1)
50C	None	n.d.	n.d.	1,196 ± 304(2)	n.d.	8,455(1)
25	None	∼71	∼29	n.d.	n.d.	n.d.
15	None	∼63	∼37	n.d.	n.d.	n.d.
Isobaric test runs						
100A	14 days	90	10	516 ± 207(4)	n.d.	n.d.
100B	3 days	89	12	814 ± 192(3)	34 ± 14(3)	592(1)
50A	1 day	87	13	1,812 ± 357(4)	n.d.	n.d.
50B	2 days	85	15	2,080(1)	n.d.	n.d.
HP decompressions						
D5	15 days	84	16	580 ± 170(2)	27 ± 7(2)	1,116 ± 285(2)
D3	5 days	82	18	590 ± 6(2)	152 ± 56(3)	1,902 ± 556(2)
D4	10 h	92	8	565 ± 68(2)	Absent	2,336(1)
D1	12 min	93	7	568(1)	Absent	494(1)
D11	1 min	90	10	574(1)	Absent	n.d.
D12	13 s	98	2	190(1)	Absent	555(1)
LP decompressions						
D15	30 days	n.d.	n.d.	n.d.	n.d.	n.d.
D6	15 days	79	21	3,500(1)	n.d.	n.d.
D7	2 days	75	25	n.d.	n.d.	n.d.
D8	5 h	75	25	3,001 ± 49(2)	n.d.	n.d.
D10	4 min	79	21	n.d.	4,728(1)	n.d.
D9	42 s	75	25	3,167(1)	1,278(1)	8,271(1)
D14	15 s	80	20	1,487(1)	545 ± 45(2)	7,301 ± 472(2)
Decompression test runs						
T1	10 h	n.d.	n.d.	663	n.d.	n.d.
T2	10 h	96	4	n.d.	Absent	n.d.

[a] Proportion in vol% recalculated on a bubble-free basis

[b] Number density per mm^2. The error for the determination of the plagioclase number densities is very variable, depending on the crystal morphology. It ranges from 10s/mm^2 for the tabular shapes to 100s/mm^2 for hollow plagioclases, and is not determinable for the dendritic morphologies

and grew from the centre to the rim, a minimum growth rate of 3.10^{-11} m/s can be estimated. At 100 and 75 MPa, crystals have the same main modes of length as for 150 MPa (10–40 μm), with an additional minor population with larger sizes (50–60 μm, up to 80 μm in length) and hollow cores. Because of these hollow cores, growth rates could not be calculated but they would be faster than 3.10^{-11} m/s, as the undercooling is higher (Swanson 1977). At 50 MPa, ∼70% of the plagioclases are 0–20 μm in length, partly overestimated in number by small pieces individualised because of the distorted crystal shapes. Number densities increase from ∼100/mm^2 at 150 MPa to ∼1,200/mm^2 at 50 MPa (Table 3). This illustrates that the higher the undercooling, the smaller the crystals and the higher the crystal density (Swanson 1977).

In runs conducted at 50–100 MPa, orthopyroxene crystallised with tabular shapes of ∼10 μm thickness (Fig. 1b) and with needle shapes of < 2 μm diameter (not analysable) below 50 MPa (Fig. 1c, d). The orthopyroxene proportion is always below 1 vol%, and its composition in enstatite mol% (En) decreases from En_{54} at 100 MPa to En_{50} at 75 MPa. The expected composition at 500 and 15 MPa, following a linear trend, would be ∼En_{47} and En_{42} respectively (Fig. 2). Number densities increase from ∼70/mm^2 at 100 MPa to ∼700/mm^2 at 50 MPa (Table 3).

A set of additional experiments was performed at 100 MPa to validate the attainment of the equilibrium after 7 days. All three experiments with duration periods of 3, 7, and 14 days gave similar phase assemblages and proportions, plagioclase and melt compositions, and H_2O contents. The only difference is the En-depleted composition of the orthopyroxene of the 3- and 14-day runs (En_{51} in #1000B and #1000A, compared to En_{54} in #1000; Table 2). This difference is thus not related to run duration but may be attributed to slight variations in the intrinsic oxygen fugacity of the vessels (depending on their age). Therefore, we conclude that run durations of 7 days are long enough to reach chemical equilibrium at pressures≥100 MPa. For pressures < 50 MPa, however, it is possible that equilibrium is not reached in 7 days, as discussed below.

A second set of runs was performed at 50 MPa for 1 and 2 days to investigate the crystallisation kinetics of the minerals. Plagioclase, orthopyroxene, and Fe-Ti oxide crystallised within 1 day, but in volume proportions lower than expected at equilibrium (13 and 15 vol% after 1 and 2 days respectively, in comparison

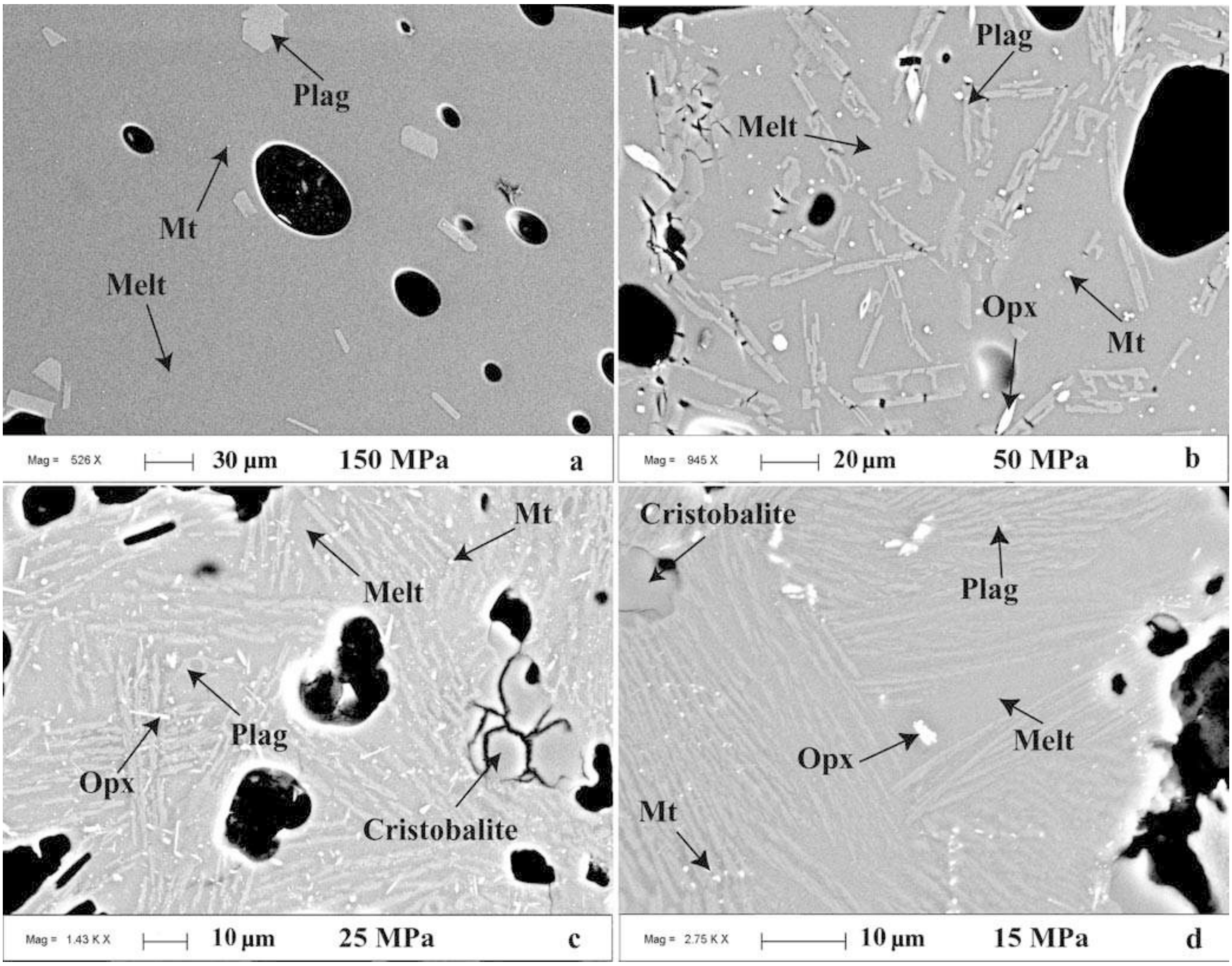

Fig. 1a–d SEM pictures of the isobaric runs (860 °C, NNO + 1, H_2O saturation, 7 days). **a** 150 MPa; **b** 50 MPa; **c** 25 MPa; **d** 15 MPa. Darkly shaded *areas* are bubbles

to 20 vol% after 7 days; Table 3). Orthopyroxene is present in form of non-analysable needles of less than 1-µm thickness.

Decompression experiments

SEM images of typical decompression run products are shown in Fig. 5. The phase assemblages and chemical compositions, and the melt porosities are presented in Table 2. The phase proportions and crystal number densities are reported in Table 3. Two HP-decompression experiments were slightly H_2O undersaturated ($0.9 < a_{H2O} < 1$) at initial pressure (#D18, #D16; Table 2) and have different phase assemblage and compositions than the H_2O-saturated charges. These runs are, however, rapidly decompressed (6 and 13 s) so that they have interest concerning H_2O exsolution kinetics. One H_2O-undersaturated isobaric run was performed at 150 MPa as a reference at equilibrium (Table 2). Therefore, we restrict the use of these products to melt H_2O content and porosity issues.

HP decompressions (150 to 50 MPa)

Melts have average anhydrous SiO_2 contents decreasing from 79.1 wt% for the 15-day decompression to 75.4 wt% for the 13-s decompression (Table 2; Fig. 6a). None of the melt contains visible cristobalite. Melt proportions linearly increase from 84 vol% when decompressed within 15 days to 98 vol% for the 13-s decompression (Table 3). The melt H_2O contents are ~2.5 wt% in the charges decompressed from 15 days to 1 min, increasing to ~4.6 wt% in the 6-s decompression run (Table 2; Fig. 6b). Melt porosities recalculated on a crystal-free basis have been determined. As shown by the isobaric products, some of the excess H_2O introduced with the glass powder in the capsule is trapped as bubbles in the viscous melt. Therefore, the porosities measured in the decompression products represent the amount of initial fluid plus the H_2O exsolved during

Fig. 2 Compositional evolution of the phases with pressure (860 °C, NNO + 1, H_2O saturation). *Open circles* are linear extrapolations. *Error bars* give the statistical errors of the measurements. *Point labels* denote the phase proportions measured in vol%

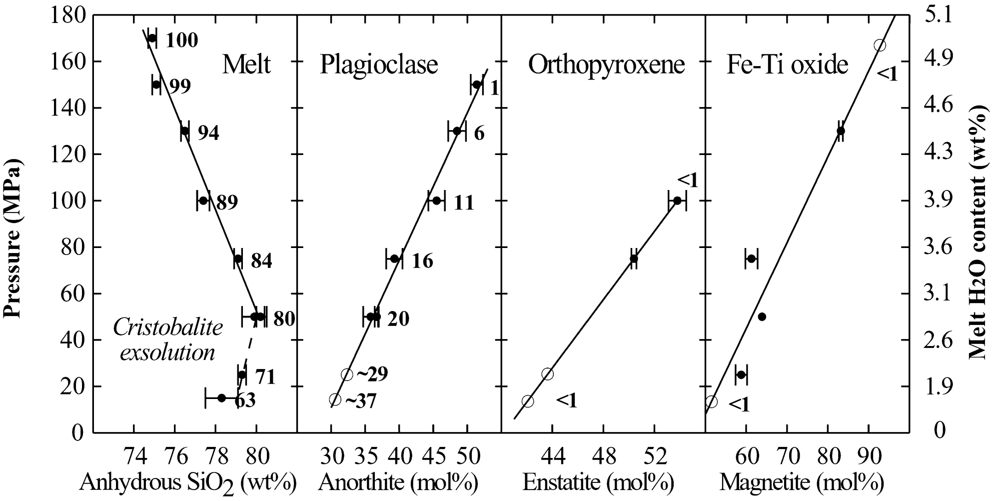

decompression. Up to 0.4 wt% H_2O in excess compared to the expected solubility at initial pressure have been introduced in the capsules, which corresponds to a maximum initial porosity of 3 and 8 vol% at 150 and 50 MPa respectively (calculated after Jaupart and Tait 1990, with a hydrated melt density of 2,300 kg/m^3 after Knoche et al. 1995, and H_2O density calculated after Saul and Wagner 1989). Melt porosities are presented in Fig. 6c. For the HP decompressions, the melt porosity represents ~40 vol% for the decompressions of 10 h and 15 days, and 20–30 vol% for decompression duration ≤ 12 min. The bubble size distributions are shown in Fig. 7a. For decompression duration shorter than 12 min, bubble radii represent a very narrow range from 0.5 to 25 μm, with more than 75% having radii < 5 μm. By contrast, bubbles have widely variable radii of 0.5 to 100 μm for decompression duration≥12 min.

Plagioclase belongs to the initial phase assemblage at 150 MPa (in volume proportion of ~1 vol%) and may be modified during decompression. The volume proportion of plagioclase increases from 2 vol% for the 13-s decompression to 16–18 vol% when decompressed in 5–15 days (Table 3; Fig. 8b). Plagioclase number densities are 190/mm^2 for the 13-s decompression and 565–590/mm^2 for the runs decompressed within 15 days to 1 min (Table 3; Fig. 8c). Regardless of the decompression rate, plagioclases have euhedral or slightly hollow tabular shapes, in agreement with growth at undercooling < 100 °C (Lofgren 1974). The main modes of the plagioclase length distributions are 10–40 μm, decreasing in frequency with increasing decompression duration. The scatter in crystal lengths increases from 10–40 μm for the charges decompressed within seconds to 10–90 μm for the 15-day decompression (Fig. 4). Plagioclases have average compositions decreasing from An_{51} for the charge decompressed in 13 s to An_{45} for the 15-day decompression (Fig. 8a). The analytical profiles suggest that during 5 to 15 days of decompression, plagioclases acquired a normal zoning with core compositions of $An_{44–50}$ and rims down to $An_{36–38}$ (Fig. 9a). Surprisingly, plagioclases tend to be inversely zoned for shorter decompressions, with core compositions of $An_{44–50}$ and rims of $An_{50–52}$ (Fig. 9b–d).

Orthopyroxene is unstable at 150 MPa but is expected to nucleate at ~100 MPa. This phase is only present in the charges decompressed in 15 and 5 days, with average compositions of En_{47} and En_{51} respectively (Table 2; Fig. 10a), and in proportions < 1 vol%. Analytical profiles in orthopyroxenes of the 5-day decompression run show zonings from En_{53} to En_{49} from core to rim. The number density of orthopyroxene is around

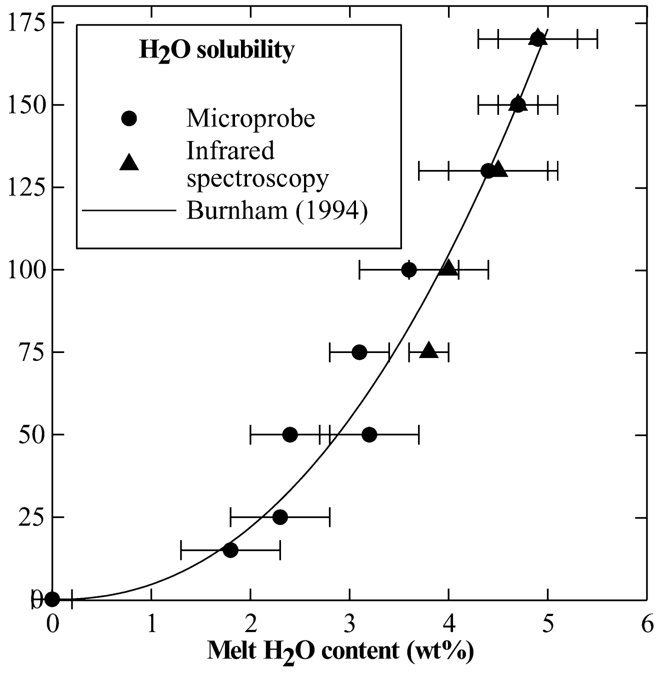

Fig. 3 H_2O solubility in the melt at 860 °C with pressure. *Error bars* give the statistical errors of the measurements (analytical errors of ±0.2 for the infrared spectroscopy, and ±0.4 for the microprobe)

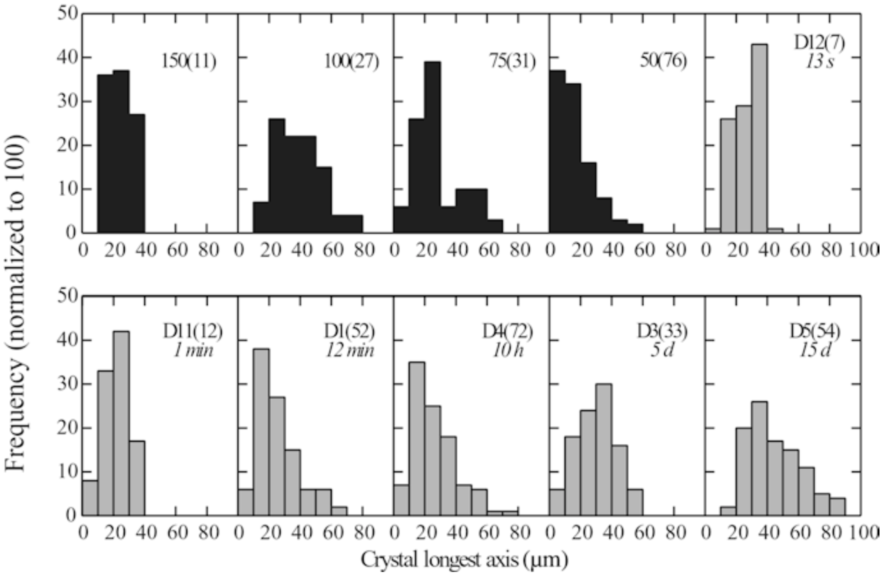

Fig. 4 Size distribution of the plagioclase crystals from the isobaric runs (150 to 50 MPa; *closed bars*) and HP-decompression runs (*shaded bars*). The *numbers* refer to the runs reported in the tables; values within brackets denote the numbers of crystals measured; values in italics denote the decompression duration

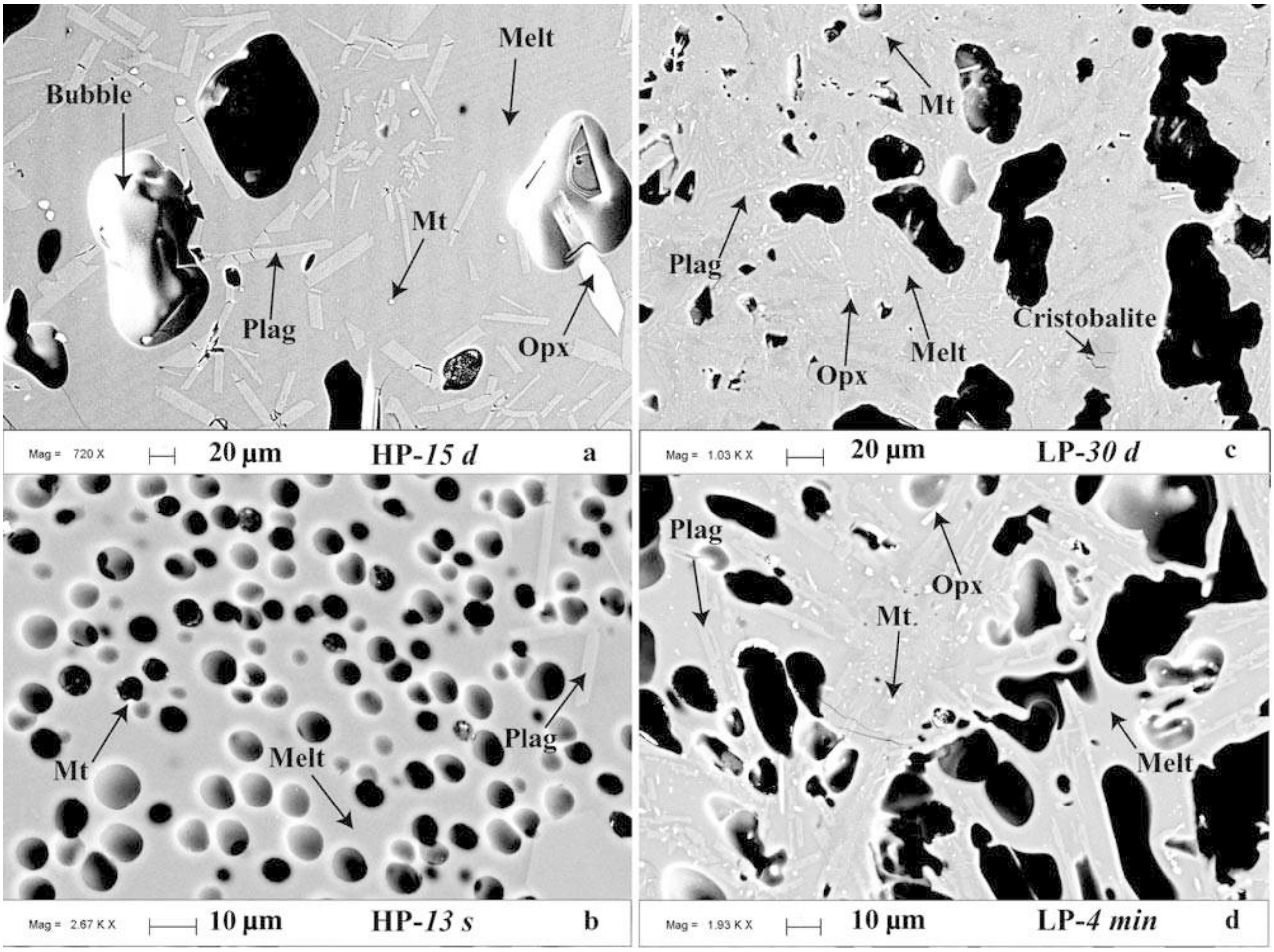

Fig. 5a–d SEM pictures of the decompression runs (860 °C, NNO + 1, H_2O saturation). **a** 150 to 50 MPa in 15 days (#D5); **b** 150 to 50 MPa in 13 s (#D12); **c** 50 to 15 MPa in 30 days (#D15); **d** 50 to 15 MPa in 4 min (#D10)

30–150/mm^2 in the 15- and 5-day decompression charges (Table 3; Fig. 10b).

Fe-Ti oxide is stable at 150 MPa, and is ubiquitous in the decompressed samples, always in proportion < 1 vol%. Fe-Ti oxides have compositions of $Mt_{63–64}$ in the charges decompressed within 5–15 days, and $Mt_{82–85}$ in

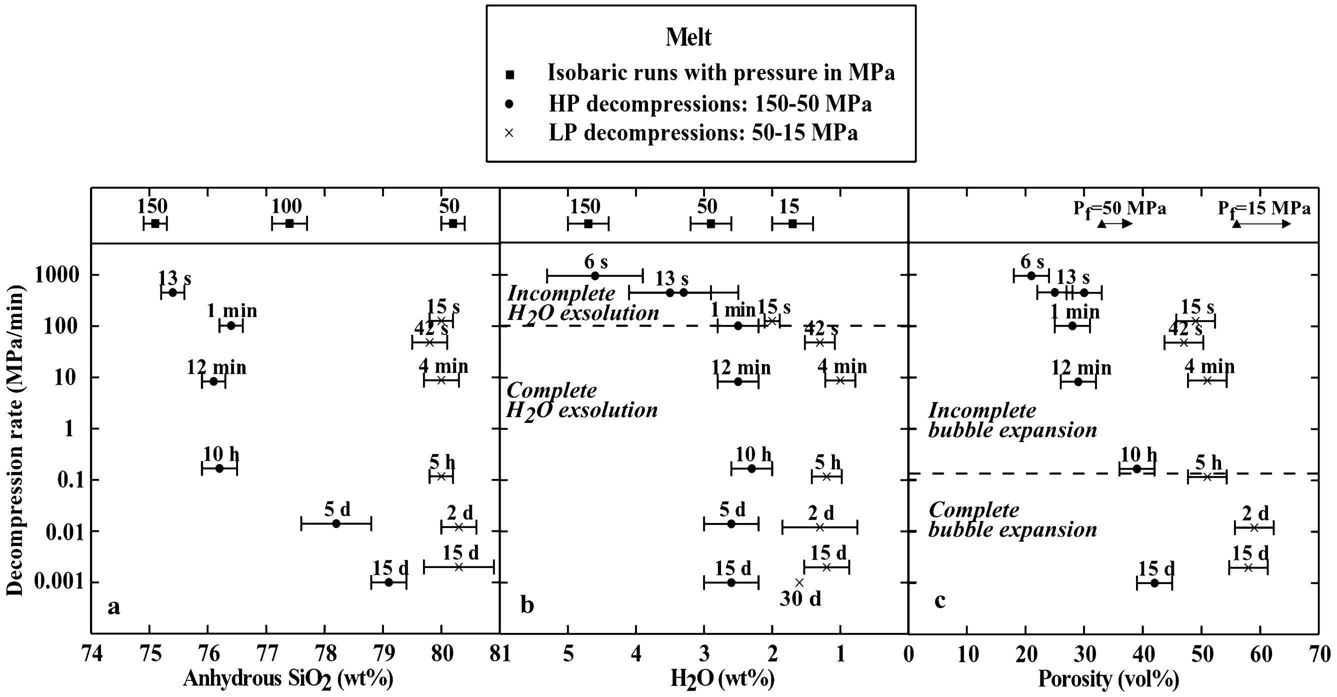

Fig. 6 Melt composition (**a**), H_2O content (**b**), and porosity (**c**) with decompression rate. Point *labels* represent the decompression duration. Error *bars* give the statistical errors of the measurements for **a** and **b** (analytical errors for the SiO_2 and H_2O contents are ± 2 and ± 0.4 wt% respectively), and the analytical error for **c**. In **c**, the *upper triangles* denote the porosity calculated for the indicated decompression range after Jaupart and Tait (1990; density of the hydrated melt of 2,300 g/m^3, Knoche et al. 1995, and H_2O density after Saul and Wagner 1989), and the *arrows* give the range of additional porosity due to initial trapped bubbles (see text)

the 1-min and 10-h decompression runs (Table 2; Fig. 10c). The number density of Fe-Ti oxide is ~2,000/mm^2 for decompression duration between 15 days and 10 h, and ~500/mm^2 when decompressed within 12 min or less (Table 3; Fig. 10d).

We performed a test experiment (#T1) consisting of 7 days at 150 MPa followed by a decompression within 10 h to 50 MPa, and then a second isobaric stage for 7 days before quenching (Table 1). The aim was to look at the effects of an equilibration period following decompression (to compare with the #D4 product decompressed in 10 h, then quenched). In the #T1 charge, the phase assemblage is Fe-Ti oxide (Mt_{64}), plagioclase (An_{45}), and orthopyroxene (En_{47}) in a melt with 79.6 wt% SiO_2 and 2.4 wt% H_2O (Table 2). Surprisingly, no cristobalite was found in the melt, although present in the isobaric run of 7 days at 50 MPa. Plagioclases are strongly normally zoned, with core compositions of ~$An_{46\text{–}48}$ which abruptly decrease to ~$An_{34\text{–}36}$ at the rims (Fig. 9b).

LP decompressions (50 to 15 MPa)

Melts display a constant anhydrous SiO_2 contents of 79–80 wt% (Fig. 6a) in proportions ranging from 75 to 80 vol% (Table 3). All charges contain cristobalite exsolutions, in proportions (not determinable) increasing with the duration of the experiment. The melt H_2O contents of the samples decompressed within 30 days to 42 s range between 1.0 and 1.6 wt%, increasing to 2.0 wt% for the 15-s decompression product. The melt porosities of the LP-decompression products are ~50 vol% for the decompressions up to 5 h, and ~60 vol% for longer duration periods (error of ± 3 vol%; Fig. 6c). The bubble radii cover a range of 0.1–100 µm, with a majority at ≤ 20 µm. For decompression duration of ≥5 h, bubbles with radii ≤ 10 µm represent less than 60% of the total number, whereas the value is ~80% for shorter decompressions (Fig. 7b).

Plagioclase accounts for ~20 vol% in the isobaric 50 MPa charge, and it represents 20–25 vol% in the decompressed charges (Fig. 8b). The crystals have hardly discernible outlines, are very elongated (up to 100 µm long, 2–5 µm thick), hollow/skeletal when decompressed in 15 s to 4 min, and skeletal/dendritic for longer decompression duration (Fig. 5c, d), reflecting growth at undercooling of 150–200 °C (Lofgren 1974). The skeletal/dentritic crystal morphology makes it impossible to obtain numerous punctual analyses and analytical profiles, and prevents the determination of size distributions by image analysis. Plagioclases have average compositions increasing from An_{30} in charges decompressed in 30 days to An_{36} when decompressed in 15 s (Table 2; Fig. 8a). The four analytical profiles measured in 10- to 40-µm-long plagioclases of the charge decompressed within 15 days do not display any particular zoning (random variations of maximal ± 3 An mol%). Plagioclase number densities are ~1,500/mm^2 in the 15-s decompression run, and 3,000–3,500/mm^2 in the

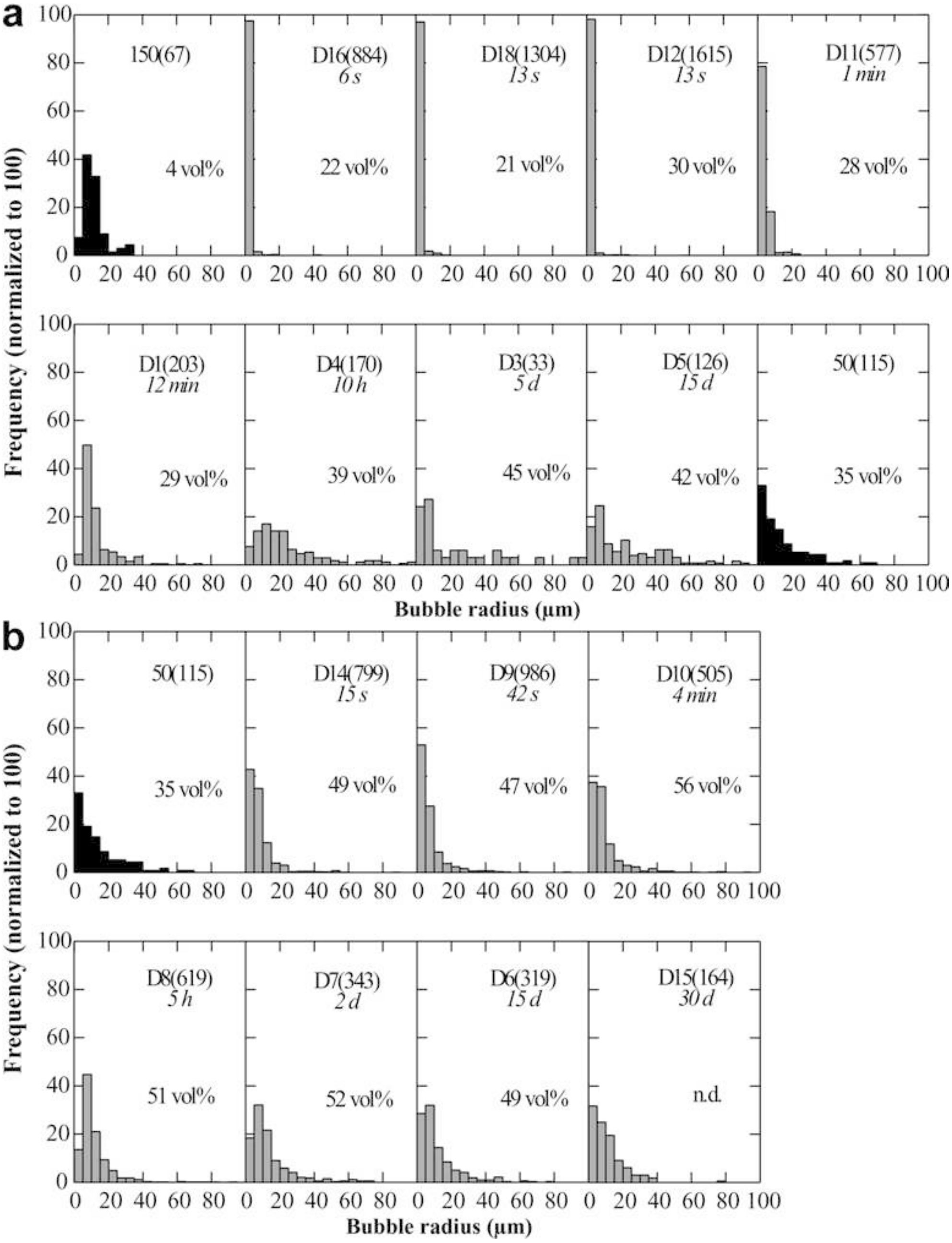

Fig. 7a, b Bubble size distribution (values within brackets denote the number of bubbles measured; values in italics are the decompression duration; melt porosity is in vol%). **a** Isobaric run at 150 and 50 MPa (*closed bars*) and HP decompressions (*shaded bars*). **b** Isobaric run at 50 MPa (*closed bars*) and LP decompressions (*shaded bars*)

charges decompressed within 15 days to 42 s (Table 3; Fig. 8c).

Orthopyroxene accounts for volume proportions < 1 vol% in the isobaric 50 MPa charge as well as in the decompression runs. The crystals are often too small for analysis. The compositions range between En_{44} and En_{48} for decompression duration between 30 days and 5 h (Fig. 10a). The number density of orthopyroxene could be determined only for the decompression duration of ≤ 4 min, decreasing from ~4,728/mm^2 for the 4-min decompression to ~545/mm^2 for the 15-s decompression run (Table 3; Fig. 10b).

Fe-Ti oxide is ubiquitous in the charges, with composition increasing from Mt_{58} to Mt_{71} for decompression duration of 30 days and 5 h respectively (Fig. 10c). The number density of Fe-Ti oxide was determined only in the 42-s and 15-s decompression runs, giving ~8,271 and 7,301/mm^2 respectively (Fig. 10d).

We performed a reversal test (#T2) consisting of 7 days at 50 MPa, followed by 10-h pressurisation to 150 MPa and a subsequent isobaric stage of 7 days before the rapid quench. The assemblage comprises Fe-Ti oxide, one residual orthopyroxene (too small for analysis), and plagioclase (< 10 µm in size, representing 4 vol%) with compositions varying between $An_{38.4}$ and $An_{50.8}$ in a homogeneous 75.8 wt% SiO_2 melt containing 4.5 ± 0.6 wt% H_2O. Except for the composition and H_2O content of the melt, the phase assemblage and

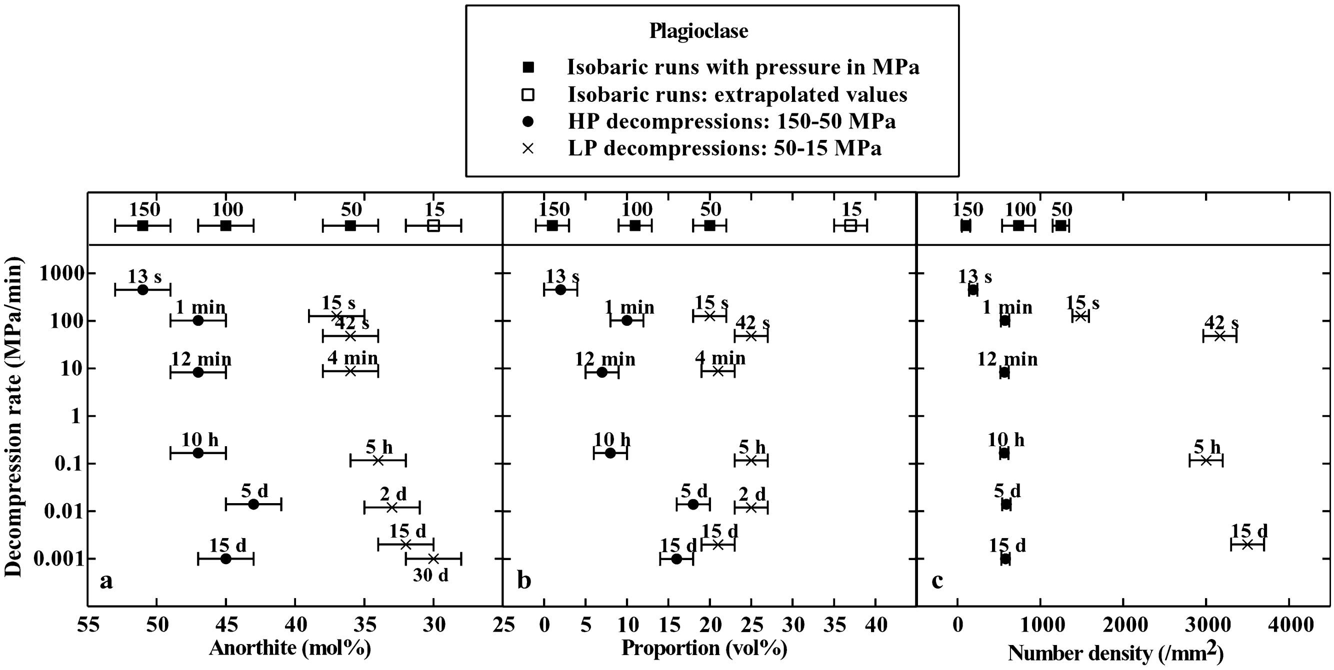

Fig. 8 Plagioclase composition (**a**), volume proportion (**b**), and number density (**c**) with decompression rate. Point *labels* represent the decompression duration. *Error bars* give the analytical errors of the measurements: ±2 mol% for **a**, ±2 vol% for **b**, and ±50, ±100, and ±200 for **c**, as explained in Table 3

compositions are different from the phase equilibrium at 150 MPa (Table 2). This discrepancy between the reversal and the forward experiment may reflect the non-attainment of equilibrium during the forward experiment at 50 MPa, as also proposed below. Nevertheless, compositional discrepancies between reversal and forward experiments cannot be taken as a definite proof for disequilibrium, as re-equilibration kinetics during crystallisation and crystal dissolution are different.

Discussion

To accommodate the decompression-induced perturbations of the phase relations, volatiles exsolve from the melts, forming and growing bubbles, while crystals nucleate, grow, and chemically equilibrate, provided that the kinetics of exsolution, growth, and re-equilibration exceed the imposed decompression duration.

Kinetics of H_2O exsolution and bubble growth

The exsolution process can be estimated from the difference between the melt H_2O content at initial and final pressure. If equilibrium prevails during decompression, the H_2O content measured in the melt matches the H_2O solubility at final pressure. If the measured H_2O content is greater than the expected solubility, the exsolution process is incomplete and the melt is H_2O supersaturated. Similarly, bubble growth in response to H_2O exsolution may be completed or not, depending on the melt rheology and the available decompression duration. If the measured melt porosity is lower than the calculated porosity at equilibrium, bubble growth is incomplete. The main consequence of a non-achievement of these processes upon decompression is the possible magma explosivity by sudden release of the excess H_2O and rapid expansion of the bubbles.

H_2O exsolution

For decompression rates < 100 MPa/min (decompression duration longer than 42 s and 1 min in the LP and HP runs), melt H_2O contents are constant, i.e. 2.5 ± 0.4 and 1.3 ± 0.5 wt% for the HP and LP decompressions respectively. These values agree within error with the 2.9 ± 0.4 and 1.7 ± 0.4 wt% H_2O expected at final pressure, i.e. 50 and 15 MPa respectively (despite a surprising 0.4 wt% difference). This suggests that H_2O exsolution from melts with viscosities up to ~10^8 Pa s (calculated after Shaw 1972) is an efficient process for these decompression rates.

For decompression rates > 100 MPa/min, however, the measured melt H_2O content is greater than the expected H_2O solubility at final pressure, with values increasing with decompression rate (Fig. 6b). This demonstrates that H_2O exsolution was not achieved. The large statistical errors around the H_2O contents of the HP decompressions > 100 MPa/min reflect heterogeneities and various advancement of the H_2O-exsolution process within the sample. We emphasise that, for both HP and LP decompressions, H_2O exsolution is a very fast process, completed within ~1 min. Therefore, most of the crystallisation probably occurs after exsolution is achieved.

Fig. 9a–d Analytical profiles of plagioclases from the HP-decompression experiments. The *0*-µm distance represents the geometrical centre of the crystal. **a** #D3; the upper curves (*closed squares*) represent profiles performed in plagioclases from the isobaric run at 150 MPa, and the *lower bar* gives the compositional range of the plagioclases from the isobaric run at 50 MPa. **b** #D4 and #T1 which is decompressed from 150 MPa in 10 h before an isobaric step of 7 days at 50 MPa. **c** #D11. **d** #D12

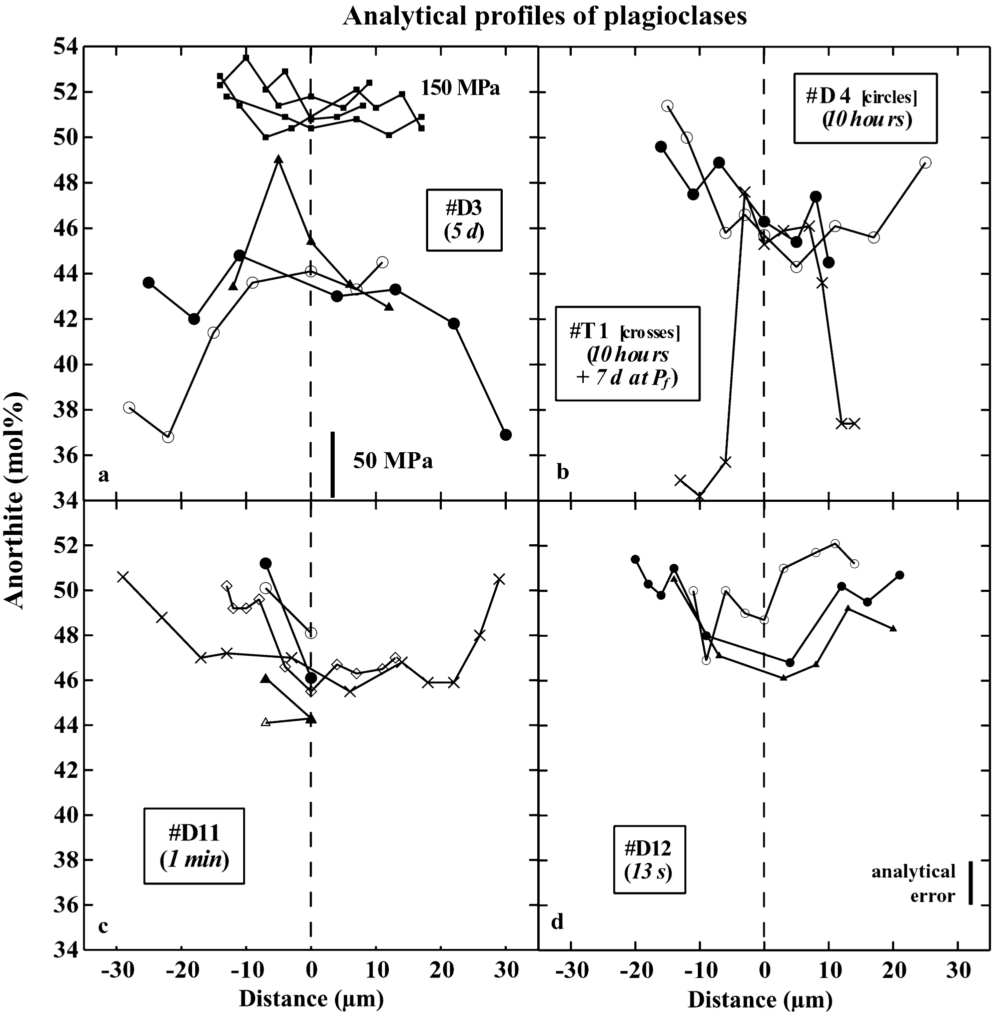

Bubble growth

The melt porosity of both HP- and LP-decompression products increases with decreasing decompression rate (Fig. 6c). For decompression rates < 0.1 MPa/min, the melt porosities of the products are in agreement within error with the calculated porosities at equilibrium, so that bubble expansion is probably achieved. For decompression rates between and 0.1 and 100 MPa/min, the melt porosities are lower than the calculated ones at equilibrium, whereas H_2O exsolution from the melt is complete (Fig. 6b, c). Therefore, in this range of decompression rates and despite exsolution completion, bubble growth in melts with viscosities up to $\sim 10^8$ Pa s (Shaw 1972) did not reach equilibrium, and bubbles were probably supersaturated in H_2O vapour when quenched at final pressure. This is one order of magnitude slower than the theoretical prediction of Proussevitch and Sahagian (1996, 1998) that bubbles in rhyolitic melts cannot grow fast enough to remain in equilibrium when ascent rates exceed 1 m/s (> 2 MPa/min). This is also one order of magnitude slower than the experimental results of Gardner et al. (1999) who concluded that bubble growth is incomplete for decompression rates≥1.5 MPa/min. These authors found that equilibrium may be approached for faster decompression rates when decompressed to low final pressures, putting forward that supersaturation is significantly reduced when porosities exceed ~10 vol% and decompression bubbles reach 5- to 10-µm diameter. For decompression rates > 100 MPa/min, both H_2O exsolution and bubble growth are not completed processes.

The bubble size distributions vary with the decompression rate (Fig. 7a, b). For both sets of decompression range, decompression rates > 10 MPa/min (duration < 5 min) generate a narrow main mode of bubbles with radii of 0–5 µm. For slower decompression rates, the main mode of the distribution becomes 5–10 µm, and populations of large bubbles with radii up to 100 µm are also present. These large bubbles may result from coalescence. The bubble size distributions also vary with the decompression range (Fig. 7a, b). For decompression rates > 10 MPa/min, the population of bubbles with radii of 0–5 µm represents more than 75% of the HP-decompression bubble number, the value being 45–55% for the LP-decompression bubbles. Such a large

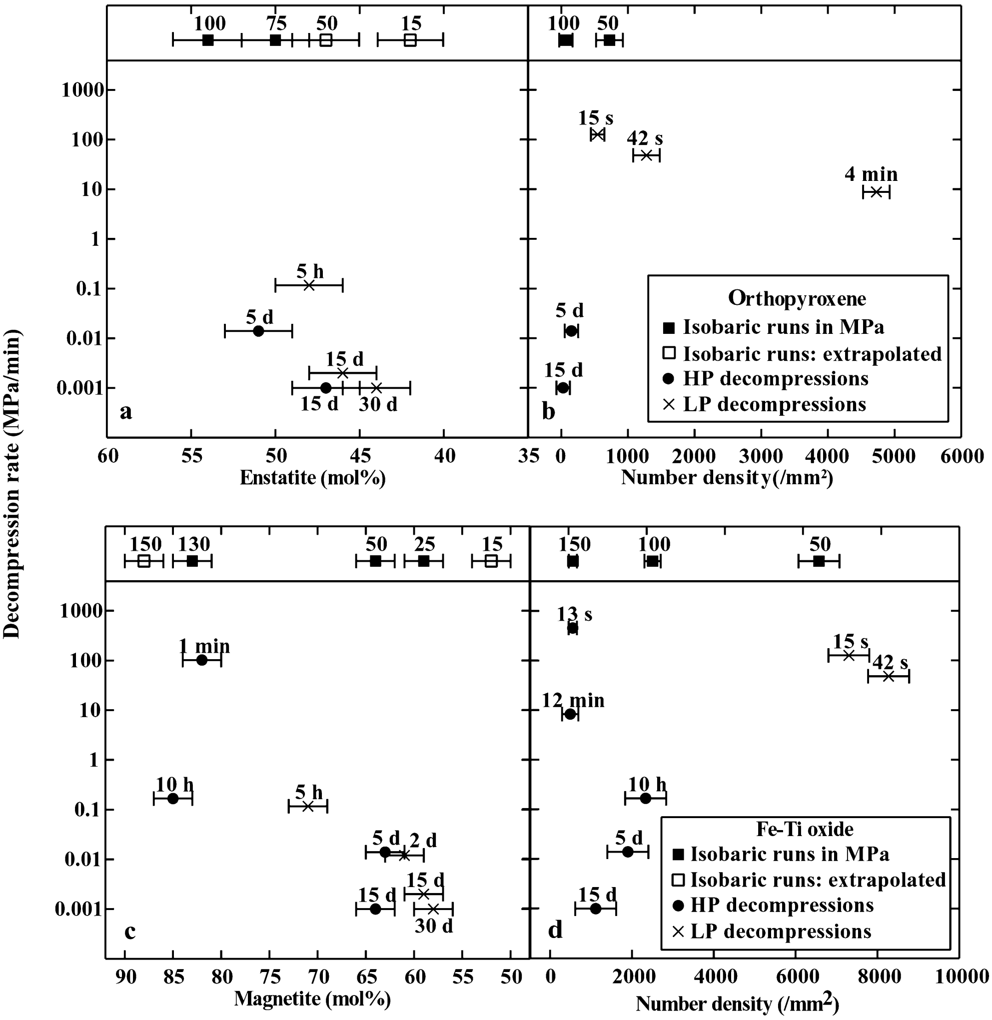

Fig. 10 Composition and number density of the orthopyroxene (**a**, **b**) and of the Fe-Ti oxide (**c**, **d**) with decompression rate. Point *labels* are the decompression duration. Error *bars* give the analytical errors of the measurements: ±2 mol% for **a** and **c**, and ±50, ±100, and ±200 for **b** and **d**

number of small bubbles in HP decompressions is favoured by high pressures, as suggested by Gardner et al. (1999).

Bubble morphology gives information on the crystallisation proportion. In the products of the LP and HP decompressions and isobaric runs, in which crystal contents are <15 vol%, bubbles are round (Fig. 5b). Crystals growing in proportions >15 vol% distort the bubble outlines (Fig. 5c, d).

Crystallisation process and kinetics

Decompression-induced crystallisation may occur in disequilibrium, depending on the kinetic barriers which resist crystallisation (i.e. melt viscosity), and on the decompression path (initial and final pressures, decompression rate) which defines the degree of undercooling or supersaturation. The undercooling influences the crystal characteristics (volume proportion, number density, size, morphology) and controls the crystallisation process, i.e. growth versus nucleation. Below, we compare the liquid-composition path and the crystallisation kinetics for both decompression sets.

Liquid-composition path

The normative compositions of the residual melts from the isobaric and decompression runs (Table 2) have been projected onto a haplogranite quartz(Qz)–albite(Ab)–orthoclase(Or) system (Blundy and Cashman 2001) in order to estimate the evolution of the melt composition with decompression (Tuttle and Bowen 1958; Cashman and Blundy 2000). We remind here that this projection was originally designed for a H_2O-saturated $Qz_{16}Ab_{75}Or_9$ starting composition (corundum <1 wt%, Cashman and Blundy 2000), whereas our $Qz_{41}Ab_{45}Or_{14}$ starting rhyolite (SHILL2) is significantly more silicic and contains several other components (e.g. An up to 15 wt%, hypersthene up to 5 wt%, and less than 1 wt% corundum, ilmenite and diopside). We recalculated the normative components for An-bearing systems following the empirical solutions proposed by Blundy and

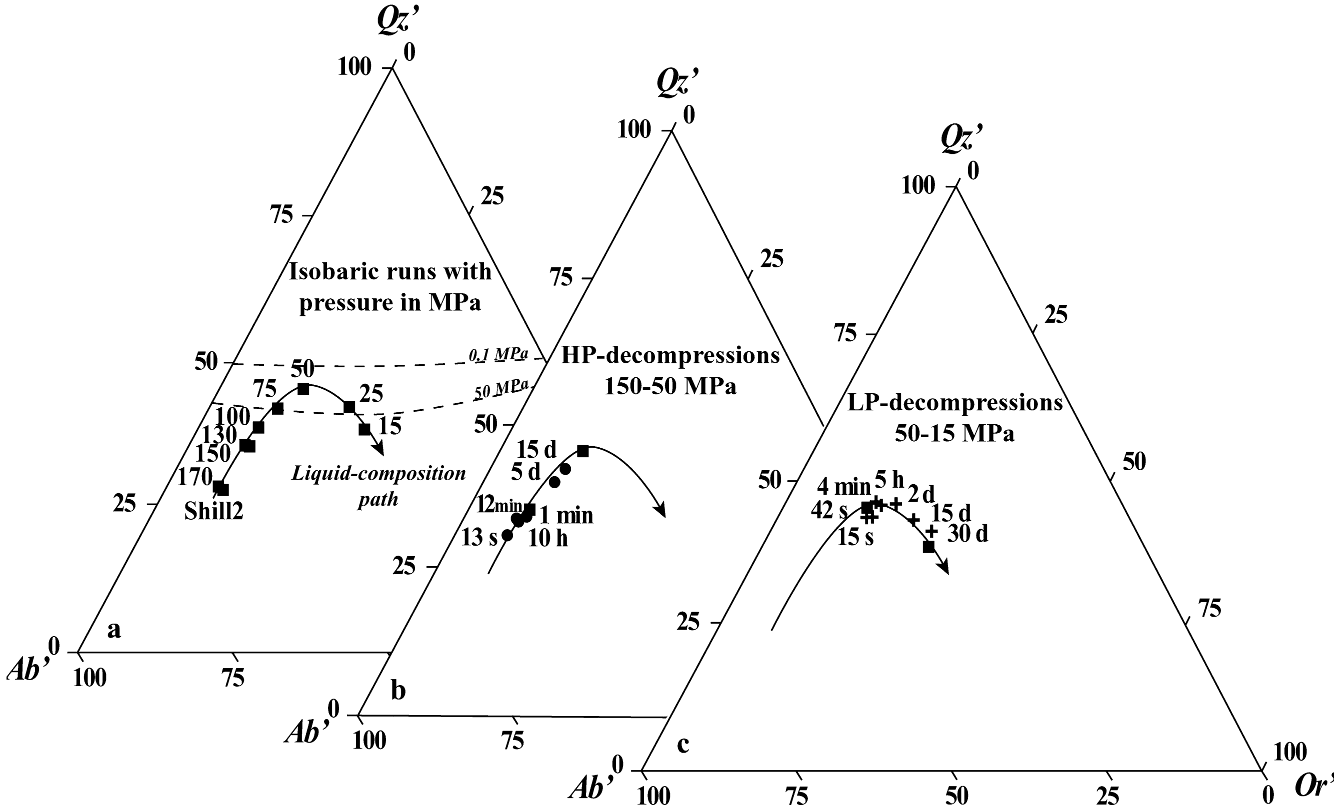

Fig. 11a–c Projection of the melt compositions in the haplogranite system corrected for An-bearing melts (Qz′–Ab′–Or′; Blundy and Cashman 2001, adapted from Tuttle and Bowen 1958). **a** Isobaric runs and starting composition (SHILL2); Qz–feldspar cotectics for the Qz–Ab–Or (An-free) system at 50 and 0.1 MPa after Tuttle and Bowen (1958). **b** HP decompressions from 150 to 50 MPa. **c** LP decompressions from 50 to 15 MPa (for **b** and **c**, point *labels* are the decompression duration, and the *squares* denote the melt compositions of the isobaric run at initial and final pressure). Errors on Qz′, Ab′, and Or′ components are up to 2 wt% (Blundy and Cashman 2001)

Cashman (2001). The evolution with pressure of the recalculated Qz′Ab′Or′ melt compositions of the isobaric charges is related to the nature and composition of the crystallising phases (Fig. 11a). With decreasing pressure from 170 to 50 MPa, plagioclase crystallises, so that the melt composition moves away from the Ab component. Below 50 MPa, the liquid line of descent converges towards the Or apex while co-precipitating plagioclase and cristobalite. Although the cotectics are not defined for pressures < 50 MPa, the liquid-composition path strongly deviates from the supposed Qz-feldspar cotectic line (Fig. 11a; Tuttle and Bowen 1958), which probably reflects insufficient plagioclase crystallisation for the melt to progress along the cotectic at low pressures. This would confirm the non-attainment of equilibrium for the isobaric runs below 50 MPa.

For both the HP- and LP-decompression runs, melt normative compositions parallel the liquid-composition path defined by the isobaric experiments (Fig. 11b, c). As demonstrated by Cashman and Blundy (2000), we confirm that the melt composition gradually changes with the decompression rate. For decompression rates > 0.01 MPa/min (duration < hours), the melt compositions are very close to that at initial pressure, suggesting no significant crystallisation re-equilibration. Only for slow decompressions (duration of several days), the final melt compositions tend to approach the compositions expected for final pressures.

Crystal growth versus nucleation

For decompression rates≥100 MPa/min (duration of 13–15 s) in both HP- and LP-decompression experiments, plagioclase proportions and number densities are comparable to the expected values at initial pressure (Fig. 8b, c). This results from the incomplete melt H_2O exsolution which prevents significant crystallisation. For slower decompression rates, the crystallisation process is different for the HP- and LP-decompression experiments.

The HP-decompression products decompressed at rates < 100 MPa/min are characterised by constant plagioclase number densities of ~575/mm^2. In comparison to the 100/mm^2 number density at initial pressure, this indicates that plagioclase nucleation occurred during decompression, but not as much as expected for the final pressure, i.e. ~1,200/mm^2 (Fig. 8c). These new plagioclases, with length ≤ 10 μm (absent at initial pressure), represent only ~5–8% of the total plagioclase number, instead of ~37% which is expected at final pressure (Fig. 4). With increasing decompression duration, the plagioclase longest axes are shifted to higher values, reflecting plagioclase growth. For the 15-day decompression, plagioclases reach a maximum length of 90 μm, whereas crystals of 0–10 μm disappear. The lack of variation in plagioclase number density, together with the increase in volume proportion (Fig. 8b) and crystal size with decreasing decompression rate, suggest that the dominant crystallisation process upon decompression is growth around pre-existing individuals rather than crystal nucleation. This is in agreement with the results of Hammer and Rutherford (2002) who found a maximum plagioclase growth rate at P~100 MPa. The growth-dominated crystallisation may be explained by the decrease of the plagioclase supersaturation in the melt, as the system has sufficient time to equilibrate at each pressure interval (Lofgren 1974; Swanson 1977; Muncill and Lasaga 1988). Orthopyroxene or Fe-Ti oxide cannot validate the growth-dominated crystallisation, as they are in proportions < 1 vol%. The number density data suggest, however, that the dominant crystallisation process did not occur through nucleation. Indeed, orthopyroxene nucleates in charges decompressed in 5 and 15 days, with number densities corresponding to that expected at its appearance pressure (~100 MPa; Fig. 10b). Fe-Ti oxide nucleates with number densities (up to 2,000/mm^2) expected for equilibrium at pressures between 150 and 100 MPa (Fig. 10d). Both results indicate that nucleation occurred mainly above ~100 MPa. We note that in the 10-h decompression duration, orthopyroxene did not crystallise, despite a 5-h time period below its appearance pressure, indicating a nucleation time lag of at least 5 h.

Irrespective of the decompression rate of the LP-decompression experiments, the volume proportion of plagioclase remains constant (20–25 vol%; Fig. 8b), corresponding to that expected at initial pressure, whereas ~37 vol% would have been expected at final pressure (extrapolated to 15 MPa; Fig. 2). This indicates no significant growth of plagioclase upon decompression. Two hypotheses may be proposed for this plagioclase growth difficulty: (1) the high SiO_2 content, low H_2O content, and high amounts of crystals in the melt cause high bulk viscosities which prevent plagioclase growth; (2) difficulties for cristobalite to exsolve upon decompression, which causes SiO_2-supersaturations of the melt and therefore prevents plagioclase growth. Unfortunately, the determination of the cristobalite volume content which could verify the latter hypothesis was impossible. For decompression rates < 50 MPa/min (duration = 42 s), the plagioclase number density increased markedly from ~1,500 to 3,000–3,500/mm^2 (Fig. 8c), suggesting that most crystallisation occurred through nucleation, with little plagioclase growth. The nucleation-dominated crystallisation is confirmed by orthopyroxene, whose number density increases markedly from ~545/mm^2 for the 15-s decompression (close to the expected value at initial pressure) to ~4,728/mm^2 for the 4-min decompression. Data on Fe-Ti oxides are too scant to investigate the crystallisation process. The high increase in the plagioclase and orthopyroxene number densities corresponds to the boundary between equilibrium versus non-equilibrium H_2O exsolution at ~100 MPa/min (Fig. 6b). This confirms that nucleation is triggered mostly by H_2O exsolution. Nucleation requires the onset of high effective supersaturation of the mineral phases (Lofgren 1974; Muncill and Lasaga 1988), which may be obtained at pressures < 50 MPa where nucleation time lags are important, crystal-growth kinetics are slow due to high bulk viscosities, and liquidus curves are at high temperature due to small H_2O contents. The release of these high supersaturations occurs through a significant nucleation event. The nucleation-dominated crystallisation at low pressure is in agreement with the results of Hammer and Rutherford (2002) who found a maximum nucleation rate at P < 25 MPa. For long post-decompression equilibration duration, however, they found that crystallisation by growth around existing crystals surpasses nucleation-dominated crystallisation, as also proposed by Cashman and Blundy (2000). In our experiments, the rapid quench which immediately followed the decompression prevented the onset of a crystallisation regime dominated by growth on existing crystals.

Chemical re-equilibration of the phases

The time competition between the decompression duration and the kinetics of atom displacement controls the advancement of the chemical re-equilibration process of the phases. Our data do not provide any conclusion about chemical re-equilibrations during the LP decompressions, because the phases have wide ranges of compositions, as they nucleate along decompression. Below, chemical re-equilibration is discussed exclusively for the HP-decompression products, for which the main crystallisation process during decompression is growth of the existing crystals.

Fe-Ti oxide

For HP-decompression duration of ≤ 10 h (rates≥0.1 MPa/min), Fe-Ti oxide did not re-equilibrate at final pressure and has compositions corresponding to 150–130 MPa. For decompression duration of ≥5 days (including the #T1 run which was decompressed in 10 h before an equilibration period of 7 days at final pressure), Fe-Ti oxide fully re-equilibrated at 50 MPa (Fig. 10c). This suggests a re-equilibration time scale for Fe-Ti oxide at pressures > 50 MPa between 10 h and 5 days. This is in agreement with the experiments of Gardner et al. (1995) and Venezky and Rutherford (1999), in which ~4 days were required to re-equilibrate Fe-Ti oxides of 5 μm at 850 °C. For decompression duration of > 10 h, Fe-Ti oxide did not significantly nucleate or increase in volume proportion, suggesting that chemical re-equilibration seems to be the favoured process for these small crystals in response to the decompression-induced perturbations.

Orthopyroxene

During the 15-day decompression, orthopyroxene crystallised (supposedly at ~100 MPa) with a number density similar to that expected at 100 MPa, suggesting that no significant amounts of new crystals appeared upon decompression to 50 MPa. The crystals have the compositions expected at final pressure (Fig. 10a), indicating that they completely re-equilibrated within the ~7.5 day period they spent between ~100 and 50 MPa. In the charge decompressed within 5 days, orthopyroxene compositions span the entire range between those expected for 100 and 50 MPa, suggesting that some of them did not completely re-equilibrate within ~2.5 days. As proposed for Fe-Ti oxide, the absence of significant nucleation or growth of orthopyroxene during HP decompressions favours chemical re-equilibration as the main process to accommodate the decompression-induced perturbations.

Plagioclase

For the HP decompressions, the main plagioclase crystallisation occurred through growth around existing crystals. Analytical profiles of plagioclases from charges decompressed in 5–15 days, and from the 10-h decompression run followed by an equilibration period of 7 days at 50 MPa show normal zonings, with core compositions of ~$An_{43–49}$ and rim compositions close to the values expected at final pressure (Fig. 9a, and #T1 in Fig. 9b). Therefore, chemical re-equilibration upon decompression occurs largely in the crystal core, with a maximum change from ~An_{51} at initial pressure to An_{43} within 15 days. Some of the large plagioclases (~20–40 μm) in the charges decompressed at rates > 0.1 MPa/min (duration of ≤ 10 h), however, are inversely zoned with rims corresponding to the composition expected at 150 MPa (~An_{51}; Fig. 9b–d), and cores down to ~An_{46} (corresponding to ~100 MPa at equilibrium). This would primarily imply that the core of such plagioclases could re-equilibrate during time scales as short as 13 s whereas rims do not change composition (Fig. 9d), which is unlikely to occur. A more plausible explanation is that some of the plagioclases which appear during the isobaric stage at 150 MPa grow with hollow cores (as noticed for the isobaric charge at 150 MPa) which are then filled by crystallisation during decompression, which is a much faster process than growth from the rims as atom mobility is limited in space. The decompression rates required to prevent normal zonings in plagioclases corroborate the rates for which the Qz′–Ab′–Or′ normative compositions of melts do not change upon decompression (Fig. 11b), i.e. > 0.1 MPa/min (decompression duration of < 10 h). This confirms that for these fast decompression rates, plagioclase does not have time to equilibrate (the crystallisation in hollow cores does not affect at all the melt surrounding the crystal rims).

Application to the ascent of silicic magmas in volcanic conduits

The aim of the present study is to relate the matrix texture and composition of a silicic magma with its ascent history in the volcanic conduit. Although the composition of our matrix melt does not exactly reproduce the pre-eruptive interstitial melt of Soufriere Hills andesite (for magma mixing reasons), our rhyolitic melt composition compares to many interstitial melts in silicic magmas. In addition, the $P–T–fO_2–H_2O$ conditions are close to those of the Soufriere Hills volcano and relevant for silicic volcanic edifices. The large range of applied decompression rates may cover the ascent rates of silicic eruptions. Therefore, the processes investigated experimentally, i.e. H_2O exsolution, bubble growth, crystallisation, and their interactions may be applicable to the natural processes.

Magma explosivity

Hypotheses for magma explosivity are related to the volatile contents. During eruption, volatile supersaturation in the melt can build up if magma ascends on time scales shorter than the volatile-exsolution process. Our results suggest that H_2O-supersaturation in a rhyolitic melt (viscosities up to 10^{7-8} Pa s) can be reached only for decompression rates > 100 MPa/min (roughly corresponding to ascent rates of > 45 m/s for a bulk density of 2,800 kg/m^3). Such ascent rates are extremely high, maybe not even reached during Plinian eruptions close to the fragmentation level (Wilson et al. 1980; Pallister et al. 1992). In addition, when the fragmentation level is lower in pressure, H_2O exsolution from the melt is facilitated (Gardner et al. 1999). Therefore, it seems unlikely that magmas sustain high melt H_2O supersaturation as they reach the surface. However, we showed that bubbles encounter difficulties to expand at decompression rates > 0.1 MPa/min. Partly expanded bubbles seem to be a pertinent means for magma to transport H_2O-vapour supersaturation en route to the surface, which may turn explosive through gas-pressure release.

Magma ascent rates

In natural systems, Plinian magmas ascend rapidly, in the order of m/s (Pallister et al. 1992), whereas dome-forming magmas ascend at rates below cm/s (Rutherford and Hill 1993; Siswowidjoyo et al. 1995; Nakada and Motomura 1995; Devine et al. 1998a). More precise data on ascent rates are, however, not available. One way to infer magma decompression path and rates could be provided by experimentally reproducing the natural matrix textures and phase compositions as a function of the decompression rate, as demonstrated by Rutherford and Hill (1993), Geschwind and Rutherford (1995) and Hammer and Rutherford (2002). We propose that the compilation of several crystal, melt, or pore features which vary with decompression rates may precisely constrain magma ascent rates. For instance, we showed that (1) the absence of a given phase in the microlite assemblage, albeit present at equilibrium, can provide constraints on the magma ascent duration; (2) compositions or chemical zonings of the microlites may be directly related to the ascent rate and depth; and (3) the amount of crystallisation of a pure SiO_2 phase in the melt characterises slow ascents of the magma at low pressures (≤ 50 MPa).

The direct application of these results to natural systems, however, would require more realistic ascent scenarios, taking into account, for instance, (1) a precise fragmentation level during Plinian eruptions, which provide the final pressure for the decompression experiments; (2) non-linear decompressions (i.e. accelerated, Gilbert and Sparks 1998); (3) horizontal variations of the decompression rate within the conduit (Massol and Jaupart 1999); and (4) non-steady magma ascent which permits re-equilibration (Hammer and Rutherford 2002).

Conclusions

1. H_2O exsolution from melts with viscosity up to 10^8 Pa s reaches equilibrium within $\sim$1 min (decompression rate $\sim$100 MPa/min). By contrast, bubble growth is a process with a longer time scale. Full expansion of the bubbles requires several hours (decompression rate $\sim$0.1 MPa/min). This may result in significant H_2O-vapour supersaturation in the growing bubbles during fast magma ascents, with possible consequences for magma explosivity.
2. The experiments highlighted the following dependencies with the decompression range: (1) considerably slow crystallisation kinetics at pressures < 50 MPa; (2) different crystallisation processes upon decompression: dominant growth of the existing crystals at $P \geq 50$ MPa and nucleation at $P \leq 50$ MPa for plagioclase.
3. The experiments highlighted the following dependencies with the decompression rate: (1) mineral compositions and volume proportions; (2) crystal-nucleation time lags and various advancement of the chemical re-equilibration process.
4. The experimentally determined kinetics of H_2O exsolution, bubble growth, and crystallisation may be used together with textural features (crystal morphologies, bubble and crystal size distributions) to infer the ascent history (depth range and ascent rate) of silicic magmas in the volcanic conduit.

Acknowledgements The authors would like to gratefully thank H. Schulze and O. Leitner for careful sample preparations, and M. Pichavant for interesting discussions. This paper has greatly benefited from the reviews of Jim Gardner and an anonymous reviewer. This work was financed by the Visitor's Program and the EU "IHP – Access to Research Infrastructures" Program (contract no. HPRI-1999-CT-00004 to D.C. Rubie) of the Bayerisches Geoinstitut.

References

Barclay J, Carroll MR, Houghton BF, Wilson CJN (1996) Pre-eruptive volatile content and degassing history of an evolving peralkaline volcano. J Volcanol Geotherm Res 74:75–87

Barclay J, Rutherford MJ, Carroll MR, Murphy MD, Devine JD, Gardner J, Sparks RSJ (1998) Experimental phase equilibria constraints on pre-eruptive storage conditions of the Soufriere Hills magma. Geophys Res Lett 25:3437–3440

Blundy J, Cashman KV (2001) Ascent-driven crystallisation of dacite magmas at Mount St. Helens, 1980–1986. Contrib Mineral Petrol 140:631–650

Burnham CW (1994) Development of the Burnham model for prediction of H_2O solubility in magmas. In: Carroll MR, Holloway JR (eds) Volatiles in magmas. Mineral Soc Am Rev Mineral 30:123–129

Cashman KV, Blundy J (2000) Degassing and crystallisation of ascending andesite and dacite. Philos Trans R Soc Lond 358:1487–1513

Devine JD, Gardner JE, Brack HP, Layne GD, Rutherford MJ (1995) Comparison of microanalytical methods for estimating H_2O contents of silicic volcanic glasses. Am Mineral 80:319–328

Devine JD, Rutherford MJ, Gardner JE (1998a) Petrologic determination of ascent rates for the 1995–1997 Soufriere Hills Volcano andesitic magma. Geophys Res Lett 25:3673–3676

Devine JD, Murphy MD, Rutherford MJ, Barclay J, Sparks RSJ, Carroll MR, Young SR, Gardner JE (1998b) Petrologic evidence for pre-eruptive pressure-temperature conditions, and recent reheating, of andesitic magma erupting at Soufriere Hills Volcano, Montserrat, W.I. Geophys Res Lett 25:3669–3672

Eichelberger JC, Carrigan CR, Westrich HR, Price RH (1986) Non-explosive silicic volcanism. Nature 323:598–602

Fenn PM (1977) The nucleation and growth of alkali feldspars from hydrous melts. Can Mineral 15:135–161

Gardner JE, Carey S, Rutherford MJ, Sigurdsson H (1995) Petrologic diversity in Mount St. Helens dacites during the last 4,000 years: implications for magma mixing. Contrib Mineral Petrol 119:224–238

Gardner JE, Hilton M, Carroll MR (1999) Experimental constraints on degassing of magma: isothermal bubble growth during continuous decompression from high pressure. Earth Planet Sci Lett 168:201–218

Geschwind CH, Rutherford MJ (1995) Crystallization of microlites during magma ascent: the fluid mechanics of 1980–1986 eruptions of Mt St Helens. Bull Volcanol 57:356–370

Gilbert JS, Sparks RSJ (1998) Future research directions on the physics of explosive volcanic eruptions. In: Gilbert JS, Sparks RSJ (eds) The physics of explosive volcanic eruptions. Geol Soc Lond Spec Publ 145:1–7

Hammer J, Rutherford MJ (2002) An experimental study of the kinetics of decompression-induced crystallization in silicic melt. J Geophys Res 107:1–24

Hammer J, Manga M, Cashman KV (1998) Non-equilibrium and unsteady fluid degassing during slow decompression. Geophys Res Lett 25:4565–4568

Hammer J, Cashman KV, Hoblitt RP, Newman S (1999) Degassing and microlite crystallization during pre-climactic events of the 1991 eruption of Mt. Pinatubo, Philippines. Bull Volcanol 60:355–380

James RS, Hamilton DL (1969) Phase relations in the system $NaAlSi_3O_8$-$KAlSi_3O_8$–$CaAl_2Si_2O_8$–SiO_2 at 1 kilobar water vapour pressure. Contrib Mineral Petrol 21:111–141

Jaupart C (1998) Gas loss from magmas through conduit walls during eruption. In: Gilbert JS, Sparks RSJ (eds) The physics of explosive volcanic eruptions. Geol Soc Lond Spec Publ 145:73–90

Jaupart C, Allègre CJ (1991) Gas content, eruption rate and instabilities of eruption regime in silicic volcanoes. Earth Planet Sci Lett 102:413–429

Jaupart C, Tait S (1990) Dynamics of eruptive phenomena. In: Nicholls J, Russell JK (eds) Modern methods of igneous petrology: understanding magmatic processes. Rev Mineral 24:213–238

Klug C, Cashman KV (1994) Vesiculation of May 18, 1980, Mount St. Helens magma. Geology 22:468–472

Klug C, Cashman KV (1996) Permeability development in vesiculating magmas: implications for fragmentation. Bull Volcanol 58:87–100

Knoche R, Dingwell DB, Webb SL (1995) Melt densities for leucogranites and granitic pegmatites: partial molar volumes for SiO_2, Al_2O_3, Na_2O, K_2O, Li_2O, Rb_2O, Cs_2O, MgO, CaO, SrO, BaO, B_2O_3, P_2O_5, F_2O_{-1}, TiO_2, Nb_2O_5, Ta_2O_5, and WO_3. Geochim Cosmochim Acta 59(22):4645–4652

Lofgren G (1974) An experimental study of plagioclase crystal morphology: isothermal crystallization. Am J Sci 274:243–273

Mangan M, Sisson T (2000) Delayed, disequilibrium degassing in rhyolite magma: decompression experiments and implications for explosive volcanism. Earth Planet Sci Lett 183:441–445

Martel C, Pichavant M, Bourdier J-L, Traineau H, Holtz F, Scaillet B (1998) Magma storage conditions and control of eruption regime in silicic volcanoes: experimental evidence from Mt. Pelée. Earth Planet Sci Lett 156:89–99

Martel C, Bourdier J-L, Pichavant M, Traineau H (2000) Textures, water content and degassing of silicic andesites from recent plinian and dome-forming eruptions at Mount Pelee volcano (Martinique, Lesser Antilles arc). J Volcanol Geotherm Res 96:191–206

Massol H, Jaupart C (1999) The generation of gas overpressure in volcanic eruptions. Earth Planet Sci Lett 166:57-70

Metrich N, Rutherford MJ (1998) Low pressure crystallization paths of H2O-saturated basaltic-hawaiitic melts from Mt. Etna: implications for open-system degassing of basaltic volcanoes. Geochim Cosmochim Acta 62:1195–1205

Mullineaux DR, Crandell DR (1981) The eruptive history of Mount St. Helens. US Geol Surv Prof Pap 1250:3–15

Muncill GE, Lasaga AC (1987) Crystal-growth kinetics of plagioclase in igneous systems: one atmosphere experiments and application of a simplified growth model. Am Mineral 72:299–311

Muncill GE, Lasaga AC (1988) Crystal-growth kinetics of plagioclase in igneous systems: isothermal H_2O-saturated experiments and extension of growth model to complex silicate melts. Am Mineral 73:982–992

Nakada S, Motomura Y (1995) Manner of magma ascent at Unzen volcano (Japan). Geophys Res Lett 22:567–570

Newhall CG, Daag AS, Delfin FG Jr, Hoblitt RP, McGeehin J, Pallister JS, Regalado MTM, Rubin M, Tubianosa BS, Tamayo RA Jr, Umbal JV (1996) Eruptive history of Mount Pinatubo. In: Newhall CG, Punongbayan RS (eds) Fire and mud. University of Washington Press, Seattle, pp 165–195

Pallister JS, Hoblitt RP, Crandell DR, Mullineaux DR (1992) Mount St. Helens a decade after the 1980 eruptions: magmatic models, chemical cycles, and a revised hazards assessment. Bull Volcanol 54:126–146

Phillips JC, Lane SJ, Lejeune A-M, Hilton M (1995) Gum rosin-acetone system as an analogue to the degassing behaviour of hydrated magmas. Bull Volcanol 57:263–268

Pownceby MI, O'Neill HStC (1994) Thermodynamic data from redox reactions at high temperatures. III. Activity-composition relations in Ni-Pd alloys from EMF measurements at 850–1250 K, and calibration of the NiO + Ni-Pd assemblage as a redox sensor. Contrib Mineral Petrol 116:327–339

Proussevitch AA, Sahagian DL (1996) Dynamics of coupled diffusive and compressive bubble growth in magmatic systems. J Geophys Res 101:17447–17455

Proussevitch AA, Sahagian DL (1998) Dynamics and energetics of bubble growth in magmas: Analytical formulation and numerical modeling. J Geophys Res 103:18223–18251

Roobol MJ, Smith AL (1976) Mont Pelée, Martinique. A pattern of alternating eruptive style. Geology 4:521–524

Rutherford MJ, Hill PM (1993) Magma ascent rates from amphibole breakdown: experiments and the 1980–1986 Mount St Helens eruptions. J Geophys Res 98:19667–19685

Saul A, Wagner W (1989) A fundamental equation for water covering the range from the melting line to 1273 K at pressures up to 25000 MPa. J Phys Chem 18(4):1537–1565

Schairer JF, Bowen NL (1935) Preliminary report on equilibrium-relations between feldspathoids, alkali-feldspars, and silica. Am Geophys Union Trans:325–328

Shaw HR (1972) Viscosities of magmatic silicate liquids: an empirical method of prediction. Am J Sci 272:870–893

Simakin AG, Armienti P, Epel'baum MB (1999) Coupled degassing and crystallization: experimental study at continuous pressure drop, with application to volcanic bombs. Bull Volcanol 61:275–287

Simakin AG, Armienti P, Salova TP (2000) Joint degassing and crystallization: experimental study with a gradual pressure release. Geochim Int 38:523–534

Siswowidjoyo S., Suryo I, Yokoyama I (1995) Magma eruption rates of Merapi volcano, Central Java, Indonesia during one century (1890–1992). Bull Volcanol 57:111–116

Stasiuk MV, Barclay J, Carroll MR, Jaupart C, Ratté JC, Sparks RSJ, Tait SR (1996) Degassing during magma ascent in the Mule Creek vent (USA). Bull Volcanol 58:117–130

Swanson S (1977) Relation of nucleation and crystal-growth rate to the development of granitic textures. Am Mineral 62:966–978

Taylor JR, Wall VC, Pownceby MI (1992) The calibration and application of accurate redox sensors. Am Mineral 77:284–295

Tuttle OF, Bowen NL (1958) Origin of granite in the light of experimental study in the system $NaAlSi_3O_8$–$KAlSi_3O_8$–SiO_2–H_2O. Geol Soc Am Mem 74

Venezky DY, Rutherford MJ (1999) Petrology and Fe-Ti oxide reequilibration of the 1991 Mount Unzen mixed magma. J Volcanol Geotherm Res 89:213–230

Villemant B, Boudon G (1998) Transition from dome-forming to plinian eruptive styles controlled by H_2O and Cl degassing. Nature 392:65–69

Villemant B, Boudon G (1999) H_2O and halogen (F, Cl, Br) behaviour during shallow magma degassing processes. Earth Planet Sci Lett 168:271–286

Westrich HR, Stockman HW, Eichelberger JC (1988) Degassing of rhyolitic magma during ascent and emplacement. J Geophys Res 93:6503–6511

Wilson L, Sparks RSJ, Walker GPL (1980) Explosive volcanic eruptions. IV. The control of magma properties and conduit geometry on eruption column behaviour. Geophys J R Astron Soc 63:117–148

Wolf KJ, Eichelberger JC (1997) Syn-eruptive mixing, degassing, and crystallization at Redoubt Volcano, eruption of December, 1989 to May 1990. J Volcanol Geotherm Res 75:19–37

Woods AW, Koyaguchi T (1994) Transitions between explosive and effusive eruptions of silicic magmas. Nature 370:641–644

Young SR, Sparks RSJ, Aspinall WP, Lynch LL, Miller AD, Robertson REA, Shepherd JB (1998) Overview of the eruption of Soufriere Hills volcano, Montserrat, 18 July 1995 to December 1997. Geophys Res Lett 25:3389–3392

Zhang Y, Belcher R, Ihinger PD, Wang L, Xu Z, Newman S (1997) New calibration of infrared measurement of dissolved water in rhyolitic glasses. Geochim Cosmochim Acta 61:3089–3100

Etude complémentaire

Stage de recherche M2 : Ahmed RADADI ALI (2005, Orléans) *La décompression expérimentale des magmas de la Montagne Pelée.*
Direction : C. Martel.

Certains taux de décompression réalisés lors de l'étude précédente ont nécessité des décompressions manuelles espacées de quelques heures (jour et nuit) sur plusieurs jours. Ceci a motivé la mise au point à l'ISTO d'un autoclave équipé d'une vanne pneumatique de décompression pilotée par un régulateur (Figure 4) de pression et la proposition d'un sujet de recherche M2 sur la décompression expérimentale des magmas de la Montagne Pelée. L'objectif était d'étudier le dégazage et la cristallisation du liquide interstitiel rhyolitique de l'andésite de la Montagne Pelée au cours de décompressions rapides de 2000 à 500 bars et de décompressions lentes de 2000 à 150 bars, simulant l'ascension du magma dans le conduit volcanique respectivement lors d'éruptions Pliniennes et d'éruptions à dôme. Une des expériences décomprimée jusqu'à 150 bars a représenté la première décompression test en capsule percée (motivant le sujet de recherche de M2 proposé l'année suivante ; A. Moussadji, 2006, présenté ci-dessus). Ces expériences ont permis d'étudier l'évolution du dégazage (porosité totale, taille et nombre de bulles) en fonction du taux de décompression et a révélé que les porosités étaient en accord avec un dégazage à l'équilibre dès les taux de décompression de 1 bar/s. L'étude de la cristallisation de microlites a été rendue difficile par le fait que les produits de départ contenaient 1 vol% de cristaux de plagioclase (le produit de départ était légèrement sous-saturé pour s'affranchir de bulles de départ). Néanmoins, les diagrammes d'évolution de la proportion volumique, du nombre et de la taille des cristaux de plagioclase en fonction du taux de décompression montrent des phases de nucléation et de croissance des plagioclases, en accord avec les résultats de Martel et Schmidt (2003).

Figure 4. Vanne de décompression automatisée sur un autoclave à joints froids et trempe rapide (ISTO). Pression maximale: 2000 bars; Température maximale: 875°C; Milieu de pression: argon, argon + hydrogène ou eau.

Etudiant en parallèle les microlites naturels des andésites de la Montagne Pelée, je me suis interrogée sur l'origine de microlites de plagioclase très calciques (> An_{80}) et j'ai décidé de "dévier" A. Radadi Ali de son objectif initial pour que nous réalisions quelques équilibres de phase dans les conditions pré-éruptives de l'andésite de la Montagne Pelée, mais à partir d'une andésite basaltique, ce qui a permis de proposer une cristallisation à partir d'un liquide mafique de recharge du réservoir pour les microlites anorthitiques de l'andésite (Martel et al., 2006).

Etude en cours

Article en préparation: MARTEL C. (2009) Magma ascent dynamics at Mt. Pelée (Martinique, Lesser Antilles) inferred from decompression-induced crystallization experiments. *Earth Planet. Sci. Lett.*

Financements : ANR CATT "EXPLANT" 01/2006-06/2009 (C. Martel)

Ce projet constitue en quelque sorte une validation des études expérimentales de dégazage et de cristallisation par décompression à la compréhension des mécanismes éruptifs des volcans d'arc, par une application spécifique au cas de la Montagne Pelée. Il s'agit de déterminer expérimentalement les vitesses d'ascension magmatique pour chaque type éruptif de la période récente du volcan, par une reproduction fidèle des caractéristiques texturales et compositionnelles des microlites naturels analysés (Martel et al., 2006 ; Martel et Poussineau, 2007). Cette étude représente également l'aboutissement de mon projet CNRS débuté en 2001 et du projet scientifique me concernant dans l'ANR CATT "EXPLANT".

Des séries d'expériences de décompression ont été réalisées dans des autoclaves à chauffage externe et trempe rapide (ISTO), à partir du verre interstitiel rhyolitique hydraté en équilibre avec les phénocristaux dans la chambre magmatique (76 pds% SiO_2 ; Norme CIPW : $Qz_{39}Ab_{31}Or_{12}An_{11}Hy_5Co_1Ilm_1$). Une série d'expériences isobares réalisées à 800, 850 et 875°C, NNO +1 et +3 (eau et argon comme milieux de pression respectifs) et à la saturation en eau pour des pressions de 2000 à 50 bars permettent d'obtenir les assemblages, les compositions et les proportions modales des phases à l'équilibre dans ces différentes conditions. Les expériences de décompression ont été réalisées à 850°C et NNO+3, à la pression initiale de 2000 bars (durée de 4-7 jours permettant l'hydratation du verre à ~6 pds% H_2O) et des pressions finales de 50-100 bars ou 300-600 bars. Le choix de ces pressions finales a été motivé par les pressions de trempe (ou fragmentation) déduites des teneurs en eau des verres naturels interstitiels pour les éruptions à dôme et Plinienne (Martel et Poussineau, 2007). Les décompressions ont été effectuées manuellement ou automatiquement grâce à la vanne pneumatique automatisée décrite ci-dessus (Figure 4), à des taux de 0.03 à 25 bar/min, suivis ou non d'un palier isobare à pression finale jusqu'à 17 jours. Certains magmas ont été décomprimés par paliers successifs, dont deux ayant subi un refroidissement de 25 et 50°C lors du dernier palier isobare.

Les caractéristiques texturales des microlites naturels de certains types d'éruption de la Montagne Pelée (Martel et Poussineau, 2007) ont déjà été reproduites par des décompressions expérimentales, notamment celles des produits des déferlantes de type Péléennes ou des nuées de type Merapi (Figure 5). En revanche, des expériences complémentaires sont nécessaires pour obtenir les caractéristiques des rares ponces Pliniennes à microlites.

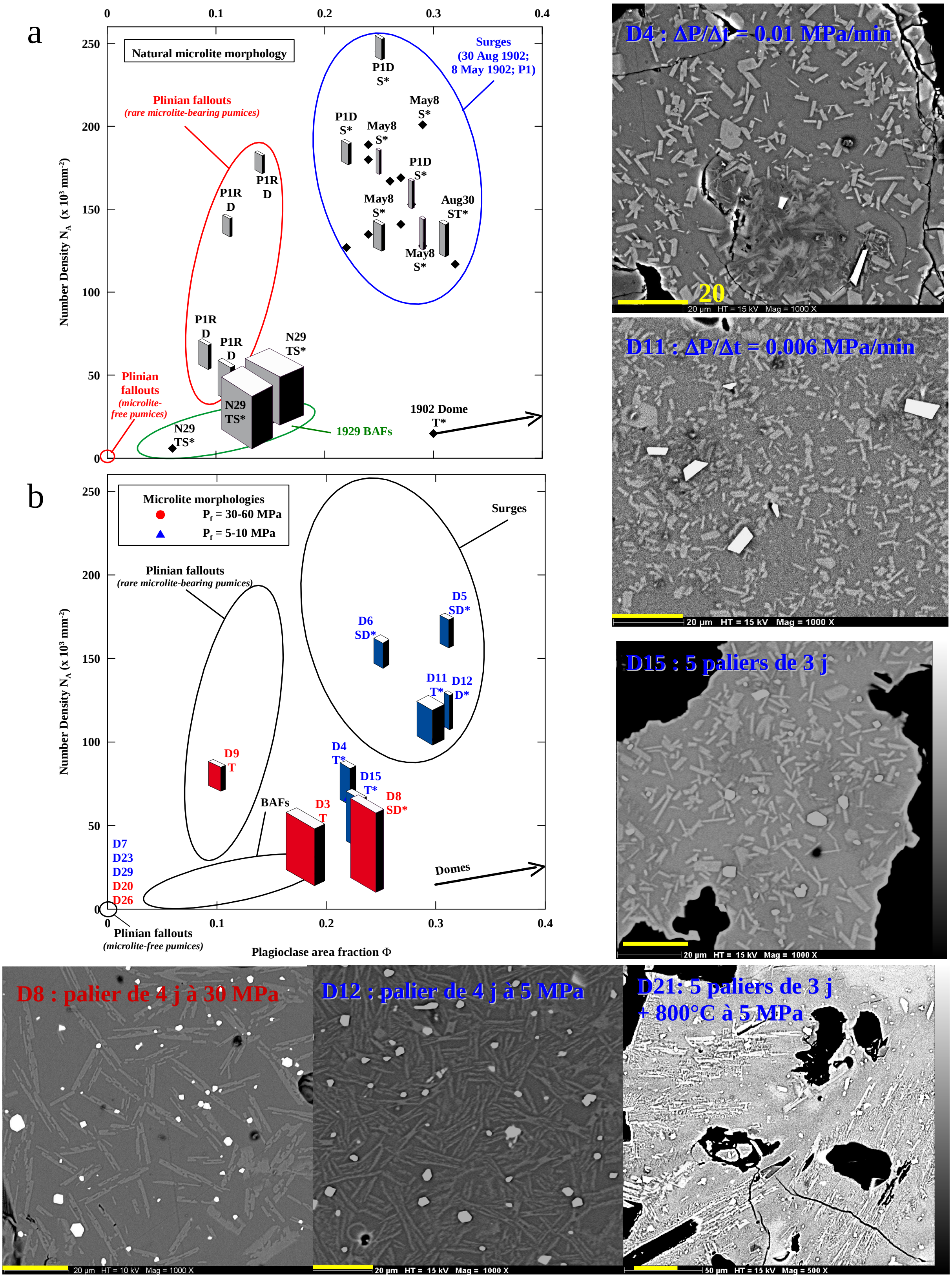

Figure 5. Densité numérique, proportion surfacique et morphologie des microlites (a) naturels, d'après Martel et Poussineau (2007) et (b) expérimentaux (expériences D2 à D29). Morphologie T= tabulaire, S= squelettique, D= dendritique; * pour la présence de plages de silice exsolvée (barre d'échelle = 20 µm). Les losanges représentent des dépôts pour lesquels l'analyse 3D des microlites n'a pas été réalisable.

I.5- FRAGMENTATION MAGMATIQUE

La fragmentation magmatique est le processus par lequel un milieu continu de magma (pouvant contenir des bulles de gaz et des cristaux) se désintègre en un milieu gazeux contenant des particules de magma.

De manière générale, un matériau ductile, tel qu'un magma, se fragmente quand la vitesse de la contrainte qu'on lui applique devient supérieure à son temps de relaxation structurale. Le temps de relaxation structurale τ (en s) est donné par la relation de Maxwell : $\tau = \eta/G$, avec η la viscosité (en Pa/s) et G son module élastique (en Pa; proportionnel au module de Young pour les contraintes extensives, et représentant la limite au-delà de laquelle la contrainte ne peut plus être accumulée sous forme élastique dans le matériau; Dingwell et Webb, 1990). Ainsi, une traction rapide sur une pâte à modeler va provoquer sa rupture, alors qu'une extension lente de même magnitude finale va l'étirer sans cassure. Au moment de sa fragmentation, le matériau ductile qui n'a pas le temps de se relaxer sous la contrainte imposée, va se comporter comme un solide, c'est-à-dire accumuler la contrainte sous forme élastique sans déformation (avec $G \sim 10^{10\ +/-0.5}$ Pa pour les liquides silicatés). Il passe alors d'un domaine où sa réponse était initialement ductile (avant fragmentation) à un domaine de réponse fragile/cassant de type solide. La limite entre ces deux domaines est la transition vitreuse, qui marque le passage d'une rhéologie de fluide Newtonien à celle d'un fluide non-Newtonien dépendant de la vitesse de déformation. La transition vitreuse dépend principalement de la vitesse de déformation (pouvant être franchie lorsque la vitesse de déformation atteint approximativement 1/1000^{e} du temps de relaxation structurale; Webb et Dingwell, 1990), mais dépend également de la température du liquide et de ses caractéristiques intrinsèques telles que sa composition ou sa teneur en éléments volatils dissous (Dingwell, 1996, 1998). Pour résumer, un liquide peut se fragmenter dès lors que la magnitude et le temps d'application de la contrainte sont suffisants pour 1) passer la transition vitreuse (ce qui n'implique pas nécessairement une fragmentation) et 2) vaincre la résistance du liquide dont la réponse est alors assimilable à celle d'un solide (Figure 6).

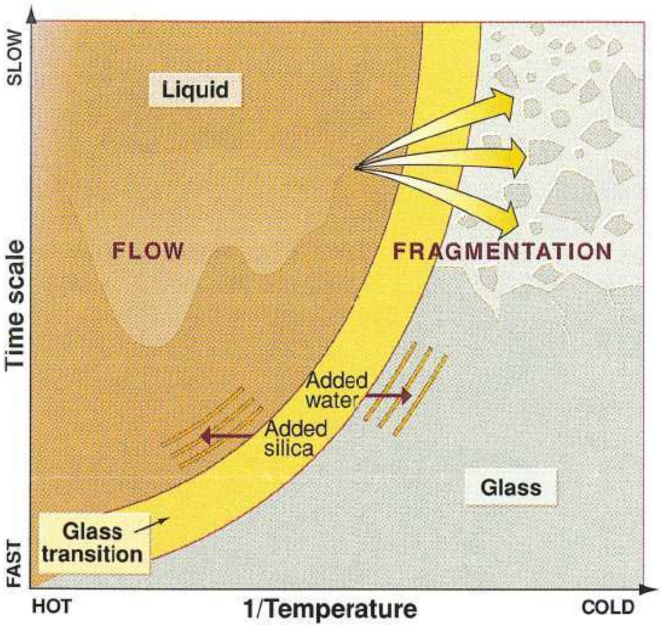

Figure 6. La transition vitreuse dans l'espace Température - Temps d'application de la contrainte (Dingwell, 1996). Les déformations plus lentes que le temps de relaxation structurale génèrent une réponse visqueuse et relaxée du liquide silicaté. Lorsque le temps d'application de la déformation approche de la transition vitreuse, le résultat est un stockage élastique de l'énergie (comportement solide) pour les faibles déformations et une fragmentation pour les fortes déformations. Des variations de teneur en silice et en eau peuvent fortement modifier la température de transition vitreuse.

Dans le cas des éruptions Pliniennes, les premiers critères de fragmentation de la colonne magmatique étaient basés sur la coalescence des bulles (Verhoogen, 1951), puis sur la surpression générée dans des bulles ayant atteint un volume maximal d'environ 75 % (correspondant à la compacité maximale du modèle d'empilement de sphères rigides) (Sparks, 1978; Wilson et al., 1980; Eichelberger et al., 1986). Cependant, de nombreuses ponces naturelles ont des porosités anté-fragmentation très variables (Gardner et al., 1996), et il a été montré que de fortes surpressions sont peu probables dans les bulles des ponces, en raison de l'importance de la coalescence des bulles et de leurs grandes tailles résultantes. Des modèles numériques d'ascension magmatique suggèrent que lorsque le magma monte suffisamment rapidement, la nucléation et la croissance des bulles de gaz peuvent être retardées jusqu'à des niveaux très proches de la surface, la diffusion des gaz dissous dans le liquide silicaté n'étant plus assez rapide pour maintenir l'équilibre avec la pression lithostatique (Proussevitch et Sahagian, 1996; Gardner et al., 1999). De fait, lorsque le magma sursaturé en gaz nucléé massivement ses bulles à basse pression, leur croissance peut être tellement rapide que le liquide silicaté qui doit s'étirer autour des bulles peut alors traverser la transition vitreuse et se retrouver dans le domaine cassant de la réponse à l'extension rapide (Zhang, 1999; Sahagian, 1999), rejoignant ainsi, pour le cas des ponces Pliniennes, le principe de fragmentation d'un liquide par passage dans le domaine fragile et par dépassement de sa résistance à la contrainte. Ceci corrobore une étude de ponces fibreuses qui révèle des marqueurs texturaux de déformations à l'état solide du liquide silicaté juste avant la fragmentation du magma (Marti et al., 1999).

L’intensité de l’explosivité se reflète dans la granulométrie des fragments produits: plus les fragments sont petits, plus la masse gazeuse relâchée a été importante. Cependant, il existe très peu d’études permettant de relier quantitativement l'intensité explosive d'une éruption (au travers de sa masse gazeuse libérée) à une granulométrie précise de fragments magmatiques (Kaminski et Jaupart, 1998). Le projet mené au BGI visait à déterminer l’influence de paramètres tels que la teneur, la taille et la forme des bulles et des cristaux sur la distribution de taille des fragments obtenus par décompression instantanée d’un magma dans des conditions de pression et de températures réalistes. Ces conditions ont été obtenues grâce à une bombe de fragmentation mise au point par Alidibirov & Dingwell (1996a et b) au BGI, composée d’un autoclave vertical à chauffage externe (< 950°C) séparé d’un réservoir sus-jacent de 2 m de haut à pression et température ambiantes par une série de diaphragmes de cuivre manufacturés pour s’ouvrir en moins d’une seconde à une pression donnée (< 300 bars). Cet appareil ne permettant que des décompressions instantanées à partir de faibles pressions, l'expérience simule une décompression par retrait rapide d’une masse sus-jacente à une colonne magmatique (e.g., par écroulement d’un dôme). Les premières études menées avec cet outil concernaient la recherche du seuil de fragmentation d’un magma en fonction de sa pression et de sa température (Spieler et al., 2003), avec l’inconvénient majeur de travailler à partir d’échantillons naturels ayant déjà fragmentés (l'avantage étant leur grande taille). Je tenais plus particulièrement à étudier les propriétés de fragmentation d’échantillons aux teneurs en eau, bulles et cristaux contrôlées et systématiques, donnant lieu à deux publications, l’une traitant de l’influence des bulles (Martel et al., 2000b, présentée ici) et l’autre des cristaux (Martel et al., 2001) sur les caractéristiques des fragments.

Article présenté: MARTEL C., DINGWELL D.B., SPIELER O., PICHAVANT M. & WILKE M. (2000) Fragmentation of foamed silicic melts: an experimental study. Earth Planet. Sci. Lett. 178, 47-58.

Financements : EC-TMR-Network (FMRX-CT96-0063) on "Hydrous Melts" ; EC (ENV4-CT-98-0703) on "The Physics of Explosive Volcanism"; DFG Grant to D.B. Dingwell.

Les échantillons ont été synthétisés à partir d'un verre haplogranitique (79 pds% SiO_2 ; Norme CIPW : $Qz_{36}Ab_{39}Or_{25}$) préalablement hydratés jusqu'à 6 pds% d'eau dans des autoclaves à chauffage interne au CRSCM/ISTO Orléans ou à l'Institut de Minéralogie de l'Université de Hanovre (Allemagne). Les cylindres (2 ou 0.8 cm de diamètre, 2 cm de long) de verre aphyrique hydraté sont ensuite placé dans l'autoclave de la bombe de fragmentation en température (360-900°C) et à une pression inférieure à sa pression de solubilité pendant 30 min de manière à ce qu'il nucléé des bulles. La rupture des diaphragmes au-dessus de l'échantillon est provoquée, engendrant la décompression instantanée de l'échantillon hydraté et vésiculé et son éventuelle fragmentation.

Une distribution de la taille des fragments récupérés dans le tank a été obtenue par tamisage manuel jusqu'à la fraction 63 µm. Les fragments sont ensuite observés au microscope électronique à balayage (MEB), pour une détermination de leur forme et de leur porosité. Suivant les expériences, les porosités des fragments s'échelonnent de 4 à 83 vol%, avec des bulles rondes (diamètres de 10 à 275 µm) ou en forme de tubes. Les formes aplaties des pyroclastes témoignent d'un mécanisme de fragmentation par spallation, typiques lors de la fragmentation de matériaux bulleux. Trois lois de distribution de taille sont généralement proposées pour décrire les populations de fragments générés dans les processus naturels ou industriels simples : log-normal pour les gouttes provenant de jets de liquides, loi de puissance pour un solide cassé au marteau et exponentiel pour des processus séquentiels d'écrasement. La distribution de ces pyroclastes expérimentaux suit une loi de puissance avec des exposants D de 2.0 à 4.1. D < 3.0 caractérise les expériences dont la porosité du magma est < 50 % et dont la distribution de taille est contrôlée par les fragments les plus larges. Au-delà de 50 % de porosité, soit D < 3.0 pour des décompressions < 150 bars, soit D > 3.0 (contrôlée par les particules fines) pour des décompressions > 150 bars. A valeur de porosité comparable, la taille des particules diminue avec la magnitude de la décompression ou lorsque les pores sont des tubes.

La comparaison de l'efficacité des différents paramètres étudiés pour obtenir une fragmentation fine montre que l'amplitude de la décompression prédomine sur la porosité, la forme des bulles ou la viscosité du magma.

ELSEVIER

Earth and Planetary Science Letters 178 (2000) 47–58

EPSL

www.elsevier.com/locate/epsl

Fragmentation of foamed silicic melts: an experimental study

C. Martel[a,*], D.B. Dingwell[a], O. Spieler[a], M. Pichavant[b], M. Wilke[c]

[a] *Bayerisches Geoinstitut, Universität Bayreuth, 95440 Bayreuth, Germany*
[b] *CNRS-CRSCM, 1A rue de la Férollerie, 45071 Orléans Cedex 2, France*
[c] *Institut für Mineralogie, Universität Hannover, Welfengarten 1, 30167 Hannover, Germany*

Received 17 February 1999; received in revised form 16 February 2000; accepted 23 February 2000

Abstract

We present the first experimental investigation of the fragmentation behavior of two-phase (melt+gas) rhyolitic systems under rapid decompression. Two-phase samples have been generated by foaming water-oversaturated rhyolitic melts up to 900°C and up to 18 MPa prior to rapid decompression in a fragmentation bomb. The fragmented particles or experimental pyroclasts were recovered for analysis. Several features of naturally foamed pumices have been reproduced, including the generation of both isotropic and tube pumices. We focus here on the fragmentation behavior. Fragmentation occurred through a layer-by-layer process, in the brittle regime of melt response. We investigated the influence of the magnitude of the decompression (4 to 18 MPa), the porosity (0 to 85 vol%) and the pore morphology (tube versus isotropic) on the fragment size distribution. Less vesicular samples (porosity $<$ 50 vol%) generate coarser fragments. Highly vesicular samples (porosity $>$ 50 vol%) yield coarser fragments when decompressed below 15 MPa and finer fragments when decompressed above 15 MPa. Increasing decompression of the vesicular samples results in a decrease in fragment size of 0.2 Φ unit/MPa. The presence of tubes instead of isotropic pores in vesicular samples generates finer fragments under decompression. Implications for dome eruptions are discussed. © 2000 Elsevier Science B.V. All rights reserved.

Keywords: fragmentation; experimental studies; magmas; pyroclastics; size distribution; domes

---

1. Introduction

Explosive silicic eruptions are controlled by a complex interplay of physical and chemical processes, leading to a wide range of eruptive features. Critical to the evaluation of monitoring data and for the development of eruptive scenarios is a realistic and detailed mechanistic picture of silicic eruptions, which are most robust if they can be confirmed by real time experimental investigation of the magma of interest, under realistic pressure–temperature conditions.

Reliable quantification of the parameterization of experimental results on magma fragmentation must be based on a solid foundation of well-characterized materials. We have chosen the best investigated silicate melt system of relevance to the earth sciences, HPG8 haplogranitic melt+water [1], which allow us to specify the physico-chemical properties (e.g. surface tension, viscosity, density, diffusivity) of the magma during the fragmenta-

---

* Corresponding author. Tel: +49-921-553712; Fax: +49-921-553769; E-mail: caroline.martel@uni-bayreuth.de

PII: S0012-821X(00)00062-5

tion event. The fragmentation of magma remains hotly debated: there is no general agreement on mechanisms [2–5]. The principal fragmentation mechanisms in bubbly melts that have been proposed are gas bubble overpressure exceeding the magma tensile strength and melt film instabilities due to the propagation of a decompression wave.

Fragmentation simulations in laboratories have been performed in shock-tube apparatus, either using liquids at room pressure and temperature or magmas. The former studies [6–8] provide the opportunity to observe the dynamics of vesiculation and fragmentation in transparent experimental devices. In the latter studies [9,10], natural magmas are rapidly decompressed and the chilled fragmented particles are recovered for characterization. These experimental simulations have been pioneering in nature and are certainly valuable but the time has now come to systematize the nature and efficiency of fragmentation as a function of the physico-chemical state of the magma and the intensive variables operative at the fragmentation event in nature.

We are interested here in the mechanism by which magmas fragment under rapid decompression using the experimental device of [9,10]. Two sets of parameters that must be constrained for these simulations are the magnitude of the decompression and the physico-chemical properties of the material prior to fragmentation. As the samples have been foamed under controlled conditions immediately prior to fragmentation, we can compare the influence of porosity, viscosity and decompression on the fragment morphology and size distribution.

2. Experimental

2.1. Fragmentation apparatus

The fragmentation device is described in [9,10]. A high-pressure and high-temperature (HPT, up to 23 MPa and 950°C) section consists of a vertically operating externally heated cold-seal pressure vessel (Nimonic 105 alloy) with a bore of 20 mm in diameter and 450 mm in length. Cylindrical samples are placed in the hot source of the HPT section on a top of a K-type thermocouple (precision of ± 1°C). The temperature gradient of a 5 cm long sample is less than 20°C [9]. The average heating rate ranges between 15°C/min at temperatures below 400°C and 5°C/min at temperatures above 650°C. The pressure medium is argon. The pressure is measured by piezoresistive pressure transducers (precision of ± 0.2 MPa). The low-pressure and low-temperature (LPT, room conditions) section is a large cylindrical tank, 2 m high and 70 cm wide. The HPT section is sealed and separated from the LPT section by one to three copper or steel diaphragms specially designed to disrupt at a given pressure depending on their thickness.

2.2. Sample preparation

A finely ground powder of HPG8 haplogranitic glass (SiO_2: 79.0, Al_2O_3: 12.0, Na_2O: 4.6, K_2O: 4.2 wt%, microprobe analyses) was loaded with 1.4 to 5.7 wt% distilled water in platinum capsules of 2 cm in diameter and 2 cm in length. Capsules were arc-welded while surrounded by liquid nitrogen to prevent water loss. Melt hydrations were performed in large diameter furnace of an internally heated pressure vessel (IHPV) at CRSCM in Orléans for ca. 1 month at 950°C and 120 MPa, then isobarically quenched. Smaller samples were prepared in platinum capsules of 8 mm diameter and 2.5 cm long, loaded for 4–6 days in a vertically working IHPV at 1000–1100°C and 300 MPa at the Mineralogical Institute of the University of Hannover. The starting glasses were all crystal-free, but small bubbles were sometimes present (see Table 1 for bubble size and volume). Doubly polished (150–220 μm thick) glass plates prepared from each end of the cylinders were used for the determination of water content by near-infrared spectroscopy (Bruker IFS 120 HR). The concentrations of H_2O and OH species were determined from the height of the absorption bands at 5230 and 4500 cm^{-1}, respectively, by using the Lambert–Beer law and the extinction coefficients of [17]. Water contents between the two ends of the glass cylinders were homogeneous within a range of 0.2 wt%, up to 0.4 wt% for two samples (Table 1).

Table 1
Experimental conditions

Expt. No.	Starting glass cylinders			Nucleation conditions			Fragment characteristics					
	Cw_{ini}[a] (wt%)	Pini[b] (MPa)	Weight (g)	T (°C)	P[c] (MPa)	t (min)	Cw_{calc}[d] (wt%)	Cw_{fin}[e] (wt%)	α_{calc}[f] (vol%)	α_{meas} (vol%)	$\text{Log}\,\eta_{ini}-\text{Log}\,\eta_{fin}$[g] (Pa s)	$\text{Log}\,\eta_{\alpha}$[h] (Pa s)
27	0°	0.1	6.166	900	10	1	0.0	0.00 I	0	4 ± 1	12.4–12.4	–
18	1.4–1.4	11	0.110*	800	4(6.3)	30	0.9	–	58 ± 2	64 ± 5	6.9–7.5	8.6
5	1.4–1.4	11	0.717°	800	4.5(6.5)	30	1.0	1.0 I	49 ± 2	61 ± 5	6.9–7.4	8.4
8	1.4–1.4°	11	7.560	900	5(7.3)	30	1.0	0.7 K	63 ± 2	61 ± 5	5.8–6.7	7.7
20	1.5–1.6	14	1.128°	760	5(6.4)	30	1.0	–	52 ± 3	58 ± 5	7.2–7.9	8.8
11	1.6–1.7°	16	2.459°	784	5(7.6)	30	1.0	1.3 K	44 ± 3	45 ± 3	6.8–7.2	7.9
10	1.7–1.8	18	2.571°	900	10(~ 12)	30	1.4	–	32 ± 3	42 ± 3	5.5–5.8	6.5
2	1.4–1.4	11	0.193°	900	10	60	1.4	1.2 I	19 ± 2	23 ± 3	5.8–6.0	–
28	1.5–1.5°	13	7.367	~ 360	10	1	1.5	–	0	< 1	12.4–12.4	12.4
16	2.6–2.6	42	7.335	750	5(8.8)	30	1.0	1.0 K	77 ± 2	74 ± 8	6.5–8.1	9.4
13	2.4–2.4°	36	0.850°	750	5(8.2)	30	1.0	1.0 K	75 ± 2	71 ± 8	6.6–8.1	9.3
7	2.0–2.2	26	7.692	800	10(11.1)	25	1.4	1.3 K	46 ± 4	62 ± 5	6.3–7.0	8.0
17	2.1–2.4	31	1.335°	750	10(11.1)	30	1.5	1.8 K	32 ± 5	43 ± 3	6.7–7.1	7.7
25	2.5°	38	7.309	630	15	1	2.5	2.4 I	5 ± 1	12 ± 3	8.2–8.3	8.3
9	3.2–3.2°	66	7.750	900	10(12)	30	1.4	1.4 K	68 ± 2	72 ± 8	4.7–5.8	7.1
29	3.3–3.4°	75	1.183°	800	10	25	1.4	1.5 I	67 ± 3	62 ± 5	5.5–6.8	7.8
22	3.7–3.9°	97	7.178	750	10(11.2)	30	1.4	1.2 K	73 ± 4	62 ± 5	5.8–7.8	8.8
24	3.9–3.9°	102	6.092	900	15(17.3)	30	1.6	1.2 K	68 ± 2	70 ± 8	4.4–6.0	7.3
14	3.9–3.9°	102	7.508	822	18	1	1.8	1.4 K	60 ± 2	61 ± 5	5.0–6.6	7.6
19	4.4–4.6	143	0.154°	800	4(6.6)	30	0.9	–	91 ± 4	–	5.0–7.5	–
1	4.4–4.6	143	0.090°	900	10	60	1.4	1.2 K	80 ± 4	83 ± 8	4.2–6.0	–
6	4.4–4.6	143	0.885°	755	15(15.3)	5	1.8	1.8 K	65 ± 4	52 ± 5	5.4–7.0	7.8
23	4.3–4.7°	140	7.622	750	15	30	1.8	1.5 K	68 ± 6	61 ± 5	5.5–7.4	8.4
21	5.6–5.8	234	1.312°	900	15(15.3)	30	16	1.6 K	80 ± 4	83 ± 8	3.8–5.7	9.1

[a] Water content at each end of the starting glass cylinder measured by infrared spectroscopy, except for experiments 9 and 10, for which the second value was obtained by Karl–Fischer titration. Analytical errors of ~0.2 wt%.

° Starting glasses with bubbles (< 3 vol%, diameter of ~50 μm), except for experiments 23 (diameter up to 150 μm) and 24 (11 vol%, diameter up to 150 μm).

[b] Solubility pressure calculated after [11] corresponding to Cw_{ini}. Pini-P gives the supersaturation pressure for vesiculation.

*For 8 mm diameter samples.

[c] Pressure of the HPT section. Number in bracket gives bursting pressure for the single diaphragm experiment (see text for details).

[d] At P, after [11].

[e] Glass water content of the fragments measured by Karl–Fischer titration (K) or infrared spectroscopy (I).

[f] Vesicularity (α) calculated after [12]: $\alpha = (1+\rho_w/((Cw_{ini}-Cw_{fin})\rho_m))^{-1}$, where ρ_w is the water density [13], ρ_m the melt density of the starting hydrated HPG8 glasses (bubble-free) by the double-weight method in air and ethanol (Mettler Toledo AG204). As this yields a glass density (~2.338 g/cm^3 for 1 wt% H_2O), we subtracted the density difference (i.e. 0.032 g/cm^3) obtained by [14] between HPG8 glass at 20°C and melt at 900°C.

[g] Melt viscosity calculated after [15] for average Cw_{ini} and Cw_{fin} at T.

[h] Bubbly-melt viscosity calculated after [16], for highly concentrated suspensions ($Phi_{max} = 85$), considering a rigid behavior of the pores under the 10^{-3} s decompression time.

2.3. Vesiculation and fragmentation experiments

The hydrated glass cylinders were polished to fit tube-shape holders (8 mm i.d. and 5 cm long or 17 mm i.d. and 25 cm long), which were loaded inside the HPT section of the fragmentation device. The HPT section was pressurized, then heated up. These conditions were maintained constant for 30 min, so that water exolution from the oversaturated melt is allowed to proceed within 1–2 h (starting at the glass transition temperature). All the experiments experienced vesiculation and subsequent rapid decompression, except experiments 1 and 2, which were isobarically quenched instead of rapidly decompressed, providing an insight into the pre-fragmentation state. The sequential occurrence of foaming and fragmentation permits the investigation of foamed materials without the potential complications arising from changes in foamed material properties due to an intermediate quenching step.

Some experiments were performed using a single diaphragm, which was disrupted by increasing the pressure in the HPT section up to the diaphragm strength (maximum increase of 4 MPa in less than 5 s). During the course of this work we improved the procedure by installing a set of three diaphragms, separated by two small-volume chambers that were independently pressurized. Pressurizing these small-volume chambers over the strength of the diaphragms while pressure is maintained constant in the HPT section leads to the simultaneous disruption of the three diaphragms and subsequent rapid decompression of the sample. Calculated decompression rates of a 5 cm long sample, range from 5 to 23 MPa/ms [1]. The sample fragments if its strength is overcome and the fragments were collected in the LPT section after rinsing with water. This wet collection procedure produces mass yields of more than 97% of the initial weight. The experimental conditions are reported in Table 1.

3. Pyroclast analysis

3.1. *Size distribution, morphology and water content of the fragments*

The recovered pyroclasts were sieved to obtain fragment size distributions (FSD). The automatic sieving was performed with care to prevent secondary breakage of these sometimes highly porous and fragile particles (errors due to loss of particles and breaking are less than 3 and 5 wt%, respectively). We did not sieve particles below 63 μm in diameter, referred as an arbitrary 40 μm diameter (4.5 Φ units). The mean and median diameters were calculated after [18].

Pyroclasts of different sizes were selected for the morphological study by scanning electron microscopy (JEOL 840A SEM). The aim was to characterize the fragment shapes and outlines in order to infer aspects of the fragmentation processes they experienced.

The glass component of the fragments was analyzed for water content by infrared spectroscopy following the procedure used for the starting hydrated glasses. Where the glass areas were too small for infrared spectroscopy measurements, the fragments were crushed below the size of the smallest bubbles for water determination by Karl–Fischer titration. If the amount of fragmented material was too low for Karl–Fischer titration analysis, water contents were calculated after [11].

3.2. *Vesicularity*

Fragments were selected for qualitative and quantitative analyses of the vesicularity. The porosity, bubble shape and bubble size distribution (BSD) were determined by image analysis from SEM pictures of the embedded fragments used

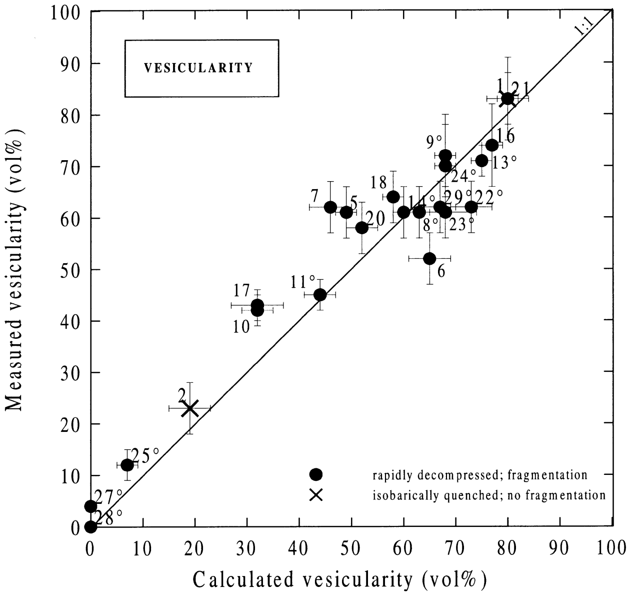

Fig. 1. Measured versus calculated vesicularity. Labels represent the experiment number (° for bubble-bearing starting samples as reported in Table 1). Error bars on measured vesicularities are determined from repeated measurements by image analysis. Error bars on the calculated vesicularities are ±2 vol% plus the water content difference between both ends of the starting glass cylinders (see Table 1).

for the fragment morphology study. The porosity was determined from the two-dimensional sections and considered equivalent to the volume percent of pores. By repeated measurements, it appeared that the higher the porosity, the larger the errors on the vesicularity (up to ±8 at 83 vol%; Table 1), probably due to pumice damage during polishing. The bubble sizes were defined by

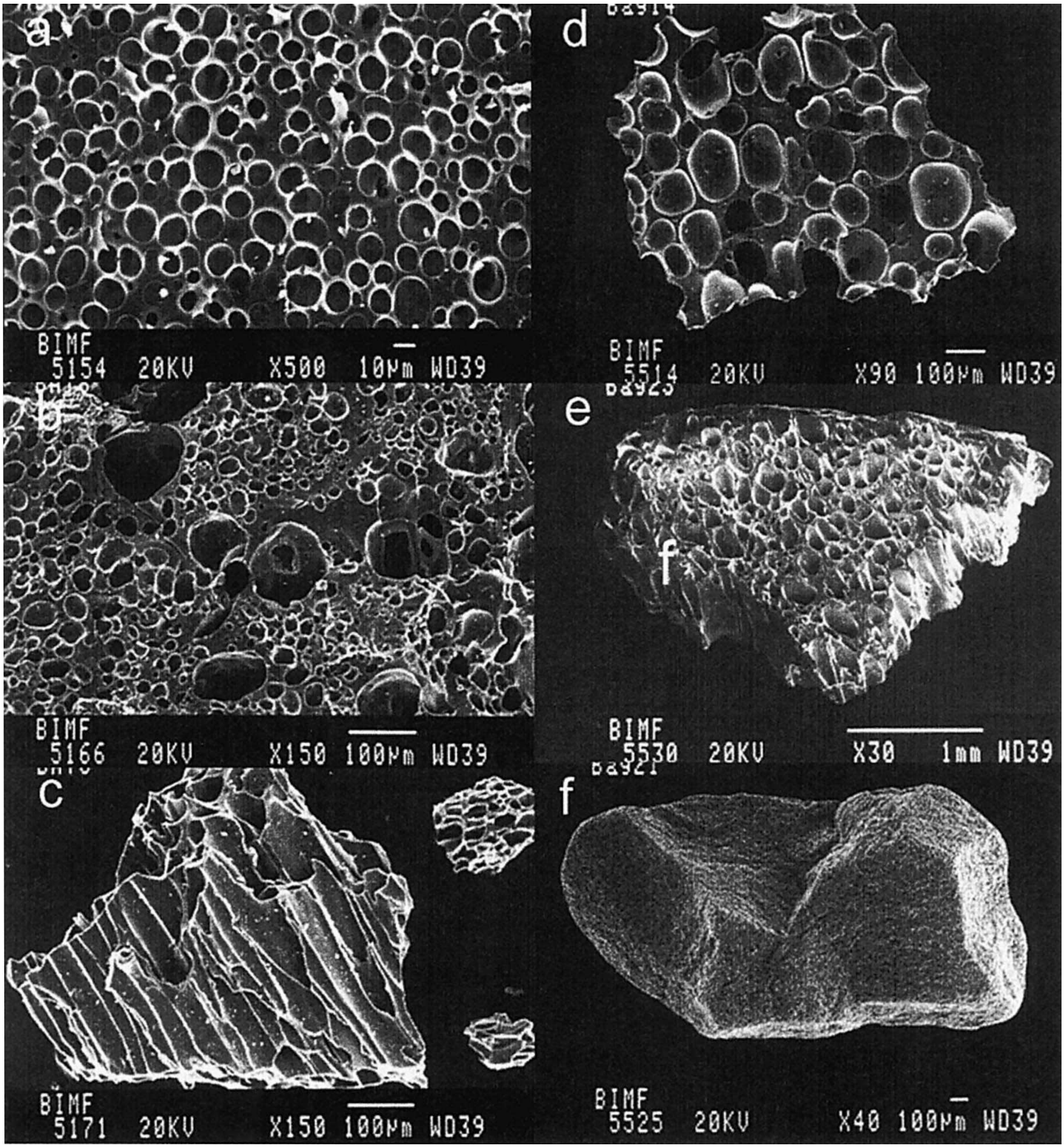

Fig. 2. SEM images showing the pore and fragment morphologies. (a) Experiment 10, (b) experiment 8, (c) experiment 6, (d) experiment 14, (e) experiment 23 and (f) experiment 21.

Table 2
Size distributions of bubbles and fragments

Expt. No.	P (MPa)	Fragment weight (g)	Porosity, α (vol%)	Bubble size distribution (diameter in μm)				Fragment size distribution (Φ unit = $-\log_2 d$ in mm)			
				Main mode (average bubble size)	Second mode	Total range	Average bubble size label[a]	Total range	Mean diameter	Median diameter	D[b]
27°	10	–	4 ± 1	7 ± 1	–	0–25	10	–	–	–	–
18	4	–	64 ± 5	40 ± 10	–	11–102	50	–	–	–	–
5	4.5	0.129	61 ± 5	~ 50	–	5–100	T50	−1.0/4.0	0.46	0.26	2.3
8°	5	7.146	61 ± 1	40 ± 10	~ 100	35–442	50	−2.5/4.5	0.32	0.27	2.1
20	5	–	58 ± 5	2 ± 1	–	1–6	10	–	–	–	–
11°	5	–	45 ± 3	2.5 ± 0.5	–	1–11	10	–	–	–	–
10	10	–	42 ± 3	10 ± 4	–	4–32	10	–	–	–	–
2	10	–	23 ± 3	38 ± 3	–	33–71	50	–	–	–	–
28°	10	7.097	< 1	33 ± 3	–	0–90	50	−2.5/4.5	−0.37	−0.41	2.1
16	5	5.252	74 ± 8	90 ± 40	275 ± 25	33–719	T100	−2.0/4.5	1.22	1.05	2.8
13°	5	0.179	71+8	~ 10	–	1–50	10	−1.5/4.0	−0.68	−0.57	2.2
7	10	4.958	62 ± 15	–	33–274	T50	−2.0/4.5	1.39	1.29	2.7	
17	10	1.159	43 ± 3	5 ± 1	–	1.4–9	10	−1.5/4.0	0.86	0.77	2.1
25°	15	6.836	12 ± 3	40 ± 10	–	34–206	50	−2.5/4.5	−0.58	−0.66	2.0
9°	10	5.546	72 ± 8	200 ± 80	–	35–442	T100	−1.0/4.5	2.00	1.96	3.3
29°	10	0.073	62 ± 5	50 ± 20	175 ± 25	32–728	50	−0.5/4.0	1.22	1.05	2.5
22°	10	5.234	62 ± 5	70 ± 10	30 ± 10	15–177	T50	−1.0/4.5	2.10	2.07	3.3
24°	15	4.793	70 ± 8	125 ± 25	270 ± 25	27–468	100	−0.5/4.5	2.26	2.26	3.9
14°	18	6.036	61 ± 5	50 ± 10	110 ± 5	23–194	T50	−0.5/4.5	2.41	2.37	4.1
19	4	–	–	–	–	–	–	–	–	–	–
1	10	–	83 ± 8	100 ± 20	215 ± 15	33–270	T100	–	–	–	–
6	15	0.290	52 ± 5	~ 40	–	10–100	T50	−0.5/4.5	2.16	2.21	3.5
23°	15	5.576	61 ± 5	70 ± 10	~ 250	23–348	T50	−1.0/4.5	2.09	2.06	3.3
21	15	0.497	83 ± 8	2.5 ± 1	9.5 ± 0.5	1–11	10	−1.5/4.5	1.70	1.65	3.1

° For bubble-bearing starting material.

[a] 10 for average bubble size (aBS) between 1 and 25 μm, 50 for aBS between 25, 75 μm and 100 for aBS above 75 μm and T for tubes.

[b] Power-law exponent.

their measured diameters. In case of very elongated pores (tubes), the full length of the elongation is not measurable because of intersection by the fragmentation planes, so that pore sizes are defined by the diameter of the section normal to the tube elongation preceded by a ‘T’ (for tube).

In each experiment, a minority of the fragments was nearly or fully glassy (i.e. very few bubbles). The vesiculation experiments (without decompression, experiments 1 and 2, Table 1) revealed that these fragments might represent the rims at the contact with the holder. These bubble-depleted parts were not considered in our vesicularity study.

4. Results

4.1. *Vesicularity, pore morphology and bubble size distribution the pyroclasts*

Low porous (<50 vol%) fragments have average vesicularities 5 to 15 vol% higher than the calculated vesicularities (Fig. 1). Vesicularities measured on highly porous fragments are in better agreement with the calculated ones, although fragments from bubble-bearing starting samples are on average 5 vol% (up to 10 vol%) less porous than the calculated values.

Pores are either isotropic (Fig. 2a,b,d) or elongated (Fig. 2c,e). Fragments less porous than 50 vol% only display isotropic pores, but above ~50 vol% porosity, pyroclasts show either tubes or isotropic pores (Table 2). The tubes are always wider than 40 μm, whereas isotropic pores are smaller than ~50 μm in diameter (except in experiment 24). Bubble size distributions are either unimodal or bimodal. Bimodal BSDs only characterize highly porous samples ($\alpha > 60$ vol%), whose starting glass cylinders contained bubbles, so that the population of large bubbles (second mode of the BSD) might represent expansion of the pre-existing pores.

4.2. *Morphology and size distribution of the pyroclasts*

Fragments exhibit plate-like shapes (Fig. 2d,e,f) and have angular outlines, irrespective of the pore size or shape.

Under rapid decompression, three samples did not experience fragmentation (experiments 18, 19, 20) and two were fragmented in a small number of particles (experiments 11, 27). For the other experiments, FSDs are reported in Table 2. The distribution is always unimodal and the particles, ranging from −2.5 to 4.5 Φ units (5.6 to 0.04 mm) correspond to coarse ash according to the classical size scale of volcanic clasts. For most of the experiments, the mean diameters are similar to the median diameters or slightly skewed to finer sizes.

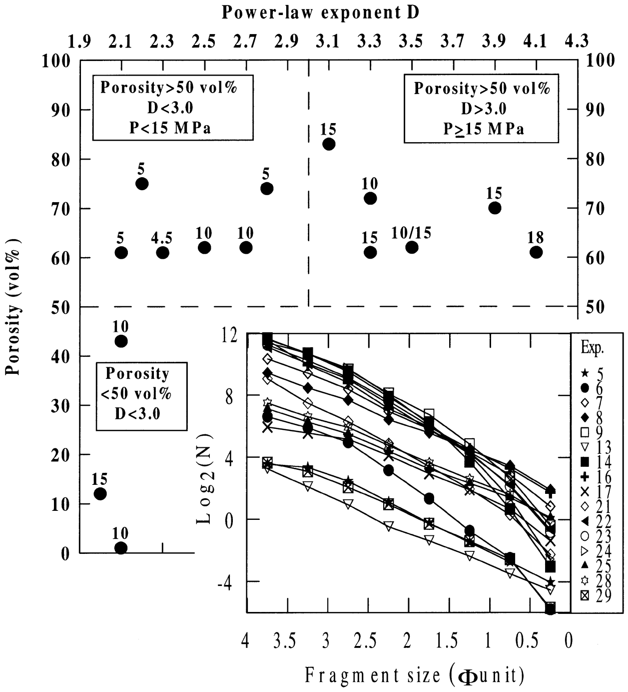

Fig. 3. Parameters controlling the FSD: porosity and pressure effects on the power-law exponent D determined by the slopes of the best fit of the data in the inset. This diagram compares the fragment size distributions with the power-law distribution given by $\log_2(N) = r^{-D}$, where N is the number of fragments with radii larger than r. The fragment number was determined by dividing the total fragment mass in each sieve (only the 0–4 Φ unit range is shown, where all experiments can be compared) by the mass of a single fragment (volume of a sphere corresponding to the sieve mesh time the glass density corrected by the porosity α given in Table 1).

5. Discussion

5.1. Pre-fragmentation conditions

5.1.1. Foaming

Our samples were able to foam under decompression as low as 1 MPa (experiment 2), which was only observed in crystal-bearing samples (heterogeneous nucleation, [19]). Therefore, we think that water nucleation in our samples was heterogeneous, probably due to tiny bubbles, microfractures or impurities in the starting glass cylinders.

A vital point in our assumption that no significant viscous strain occurs during or after fragmentation is the question whether or not fragment porosity equals pre-fragmented foam porosity. The water solubilities calculated for the HPT section conditions agree with measured water contents within 0.4 wt% (Table 1), so that water did not diffuse from the melt to the bubbles during fragmentation. However, calculated cooling times up to 10 s for a particle radius of 2 mm (thermal diffusivity of 4×10^{-7} m^2/s) are larger than the decompression time (10^{-3} s [1]), so that the gas in the fragments are likely to expand after decompression, especially at melt viscosities below 10^8 Pa s for which bubble growth is not impeded. Our experimental pyroclasts are mostly more porous with respect to the calculated vesicularities (except fragments from bubble-bearing starting materials), suggesting that the actual porosity of the pyroclasts might overestimate the porosity prior to fragmentation on average by 5 vol% and up to 15 vol% (Table 1).

5.1.2. Isotropic versus tube pumices

Either isotropic or tube pumices were generated in the experiments. A crucial point for our study is the determination of the pre-fragmentation pore characteristics, i.e. whether tube pumices were formed before or during fragmentation. Tubes can certainly be formed before decompression, as illustrated by the tubes in experiment 1 where no decompression and fragmentation occurred. In order to determine whether tubes can also occur during decompression, we compared the timescales of fragment cooling and bubble elongation. Bubble elongation is parameterized by the capillary number (Ca), giving the ratio of the viscous forces which act to deform a bubble to the interfacial forces which tend to maintain the sphericity [20]: $\mathrm{Ca} = \varepsilon\eta R/\sigma$ (ε is the strain rate, η is the melt viscosity, R is the bubble radius and σ is the surface tension). A Ca number of 1 represents the maximum strain rate due to flow around the bubble that may occur without deforming the bubble to a non-spherical shape [21]. For $\mathrm{Ca} = 1$, $\eta = 10^{5.7}$ Pa s, $R = 25$ μm and $\sigma = 0.15$ N m^{-1} [22], ε is of the order of 10^{-2} s^{-1}, giving a time scale of 100 s (up to 10^4 s for $\eta = 10^{8.1}$ Pa s). The slowest cooling time of ~10 s (see above) is shorter than the bubble elongation timescale, so that bubbles are very unlikely to elongate during or after decompression.

The reason why either isotropic or tube pores are generated is not yet elucidated. However, it seems to be related to bubble size. Indeed, isotropic pumices were generated when bubbles did not grow above ~50 μm in diameter (even at total porosities higher than 70 vol%), but once they grew up to ~50 μm at a total porosity larger than ~50 vol%, pores end up as tubes (except for experiment 24). It seems that ~50 vol% of porosity is the maximal volume for packing spheres of ~50 μm in our experimental configuration where the sample holder closely surrounds the samples, thus restricting lateral bubble expansion.

5.2. Fragmentation conditions

5.2.1. Fragmentation mechanism

From the plate-like shape fragments they recovered from experiments carried out using Mount St. Helens dacite and from observation through high-speed cameras [23], Alidibirov and Dingwell [24] concluded that the main fracturing process occurring in the fragmentation bomb apparatus is a spallation fragmentation. The spallation fragmentation wave refers to the decompression of magma containing pressurized gas vesicles (either close or open porosity). Fragmentation is initiated by the disruption of the interbubble partitions due to the pressure differential between gas in pores

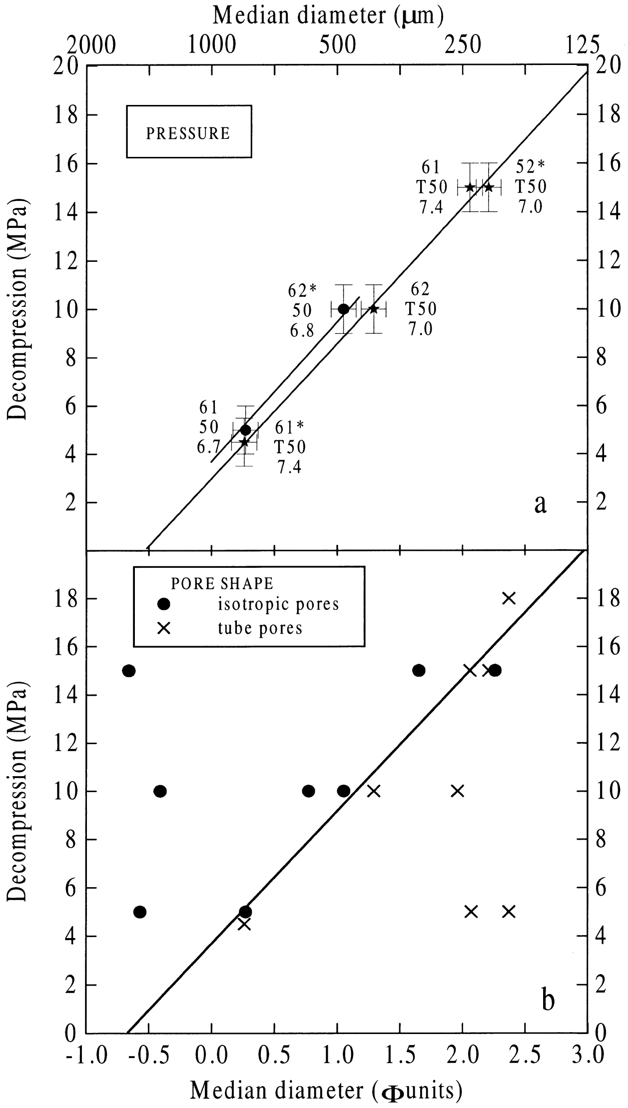

Fig. 4. Parameters controlling the FSD. Median diameter in Φ unit = $-\log_2 d$, where d is the diameter in mm (error of ±0.1 Φ unit). (a) Decompression effect. Labels represent the vesicularity in vol% (* for 8 mm in diameter starting glass cylinders), the average bubble size in µm (T for tubes) and the logarithm of the melt viscosity (see Tables 1 and 2). Error of ±2 MPa correspond to a scatter in the porosity of ±5 vol%. The slopes gives a fragment size decrease of 0.2 Φ/MPa. (b) Effect of the pore shape. The line represents the decompression effect of FSD as given in (a).

and ambient pressure, and propagates downwards into the next layer of pores. Our plate-like shape pyroclasts are very likely to have experienced the same layer-by-layer fragmentation process.

Three size distributions are commonly proposed to account for fragment populations generated in industrial and natural processes: log-normal, power-law and exponential [25]. Fragmentation of a solid by an explosion or with a hammer generates a power-law distribution (log-normal distributions rather describe droplets produced by the breakup of a liquid jet and the exponential distributions characterize sequential processes such as grinding and milling). The inset of Fig. 3 shows that the fragment sizes plotted in the power-law typical coordinates give almost straight lines, suggesting that the FSDs produced by a spallation fragmentation are close to follow a power-law, with exponents D ranging from 2.0 to 4.1 (Table 2).

5.2.2. *Brittle versus ductile fragmentation*

Recently, brittle versus ductile fragmentation of the magma has been discussed [2]. If the applied stress is sufficient to push the strain response of the magma into the glass transition region and overcome its strength, the magma fragments brittle. The following observations of the fragment outlines and calculations allow us to resolve whether a brittle or ductile fragmentation occurred. The tube pumices have outlines sharply cutting the tubes (e.g. Fig. 2c). By a ductile fragmentation, these tubes would have been distorted, tapered or necked at their tips. The brittle fragmentation is confirmed by the process timescales. When the application time of the stress is shorter than the relaxation time required for the melt to deform in a viscous manner, brittle fragmentation can occur. The relaxation time (τ_s) of a product in response to an applied stress is given by the Maxwell relation: $\tau_s = \eta / G$, where η is the viscosity and G the elastic modulus which is proportional to Young's modulus for tensile stresses. For a Young's modulus of 10^{10} Pa, corresponding to a dacitic glassy matrix [26] and bubbly-melt viscosities between 10^7 to $10^{9.4}$ Pa s (Table 1), τ_s ranges from 10^{-3} to 10^{-1} s, respectively. The decompression time Δt_{dec} ($\sim 10^{-3}$ s) is shorter than τ_s, thus suggesting a brittle fragmentation. An exception is experiment 10, having a relaxation time τ_s of $\sim 10^{-3.5}$ s, thus permitting a short viscous deformation during fragmentation.

The decompression threshold at which fragmentation occurs gives the strength of the material. No fragmentation occurred in experiment 20 under rapid decompression at 5 MPa (porosity of 58 vol%, melt viscosity of $10^{7.9}$ Pa s). The sample from experiment 11 was however slightly fragmented at 5 MPa (porosity of 45 vol%, melt viscosity of $10^{7.2}$ Pa s). This suggests a strength for our samples of ~ 5 MPa.

5.2.3. Parameters controlling the fragment size

We investigated the effects of the porosity and pressure on the power-law exponent D (Fig. 3). Samples less porous than 50 vol% are characterized by $D < 3.0$, reflecting that the FSDs are controlled by the large fragments. Above 50 vol% of porosity, FSDs are characterized either by $D < 3.0$ when samples were fragmented below 15 MPa or by $D > 3.0$ when fragmented from 15 MPa (except experiments 9 and 22). This suggests that dense material (porosity < 50 vol%) does not fragment finely under rapid decompression up to 15 MPa. Vesicular material (porosity > 50 vol%) only fragments into fine particles at high decompressions (> 15 MPa). Kaminski and Jaupart [27] used $D < 3.0$ to argue for primary fragmentation (a single event) and $D > 3.0$ for secondary fragmentation (such as repeat fragment collisions). They performed experiments by hitting pumices with a hammer, where the size and the number of the fragments produced depend on the energy input (at small energy input, only small pieces at the surface of the sample can be broken). In contrary, the spallation fragmentation always concerns the whole sample, as the over-pressurized layer of bubbles bursting into the free surface exposes the next layer to fragmentation. Two hypotheses can be proposed for $D > 3.0$ in our experiments, depending on how the physic of the fragmentation mechanisms compares with the experiments of [27]: primary break-up in a context of spallation fragmentation if the processes do not compare or secondary fragmentation of highly vesiculated melts (< 50 vol%) decompressed from 15 MPa (evidence for secondary fragmentation is however not supported by any peculiarities of the fragment shape or texture).

The pressure effect on the FSDs of vesicular samples (porosity > 50 vol%) was further investigated by comparing experiments where starting material have comparable pre-fragmentation physical properties. Fig. 4a shows that the higher the decompression, the finer the particles. The correlation between pressure and fragment size suggests a fragment size decrease of 0.2 Φ unit/MPa. Higher decompressions indeed involve larger released energy applying on any flaws and heterogeneities of the sample through which failure will be initiated. Fig. 4b shows the effect of the pore shape on the FSDs, suggesting that tube pumices are generally more finely fragmented than samples with isotropic pores. This could reflect the low strength of a material containing tube pores due to thin walls in between the tubes. The effect of the melt viscosity on FSD is not straightforward and would require further systematic investigations to be determined.

5.2.4. Applicability to dome explosions

Our experimental device generating fragmentation by rapid decompression best simulates dome explosions, consequently to a destabilization (e.g. landslide) whereby the underlying pressurized magma is suddenly exposed to much lower pressures. Melnik and Sparks [28] have recently theoretically demonstrated that ground deformation patterns or vulcanian eruptions observed in Soufriere Hills dome (Montserrat) [29] could be attributed to pressurization at shallow levels (upper part of the conduit) rather than in the deep magma chamber. Our experiments are consistent with this model, by showing that small overpressures (less than 20 MPa) can lead to magma fragmentation when rapidly decompressed. In addition, we suggest that the magnitude of the decompression is a parameter much more efficient in dome explosions than melt porosity, bubble shape or melt viscosity of the pre-fragmented magma. However, our starting samples are crystal-free, thus having physical properties, which do not match those of magmas in common domes. Experimental investigation using crystal-bearing samples is in progress.

Acknowledgements

This work was supported by the EC-TMR-network (FMRX-CT96-0063) on 'hydrous silicate melts' and by the EC (ENV4-CT98-0703) on 'The Physics of Explosive Volcanism', as well as DFG grants to D.B.D. We thank B.C. Schmidt for discussion. We are grateful to G. Hermannsdörfer for technical assistance, O. Leitner for careful sample preparation and C. Drummer for assistance with the SEM study. We acknowledge R.S.J. Sparks and O. Navon for helpful reviews. ***[FA]***

References

[1] D.B. Dingwell, Magma degassing and fragmentation: recent experimental advances, in: A. Freundt, M. Rosi (Eds.), From Magma to Tephra; Modeling Physical Processes of Explosive Volcanic Eruptions, 1998, pp. 1–23.

[2] D.B. Dingwell, Recent experimental progress in the physical description of silicic magma relevant to explosive volcanism, in: J.S. Gilbert, R.S.J. Sparks (Eds.), The Physics of Explosive Volcanic Eruptions, Geol. Soc. London Spec. Publ. 145, 1998, pp. 9–26.

[3] H.M. Mader, J.C. Phillips, R.S.J. Sparks, B. Sturtevant, Dynamics of explosive degassing of magma: observations of fragmenting two-phase flows, J. Geophys. Res. 101 (1996) 5547–5560.

[4] M. Alidibirov, A model for viscous magma fragmentation during volcanic blasts, Bull. Volcanol. 56 (1994) 459–465.

[5] P. Papale, Strain-induced magma fragmentation in explosive eruptions, Nature 397 (1999) 425–428.

[6] H.M. Mader, Y. Zhang, J.C. Phillips, R.S.J. Sparks, B. Sturtevant, E. Stolper, Experimental simulations of explosive degassing of magma, Nature 372 (1994) 85–88.

[7] R.S.J. Sparks, J. Barclay, C. Jaupart, H.M. Mader, J.C. Phillips, Physical aspects of magmatic degassing I. Experimental and theoretical constraints on vesiculation, in: M.R. Carroll, J.R. Holloway (Eds.), Volatiles in Magmas, Reviews in Mineralogy 30, Mineral. Soc. Am., 1994, pp. 413–445.

[8] Y. Zhang, B. Sturtevant, E.M. Stolper, Dynamics of gas-driven eruptions: experimental simulations using CO_2-H_2O-polymer system, J. Geophys. Res. 102 (1997) 3077–3096.

[9] M. Alidibirov, D.B. Dingwell, Magma fragmentation by rapid decompression, Nature 380 (1996) 146–148.

[10] M. Alidibirov, D.B. Dingwell, An experimental facility for the investigation of magma fragmentation by rapid decompression, Bull. Volcanol. 58 (1996) 411–416.

[11] C.W. Burnham, Development of the Burnham model for prediction of H_2O solubility in magmas, in: M.R. Carroll, J.R. Holloway (Eds.), Volatiles in Magmas, Reviews in Mineralogy 30, Mineral. Soc. Am., 1994, pp. 123–129.

[12] C. Jaupart, S. Tait, Dynamics of eruptive phenomena, in: J. Nicholls, J.K. Russell (Eds.), Modern Methods of Igneous petrology: Understanding Magmatic Processes, Reviews in Mineralogy 24, Mineral. Soc. Am., 1989, pp. 213–238.

[13] A. Saul, W. Wagner, A fundamental equation for water covering the range from the melting line to 1273 K at pressures up to 25 000 MPa, J. Phys. Chem. 18 (1989) 1537–1565.

[14] R. Knoche, D.B. Dingwell, S.L. Webb, Melt densities for leucogranites and granitic pegmatites: partial molar volumes for SiO_2, Al_2O_3, Na_2O, K_2O, Li_2O, Rb_2O, Cs_2O, MgO, CaO, SrO, BaO, B_2O_3, P_2O_5, $F_2O_{\ 1}$, TiO_2, Nb_2O_5, Ta_2O_5 and WO_3, Geochim. Cosmochim. Acta 59 (1995) 4645–4652.

[15] K.U. Hess, D.B. Dingwell, Viscosities of hydrous leucogranitic melts: non-arrhenian model, Am. Miner. 81 (1996) 1297–1300.

[16] N.A. Frankel, A. Acrivos, The constitutive equation for emulsion, J. Fluid Mech. 44 (1970) 65–78.

[17] M. Nowak, H. Behrens, The speciation of water in haplogranitic glasses and melts determined by in situ near-infrared spectroscopy, Geochim. Cosmochim. Acta 59 (1995) 3445–3450.

[18] R.L. Folk, W.C. Ward, Brazos River bar: a study in the significance of grain size parameters, J. Sedim. Petrol. 27 (1957) 3–26.

[19] O. Navon, V. Lyakhovsky, Vesiculation processes in silicic magmas, in: J.S. Gilbert, R.S.J. Sparks (Eds.), The Physics of Explosive Volcanic Eruptions, Geological Society, London, Spec. Publ. 145, 1998, pp. 27–50.

[20] D.J. Stein, F.J. Spera, Rheology and microstructure of magmatic emulsions: theory and experiments, J. Volcanol. Geotherm. Res. 49 (1992) 157–174.

[21] K.V. Cashman, M.T. Mangan, Physical aspects of magmatic degassing II. Constraints on vesiculation processes from textural studies of eruptive products, in: M.R. Carroll, J.R. Holloway (Eds.), Volatiles in Magmas, Reviews in Mineralogy 30, Mineral. Soc. Am., 1994, pp. 447–478.

[22] N.S. Bagdassarov, A. Dorfman, D.B. Dingwell, Effect of alkalis, phosphorus and water on surface tension of haplogranite melt, Am. Miner. 85 (1999) 33–40.

[23] M. Alidibirov, V. Panov, Magma fragmentation dynamics: experiments with analogue porous low-strength material, Bull. Volcanol. 59 (1998) 481–489.

[24] M. Alidibirov, D.B. Dingwell, Three fragmentation mechanisms for highly viscous magma under rapid decompression, J. Volcanol. Geotherm. Res., in press.

[25] S. Redner, Fragmentation, in: H.J. Herrmann, S. Roux (Eds.), Random Material and Processes, Statistical Mod-

els for the Fracture of Disordered Media, North-Holland, New York, 1990, pp. 321–348.

[26] M. Alidibirov, D.B. Dingwell, R.J. Stevenson, K.U. Hess, S.L. Webb, J. Zinke, Physical properties of the 1980 Mount St. Helens cryptodome magma, Bull. Volcanol. 59 (1997) 103–111.

[27] E. Kaminski, C. Jaupart, The size distribution of pyroclasts and the fragmentation sequence in explosive volcanic eruptions, J. Geophys. Res. 103 (1998) 29759–29779.

[28] O. Melnik, R.S.J. Sparks, Nonlinear dynamics of lava dome extrusion, Nature 402 (1999) 37–41.

[29] B. Voight et al., Magma flow instability and cyclic activity at Soufriere Hills Volcano, Montserrat, B.W.I., Science 283 (1999) 1138–1142.

Etude complémentaire

Article: MARTEL C., DINGWELL D.B., SPIELER O., PICHAVANT M. & WILKE M. (2001) Experimental fragmentation of crystal- and vesicle-bearing silicic melts. *Bull. Volcanol. 63, 345-359*.

Financements : EC (ENV4-CT-98-0703) on "The Physics of Explosive Volcanism".

Dans le but de mieux simuler le processus de fragmentation de produits de dôme, les expériences de fragmentation précédentes ont été complétées par une étude de l’influence des cristaux sur la distribution de taille des fragments. La préparation des échantillons est similaire à celle décrite précédemment, mais comprend l’ajout avant hydratation de 20, 35 et 45 vol% de cristaux d’alumine tamisés à 350 µm, et 5 échantillons contenant en plus des cristaux d’alumine tamisés à 90 µm pour simuler l’effet de microlites entre des phénocristaux. La distribution de taille des fragments récupérés est ici obtenue grâce à un *laser particle sizer* jusqu’à la fraction 0.5 µm. Les distributions de taille de fragment sont généralement polymodales, avec un pic étroit à 350 µm correspondant à la taille des phénocristaux (fragments composés d’un cristal), un large pic à ~70 µm correspondant à la taille de cristaux se fracturant lors de la phase d’hydratation, un pic à ~1500 µm dont la hauteur augmente avec la teneur en cristaux, et un pic à 4000 µm pour les expériences décomprimées à faible température (600°C) ou faible pressions (60 bars). Contrairement aux échantillons aphyriques, la présence de cristaux ne permet plus le développement de bulles > 80 µm de diamètre et sous forme de tubes, même à des porosités > 50 vol%. De manière générale, le seuil de la pression de fragmentation augmente avec la teneur en cristaux.

En conclusion de cette étude expérimentale, il a été possible de définir l’influence sur la distribution de taille des fragments de paramètres tels que la magnitude de la décompression, la teneur et la taille initiales des bulles et des cristaux. Cependant, le problème majeur pour une extrapolation aux produits naturels, i.e., retrouver la magnitude de la décompression en fonction d’une étude texturale et de distribution de tailles des pyroclastes, reste un problème d’échelle entre le laboratoire et le volcan… Autrement dit, quelle devrait être la taille d’un échantillon expérimental pour que sa distribution de taille de fragment ne soit pas une fonction de son volume initial ? Des comparaisons ont été faites entre les échantillons synthétiques de ces deux études (0.8 et 2 cm de diamètre pour 2 cm de long) et les échantillons naturels de 5 cm de diamètre utilisés par Spieler et al. (2003), montrant que certains échantillons de 2 et 5 cm de diamètre décomprimés à haute pression (250 bars) présentaient des distributions de taille similaires. Cependant, les fragments les plus larges obtenus sur certains échantillons de 0.8 cm de diamètre et sur ceux décomprimés à basse pression avaient des tailles en relation avec le diamètre initial. Actuellement, les bombes de fragmentation (installées depuis au LMU à Munich) permettent l’utilisation d’échantillons de plus gros volume, ce qui est certes une amélioration, mais ne résout pas la vraie question du rapport entre une magnitude de décompression et le diamètre minimal d’un échantillon pour que sa distribution de taille de fragments en soit indépendante, et il y ait alors un véritable moyen de déterminer les valeurs des décompressions subies par une colonne magmatique à partir de la distribution de taille des pyroclastes d’une éruption donnée. Sinon, l’outil expérimental ne peut être utilisé que pour l’obtention de données qualitatives sur les fragments (tailles, morphologies), pour des comparaisons relatives de l’influence de divers paramètres, ou pour des caractérisations de l'onde de fragmentation (vitesse de propagation).

I.6- CONCLUSIONS GENERALES

L’objectif que j'ai poursuivi ces 15 dernières années concerne la compréhension des mécanismes éruptifs des volcans d’arc, et en particulier des causes menant aux différents styles éruptifs observés et dont les impacts en termes de risques et de gestions des crises volcaniques sont extrêmement différents. La comparaison des échantillons naturels avec les produits d’expériences d’équilibre de phases a permis de déterminer que pour les réservoirs magmatiques de petit volume, les conditions de stockage des magmas des futures éruptions Pliniennes et à dôme pouvaient être comparables. La détermination des conditions pré-éruptives, que ce soit au travers de l’utilisation de géothermo/baro/hygromètres sur les produits naturels ou par une étude plus fine combinant les produits naturels et expérimentaux, constitue une étape nécessaire avant toute étude des conditions éruptives d’un système volcanique, ne serait-ce que pour la détermination des paramètres syn-éruptifs initiaux, en particulier, la pression, la température, la teneur en volatils dissous et la composition du magma en sortie de réservoir magmatique.

Le paramètre syn-éruptif majeur à déterminer est alors la vitesse d’ascension du magma, directement responsable du caractère à l’équilibre ou en déséquilibre du dégazage et de la cristallisation dans le conduit volcanique. Les seuls témoins des vitesses d’ascension magmatique que nous ayons en l’absence de suivi sismique des crises éruptives se retrouvent au travers de la porosité et des microlites des pyroclastes naturels. Les projets réalisés de décompressions expérimentales ont en particulier permis d’associer un taux de décompression à une densité numérique, une proportion volumique et une taille de bulles et/ou de microlites. Les expériences de fragmentation magmatique ont ensuite permis de comparer l’influence de ces paramètres, i.e., la proportion et la taille des bulles et des cristaux, ainsi que la pression de fragmentation sur la distribution de taille des pyroclastes éjectés. A mon sens, les publications résultant de mon activité de recherche constituent de réelles avancées dans la compréhension des différents processus pré- et syn-éruptifs de ce type de volcanisme.

Parce qu'elle permet de replacer les magmas dans leurs conditions naturelles de pression, température, et oxydoréduction, l'approche expérimentale apporte des informations de première importance sur les processus magmatiques, en retour validés par l'adéquation avec les produits naturels. Cependant, un certain nombre de points récurrents sont régulièrement source de questionnement:

- *Choix de l'échantillon de départ pour les expériences.* La détermination des conditions de stockage d'un magma au travers d'expériences de cristallisation de phase à l'équilibre, nécessite le choix d'une composition de liquide magmatique représentative de celle de la roche totale du magma en équilibre thermodynamique dans le réservoir (Pichavant et al., 2007). La stratégie expérimentale jusqu'à présent adoptée est de fondre les produits émis en surface (en considérant que les phénocristaux n'ont a priori pas été modifiés au cours de l'éruption et que la composition chimique du liquide silicaté baignant ces phénocristaux est retrouvée par fusion du verre résiduel avec ses microlites). En revanche, la teneur initiale en éléments volatils dissous dans le liquide silicaté a été est perdue par dégazage du magma au cours de l'ascension et constitue une inconnue investiguée par ajout de différentes proportions d'éléments volatils (H_2O, CO_2, SO_2, etc…). Cependant, au cours de leur différentiation, certains réservoirs subissent des intrusions répétées de magmas provenant de réservoirs plus profonds, témoignés dans les produits émis par des traces de mélanges mécaniques sous forme d'enclaves ou de rubanements, et à l'échelle cristalline, de reliques de minéraux déstabilisés, de phénocristaux intensément zonés, et même de microlites cristallisés à partir du liquide mafique au contact du magma résidant plus froid. La difficulté de l'expérimentaliste à la recherche des conditions de stockage des magmas consiste alors à s'affranchir au maximum de ces magmas étrangers au réservoir considéré. Ceci suppose une étude détaillée préalable des produits naturels afin d'identifier et d'évaluer l'importance des reliques de ces compositions étrangères, puis devrait comporter un procédé permettant de s'en affranchir dans le verre de départ des expériences (par exemple "retirer" les cœurs zonés des phénocristaux, physiquement par tri manuel ou virtuellement par composition reconstituée)... Une alternative fréquemment utilisée à ces expériences de cristallisation consiste à opérer par expériences de fusion + recristallisation partielles. Dans ce cas, le produit naturel émis est directement utilisé comme produit de départ, sans cycles préalables de fusion, replacé avec différentes natures et teneurs de volatils dissous dans des conditions permettant la fusion du verre interstitiel et de la périphérie des phénocristaux dont la composition est supposée en équilibre thermodynamique avec les conditions de réservoir superficiel. Cette proportion de liquide fondu (interstitiel + microlites + bordure des phénocristaux) constitue alors le produit de départ qui va recristalliser, comme pour les expériences précédentes de cristallisation, sous diverses conditions de P, T, fO_2 jusqu'à ce que la nature, la proportion et la composition des phases recristallisant soient comparables aux produits naturels. Ces expériences de fusion + recristallisation partielles permettent en théorie une meilleure simulation des compositions des magmas du réservoir superficiel dans le cas de forts mélanges magmatiques, et présentent en plus l'avantage d'être moins sensibles aux problèmes de nucléation des minéraux. Cependant, d'une part il n'est pas toujours aisé de contrôler la fusion partielle et d'autre part, les phases recristallisent généralement en bordure des phénocristaux existants (sites de nucléation préférentiels), parfois sur quelques microns, rendant ainsi parfois l'identification des phases néoformées et leur analyse chimique relativement difficile.

- *Limitation techniques à l'étude des processus magmatiques.* Les méthodes d'observation in-situ (au travers d'outils transparents haute pression et haute température) sont a priori idéales pour l'étude de la vésiculation des bulles, car elles permettent l'observation directe et complète (sans hiatus) du processus, en s'affranchissant d'un lourd programme expérimental sérié en temps dans des autoclaves classiques (sans fenêtres transparentes). Cependant, l'outil transparent idéal n'est techniquement pas encore au point… L'autoclave utilisé par C. Gondé au cours de sa thèse n'a pas la résolution optique nécessaire et pose des problèmes de perte en eau de l'échantillon (en l'absence d'encapsulage). Bien que techniquement difficiles, les modifications à apporter à cet outil sont réalisables. Cependant, l'utilisation de cellules à enclumes de diamant non hydrothermales, permettant une décompression isotherme (cellules à membranes par exemple), apparaît à présent comme le moyen le plus prometteur pour l'étude du dégazage, et est en cours de réflexion pour les années à venir. Un autre exemple de limitation apportée par les outils expérimentaux à l'étude des processus magmatiques est celui de la fragmentation magmatique dans le cas des éruptions Pliniennes, pour lesquelles aucun outil expérimental ne permet une étude en conditions réalistes (composition, pression, température, vitesse d'ascension), c'est-à-dire par décompression d'un magma en mouvement.

- *Extrapolation des expériences à l'échelle naturelle.* Dans le cas des expériences de fragmentation par décompression instantanée, la recherche du seuil de la pression de fragmentation du magma me paraît pertinente et applicable aux magmas naturels, parce que la rupture de cohésion interne du magma dépend de propriétés physico-chimiques indépendantes de la quantité de matériau mis en jeu (hormis la question de l'extrapolation des propriétés des ondes de choc et de fragmentation confinées dans un autoclave isochore au conduit ou dôme volcanique). En revanche, les études que j'ai menées sur l'influence de la taille des bulles et des cristaux sur la distribution de taille finale des fragments (FSD; Fragment Size

Distribution) posent assurément un problème d'échelle et d'applicabilité directe des résultats obtenus à partir de cylindres expérimentaux à une vraie taille de conduit magmatique. Le problème revient à obtenir une relation entre la FSD et les paramètres investigués (taille des bulles et/ou cristaux et magnitude de la décompression) indépendante de la taille du cylindre expérimental initial. Ce cas paraît envisageable pour les décompressions pulvérisant les échantillons, pour lesquels la taille moyenne des fragments récoltés est plusieurs ordres de grandeur plus petite que celle du cylindre initial. Plus la différence entre la taille des fragments et celle du cylindre initial diminue, plus il y a de risque que la FSD soit en partie contrôlée par la taille de l'échantillon de départ, et ce risque doit être évalué dans le cas d'une éventuelle poursuite de l'étude. Ce problème récurrent de mise à l'échelle naturelle des produits expérimentaux peut également se poser dans le cas de l'étude du dégazage, pour lequel la taille des bulles peut être limitée par la taille de la charge expérimentale et n'est pas directement transposable à la distribution de taille des bulles des échantillons naturels. Ce problème ne concerne a priori pas les déterminations de pression de nucléation ou de densité numérique initiale de bulles, mais potentiellement le processus de croissance et de coalescence.

Il ne s'agit pas ici d'épiloguer sur la taille ou la nature des dispositifs expérimentaux qui ne seront jamais à l'échelle du volcan ou des analogues expérimentaux qui ne seront jamais aussi complexes que les produits naturels, mais de s'astreindre à réfléchir sur les conditions et les limites d'extrapolation des choix stratégiques (outils, matériaux, et processus étudiés) et d'apprécier au plus juste leur applicabilité aux processus volcaniques.

Malgré ces problèmes récurrents à l'expérimentation, la stratégie d'approche des processus magmatiques en couplant une étude des produits naturels et des expériences haute pression et haute température me paraît fournir des informations uniques et très complémentaires des études de terrain en amont sur les dépôts et dynamismes éruptifs, et en aval sur les modélisations numériques des éruptions. Malgré les efforts déployés, les causes du passage d'éruptions effusives à explosives des volcans d'arc ne me semblent pas clairement définies. En effet, l'explosivité de l'éruption est directement reliée au devenir du gaz s'exsolvant du liquide silicaté, et les études sur le dégazage bulles ont notamment contribuées à définir les conditions de nucléation et de croissance des bulles. Cependant, maintenant que l'on peut définir les densités numériques et les vitesses de croissance des bulles en fonction d'un certain nombre de paramètres, il s'avère impératif d'étudier les possibilités de perte de ces gaz pour progresser dans la compréhension de la dualité des éruptions explosives versus effusives. De même, la possibilité à basse pression de cristallisation massive de microlites liée à cette exsolution des volatils peut avoir des conséquences majeures sur la possibilité de repressuriser un magma, notamment par augmentation drastique de sa viscosité et par exsolution subséquente de silice pouvant colmater les pores (Sparks, 1997).

A partir des études de dégazage magmatique et de cristallisation de microlites, et avec l'objectif de se rapprocher encore plus près des processus responsables du potentiel explosif d'un magma, je projette à présent deux études majeures :

a) ***l'évolution de la perméabilité des magmas*** **au cours de leur ascension ou de leur déformation dans le conduit volcanique;**

b) ***une modélisation thermodynamique du processus de cristallisation,*** **permettant notamment une reconstitution des conditions de cristallisation des microlites.**

Ces deux points constituent l'objet de la section III- ***Projets de recherche*****.**

PARTIE II- ENSEIGNEMENT, ENCADREMENT, RESPONSABILITES SCIENTIFIQUES ET ADMINISTRATIVES

II.1- ENSEIGNEMENT

2 h de cours / an depuis 2005 sur la "Dynamique éruptive" (niveau M1)
TP de paléontologie et de cartographie en 1996 (niveau DEUG)

II.2- ENCADREMENT D'ETUDIANTS

Thèses universitaires

Edith MOLLARD (débutée en 2007, Orléans) *Cinétiques syn-éruptives de croissance des plagioclases dans les magmas différenciés*.
Direction : J.-L. Bourdier ; Encadrement : C. Martel (90 %).
Financement : Bourse MRT.
Financement des moyens : ANR CATT "Explosivité des dômes de lave, approche analytique, expérimentale et numérique ; Application aux volcans antillais" (EXPLANT); 03/2006-03/2009 (C. Martel).

Charlotte GONDE (2008, Orléans) *Etude expérimentale in-situ du dégazage d'un magma rhyolitique*.
Direction : M. Pichavant; Co-encadrement : H. Bureau (LPS Saclay / IMPMC) et C. Martel (50 %).
Financement : Bourse CEA.
Financement des moyens : ANR CATT "Explosivité des dômes de lave, approche analytique, expérimentale et numérique ; Application aux volcans antillais" (EXPLANT) 03/2006-03/2009 (C. Martel).

Stéphane POUSSINEAU (2005, Orléans) *Dynamique des magmas andésitiques : approche expérimentale et pétrostructurale ; Application à la Soufrière de Guadeloupe et à la Montagne Pelée*.
Direction : J.-L. Bourdier; Co-encadrement : M. Pichavant, L. Arbaret et C. Martel (20 %).
Financement : Bourse MRT.
Financement des moyens : Programme National sur les Risques Naturels (PNRN) "Systèmes magmatiques et styles éruptifs violents aux Antilles : processus physico-chimiques fondamentaux" 2001-2002 (M. Pichavant et B. Villemant).

Stages de Recherche de Master 2

Alain MOUSSADJI (2006, Orléans) *Dégazage expérimental d'un magma rhyolitique*.
Co-direction : C. Martel (50 %) et A. Burgisser.

Ahmed RADADI ALI (2005, Orléans) *La décompression expérimentale des magmas de la Montagne Pelée.*
Direction : C. Martel (100%).

Stages de Recherche de Master 1 et autres

Elisabeth TRY (2008, Orléans) *Etudes pétrographiques et minéralogiques de quelques éruptions Pliniennes de la période récente de la Montagne Pelée.*
Co-direction : M. Pichavant et C. Martel (50 %).

Félix CHAUVEAU (Février 2008) Stage d'observation en entreprise de niveau 3^{e}.
Direction : C. Martel.

II.3- ADMINISTRATION DE LA RECHERCHE

- Membre élu au Comité d'Experts disciplinaire (CED) de l'Université d'Orléans en section 35-36 (Collège B) depuis 2009.
- Membre nommé au Comité Thématique "Risques et Catastrophes Telluriques" de la Section Sciences de la Terre de l'INSU depuis 2009.
- Membre élu du Conseil de Laboratoire de l'ISTO depuis 2008.

- Animatrice scientifique de l'équipe « Magmas et Liquides silicatés » en 2006-2007.
- Membre suppléant du collège B de la Commission de Spécialistes de l'Université d'Orléans en section 35-36 de 2005 à 2008.

II.4- EVALUATIONS DE PROJETS ET D'ARTICLES SCIENTIFIQUES

- Rapporteur sollicité pour les revues internationales suivantes (~2 / an):

  Contributions to Mineralogy and Petrology (3)
  Earth and Planetary Sciences Letters (1)
  Geochimica and Cosmochimica Acta (1)
  Geology (2)
  Geophysical Reasearch Letters (3)
  Journal of Petrology (1)
  Journal of Volcanology and Geothermal Research (4)

  .

- Rapporteur sollicité pour l'évaluation de projets internationaux (Israelian Foundation) et nationaux (ACI, SEDIT, Mi-Lourds…)

- Participation à 1 audition pour recrutement de poste ITA.

- Rapporteur extérieur de la Thèse de Giada Iacono-Marziano (2005, Italie).

II.5- PARTICIPATIONS AUX PROGRAMMES DE RECHERCHES NATIONAUX ET INTERNATIONAUX

Les différents projets sur lesquels j'ai émargés depuis 1994 et les demandes de financements réalisées sont synthétisées dans le Tableau 3 ci-dessous.

Le 1er projet PNRN (1994-1997) a permis de financer une partie du fonctionnement de ma thèse.

Les projets européens ont financé la totalité des dépenses relatives à mon post-doctorat en Allemagne.

L'acquisition de la Presse Paterson à l'ISTO a bénéficié des financements de la Région Centre, de l'ACI Jeunes Chercheurs (co-porteurs: L. Arbaret et C. Martel), du programme national Mi-Lourds de l'INSU, d'une partie de la CRV (Coordination de la Recherche en Volcanologie) et des Fonds Propres de l'ISTO.

Tableau 3. Demandes de financements scientifiques.

Cadre	**Type de programme**	**Titre du projet**	**Porteurs**	**Ma participation**	**Dates**	**Somme allouée**
Projets en cours	BQR Univ. Orléans	Evolution syn-éruptive de la perméabilité des magmas	**Martel C**	80 %	2009	9.1 k€ demandés
Projets d'entrée au CNRS	ANR thématique CATT	Explosivité des dômes de lave - Approche analytique, expérimentale et numérique Application aux volcans Antillais	**Martel C**	80 %	Juin 2009 2006	350 k€
	ANR Blanc	Usine de différenciation des Antilles	Chauvel C Pichavant M	30 %	2008 2006	124 k€
	ACI thématique	Dynamique éruptive des volcans antillais	Druitt TH	100 %	2005 2003	?
	DyEti	?	Chauvel C	30 %	2005 2003	?
	PNRN (CNRS/INSU)	Systèmes magmatiques et styles éruptifs violents aux Antilles : Processus physico-chimiques fondamentaux	Pichavant M Villemant B	30 %	2002 2001	?
Acquisition Presse Paterson	ACI Jeunes Chercheurs	Suspensions magmatiques	Arbaret L **Martel C**	70 %	2007 2005	130 k€
	Equipement Mi-Lourds INSU	Propriétés des suspensions magmatiques dans un champ de pression anisotrope	Pichavant M	75 %	2003 et 2005	60 k€
	Région Centre				2004	140 k€
	CRV	Propriétés rhéologiques des dômes andésitiques	Arbaret L **Martel C**	50 %	2003 2001	10 k€
Post-doctorat	BGI Visitors' Program	-	Rubie DC	100 %	2001 2000	?
	EU	IHP – Access to Research Infrastructures	Rubie DC	100 %	2000 1999	?
	EC	The physics of explosive volcanism	Dingwell DB	100 %	1999 1998	?
	EC-TMR Network	Hydrous silicate melts	Dingwell DB	100 %	1998 1997	?
Doctorat	PNRN (CNRS/INSU)	Risque volcanique	?	100 %	1997 1994	?

La réalisation de mon projet d'entrée au CNRS a bénéficié de différents financements ACI (Actions Concertées Incitatives) et ANR (Agence Nationale de la Recherche). La fin de ce projet est notamment incluse dans l'ANR thématique CATT (CAtastrophe Telluriques et Tsunami) que je coordonne depuis 2006 et jusqu'à Juin 2009:

ANR CATT "EXPLANT", Janvier 2006 – Juin 2009

"Explosivité des dômes de lave - Approche analytique, expérimentale et numérique Application aux volcans" (acronyme: EXPLANT).

Ce projet ANR a été financé à hauteur de 350 k€ et regroupe 4 partenaires et 24 personnes listées ci-dessous:

Partenaire 1: ISTO (Institut des Sciences de la Terre d'Orléans): 214 k€
Martel C (CR; Coord.), Arbaret L (MC), Bourdier JL (Pr), Burgisser A (CR), Champallier R (IE), Gaillard F (CR), Lesne P (Doc), Mollard E (Doc), Picard D (Doc), Pichavant M (DR), Poussineau S (PostDoc), Scaillet B (DR).
Partenaire 2 : LMV (Laboratoire Magma et Volcans, Clermont-Ferrand): 75.5 k€
Druitt TH (Pr; Resp.), Cluzel N (Doc/IE), Giachetti T (doc), Kelfoun K (MC), Laporte D (DR), Provost A (Prof).
Partenaire 3: CRPG (Centre de Recherche Pétrographique et Géochimique, Nancy): 26 k€
Deloule E (DR; Resp.), Champenois M (Ing), Rollion C (Ing).
Partenaire 4: LPS (Laboratoire Pierre Süe, Saclay): 34.5 k€
Bureau H (CR; Resp.), Gondé C (Doc), Massare D (Ing).

II.6- COLLABORATIONS SCIENTIFIQUES PRINCIPALES DEPUIS 1996

BOURDIER Jean-Louis, ISTO, Orléans*
BUREAU Hélène, IMPMC, Paris 7*
BURGISSER Alain, ISTO, Orléans
CHAMPALLIER Rémi, ISTO, Orléans*
DELOULE Etienne, CRPG, Nancy*
DINGWELL Don, IMU, Munich, Allemagne
GOURGAUD Alain, LMV, Clermont-Ferrand
HOLTZ François, Université de Hanovre, Allemagne
PICHAVANT Michel, ISTO, Orléans
RAEPSAET Caroline, LPS, Saclay*
SCAILLET Bruno, ISTO, Orléans
SCHMIDT Burkhard, GZG, Göttingen, Allemagne
SPIELER Oliver, IMU, Munich, Allemagne
WILKE Max, Université de Hanovre, Allemagne

(* collaborations pour les projets en cours)

PARTIE III- PROJET DE RECHERCHE

Dégazage et cristallisation syn-éruptifs: rôle sur l'explosivité des volcans d'arc

III-1- INTRODUCTION

Quand et de quelle nature sera la prochaine éruption d'un volcan d'arc donné ? C'est sûr, on est encore très loin de proposer une réponse fiable, en partie parce qu'à la base, on ne peut pas encore répondre sans équivoque à la question des causes de l'occurrence de l'un ou l'autre des divers styles éruptifs observés. Il est probable que la recherche de ces causes nécessitera encore plusieurs dizaines d'années d'études. Les avancées scientifiques des vingt dernières années sont pourtant remarquables: on a aujourd'hui les moyens de déterminer les conditions de stockage, d'écoulement, de dégazage et de cristallisation au cours de l'ascension et d'appréhender les cinétiques de ces processus. Les simulations réalisées à partir des données obtenues permettent d'envisager des scénarios éruptifs très variables et complexes (Melnik et Sparks, 2002a et b).

Deux types d'objectifs généraux a priori contradictoires me semblent importants à atteindre pour progresser davantage, à savoir a) persévérer dans l'investigation fine des processus pré- et syn-éruptifs d'un système volcanique donné, et b) élaborer des modèles applicables aux mécanismes éruptifs des volcans d'arc en général :

a) Investigation fine des processus pré- et syn-éruptifs. La plupart des projets que j'ai menés jusqu'à présent avaient cet objectif, notamment au travers d'une systématique d'individualisation des effets de différents paramètres sur l'évolution des processus de dégazage, cristallisation ou fragmentation magmatiques. La détermination expérimentale des conditions pré- et syn-éruptives de la Montagne Pelée permet incontestablement de mieux comprendre les modes de stockage et de remplissage de sa chambre magmatique, ainsi que ses conditions d'ascension, étapes indispensables à l'objectif à long terme de la prédiction éruptive. Bien que ce type d'étude soit un travail de longue haleine, en raison notamment de la nécessité de bien connaître les produits naturels et de la lourdeur naturelle de la pétrologie expérimentale, je compte poursuivre ce type d'approche pour d'autres systèmes volcaniques, de manière non restrictive au volcanisme d'arc. J'ai par exemple en cours un projet de détermination des conditions pré-éruptives des trachytes de la Chaîne des Puys (Massif Central), intéressant d'une part localement pour une meilleure compréhension de nos volcans (métropolitains!) et d'autre part, internationalement en raison du manque de données de relations de phases pour les compositions trachytiques pourtant courantes pour le volcanisme de contexte extensif (ex: Italie). Ce projet commencé en collaboration avec Rémi Champallier il y a deux ans a été intégré en Juin 2008 dans une demande d'ANR thématique RISKNAT "REVEIL" (P. Boivin) qui a été refusée en Octobre 2009, et se poursuit actuellement sans financement spécifique. J'ai également en projet la détermination des conditions syn-éruptives de Soufrière Hills à Montserrat, au travers d'une étude des microlites des ponces andésitiques vulcaniennes (dont l'échantillonnage a été effectué au cours de deux campagnes en Juillet 2006 et 2008 dans le cadre de l'ANR CATT "EXPLANT"), pour remonter aux conditions d'ascension d'un magma donnant des éruptions vulcaniennes. Ces deux projets initiés sur la Chaîne des Puys et Montserrat répondent à des problématiques scientifiques ciblées, traitées par des méthodes comparables à celles que j'ai utilisées jusqu'à présent (raison pour laquelle je ne détaille pas davantage ces projets). Par ailleurs, je souhaite apporter de nouvelles informations sur le processus de dégazage, par une étude in-situ du développement de la perméabilité des magmas, dont les intérêts scientifiques et les moyens humains, techniques et financiers sont développés ci-dessous au § III.1.

b) modéliser les mécanismes éruptifs des volcans d'arc, en rassemblant les données systématiquement acquises pour un système volcanique spécifique (composition et conditions définies). La modélisation empirique ou thermodynamique permet une compréhension élargie des processus et une application plus généralisable aux volcans les moins étudiés. Dans ce but, j'envisage une étude de synthèse rassemblant les données compositionnelles et texturales des microlites naturels (Pinatubo: Hammer et al. (1999), Merapi: Hammer et al. (2000); St Helens: Cashman et McConnell (2005); Montagne Pelée: Martel et Poussineau (2007); Soufriere Hills: Clarke et al. (2007) et étude en cours) et d'expériences de décompression (Hammer et Rutherford, 2002; Couch et al., 2003; Martel et Schmidt, 2003; Martel, en préparation; thèse E. Mollard en cours), avec pour objectif une modélisation des conditions d'ascension des magmas andésitiques et des styles éruptifs en résultant. Cette synthèse de données pourraient par ailleurs alimenter des modèles numériques d'écoulement magmatique dans le conduit volcanique (ex: CONFLOW de Mastin et Ghiorso, 2000; Melnik et Sparks, 2002b), en apportant des précisions sur les variations des taux de décompression (linéaires dans ces modèles) et les éventuels paliers isobares à prendre en compte. Ce projet est détaillé au § III.2.

III.2- EVOLUTION DE LA PERMEABILITE DES MAGMAS EN COURS D'ERUPTION

Financements envisagés : Demande de financement Bonus Qualité Recherche (BQR) déposé le 9 Mars 2009 auprès de l'Université d'Orléans (9.1 k€; C. Martel). Projet de financement de plus grande envergure prévu en 2010.

Problématique. Les transitions brutales entre des éruptions explosives et effusives souvent observées sur les volcans des zones de subduction peuvent être appréhendées comme une compétition entre l'augmentation de la pression des gaz au sein du magma menant à des conditions de fragmentation explosive, menant notamment à des éruptions pliniennes (Sparks, 1978; Wilson et al., 1980) ou des nuées ardentes de type vulcanien, péléen ou Merapi (Alidibirov and Dingwell, 1996a) et la perte des volatils qui empêche le développement de larges surpressions gazeuses et permet la densification du magma et sa mise en place effusive (Eichelberger et al., 1986; Jaupart et Allègre, 1991; Woods et Koyaguchi, 1994; Edmonds et al., 2003; Melnik et al., 2005).

Le seuil de fragmentation a longtemps été basé sur le seul critère de la porosité globale du magma, fixé à 70-80 vol% et justifié par l'empilement maximal de sphères (bulles de gaz) pouvant être contenues dans un volume de liquide (Sparks, 1978). Cependant, un certain nombre d'études ont depuis montré que la fragmentation opère sur une gamme de porosités beaucoup plus étendue, ne permettant plus de relier simplement le potentiel explosif d'un magma à sa porosité totale (e.g., Klug et Cashman, 1996). En effet, la capacité d'un magma à perdre ou à conserver ses gaz est liée au caractère connecté ou fermé de son réseau de pores, c'est-à-dire à la géométrie, taille et forme des bulles, plutôt qu'à leur volume total (même si une forte porosité a plus de chance d'être ouverte que fermée). Ainsi, au-delà de la porosité, c'est la perméabilité magmatique qui apparaît comme le facteur déterminant dans le développement du potentiel explosif d'une éruption.

La perméabilité traduit la capacité d'un matériau à laisser passer un fluide au travers de son réseau poreux et est une caractéristique intrinsèque du matériau indépendante du fluide. Dans le cas des magmas, la difficulté provient de la détermination précise du réseau poreux, résultat de plusieurs processus tels que la nucléation, la croissance, la coalescence et la déformation des bulles. Les événements de nucléation de bulles intervenant au cours de l'ascension du magma vont définir une densité numérique de bulles, dont l'importance est de contraindre l'épaisseur de liquide silicaté à amincir pour que deux bulles croissantes puissent entrer en contact. Cependant, même si les bulles entrent en contact, elles ne pourront coalescer que dans des conditions favorables de viscosité du magma et de surface de tension entre le liquide silicaté et le gaz, pouvant alors créer des réseaux de chenaux de bulles le rendant perméable.

Par conséquent, au cours de l'éruption, le réseau poreux du magma est en constante évolution. La connaissance actuelle de l'évolution de la perméabilité des magmas provient d'une combinaison d'études de produits naturels, d'expériences de laboratoire et de simulations numériques. Les perméabilités mesurées sur des pyroclastes volcaniques montrent une gamme allant de 10^{-9} et 10^{-16} m^2 pour des porosités de 2 à 90 vol%, la relation générale entre la perméabilité et la porosité étant de type loi de puissance (Figure 7). On peut y remarquer que la perméabilité des pyroclastes de plus de 65 % de porosité est relativement constante autour de 10^{-12} m^2, alors qu'il existe une variabilité de plus de six ordres de grandeur autour des porosités plus faibles. De même, le seuil de percolation (en dessous duquel la perméabilité est nulle) varie selon les études depuis 60-70 % (Eichelberger et al., 1986; Westrich et Eichelberger, 1994) à ~30 % (Klug and Cashman, 1996; Saar et Manga, 1999; Blower, 2001; Mueller et al., 2005; Burgisser et Gardner, 2005).

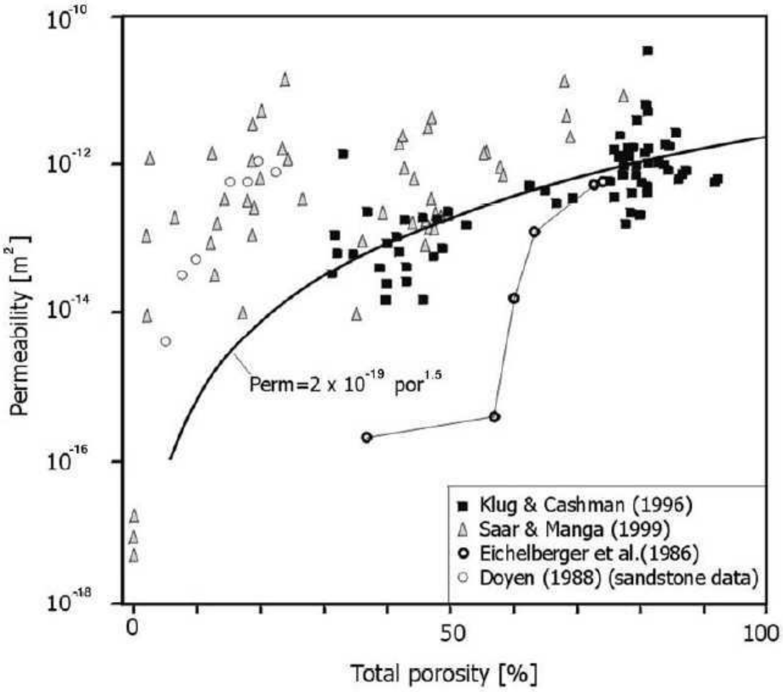

Figure 7. Données de perméabilité en fonction de la porosité (Mueller et al., 2005). La ligne épaisse représente le meilleur fit des données de Klug et Cashman (1996) donnant une équation de la forme : Perméabilité ~ $(\text{Porosité})^{3.5}$.

Ces variabilités autour de la relation perméabilité-porosité peuvent avoir plusieurs explications :

- *le mode de calcul de la perméabilité des produits*. En effet, la loi de Darcy utilisée pour déterminer la perméabilité prédit une relation linéaire entre la vitesse du fluide et le gradient de pression appliqué, soit une validité pour un écoulement laminaire (faible nombre de Reynolds). Cependant, en raison de la fréquente tortuosité du réseau poreux des pyroclastes et/ou d'un fort gradient de pression parfois appliqué pour la mesure de la perméabilité, l'écoulement fluide devient turbulent, et la relation entre la vitesse du fluide et le gradient de pression devient parabolique. Ces considérations nécessitent alors l'insertion de facteurs correctifs à la loi de Darcy, ce qui n'a été pris en compte que dans les travaux les plus récents (Rust et Cashman, 2004; Mueller et al. 2005; Bouvet de Maisonneuve et al., sous presse);
- *des différences dans les facteurs facilitant la coalescence des bulles*, telles qu'une distribution polymodale de taille de bulles ou une anisotropie de forme permettant d'augmenter la perméabilité dans le sens de l'allongement des bulles (Stasiuk et al., 1996; Saar et Manga, 1999; Blower, 2001);
- *des différences de cristallinité ou de fracturation des magmas*, pouvant avoir un effet important sur le seuil de percolation (Blower, 2001; Melnik et Sparks, 2002a).
- *des différences de géométrie et de taille des ouvertures des pores,* surtout pour les faibles porosités, rendant compte d'une hystérésis à porosité égale entre la perméabilité d'un magma en train de vésiculer et celle d'un magma en train de s'effondrer par perte des gaz (Rust et Cashman, 2004).
- *l'hétérogénéité des échantillons naturels d'un même dépôt* quant à la distribution spatiale, la taille, l'orientation des bulles, et la cristallinité peut générer à elle seule plus d'un ordre de grandeur de variabilité de la perméabilité (Mueller et al., 2005).

Projet proposé. Ces fortes variabilités entre le seuil de percolation, la perméabilité et la porosité des magmas, le fait de mesurer les perméabilités sur un échantillon en dehors de son contexte magmatique réel, et au vu de l'importance reconnue du développement de la perméabilité sur le potentiel explosif d'une éruption, je projette une étude de l'évolution de la perméabilité de magmas en contexte éruptif, c'est-à-dire au cours de sa décompression ou de sa déformation, par mesures in-situ de perméabilité au moyen du module de porosimètrie de la presse de déformation de type Paterson de l'ISTO.

La presse Paterson, acquise à l'ISTO en 2005 (Figure 8), est constituée d'un autoclave à chauffage interne (pression d'argon ~1-5 kbars; températures $\leq$ 1400°C) équipé de modules de déformation en torsion et en coaxial (compression/extension), de deux modules de porosimétrie (actuellement en test) et d'une cellule de mesure haute sensibilité spécialement conçue et récemment testée pour l'étude des matériaux peu visqueux (de la gamme des liquides silicatés). Il n'existe actuellement aucune expérience de mesure de la perméabilité de magmas dans des conditions aussi réalistes.

Je propose d'étudier le seuil de percolation et l'évolution de la perméabilité de liquides silicatés bulleux parfaitement caractérisés, par des mesures in-situ de leur perméabilité au cours, 1) d'une décompression pendant laquelle les bulles nucléées grossissent, éventuellement coalescent et se connectent entre elles, et 2) de leur déformation en torsion, c'est-à-dire en fonction de leur nombre capillaire (paramètre décrivant le rapport des forces visant à déformer la bulle sur celles cherchant à maintenir la sphéricité, i.e. le rapport de la vitesse de déformation sur les surfaces de tension), afin de déterminer l'effet de forts allongements des bulles sur leur seuil de connectivité. L'utilisation du module de porosimétrie couplé à une déformation (module de torsion) ou une décompression de l'échantillon constitue un défi technique, notamment en raison des fortes augmentations de volume de l'échantillon induites par le dégazage. Par conséquent, afin d'optimiser ces expériences, un certain nombre de tests préalables sont nécessaires. En particulier, la mise au point d'un protocole est nécessaire pour obtenir des échantillons aux porosités et densités numériques variables et reproductibles. Après l'expérience, les échantillons seront récupérés pour des analyses tridimensionnelles de la porosité par microtomographie X de résolution 1 µm (appareil arrivé à l'ISTO début Mars 2009), permettant de visualiser en trois dimensions la géométrie du réseau poreux.

Figure 8. Presse Paterson de l'ISTO. Autoclave à chauffage interne équipé de modules de déformation en torsion et co-axiale, de deux modules de porosimétrie, et d'une cellule haute sensibilité spécifiquement dédiée à la déformation des matériaux peu visqueux de la gamme des liquides silicatés.

Ce projet est avant tout un défi scientifique, car la naissance et le développement du potentiel explosif d'un magma en cours d'éruption semble étroitement lié au développement de la perméabilité du magma, desservi par un volet expérimental innovant et ambitieux rendu possible par les récentes acquisitions de la presse Paterson et du microtomographe.

Compétences pour la réalisation du projet. La Presse Paterson est un outil que nous maîtrisons à présent au laboratoire (Arbaret et al., 2007; Champallier et al., 2008). Le fonctionnement de la cellule haute sensibilité spécialement dédiée à l'étude des magmas a été validé par les travaux de thèse de D. Picard (soutenue à Orléans en Mars 2009). Des mesures de perméabilité en statique (sans déformation) avec le module de porosimétrie donnent actuellement des résultats très satisfaisants (projet Y. Branquet et S. Sizaret, ISTO). J'apporte mon expertise sur les problématiques de vésiculation des bulles par décompression (Martel et Bureau, 2001; Martel et Schmidt, 2003; Thèse C. Gondé, Orléans 2008).

Financements envisagés. Une demande de financement (9.1 k€) pour une série d'expériences de prospection sur le sujet a été demandée à l'Université d'Orléans (BQR), afin de tester la validité de mesures in-situ de perméabilités magmatiques en décompression et déformation dans la presse Paterson. Les résultats de cette étude conditionneront une demande de financement de plus grande envergure en 2010.

III.3- MODELISATION THERMODYNAMIQUE DE LA CRISTALLISATION PAR DECOMPRESSION

La cinétique de cristallisation des magmas a depuis longtemps été reconnue comme un facteur clef dans l'interprétation des textures des roches ignées, permettant de remonter à leurs conditions de cristallisation à partir de la morphologie de leurs cristaux. En particulier, des expériences en refroidissement à différents *undercooling* (ΔT en °C, différence entre la température liquidus du minéral et sa température réelle de cristallisation) et des simulations numériques ont été développées à partir de liquides pour reproduire les différentes textures cristallines des roches naturelles. Pour des études concernant le plagioclase, phase phénocristalline et microlitique la plus abondante dans les compositions andésitiques à rhyolitiques, on peut citer par exemple les travaux de Lofgren (1980), Kirkpatrick (1981) et références incluses, Loomis (1981), Muncill et Lasaga (1987, 1988), Brandeis et Jaupart (1987), Toramaru (1991, 2001), Kile et Eberl (2003). Bien que les premières études aient longtemps souffert d'un manque de données appropriées (viscosité et diffusivité des éléments dans des liquides silicatés hydratés), résultant en de sévères écarts entre les expériences et les modélisations thermodynamiques (Muncill et Lasaga 1988), elles ont cependant permis de cerner le processus de cristallisation par refroidissement et les paramètres régissant la nucléation, la distribution de taille et la forme des cristaux. Ainsi, la cristallisation est un processus gouverné par les mécanismes de diffusion et d'incorporation des éléments à l'interface liquide/cristal, numérisé en fonction de ΔT par les équations de conservation de masse, de relation d'équilibre thermodynamique liquide/cristal, de cinétique de nucléation et de croissance. Récemment, Toramaru (2001) a apporté des quantifications de l'effet de la vitesse de refroidissement et de différents mécanismes de croissance sur les paramètres de nucléation et de taille des cristaux dans un système eutectique binaire. Ces modélisations thermodynamiques de cristallisation par refroidissement sont encore actuellement en cours d'investigation, notamment avec l'objectif d'un développement pour des systèmes de compositions plus complexes et plus réalistes pour des roches magmatiques.

Les intrusions plutoniques cristallisent préférentiellement par refroidissement au cours de leur emplacement à une profondeur donnée (pression constante, température décroissante). En revanche, les roches volcaniques en cours d'éruption cristallisent plutôt par perte en volatils du magma en réponse à la décompression adiabatique (température constante, pression décroissante). Quelques études expérimentales récentes ont été menées pour déterminer l'effet de la vitesse et de la magnitude de la décompression de liquides rhyolitiques saturés en eau sur les modalités de cristallisation (dominance de la nucléation versus croissance) et sur les caractéristiques texturales et compositionnelles des cristaux

(Hammer et Rutherford, 2002 ; Martel et Schmidt, 2003 ; Couch et al., 2003 ; Martel, en préparation). A partir de ces données expérimentales, j'envisage de développer des modélisations thermodynamiques de la croissance des plagioclases, valides pour une gamme déterminée de compositions et de conditions de pression, température et teneur en volatils, et avec une application spécifique à l'ascension de magmas riches en silice dans un conduit volcanique. L'idée est d'adapter pour une cristallisation isotherme par décompression, les modélisations existantes de nucléation et de croissance isobares des plagioclases par refroidissement, dont la base est la théorie classique de la nucléation cristalline et les différents modèles de croissance (par diffusion et/ou mécanismes à l'interface liquide/solide). La différence de température ΔT représentant le moteur de la cristallisation isobare se retrouve également au cours de la décompression isotherme d'un liquide silicaté saturé en eau, puisque que la température d'apparition du plagioclase augmente avec la perte en eau (Figure 9). Une première approche de modélisation de la nucléation des plagioclases par décompression a été réalisée par Hammer (2004), à partir des résultats des expériences de décompression d'un liquide rhyolitique saturé en eau (Hammer et Rutherford, 2002). En ce qui concerne la croissance des plagioclases, je propose une première approche par réitérations d'une croissance isobare à chaque pas de la décompression. La modélisation de la croissance cristalline envisagée ici apparaît déjà relativement complexe, notamment en raison des différents mécanismes potentiels de croissance du plagioclase. Cependant, la croissance cristalline est un processus largement étudié par la communauté scientifique des Sciences de la Terre, de l'Univers, et des Matériaux, offrant un choix de collaborations. La finalité de ce projet est de pouvoir remonter aux conditions d'ascension d'un magma (notamment les vitesses d'ascension) à partir d'une seule étude des microlites et des verres naturels des produits éruptifs d'un volcan, par l'application d'une équation de nucléation et de croissance cristalline.

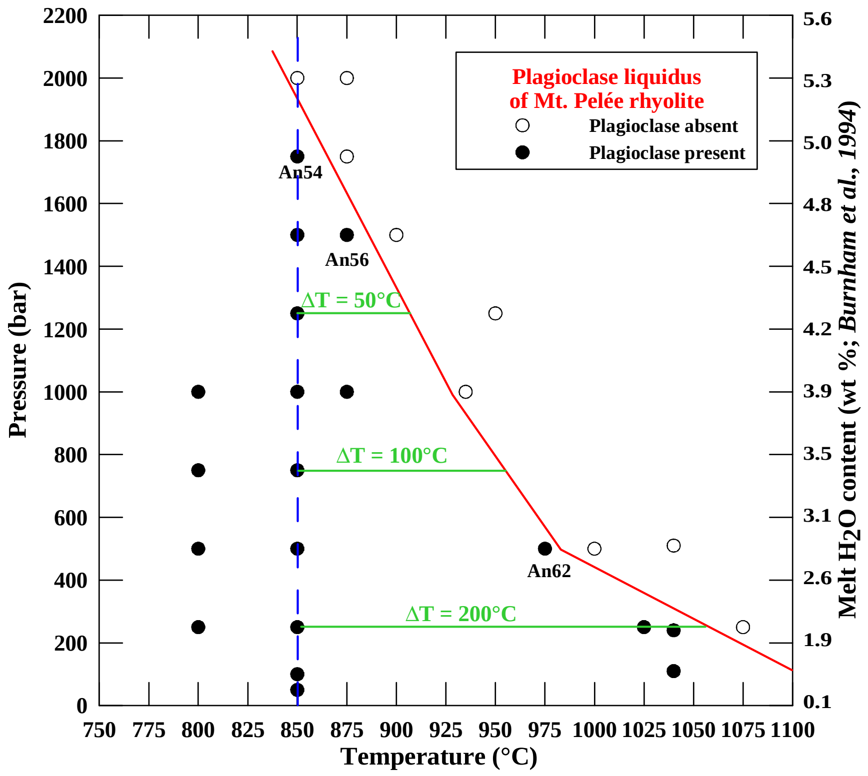

Figure 9. Condition pression - température d'apparition du plagioclase dans le verre rhyolitique saturé en eau de la Montagne Pelée (Martel, en prép.). A une pression donnée, l'*undercooling* ΔT responsable de la morphologie du plagioclase (i.e., tabulaire, squelettique, dendritique) est la différence entre la température du liquidus et la température réelle de cristallisation du plagioclase (ΔT = 100°C à 750 bars et 850°C); An54 à A62 représente le pourcentage molaire d'anorthite du plagioclase au liquidus.

Afin de démarrer ce projet, j'ai proposé en 2007 un sujet de thèse ayant pour objectif l'acquisition de données expérimentales de nucléation et de croissance de plagioclase par décompression et leur modélisation thermodynamique.

Thèse : Edith MOLLARD (débutée Septembre 2007, Orléans) *Cinétiques syn-éruptives de croissance des plagioclases dans les magmas différenciés.*
Direction : J.-L. Bourdier ; **Encadrement :** C. Martel.
Financements : Bourse MRT. **Moyens** : ANR CATT "EXPLANT" (C. Martel) 03/2006-06/2009.

Le sujet consiste dans un premier temps à obtenir un modèle empirique de nucléation et de croissance de plagioclase par décompression isotherme d'un liquide silicaté saturé en eau, à partir de données expérimentales obtenues par expériences de décompression sériées en temps, puis d'élaborer un modèle thermodynamique en accord avec les données expérimentales. L'application principale de cette modélisation est la détermination des vitesses d'ascension d'un magma à partir de l'étude texturale et compositionnelle de ses microlites de plagioclase.

Les expériences de décompression sont réalisées à partir de deux verres de départ préparés par SCHOTT AG (Allemagne): une haplotonalite (77.5 pds% SiO_2 ; Norme CIPW : $Qz_{36}Ab_{55}An_9$) volontairement simple de composition pour faciliter la future modélisation thermodynamique, et le verre interstitiel rhyolitique de la Montagne Pelée (76 pds% SiO_2 ; Norme CIPW : $Qz_{39}Ab_{31}Or_{12}An_{11}Hy_5Co_1Ilm_1$) pour une composition chimique plus réaliste. Ces deux compositions sont préalablement saturées en eau (6-7 % H_2O) à 2 kbars et 875°C dans des autoclaves à chauffage interne (ISTO), puis décomprimés à partir de 2 kbars et 875°C dans des autoclaves à chauffage externe et trempe rapide (ISTO). Deux séries d'expériences sont réalisées : des décompressions rapides (~10 min) jusqu'à une pression finale variable entre 2000 et 100 bars et des décompressions suivant des taux variables entre 0.01 et 10 bar/min. Les deux séries d'expériences sont sériées en temps, trempées après quelques heures jusqu'à plusieurs semaines, afin d'étudier les cinétiques des processus. Les taux de nucléation et de croissance des plagioclases sont déduits respectivement du nombre et des paramètres de formes des cristaux, analysés par traitement d'image et par microtomographie X (appareil arrivé à l'ISTO début Mars 2009). La modélisation thermodynamique de la cristallisation sera préférentiellement réalisée à partir des expériences dans lesquelles la croissance du plagioclase est isobare (composition fixe, analysée par microsonde électronique). Les discussions inhérentes à ce sujet découleront de la comparaison entre:

- l'haplotonalite et la rhyolite de la Montagne Pelée, permettant d'apprécier l'influence de la composition chimique sur le processus de cristallisation ;
- les produits expérimentaux et naturels de la Montagne Pelée (Martel et Poussineau, 2007; Martel, en prép.) permettant d'interpréter au plus près les conditions de cristallisation des microlites naturels ;
- la composition de la Montagne Pelée et celle de Soufrière Hills (Montserrat) au travers des textures et compositions des microlites des ponces vulcaniennes, permettant de valider le caractère plus général du modèle élaboré.

Bien que la réalisation des expériences ne nécessite pas de développements techniques particuliers par rapport au dispositif en place, le programme expérimental de ce projet est relativement chargé, notamment en raison de la systématique recherchée et des sériages en temps des expériences. Le temps passé à constituer une base de données expérimentales de qualité pour le travail de modélisation thermodynamique de la croissance cristalline se fait évidemment au détriment du temps restant pour la modélisation, dont la réalisation apparaît déjà ardue dans le cas présent de compositions liquides et cristallines complexes et en simulation de décompression (impliquant des changements de compositions et de rhéologie). Cependant, les principes de base de la modélisation devraient être posés, probablement en collaboration avec des thermodynamiciens spécialistes de la croissance cristalline, et permettre de poursuivre les recherches hors du cadre de cette thèse.

Ce projet général de modélisation thermodynamique de la croissance des plagioclases par décompression bénéficiera de deux projets complémentaires présentés ci-dessous permettant de progresser dans la compréhension du processus de cristallisation des microlites : le développement d'un modèle de solubilité de l'eau dans les plagioclases et une étude expérimentale du bilan thermique au cours de l'ascension d'un magma.

Etude complémentaire

Solubilité de l'eau dans les plagioclases

Collaborations : E. Deloule (CRPG Nancy), H. Bureau (IMPMC Paris 7).
Financements envisagés : Demande de temps de faisceau à la microsonde ionique du CRPG Nancy et à la microsonde nucléaire de Saclay.

La teneur en éléments volatils dissous dans un verre résiduel peut rendre compte de la pression de trempe du magma grâce à des modèles de solubilité des volatils (ex: Burnham et al., 1994). On peut également remonter aux conditions P-T de formation d'un assemblage naturel de plagioclase + liquide silicaté, à partir de séries d'expériences d'équilibre de phases et des analyses chimiques des cristaux, des verres et de leurs volatils dissous (Putirka, 2005). Une alternative à la lourdeur expérimentale et analytique de cette approche pourrait être apportée par des méthodes d'analyse de l'eau dans les plagioclases, avec l'espoir que la teneur en eau dissoute dans le plagioclase soit significativement dépendante de la pression d'eau du liquide silicaté à partir duquel il cristallise. Récemment, des mesures de teneur en eau dans des feldspaths potassiques ont été obtenues par des méthodes spectroscopiques (infrarouge et résonance magnétique nucléaire), suggérant 365 à 915 ppm d'eau dans des anorthoses (Xia et al., 2006), 1000-1400 ppm dans un microcline, 170 ppm dans une sanidine (Johnson et Rossman, 2003), et jusqu'à 900 ppm dans des plagioclases (Xia et al., 2006; Yang et al., 2008). Ces études ne cachent néanmoins pas la difficulté à interpréter les spectres obtenus, en raison de la présence dans ce groupe minéral de la plus large gamme d'espèces hydroxylées différentes (OH^-, H_2O, NH_4^+), surajoutée à la présence de micro-inclusions fluides, de molécules organiques de surface et à la complexité naturelle du réseau cristallin des tectosilicates. Bien que les feldspaths volcaniques ne contiennent a priori que l'espèce structurale OH, la forme et la position des pics obtenus par infrarouge sont dépendantes de la composition du cristal (Johnson et Rossman, 2004).

Par conséquent, Etienne Deloule, co-auteur des publications précédentes concernant l'analyse de l'eau par spectroscopie infrarouge dans des plagioclases du faciès granulitique (Xia et al., 2006 et Yang et al., 2008), a initié un projet d'analyse de l'eau dans les plagioclases par des méthodes de faisceau d'ions, afin d'établir une relation entre les conditions de cristallisation d'un plagioclase et sa teneur en eau intrinsèque. Des analyses préliminaires de l'eau dans des plagioclases expérimentaux par sonde ionique ont été réalisées dans le cadre de l'ANR CATT "EXPLANT" (C. Martel), laissant supposer des teneurs relativement élevées (~2000 ppm) et des feldspaths et plagioclases standards aux compositions homogènes ont été définis (orthose, anorthite, albite) afin de pouvoir poursuivre le travail sur les plagioclases expérimentaux. Il s'agit maintenant de réaliser des analyses plus systématiques, afin de déterminer les paramètres influençant la teneur en eau des plagioclases expérimentaux (pression, température, composition du liquide initial, etc…). L'application volcanologique de ces corrélations est la possibilité de déterminer directement les conditions (notamment la pression) de cristallisation d'un plagioclase naturel à partir de sa teneur en eau, et de remonter ainsi à l'histoire du stockage et de l'ascension du magma dans le conduit volcanique. Les difficultés majeures de ce projet sont avant tout la résolution spatiale de la microsonde ionique face à des cristaux expérimentaux d'au mieux 20 µm de large (5-10 µm en moyenne) et les faibles teneurs suspectées à des pressions < 2 kbars.

En parallèle de la sonde ionique, une autre technique d'analyse par faisceau d'ions, l'ERDA (Elastic Recoil Detection Analysis), a récemment été utilisée avec succès pour la détermination des teneurs en eau de pyroxènes mantelliques (Bureau et al., 2003). Cette méthode permet le dosage d'éléments légers comme l'hydrogène par détection des atomes de recul sous un faisceau incident d'hélium accélérés à quelques MeV. Nous avons décidé en collaboration avec Hélène Bureau de tenter l'analyse des plagioclases naturels et expérimentaux, avec le même objectif que précédemment, à savoir la détermination d'un géobaromètre à partir des teneurs en eau des plagioclases. L'analyse de l'eau par ERDA constitue un défi technique, notamment en ce qui concerne la résolution spatiale. En effet, l'analyse de l'hydrogène s'opère en mode incliné (70° entre le faisceau d'ions et la surface de l'échantillon), soit une résolution spatiale minimale de 2 x 8 µm (pour des microlites, rappelons-le, de 5-10 µm en moyenne, 20-50 µm au maximum). Cependant récemment, des avancées techniques prometteuses ont été réalisées concernant notamment la résolution spatiale (µ-ERDA ; Raepsaet et al., 2008). En outre, cette méthode présente l'avantage d'une analyse non destructive (permettant la validation de la mesure par d'autres méthodes analytiques), d'une très haute sensibilité de détection (appréciable pour les faibles teneurs en eau attendues), et d'une option cartographie permettant d'une part l'analyse simultanée des cristaux et du verre, et d'autre part l'acquisition d'analyses en éléments majeurs par détection RBS (Rutherford Backscattering Spectrometry ; cinématique similaire à l'ERDA, mais concernant les particules rétrodiffusées). Ce projet faisait initialement partie d'une demande d'ANR Blanc "FLUIBA" (C. Raepsaet, coord.) refusée en septembre 2008. Les premières analyses ERDA à la microsonde nucléaire ont néanmoins été effectuées au LPS à Saclay, en Novembre 2008 grâce à l'acceptation de ma demande de temps de faisceau (2 UT). Les échantillons analysés sont de larges plagioclases naturels du dôme de 1929 de la Montagne Pelée, révélant des teneurs en eau de 260 ppm pds dans une anorthite 85-90 mol% et 273 ppm dans une anorthite 50-55 mol% (Figure 10). Ces résultats sont en contradiction avec la dépendance à la composition du feldspath de la teneur en eau, suggérée par Johnson et Rossman (2004), mais pourrait s'expliquer par une cristallisation du plagioclase à partir d'un liquide silicaté, aux compositions, températures et pressions totales certes différentes, mais à la teneur en eau potentiellement similaire, i.e., ~6 pds% (Martel et al., 1998; Pichavant et al., 2002). Une nouvelle demande de temps de faisceau à la microsonde nucléaire a été déposée en Février 2009 pour rechercher une éventuelle dépendance de la teneur en eau du plagioclase avec la pression partielle d'eau dans le liquide silicaté à partir duquel il cristallise.

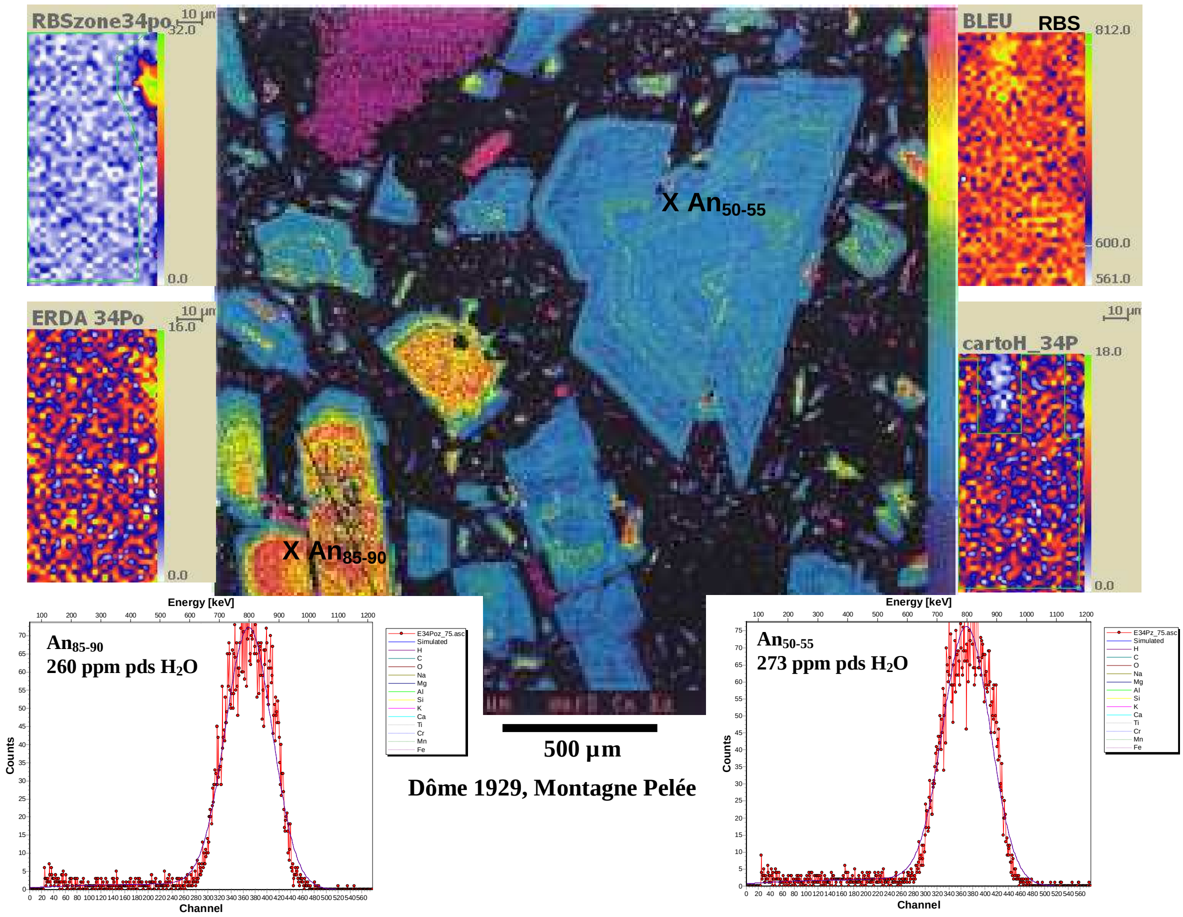

Figure 10. Analyse de l'eau par ERDA dans deux plagioclases du dôme de 1929 de la Montagne Pelée. Au centre, cartographie en calcium par microsonde électronique (Martel, thèse 1996); en haut, cartographie RBS; dessous, cartographies ERDA; en bas, spectres ERDA traités par le logiciel RISMIN.

Etude complémentaire

Bilan thermique de dégazage et de cristallisation d'un liquide rhyolitique

Collaboration : R. Champallier (ISTO)
Financements envisagés : à déterminer.

La motivation de cette étude est d'estimer la pertinence du choix d'une température constante pour les simulations expérimentales et numériques de l'ascension du magma dans un conduit. En effet, bien que de récentes études par mesures calorimétriques suggèrent que les variations de températures liées à l'exsolution de l'eau soient négligeables (± quelques degrés jusqu'à 5 pds% d'eau exsolvée ; Richet et al., 2006), la détente du gaz exsolvé est une réaction globalement endothermique (Sahagian et Proussevitch, 1996), alors que la cristallisation de microlites est exothermique. Il a été récemment proposé que la chaleur latente de cristallisation au cours de l'ascension du magma pouvait atteindre 100°C (Couch et al., 2001 ; Blundy et al., 2006).

Avec l'objectif d'apporter de nouvelles informations obtenues par une approche expérimentale, et parce que je suis un peu sceptique sur la possibilité d'augmenter la température du magma de 100°C par chaleur latente de cristallisation (d'autant plus que l'étude de Blundy et al. (2006) repose sur différents géothermomètres appliqués à des phases naturelles facilement rééquilibrables ou modifiables au cours de l'ascension), je propose de mesurer les variations de températures liées la cristallisation et au dégazage syn-éruptifs. L'ascension du magma sera simulée par des expériences de décompressions d'un liquide silicaté hydraté dans des autoclaves à chauffage externe et trempe rapide. Différents taux de décompression seront testés afin de mesurer les variations de température liées 1) au dégazage de l'eau non accompagné de cristallisation; 2) à la cristallisation sans contribution du dégazage ; et 3) au processus couplé dégazage et cristallisation proche des conditions naturelles. L’application directe de ce projet est d’obtenir un bilan thermique dégazage + cristallisation pour différentes vitesses d’ascension et scénarios éruptifs réalistes de volcans d’arc, permettant de réajuster au plus près les paramètres des simulations expérimentales et numériques de ces éruptions.

REFERENCES BIBLIOGRAPHIQUES

Alidibirov M. and Dingwell D.B. (1996a) Magma fragmentation by rapid decompression. Nature 380, 146-148.

Alidibirov M. and Dingwell D.B. (1996b) An experimental facility for the investigation of magma fragmentation. Bull. Volcanol. 58, 411-416.

Arbaret L., Bystricky M., and Champallier R. (2007) Microstructures and rheology of hydrous synthetic magmatic suspensions deformed in torsion at high pressure. J. Geophys. Res. B112, B10208.

Blower J.D. (2001) Factors controlling permeability-porosity relationships in magma. Bull. Volcanol. 63, 497-504.

Blundy J., Cashman K.V., and Humphreys M.C.S. (2006) Magma heating by decompression-driven crystallization beneath andesite volcanoes. Nature 443, 76-80.

Bouvet de Maisonneuve C., Bachmann O., and Burgisser A. (in press) Characterization of juvenile pyroclasts from the Kos Plateau Tuff (Aegean Arc): insights into the eruptive dynamics of a large rhyolitic eruption. Bull. Volcanol.

Brandeis G. and Jaupart C. (1987) The kinetics of nucleation and crystal growth and scaling laws for magmatic crystallization. Contrib. Mineral. Petrol. 96, 24-34.

Browne B.L., Eichelberger J.C., Patino L.C., Vogel T.A., Uto K., and Hoshizumi H. (2006) Magma mingling as indicated by texture and Sr/Ba ratios of plagioclase phenocrysts from Unzen volcano, SW Japan. J. Volcanol. Geotherm. Res. 154, 103-116.

Bureau H., Trocellier P., Shaw C., Khodja H., Bolfan-Casanova N., and Demouchy S. (2003) Determination of the concentration of water dissolved in glasses and minerals using nuclear microprobe. Nucl. Instr. Methods Phys. Res. B210, 434-440

Burgisser A. and Gardner J.E. (2005) Experimental constraints on degassing and permeability in volcanic conduit flow. Bull. Volcanol. 67, 42-56.

Burnham C.W. (1994) Development of the Burnham model for prediction of H_2O solubility in magmas. In Volatiles in Magmas, M.R. Carroll and J.R. Holloway eds. Reviews in mineralogy, 30, Mineral. Soc. Am. 123-129.

Cashman K.V. and McConnell S.M. (2005) Multiple levels of magma storage during the 1980 summer eruptions of Mount St. Helens, WA. Bull. Volcanol. 68, 57-75.

Champallier R., Bystricky M., and Arbaret L. (2008) Experimental investigation of magma rheology at 300 MPa: From pure hydrous melt to 76 vol.% of crystals. Earth Planet. Sci. Lett. 267, 571-583.

Clarke A.B., Stephens S., Teasdale R., Sparks R.S.J., and Diller K. (2007) Petrologic constraints on the decompression history of magma prior to Vulcanian explosions at the Soufrière Hills volcano, Montserrat. J. Volcanol. Geotherm. Res. 161, 261-274.

Couch S., Sparks, R.S.J., and Carroll M.R. (2001) Mineral disequilibrium in lavas explained by convective self-mixing in open magma chambers. Nature 411, 1037-1039.

Couch S., Sparks, R.S.J., and Carroll M.R. (2003) The kinetics of degassing-induced crystallization at Soufrière Hills volcano, Montserrat. J. Petrol. 44, 1477-1502.

Dingwell D.B. (1996) Volcanic Dilemma: flow or blow? Science 273, 1054-1055.

Dingwell D.B. (1998) The glass transition in hydrous granitic melts. Phys. Earth Planet. Int. 107, 1-8.

Dingwell D.B. and Webb S.L. (1990) Relaxation in silicate melts. Eur. J. Mineral. 2, 427-449.

Doyen P.M. (1988) Permeability, conductivity, and pore geometry of sandstone. J. Geophys. Res. 93, 7729-7740.

Dunbar N.W. and Hervig R.L. (1992) Petrogenesis and volatile stratigraphy of the Bishop Tuff: Evidence from melt inclusion analysis. J. Geophys. Res. 97, B11, 15129-15150.

Edmonds M., Oppenheimer C., Pyle D.M., Herd R.A., and Thompson G. (2003) SO_2 emissions from Soufrière Hills Volcano and their relationship to conduit permeability, hydrothermal interaction and degassing regime. J. volcanol. Geotherm. Res. 124, 23-43.

Eichelberger J.C., Carrigan C.R., Westrich H.R., and Price R.H. (1986) Non-explosive silicic volcanism. Nature 323, 598-602.

Gardner J.E., Hilton M., and Carroll M.R. (1999) Experimental constraints on degassing of magma : isothermal bubble growth during continuous decompression from high pressure. Earth Planet. Sci. Lett. 168, 201-218.

Gardner J.E., Hilton M., and Carroll M.R. (2000) Bubble growth in highly viscous silicate melts during continous decompression from high pressure. Geochim. Cosmochim. Acta 64, 1473-1483.

Gardner J.E., Thomas R.M.E., Jaupart C., and Tait S. (1996) Fragmentation of magma during plinian volcanic eruptions. Bull. Volcanol. 58, 144-162.

Gondé C., Massare D., Bureau H., Martel C., Pichavant M., and Clocchiatti R. (2006) In situ study of magmatic processes: a new experimental approach. High Pressure Res. 26, 243-250.

Hammer J.E. (2004) Crystal nucleation in hydrous rhyolite: experimental data applied to classical theory. Am. Mineral. 89, 1673-1679.

Hammer J.E., Cashman K.V., Hoblitt R.P., and Newman S. (1999) Degassing and microlite crystallization during pre-climactic events of the 1991 eruption of Mt. Pinatubo, Philippines. Bull. Volcanol. 60, 355-380.

Hammer J.E., Cashman K.V., and Voight B. (2000) Magmatic processes revealed by textural and compositional trends in Merapi dome lavas. J. Volcanol. Geotherm. Res. 100, 165-192.

Hammer J.E. and Rutherford M.J. (2002) An experimental study of the kinetics of decompression-induced crystallization in silicic melts. J. Geophys. Res. 107, ECV8 1-23.

Jaupart C. and Allègre C.J. (1991) Gas content, eruption rate and instabilities of eruption regime in silicic volcanoes. Earth Planet. Sci. Lett. 102, 413-429.

Jaupart C. and Tait S. (1990) Dynamics of eruptive phenomena. In : Modern methods of igneous petrology: understanding magmatic processes, J. Nicholls and J.K. Russell (Eds.). Rev. Mineral., Mineral. Soc. Am. Rev. 24, 213-238.

Johnson E.A. and Rossman G.R. (2003) The concentration and speciation of hydrogen in feldspars using FTIR and ^{1}H MAS NMR spectroscopy. Am. Mineral. 88, 901-911.

Johnson E.A. and Rossman G.R. (2004) A survey of hydrous species and concentrations in igneous feldspars. Am. Mineral. 89, 586-600.

Kaminski E. and Jaupart C. (1998) The size distribution of pyroclasts and the fragmentation sequence in explosive volcanic eruptions. J. Geophys. Res. 103, B12, 29759-29779.

Kile D.E. and Eberl D.D. (2003) On the origin of size-dependent and size-independent crystal growth: influence of advection and diffusion.

Kirkpatrick R.J. (1981) Kinetics of crystallization of igneous rocks. In : Kinetics of geochemical processes, A. Lasaga and R.J. Kirkpatrick (Eds.) Mineral. Soc. Am. Washington D.C. 8, 321-397.

Klug C. and Cashman K.V. (1996) Permeability development in vesiculating magmas: implications for fragmentation. Bull. Volcanol. 58, 87-100.

Lofgren G. (1980) Experimental studies on the dynamic crystallization of silicate melts. In : Physics of magmatic Process, R.B. Hargraves (Ed.). Princetown Univ. Press, 488-551.

Loomis T.P. (1981) An investigation of disequilibrium growth processes of plagioclase in the system anorthite-albite-water by methods of numerical simulation. Contrib. Mineral. Petrol. 76, 196-205.

Mangan M. and Sisson T. (2000) Delayed, disequilibrium degassing in rhyolite magma: decompression experiments and implications for explosive volcanism. Earth Planet. Sci. Lett. 183, 441-445.

Martel C., Bourdier J.-L., Pichavant M., Traineau H. (2000a) Textures, water content and degassing of silicic andesites from recent plinian and dome-forming eruptions at Mount Pelee volcano (Martinique, Lesser Antilles arc). J. Volcanol. Geotherm. Res. 96, 191-206.

Martel C. and Bureau H. (2001) In-situ high-pressure and high-temperature bubble growth in silicic melts. Earth Planet. Sci. Lett. 191, 115-127.

Martel C., Pichavant M., Bourdier J.-L., Traineau H., Holtz F., and Scaillet B. (1998) Magma storage conditions and control of eruption regime in silicic volcanoes: experimental evidence from Mt. Pelée. Earth Planet. Sci. Lett. 156, 89-99.

Martel C., Pichavant M., Holtz F., Scaillet B., Bourdier J.-L., and Traineau H. (1999) Effect of fO_2 and H_2O on andesite phase relations between 2 and 4 kbars. J. Geophys. Res. 104, 29453-29470.

Martel C., Dingwell D.B., Spieler O., Pichavant M., and Wilke M. (2000b) Fragmentation of foamed silicic melts: an experimental study. Earth Planet. Sci. Lett. 178, 47-58.

Martel C., Dingwell D.B., Spieler O., Pichavant M. and Wilke M. (2001) Experimental fragmentation of crystal- and vesicle-bearing silicic melts. Bull. Volcanol. 63, 345-359.

Martel C. and Poussineau S. (2007) Diversity of eruptive style inferred from the microlites of Mt. Pelée andesite (Martinique, Lesser Antilles). J. Volcanol. Geotherm. Res. 166, 233-254.

Martel C., Radadi Ali A., Poussineau S., Gourgaud A., and Pichavant M. (2006) Basalt-inherited microlites in silicic magmas: evidence from Mt. Pelée (Martinique, F.W.I.). Geology 34, 905-908.

Martel C. and Schmidt B.C. (2003) Decompression experiments as an insight into ascent rates of silicic magmas. Contrib. Mineral. Petrol. 144, 397-415.

Marti J., Soriano C., Dingwell D.B. (1999) Tube pumices as strain markers of the ductile-brittle transition during magma fragmentation. Nature 402, 650-653.

Mastin L.G. and Ghiorso M.S. (2000) A Numerical Program for Steady-State Flow of Magma-Gas Mixtures Through Vertical Eruptive Conduits.USGS Open-File Report 00-209.

Melnik O., Barmin A.A., and Sparks R.S.J. (2005) Dynamics of magma flow inside volcanic conduits with bubble overpressure buildup and gas loss through permeable magma. J. Volcanol. Geotherm. Res. 143, 53-68.

Melnik O. and Sparks R.S.J. (2002a) Dynamics of magma ascent and lava extrusion at Soufriere Hills Volcano, Montserrat. In : The eruption of Soufriere Hills Volcano, Montserrat, from 1995 to 1999, T.H. Druitt and B.P. Kokelaar (Eds.). Geol. Soc. London Mem. 21, 153-171.

Melnik O. and Sparks R.S.J. (2002b) Modeling conduit flow dynamics during explosive eruptions at Soufriere Hills Volcano, Montserrat. Geol. Soc. London Mem. 21, 307-317**.**

Morgan D.J. and Jerram D.A. (2006) On estimating crystal shape for crystal size distribution analysis. J. Volcanol. Geotherm. Res. 154, 1-7.

Mourtada-Bonnefoi C. and Laporte D. (2002) Homogeneous bubble nucleation in rhyolitic magmas : an experimental study of the effect of H_2O and CO_2. J. Geophys. Res. 107(B4) 10.1029/2001JB000290.

Mourtada-Bonnefoi C. and Laporte D. (2004) Kinetics of bubble nucleation in a rhyolitic melt: an experimental study of the effect of ascent rate. Earth Planet. Sci. Lett. 218, 521-537.

Mueller S., Melnik O., Spieler O., Scheu B., and Dingwell D.B. (2005) Permeability and degassing of dome lavas undergoing rapid decompression: an experimental determination. Bull. Volcanol. 67, 526-538.

Muncill G.E. and Lasaga A.C. (1987) Crystal-growth kinetics of plagioclase in igneous systems: one-atmosphere experiments and application of a simplified growth model. Am. Mineral. 72, 299-311.

Muncill G.E. and Lasaga A.C. (1988) Crystal-growth kinetics of plagioclase in igneous systems: isothermal H_2O-saturated experiments and extension of growth model to complex silicate melts. Am. Mineral. 73, 982-992.

Pichavant M., Costa F., Burgisser A., Scaillet B., Martel C., and Poussineau S. (2007) Equilibration scales in silicic to intermediate magmas – Implications for experimental studies. J. Petrol. 48, 1955-1972.

Pichavant M., Martel C., Bourdier J.-L., and Scaillet B. (2002) Physical conditions, structure, and dynamics of a zoned magma chamber: Mount Pelée (Martinique, Lesser Antilles Arc). J. Geophys. Res. 107, N°B5, 10.1029.

Proussevitch A.A. and Sahagian D.L. (1996) Dynamics of coupled diffusive and compressive bubble growth in magmatic systems. J. Geophys. Res. 101, B8, 17447-17455.

Putirka K.D. (2005) Igneous thermometers and barometers based on plagioclase + liquid equilibria: tests of some existing models and new calibrations. Am. Mineral. 90, 336-346.

Raepsaet C., Bureau H., Khodja H., Aubaud C., and Carraro A. (2008) μ-Erda developments in order to improve the water content determination in hydrous and nominally anhydrous mantle phases**.** Nucl. Instr. Methods Phys. Res. B266, 1333-1337.

Richet P., Hovis G., and Whittington A. (2006) Water and magmas: thermal effects of exsolution. Earth Planet. Sci. Lett. 241, 972-977.

Rust A.C. and Cashman K.V. (2004) Permeability of vesicular silicic magma: inertial and hysteresis effects. Earth Planet. Sci. Lett. 228, 93-107.

Rutherford M.J., Sigurdsson H., Carey S., and Davis A. (1985) The may 18, 1980, eruption of Mount St. Helens 1. Melt composition and experimental phase equilibria. J. Geophys. Res. 90, N° B4, 2929-2947.

Saar M.O. and Manga M. (1999) Permeability-porosity relationship in vesicular basalts. Geophys. Res. Lett. 26, 111-114.

Sahagian D.L. (1999) Magma fragmentation in eruptions. Nature 402, 589-591.

Sahagian D.L. and Proussevitch A.A. (1996) Thermal effects of magma degassing. J. Volcanol. Geotherm. Res. 74, 19-38.

Sparks R.S.J. (1978) The dynamics of bubble formation and growth in magmas: a review and analysis. J. Volcanol. Geotherm. Res. 3, 1-37.

Sparks R.S.J. (1997) Causes and consequences of pressurisation in lava dome eruptions. Earth Planet. Sci. Lett. 150, 177-189.

Spieler O., Alidibirov M., and Dingwell, D.B. (2003) Grain-size characteristics of experimental pyroclasts of 1980 Mount St. Helens cryptodome dacite: effects of pressure drop and temperature. Bull. Volcanol. 65, 90-104.

Stasiuk M.V., Barclay J., Carroll M.R., Jaupart C., Ratté J.C., Sparks R.S.J., and Tait S.R. (1996) Degassing during magma ascent in the Mule Creek vent (USA). Bull. Volcanol. 58, 117-130.

Toramaru A. (1991) Model of nucleation and growth of crystals in cooling magmas. Contrib. Mineral. Petrol. 108, 106-117.

Toramaru A. (2001) A numerical experiment of crystallization for a binary eutectic system with application to igneous textures. J. Geophys. Res. 106, 4037-4060.

Tsuchiyama A. (1985) Dissolution kinetics of plagioclase in the melt of the system diopside-albite-anorthite, and the origin of dusty plagioclase in andesites. Contrib. Mineral. Petrol. 89, 1-16.

Venezky D.Y. and Rutherford M.J. (1999) Petrology and Fe-Ti oxide reequilibration of the 1991 Mount Unzen mixed magma. J. Volcanol. Geotherm. Res. 89, Unzen volcano Special issue, 213-230.

Verhoogen J. (1951) Mechanisms of ash formation. Am. J. Sci. 249, 729-739.

Webb S.L. and Dingwell D.B. (1990) The onset of non-Newtonian rheology of silicate melts – A fiber elongation study. Phys. Chem. Min. 17, 125-132.

Westrich H.R. and Eichelberger J.C. (1994) Gas transport and bubble collapse in rhyolitic magma: an experimental approach. Bull. Volcanol. 56, 447-458.

Wilson L., Sparks R.S.J., and Walker G.P.L. (1980) Explosive volcanic eruptions- IV. The control of magma properties and conduit geometry on eruption column behaviour. Geophys. J. R. astr. Soc. 63, 117-148.

Woods A.W. and Koyaguchi T. (1994) Transitions between explosive and effusive eruptions of silicic magmas. Nature 370, 641-644.

Xia Q.K., Yang X.Z., Deloule E., Sheng Y.M., Hao Y.T. (2006) Water in the lower crustal granulite xenoliths from Nushan, eastern China. J. Geophys. Res. 111, B11202.

Yang X.-Z., Deloule E., Xia Q.-K., Fan Q.-C., Feng M. (2008) Water contrast between Precambrian and Phanerozoic continental lower crust in eastern China. J. Geophys. Res., 113, B08207, doi:10.1029/2007JB005541.

Zhang Y. (1999) A criterion for the fragmentation of bubbly magma based on brittle failure theory. Nature 402, 648-650.

LISTE DES PUBLICATIONS

Type de publication	**Total**	**1^er^ auteur**	**2^e^ auteur**	**3 à 5e auteur**
Rang A	14	10	1	3
Congrès	42 (1 invité)	30	6	6
Vulgarisation/Mémoires	3	3	0	0
Séminaires	4	4	0	0

PUBLICATIONS DE RANG A

14) MARTEL C. & POUSSINEAU S. (2007) Diversity of eruptive styles inferred from the microlites of Mt Pelée andesite (Martinique, Lesser Antilles). *J. Volcanol. Geotherm. Res. 166, 233-254.*

13) PICHAVANT M., COSTA F., BURGISSER A., SCAILLET B., **MARTEL C.** & POUSSINEAU S. (2007) Equilibration scales in silicic to intermediate magmas - Implications for experimental studies. *J. Petrol. 48, 1955-1972.*

12) MARTEL C., RADADI ALI A., POUSSINEAU S., GOURGAUD A. & PICHAVANT M. (2006) Basalt-inherited microlites in silicic magmas: evidence from Mt. Pelée (Martinique, F.W.I.). *Geology 34, 905-908.*

11) GONDE C., MASSARE D., BUREAU H., **MARTEL C**., PICHAVANT M., CLOCCHIATTI R. (2006) In situ study of magmatic processes: a new experimental approach. *High Pressure Research 26, 243-250.*

10) MARTEL C. & SCHMIDT B.C. (2003) Decompression experiments as an insight into ascent rates of silicic magmas. *Contrib. Mineral. Petrol. 144, 397-415.*

9) PICHAVANT M., **MARTEL C.**, BOURDIER J.-L. & SCAILLET B. (2002) Physical conditions, structure and dynamics of a zoned magma chamber: Mt. Pelée (Martinique, Lesser Antilles arc). *J. Geophys. Res. 107, 10.1029.*

8) MARTEL C. & BUREAU H. (2001) In-situ high-pressure and high-temperature bubble growth in silicic melts. *Earth Planet. Sci. Lett. 191, 115-127.*

7) MARTEL C., DINGWELL D.B., SPIELER O., PICHAVANT M. & WILKE M. (2001) Experimental fragmentation of crystal- and vesicle-bearing silicic melts. *Bull. Volcanol. 63, 345-359.*

6) MARTEL C., DINGWELL D.B., SPIELER O., PICHAVANT M. & WILKE M. (2000) Foaming and fragmentation in silicic melts: an experimental study. *Earth Planet. Sci. Lett. 178, 47-58.*

5) MARTEL C., BOURDIER J.-L., PICHAVANT M. & TRAINEAU H. (2000) Textures, water content and degassing conditions of silicic andesites from recent plinian and dome-forming eruptions at Mt Pelée, Martinique. *J. Volcanol. Geotherm. Res. 96, 191-206.*

4) SCAILLET B., WHITTINGTON A., **MARTEL C.**, PICHAVANT M. & HOLTZ F. (2000) Phase equilibrium constraints on the viscosity of silicic magmas II. Implication for mafic-silicic mixing processes. *Trans. Roy. Soc. Edinburgh et Geol. Soc. Am. Bull. 91, 61-72.*

3) MARTEL C., PICHAVANT M., HOLTZ F., SCAILLET B., BOURDIER J.-L. & TRAINEAU H. (1999) Effect of fO_2 and H_2O on andesite phase relations between 2 and 4 kbar. *J. Geophys. Res. 104, B12, 29453-29470.*

2) MARTEL C., PICHAVANT M., BOURDIER J.-L., TRAINEAU H., HOLTZ F. & SCAILLET B. (1998) Pre-eruptive conditions and control of explosive volcanism at Mount Pelée (Martinique, F.W.I.). *Earth Planet. Sci. Lett. 156, 89-99*.

1) MARTEL C., LENAT J.-F. & PROVOST A. (1993) Croissance des volcans: l'effet de la mise en place des systèmes intrusifs. *C. R. Acad. Sci. Paris 316, Série II, 677-683*.

Tableau 4. Index de citations des 14 publications numérotées ci-dessus (données ISI Web of Knowledge, au 12 Mars 2009).

N°	Auteurs	Revue	Année	Citations	Citations/an
2)	Martel et al.	EPSL	1998	56	4.7
3)	Martel et al.	JGR	1999	36	3.6
10)	Martel et Schmidt	CMP	2003	30	4.3
6)	Martel et al.	EPSL	2000	22	2.2
5)	Martel et al.	JVGR	2000	22	2.2
7)	Martel et al.	BV	2001	16	1.8
9)	Pichavant et al.	JGR	2002	11	1.4
4)	Scaillet et al.	TRSE	2001	9	1.0
8)	Martel et Bureau	EPSL	2001	8	0.9
13)	Pichavant et al.	JP	2007	4	1.3
12)	Martel et al.	Geology	2006	2	0.5
11)	Gondé et al.	HPR	2006	1	0.2
14)	Martel et Poussineau	JVGR	2007	0	0.0
1)	Martel et al.	CRAS	1993	0	0.0
		Total		**217**	**15.5**

H-INDEX = 8*

** signifie que 8 publications de la liste sont citées au moins 8 fois*

VULGARISATION / MEMOIRES

MARTEL C. (2004) Les volcans de laboratoire. *Journal de la Délégation Centre-Auvergne-Limousin, Microscoop Hors série 12, 6-7.*

MARTEL C. (1996) Conditions pré-éruptives et dégazage des magmas andésitiques de la Montagne Pelée (Martinique, F.W.I.): étude pétrologique et expérimentale. *Thèse de l'Université d'Orléans, 250 p.*

MARTEL C. (1992) Modélisation de la croissance des volcans. Mémoire de DEA, Université de Clermont-Ferrand.

COMMUNICATIONS A DES CONGRES

42) MARTEL C. (2008) Experimentally-determined magma ascent rates at Mt. Pelée (Lesser Antilles). IAVCEI Reykjavik, Islande.

41) MARTEL C., RADADI ALI A., PICHAVANT M. (2008) Magma recharge recorded in microlites: evidence from Mt Pelée (Martinique, lesser Antilles). EUG, Vienne, Autriche (Présentation invitée)**.**

40) MARTEL C., RADADI ALI A., POUSSINEAU S., GOURGAUD A., PICHAVANT M. (2006) Complex microlite genesis in Mt. Pelée andesite (Martinique, F.W.I.). EMPG XI, Bristol, Angleterre.

39) GONDE C., MASSARE D., BUREAU H., **MARTEL C.**, PICHAVANT M., CLOCCHIATTI R. (2005) An experimental tool to look in a magma chamber. AGU, San Francisco, USA.

38) MARTEL C., RADADI ALI A., POUSSINEAU S., PICHAVANT M. (2005) Petrological and experimental constraints on microlite crystallization and degassing at Mount Pelée (Antilles). Meeting: THE SOUFRIÈRE HILLS VOLCANO – TEN YEARS ON, Montserrat.

PICHAVANT M., SCAILLET B. & **MARTEL C**. (2003) Experimental phase equilibria: data and models. ESF (European Science Foundation), Rome, Italy.

37) MARTEL C. & SCHMIDT B.C.(2002) Experimental simulation of Plinian and Pelean magma ascent. IAVCEI Saint Pierre, Martinique, France.

36) MARTEL C., PICHAVANT M., BOURDIER J.-L., SCAILLET B. & TRAINEAU H. (2002) Pre-eruptive conditions of Mount Pelée andesite. IAVCEI Saint Pierre, Martinique, France.

35) POUSSINEAU S., **MARTEL C.**, NAVIERE C., PICHAVANT M., BOURDIER J.-L. & ARBARET L.(2002) Preliminary decompression experiments of 1902 and 1929 andesites from Mount Pelée (Martinique): implications for "Pelean style" degassing. IAVCEI Saint Pierre, Martinique, France.

34) PICHAVANT M., **MARTEL C.**, BOURDIER J.-L. & SCAILLET B.(2002) Physical conditions and dynamics of the Mt. Pelée zoned magmatic system origin of the andesites. IAVCEI Saint Pierre, Martinique, France.

33) MARTEL C. & SCHMIDT B.C.(2002) Simulation de l'ascension de magmas rhyolitiques par des expériences de décompression. 19e RST, Nantes, France.

32) PICHAVANT M., **MARTEL C.**, BOURDIER J.-L. & SCAILLET B.(2002) Stockage pré-éruptif des magmas à la Montagne Pelée: les résultats récents. 19e RST, Nantes, France.

31) POUSSINEAU S., **MARTEL C.**, BOURDIER J.-L., ARBARET L. & PICHAVANT M.(2002) Texture des mésostases des andésites des éruptions de 1090 et 1929 à la Montagne Pelée (Martinique): contraintes sur le dégazage dans le dynamisme éruptif "péléen". 19e RST, Nantes, France.

30) MARTEL C. & SCHMIDT B.C.(2002) Decompression experiments as an insight into ascent rates of silicic magmas. EMPG IX Zürich, Suisse.

29) MARTEL C. & SCHMIDT B.C.(2001) Experimental simulation of the ascent of Soufriere Hills magmas (Montserrat): degassing and crystallisation kinetics. E.U. Access to Research Infrastructures Programme, Verbania, Italie.

28) MARTEL C., DINGWELL D.B., SPIELER O., PICHAVANT M. & WILKE M.(2001) Fragmentation behavior under rapid decompression of bubble- and crystal-bearing silicic melts. PAC RIM IV (An international conference on advanced ceramics and glasses), Maui Hawaii, USA.

27) MARTEL C., DINGWELL D.B., SPIELER O., PICHAVANT M. & WILKE M.(2000) Experimental fragmentation of bubble- and crystal-bearing haplogranite melts. EMPG VIII Bergamo, Italie.

26) MARTEL C., NAVIERE C., PICHAVANT M. & BOURDIER J.-L.(2000) Simulation expérimentale de l'ascension des magmas andésitiques de la Montagne Pelée. 18e RST Paris.

25) PICHAVANT M., **MARTEL C.**, BOURDIER J.-L. & SCAILLET B.(2000) Différentiation et origine des andésites de l'arc Caraïbe: exemple de la Montagne Pelée. 18e RST Paris.

24) MARTEL C., DINGWELL D.B., SPIELER O., PICHAVANT M. & WILKE M.(2000) Experimental fragmentation of crystal- and vesicle-rich magmas. EGS Nice, France.

23) MARTEL C. & BUREAU H.(2000) In-situ high-pressure and high-temperature bubble growth in silicic melts. DMG, Heidelberg, Allemagne.

22) MARTEL C. & BUREAU H. (2000) In-situ high-pressure and high-temperature bubble growth in silicic melts. AGU, San Francisco, USA.

21) MARTEL C., DINGWELL D.B., SPIELER O., PICHAVANT M. & WILKE M. (1999) Foaming and fragmentation in rhyolitic melts. EGS La Haye, Pays-Bas.

20) MARTEL C., DINGWELL D.B., SPIELER O., PICHAVANT M. & WILKE M. (1999) Fragmentation of bubble- and crystal-bearing haplogranite melts : an experimental study. IUGG Birmingham, UK.

19) MARTEL C., DINGWELL D.B., SPIELER O., PICHAVANT M., WILKE M. (1999) Fragmentation of bubble- and crystal-bearing haplogranite melts: an experimental study. AGU San Francisco, USA.

18) DINGWELL D.B, ALIDIBIROV M., **MARTEL C.** and SPIELER O. (1998) In Situ experimental investigation of foaming and fragmentation in viscous magmas: physico-chemical implications for volcanic and sub-volcanic systems. Québec, Canada.

17) MARTEL C., ALIDIBIROV M., PICHAVANT M. & DINGWELL D. (1998) Vesiculated silicic magma fragmentation under rapid decompression: a systematic experimental study. EMPG Orléans, France.

16) MARTEL C., DINGWELL D.B., SPIELER O., PICHAVANT M. & HOLTZ F. (1998) Systematic foaming and fragmentation in synthetic melts. AGU San Francisco, USA.

15) MARTEL C., BOURDIER J.-L., PICHAVANT M., HOLTZ F., SCAILLET B. & TRAINEAU H. (1997) Degassing of plinian versus pelean andesites at Mt Pelée, Martinique. IAVCEI Puerto Vallarta, Mexique.

14) MARTEL C., PICHAVANT M., BOURDIER J.-L. & TRAINEAU H. (1997) Causes of effusive and explosive eruptions of silicic volcanoes: example of Mt Pelée andesites (F.W.I.). EUG Strasbourg, France.

13) MARTEL C., PICHAVANT M., ALIDIBIROV M. & DINGWELL, D. (1997) Systematic experimental investigation of degassing and fragmentation processes in silicic volcanism. Materials Recycling Near Convergent Plate Boundaries Meeting, Puerto Azul, Philippines.

12) MACDONALD R., PICHAVANT M., BOURDIER J.-L. & **MARTEL C.** (1997) Experimental evidence on the origin and fractionation of arc magmas. Materials Recycling Near Convergent Plate Boundaries Meeting, Puerto Azul, Philippines.

11) MARTEL C., PICHAVANT M., BOURDIER J.-L., TRAINEAU H., HOLTZ F. & SCAILLET B. (1996) Experimental studies applied to the dynamics of magmatic systems: the example of Mt Pelée volcano (Martinique, F.W.I.). Magmatic Processes, Bristol, UK.

10) MARTEL C., PICHAVANT M. & BOURDIER J.-L. (1996) Détermination expérimentale des conditions pré-éruptives des andésites de la Montagne Pelée (Martinique) et implication sur les dynamismes éruptifs. 16^{e} RST Orléans, France.

9) PICHAVANT M., BOURDIER J.-L. & **MARTEL C.** (1996) Origine des andésites de la Montagne Pelée (Martinique). 16^{e} RST Orléans, France.

8) BOURDIER J.-L., KOMOROWSKI J.-C., **MARTEL C.**, BOUDON G., PICHAVANT M., TRAINEAU H. & VILLEMANT B. (1996) Morphoscopie et texture des laves des éruptions de 1902 et 1929 à la Montagne Pelée. 16^{e} RST Orléans, France.

7) BOUDON G., KOMOROWSKI J.-C., VILLEMANT B., BOURDIER J.-L., **MARTEL C.**, TRAINEAU H. & PICHAVANT M. (1996) Dynamisme péléen et pliniens lors de l'éruption de 650 ans B.P. à la Montagne Pelée: stratigraphie, lithologie, vésicularité, géochimie des produits. 16^{e} RST Orléans, France.

6) MARTEL C. & PICHAVANT M. (1996) Expériences haute pression appliquées aux processus volcanologiques. Rencontres Hautes Pressions d'Arcachon, France.

5) MARTEL C., PICHAVANT M., BOURDIER J.-L., HOLTZ F. & SCAILLET B. (1996) Phase equilibria of Mt Pelée andesites. EMPG Bayreuth, Allemagne.

4) MARTEL C., PICHAVANT M., HOLTZ F., SCAILLET B., BOURDIER J.-L. & TRAINEAU H. (1996) Andesite storage and control of eruptive style at Mt Pelée. AGU San Francisco USA.

3) PICHAVANT M., **MARTEL C.** & BOURDIER J.-L. (1996) Significance of amphibole in the recent andesites of Mt Pelée. AGU San Francisco, USA.

2) MARTEL C., PICHAVANT M., BOURDIER J.-L., HOLTZ F. & SCAILLET B. (1995) Experimentally determined pre-eruptive conditions (P, T, fH_2O, fO_2) at Mt Pelée, Martinique, with implications for eruptive dynamics. EUG Strasbourg, France.

1) MARTEL C., BOURDIER J.-L., PICHAVANT M. & TRAINEAU H. (1994) Lithology of plinian and pelean juvenile products. IAVCEI Ankara, Turquie.

PRINCIPAUX SEMINAIRES

MARTEL C. (2006) Problématique des inclusions vitreuses des andésites de la Montagne Pelée (Martinique). Centre de Recherches Pétrographiques et Géochimiques, Journées Scientifiques sur les inclusions vitreuses, Nancy.

MARTEL C. (2005) Les volcans de laboratoire. Laboratoire Pierre Süe, Saclay.

MARTEL C. (1999) Foaming and fragmentation in rhyolitique melts. BGI, Bayreuth, Allemagne.

MARTEL C. (1997) Experimental tools applied to volcanological questions. BGI, Bayreuth, Allemagne.